Development of Supramolecular Non-gated and Stimuli-responsive Channels for Selective Ion Transport and Chemotherapeutic Applications

A Thesis

Submitted in Partial Fulfillment of the Requirements

for the Degree of

Doctor of Philosophy

by

Javid Ahmad Malla

ID: 20153373

Research Supervisor: **Dr. Pinaki Talukdar**

Indian Institute of Science Education and Research (IISER), Pune.

2019

भारतीय विज्ञान शिक्षण एवं अनुसंधान संस्थान
INDIAN INSTITUTE OF SCIENCE EDUCATION AND RESEARCH (IISER) PUNE
(An Autonomous Institution of Ministry of Human Resource Development, Govt. of India)
Dr. Homi Bhabha Road, Pune – 411008.

Prof. Pinaki Talukdar
Department of Chemistry,
IISER Pune, Pune
Maharsahtra.
411008.

Certificate

Certified that the work incorporated in the thesis entitled "***Development of Supramolecular Non-gated and Stimuli-responsive Channels for Selective Ion Transport and Chemotherapeutic Applications"*** submitted by **Mr. Javid Ahmad Malla** was carried out by the candidate, under my supervision. The work presented here or any part of it has not been included in any other thesis submitted previously for the award of any degree or diploma from any other university or institution.

Pinaki Talukdar

Date: 13 March 2020 **Prof. Pinaki Talukdar**

Place: Pune (Research Advisor)

Email: ptalukdar@iiserpune.ac.in Tel.: 020 2590 8098 Web: http://www.iiserpune.ac.in/~ptalukdar/

भारतीय विज्ञान शिक्षण एवं अनुसंधान संस्थान
INDIAN INSTITUTE OF SCIENCE EDUCATION AND RESEARCH (IISER) PUNE
(An Autonomous Institution of Ministry of Human Resource Development, Govt. of India)
Dr. Homi Bhabha Road, Pune – 411008.

Declaration

I declare that this written submission represents my ideas in my own words and where other's ideas have been included; I have adequately cited and referenced the original sources. I also declare that I have adhered to all principles of academic honesty and integrity and have not misinterpreted or fabricated any idea/data/fact/source in my submission. I understand that violation of above will cause for disciplinary action by the Institute and can also evoke the penal action from the sources which have thus not been properly cited or from whom proper permission has not been taken when needed.

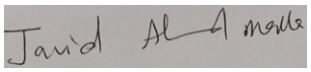

Date: 13 March 2020 **Mr. Javid Ahmad Malla**

Place: Pune ID: 20153373

Acknowledgement

The Ph.D. journey became a very memorable journey of my life with a lot of memories. There were always some people who stood by me in every situation, without whom my journey could have been incomplete. So before I discuss my Ph.D. journey I would like to give my gratitude to them.

I would like to give my sincere thanks to my thesis supervisor Dr. Pinaki Talukdar for his support, encouragement and his priceless suggestions during my entire Ph.D. tenure. I can't forget the kind of inspirations and encouragements that he presented during the tough moments of my journey in his lab. He always stood behind me in every odd and even situation. The freedom he provided me to execute my research projects in the best possible way is worth to remember. I have learned a lot about research planning and execution during discussions with him which has helped me to get an enhanced interest in pursuing research in the future.. Apart from his support in research, he stood and guided me during tough times of my life. His qualities as a supervisor can't be stated in words, I can simply say that without his guidance and persistent support this thesis could not have been completed.

I would like to express my sincere gratitude to my research advisory committee (RAC), Dr. S. G. Srivatsan, Dr. Mayurika Lahiri, and Dr. Sudipta Basu, for their valuable suggestions during the RAC meetings. Through their suggestions, it became possible for me to push my boundaries beyond my thinking.

I am thankful to Dr. Mayurika Lahiri for allowing me to work in her lab. It was like a second lab for me in IISER Pune. The friendly and healthy environment I got from her lab members is worth to remember. In particular, I am thankful to Rintu, Aishwarya, Virender, Abhijit and Rupa from whom I have learned various biological experiments.

I would like to express my gratitude to Dr. Shilpy Sharma (S. P. Pune University) for her valuable discussions and support in making my results and thesis more effective from the experimental point of view. I appreciate her kindness and helping nature. I am also thankful to Dr. Arnab Mukherjee who helped me to give proper theoretical validation to my hypothesis and results.

My sincere thanks to all my lab members Dr. Sharad Deshmukh, Dr. Dinesh Chauhan, Dr. Tanmoy Saha, Dr. Arundhati Roy, Dr. Sopan Shinde, Dr. Harshali, Debashis (Debu), Rashmi, Manzoor, Avisikta, Naveen, Swati, Sandeep, Abhishekh and Akram for maintaining a healthy and friendly environment in the lab. In particular, I would like to give my special gratitude to Dr. Sharad who has trained me during the initial phase of my Ph.D. I always felt encouraged by him. The interactionwe had has helped me a lot in improving my research skills. I am also thankful to Dr. Arundhati Roy and Dr. Tanmoy Saha from whom I learned the various aspects of ion transport.

I am also grateful to all the non-teaching staff including Ms. Swati and Mr. Mahesh (MALDI), Ms. Naina (AFM), Ms, Diplai and Mr, Chinmay (NMR), Mr. Tushar, Mr. Sandeep and Ms. Naina (HRMS), Mr. Mayuresh, Mr. Sanjay, for their constant support.

I am also thankful to my IISER friends including Saleem, Motaleb, Wasim, Nirshad, Zahid, Firdousi, Sarita, Dr. Nayeem (Nayeem Bhai), Danish, Jabed, Nasir, Manish, and Renuka with whom I have spent great and memorable moments of my life. Apart from friends at IISER, I am very grateful to Arif and Farheen who were always a source of encouragement to me throughout my Ph.D. tenure.

I am profoundly grateful to my parents (Mr. Ab. Rashid and Mrs. Hajra) for their unconditional love and support throughout my academic carrier. It is due to their unconditional trust and faith in me that has inspired me to reach this position. It is my great pleasure to acknowledge my late uncle (Mr. Farooq Ahmad) and my late grandparents (Haji Ab. Ahad and Arzaani Bagum) who have always pampered me in every corner of my life. In particular, I am very grateful to my elder brother (Mr. Khalid) for his moral support and guidance which helped me to shape up my academic journey. I am also thankful to my sisters (Ishrat and Rabia) and my sister in law (Nusrat).

I am thankful to IISER Pune for my research fellowship during the course of my Ph.D. Finally, I would like to thank all those people whose names I missed here, despite their unconditional support to make my journey successful. To sum up in a few words…It was a great and wonderful journey…

Table of Contents

Table of Contents

Table of Contents

A

α	Alpha
Å	Angstrom
A	Absorbance
Ar	Aromatic
Ac	Acetyl
ATP	Adenosine Tri-Phosphate
ANOVA	Analysis of variance

B

β	Beta
br	Broad singlet
BLM	Black lipid membrane
Boc	*tert*-Butoxycarbonyl

C

c	Concentration
cm	Centimeter
CF	Carboxyfluorescein
Calc	Calculated
CFTR	Cystic Fibrosis Transmembrane Conductance Regulator
CLC	Chloride Channel
CLCA	Calcium-activated Chloride Channel
CLIC	Chloride intracellular channel protein
CLNS1A	Chloride Nucleotide-Sensitive Channel 1A
$CHCl_3$	Chloroform
$CDCl_3$	Deuterated chloroform
CH_3CN	Acetonitrile
CsCl	Cesium chloride
CCDC	Cambridge Crystallographic Data Centre

D

δ	Delta (Chemical shift)
°C	Degree Celsius
d	Doublet
dd	Doublet of doublet
dt	Doublet of triplet
DPhPC	2-diphytanoyl-*sn*-glycero-3-phosphocholine
DMSO	Dimethylsulfoxide
DMF	Dimethylformamide
DCM	Dichloromethane
DMEM	Dulbecco's Modified Eagle's Medium
DFT	Density Functional Theory

E

EYPC	L-α-phosphatidylcholine from egg-yolk
EC_{50}	Effective concentration at half maximal activity
EtOAc	Ethylacetate
EtOH	Ethanol
Et_3N	Triethylamine
ESI	Electrospray ionization
EDC·HCl	1-(3-Dimethylaminopropyl)-3-ethylcarbodiimide hydrochloride

F

F_t	Fluorescence intensity at time *t*
FBS	Fetal bovine serum

G

G_{hyd}	Free energy of hydration

H

Hz	Hertz
h	Hour
HPTS	8-Hydroxypyrene-1,3,6-trisulfonate trisodium salt
HOBt	Hydroxybenzotriazole
HEPES	4-(2-hydroxyethyl)-1-piperazineethanesulfonic acid
HCl	Hydrochloric acid
HPLC	High performance liquid chromatography
HRMS	High Resolution Mass Spectrometry
HBSS	Hank's balanced salt solution

I

I_F	Normalized Fluorescence Intensity
IR	Infrared spectroscopy

J

J	Coupling constant
J	Joule

K

k	Rate constant
K	Equilibrium constant
K_2CO_3	Potassium carbonate
KCl	Potassium chloride
KBr	Potassium bromide
KOH	Potassium Hydroxide

L

λ	Lambda
LUV	Large unilamellar vesicle

logP	Partition Coefficient
LiCl	Lithium chloride

M

m	Multiplet
M	Molar
μM	Micromolar
μL	Microliter
M.P.	Melting Point
MHz	Mega hertz
min	Minute(s)
max	Maximum
mg	Milligram(s)
mol	Mole
mmol	Millimole(s)
mM	Millimolar
mL	Milliliter
M. Wt.	Molecular weight
MALDI	Matrix Assisted Laser Desorption Ionization
MeOH	Methanol
Me	Methyl
MTT	3-(4,5-dimethylthiazol-2-yl)-2,5-diphenyl tetrazolium bromide
MMP	Mitochondrial membrane potential
MD	Molecular dynamics

N

n	Hill coefficient
nm	Nanometer
nM	nanomolar
NMR	Nuclear magnetic resonance
Na_2SO_4	Sodium sulfate

NaCl	Sodium chloride
NaBr	Sodium bromide
NaI	Sodium iodide
$NaNO_3$	Sodium nitrate
$NaClO_4$	Sodium perchlorate
NaOH	Sodium hydroxide

O

obs	Observed
ORTEP	Oak Ridge Thermal Ellipsoid plot

P

Ph	Phenyl
pM	Picomolar
ppm	Parts per million
pS	Picosiemens
pA	Picoampere
PARP	Poly(ADP- ribose) polymerase
PBS	Phosphate-buffered saline
PTP	Permeability transition pore
PAGE	Polyacrylamide gel electrophoresis
PVDF	Polyvinylidene fluoride

R

R	Ideal gas constant
ρ	Resistivity
rt	Room temperature
RbCl	Rubidium chloride
ROS	Reactive oxygen species

S

s	Second(s)
SCXRD	Single crystal X-ray diffraction
SDS	Sodium dodecyl sulfate

T

t	Triplet
td	Triplet of doublets
t	Time
Tx	Triton X-100
TLC	Thin Layer Chromatography
THF	Tetrahydrofuran
TFA	Trifluoroacetic acid
TBA	Tetrabutyl ammonium
TOF	Time of flight

V

V_m	Membrane Potential
V or Vln	Valinomycin
VDAC	Voltage activated anion channel

Y

Y	Fractional fluorescence intensity

The fundamental aim of this thesis is the development of new artificial ion transport systems for therapeutic applications. The main focus of my research was to develop the biomimetic supramolecular ion channels which can perform the ion transport across the liposomal and cell membrane with potential therapeutic applications. The remarkable challenge was to develop the approaches for the stimulus-responsive nature of the channels which could open new ways to carry out the transport selectively in the desired cells. We have successfully developed new approaches that ensure the disassembly of these supramolecular architectures in the membrane phase and upon specific signal, the self-assembly can be reassured for the formation of an active ion channel. Further, these systems were found to have efficient apoptosis-inducing activity as well as the induction of autophagy in cancer cells. These studies would pave a new way for the developments of therapeutics for cancer treatment.

Chapter 1: Introduction

The transmembrane transport of nutrients (ions and other solutes) is an essential process to ensure the normal physiological functioning of cells. However, this membrane transport is hampered by the selective nature of the cell membrane which allows certain non-polar species to pass through but restricts the movement of polar species like ions and other polar molecules. To ensure the transport of these essential nutrients, nature has endowed cells with special types of machinery in the form of transmembrane proteins (channels and carriers) which ensure these transport processes for maintaining the normal cellular functions. Any defect to these transport systems (channelopathies) causes defective ion transport which is related to a lot of life-threatening diseases like Dent's disease, Barters syndrome, cystic fibrosis, Episodic ataxia, Hyperkalemic periodic paralysis, etc. Along with other therapeutic approaches for these channelopathies, channel replacement therapy is getting the attention of the scientific community which stands as an inspiration for the new developments in the field of artificial ion transport systems. Furthermore, the direct correlation between the apoptosis and ionic influx has again renewed the interests in this research area and more developments are in progress.

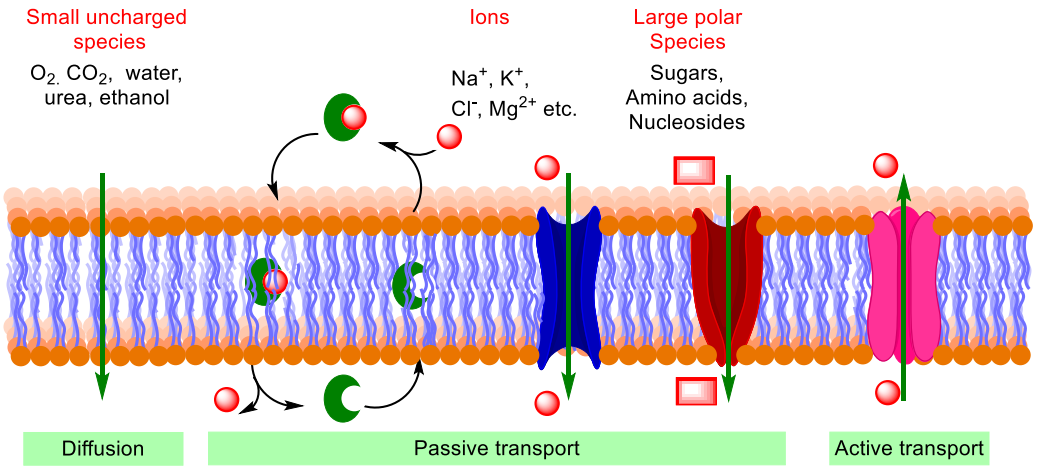

Figure 1. *Schematic representation of membrane transport processes*

Chapter 2: Anion Seletive Ion Channel Constructed from Self-Assembly of Bis-Cholate Substituted Fumaramide

The bis-cholate substituted fumaramide barrel-stave supramolecular anion channel was designed. The positioning of the steric and rigid cholate moieties away from the fumaramide core favored their intermolecular hydrogen-bonded barrel-stave self-assembly in the lipid bilayer membrane. The hydroxyl groups of cholate moieties and alkene π-electron cloud of fumaramides leads to the formation of lumen with polar channel interior, which is suitable for anion binding. Such a channel favors the antiport mechanism of anion transport with the highest selectivity towards the chloride ion. The corresponding *cis* congener was found to be relatively inactive for ion transport at identical concentrations. The planar bilayer conductance measurements confirmed the formation of ion channels of diameter 4.1 ± 0.12 Å and provided additional support to chloride selectivity. The geometry optimized structure of the proposed channel with internal chloride ions confirmed the formation of C=O•••H-N hydrogen-bonded channel and anion recognition by anion-π interactions from electron-deficient C=C moieties and hydrogen bonding from hydroxyl groups.

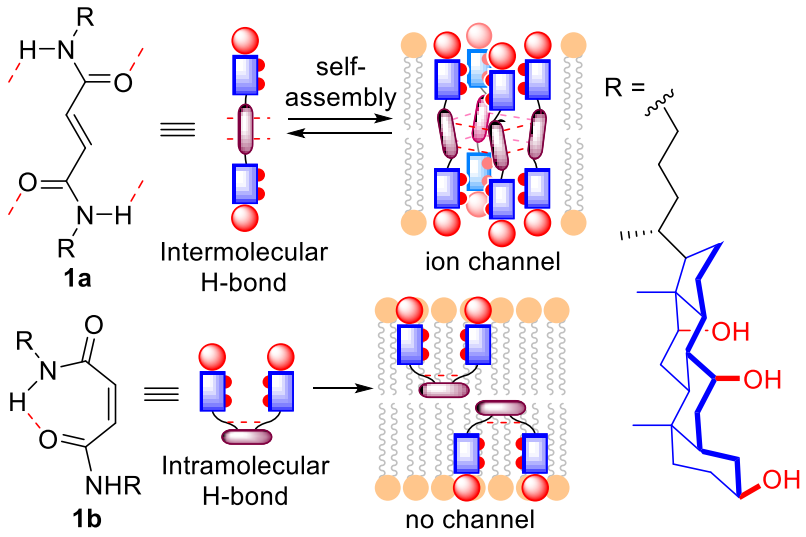

Figure 2. *Schematic representation of the deigned bis-cholate fumaramide based anion channel.*

****

Chapter 3: Apoptosis-Inducing Activity of a Fluorescent Barrel Rosette M^+/Cl^- Channel

We have introduced the concept of inducing the selective membrane filter for M^+/Cl^- transport across the lipid bilayer membrane, through the inherently fluorescent 2-hydroxy-N^1,N^3-diarylisophthalamides which form efficient ion channels in the lipid bilayer membranes. The variation of the aromatic side arms was used to tune the ion transport activity across large

unilamellar vesicles. The channel formation was validated by planar bilayer conductance measurements studies, which gave ion conductance of 100 ± 2 pS. The permeability ratio, P_{Cl^-}/P_{K^+} = 8.29 ± 1, indicates higher selectivity for Cl^- ions compared to K^+ ions. The channel facilitates the transport of chloride, potassium, and sodium across the cellular membrane, and the process resulted in the perturbation of the ionic homeostasis of cells leading to significant cell death through the mitochondrial pathway of apoptosis. These results will help in the future to envision new developments in the field of synthetic ion transport systems for their therapeutic applications.

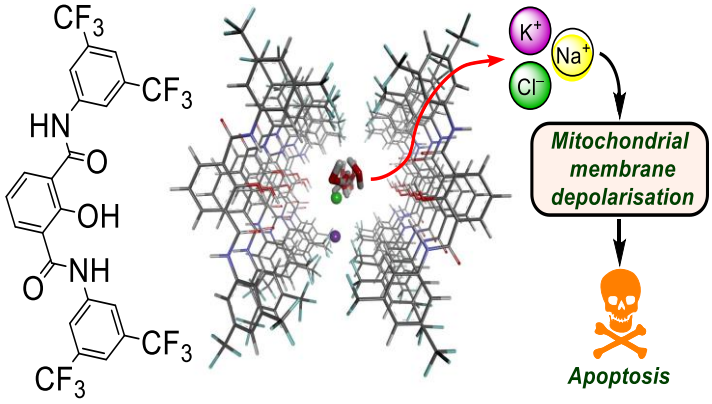

Figure 3. *Schematic representation of the deigned M^+/Cl^- ion channel.*

****

Chapter 4: A Glutathione Activatable Ion Channel Induces Apoptosis in Cancer Cells by Depleting Intracellular Glutathione Levels

Although the synthetic channels can switch the cancer cells to apoptosis, however, the system can't differentiate between healthy cells and cancer cells, along with the cancer cells the innocent healthy cells have to be sacrificed. Therefore, to overcome the problem there is a need to develop stimulus responsive systems which can be activated by a suitable signal. In this regard, intracellular glutathione (GSH) levels of cancer cells, owing to the multiple roles in cancer cells, can be used as stimulus to activate the ion transport process selectively in cancer cells and induce the apoptosis.We have developed a novel glutathione-activatable synthetic ion channel system that induces the caspase-dependent apoptosis in MCF-7 cells. The intracellular glutathione releases the channel-forming N^1,N^3-dialkyl-2-hydroxyisophthalamide system (**1b**) from its 2,4-nitrobenzenesulfonyl (DNS) protected protransporter **2**, which forms transmembrane ion channels capable of conducting M^+/Cl^-symport across biological membranes. This symport is associated with increased ROS levels which in turn reduced intracellular GSH levels; altered mitochondrial membrane permeability (MMP); mediated cytochrome c release associated with activation of caspase 9 and PARP cleavage – the major inducers of apoptosis. These results were further confirmed using a 3D model of MCF-7 cells wherein the addition of compound **2** was

able to restrict growth and proliferation of the spheroids, similar to those reported for DOX – a standard drug used for breast cancer treatment. These studies will provide attractive approaches to explore the application of synthetic ion transport systems for therapeutic approaches.

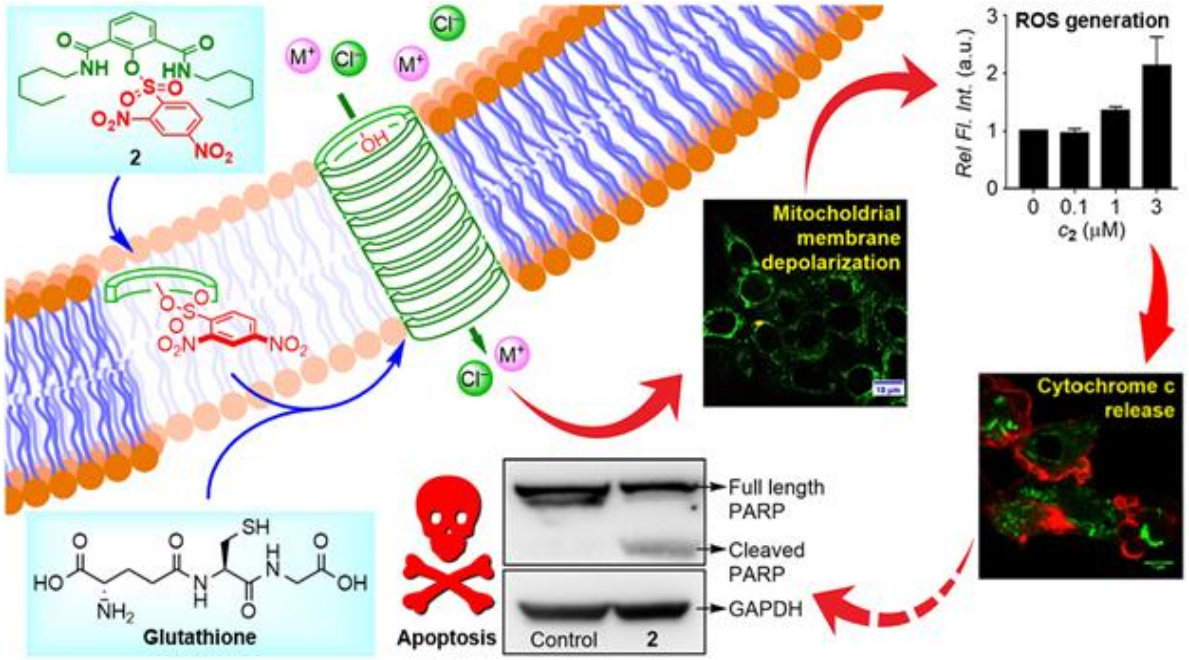

Figure 4. *Schematic representation of the working principle of glutathione activatable ion channel in cells.*

****

Chapter 5: Esterase Activatable Synthetic M^+/Cl^- Channel Induces Apoptosis and Disrupts Autophagy in Cancer Cells

The strategy is of glutathione activatable ion transport in cancer cells is of great potential for next-generation therapeutic applications. However, the next question that pops up is "what is the scope of such systems with respect to the application of different stimuli". In other words, can we use this system by using some other kind of stimulus to activate the ion transport through the channel? Among the different stimuli, enzymes caught our interest. The enzymes serve as gates for activation and deactivation of Na-K-2Cl (NKCC) and K-Cl (KCCs) cotransporters. The gating occurs via phosphorylation and dephosphorylation of serine, threonine and tyrosine units, for both NKCCs and KCCs in a reciprocal manner. The phosphorylation process is known to activate the NKCCs but inhibit KCCs whereas the dephosphorylation activates the KCCs and inhibits the NKCCs. As we have already shown that compound **1b** (from chapter 4) acts as the M^+/Cl^- co-transporting channel, so to make it enzyme responsive can be really an interesting study, as it can be the closest synthetic mimic of NKCCs and KCCs. Further, it will ensure that the different stimuli can be used to activate the transport through the channel, which will help to make it more selective for cancer cells compared to healthy cells. In this chapter, we have

introduced the novel concept of esterase activatable synthetic ion channels which can be activated by intracellular esterase enzymes. The successful activation of ion channel inside cells leads to ion transport across the plasma membrane, which switches the cells to apoptosis through the mitochondrial pathway. Further, the channel can dissipate the pH gradient of the lysosomes, which leads to lysosomal dysfunctions, and ultimately leads to autophagy induction in MCF-7 cells.

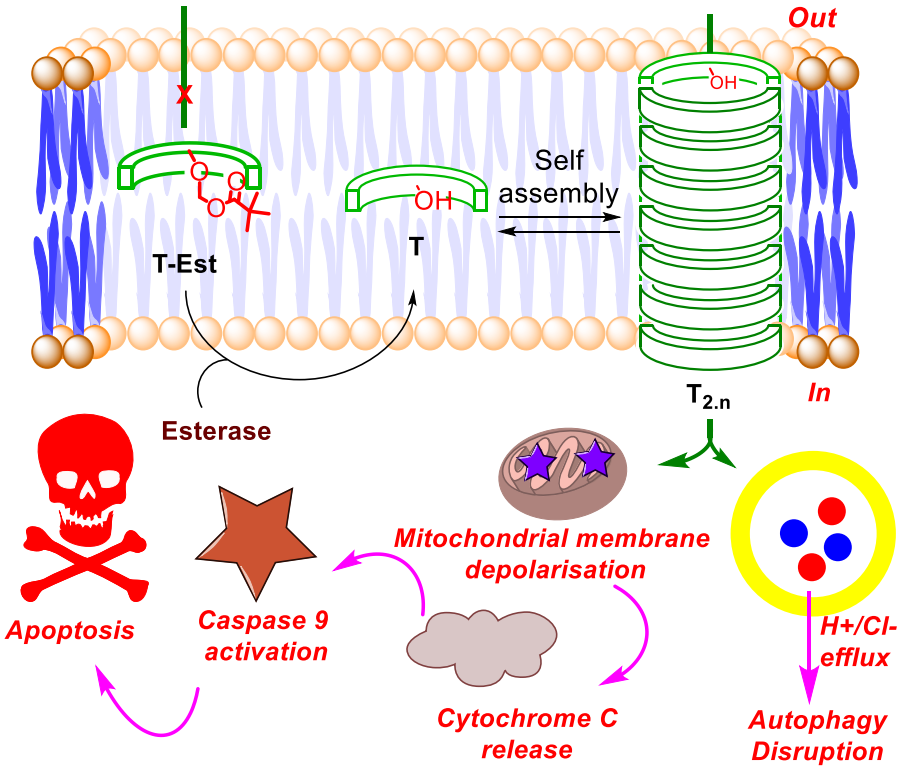

Figure 5. *Schematic representation of the working principle of esterase activatable ion channel in cells.*

Chapter 1

Introduction

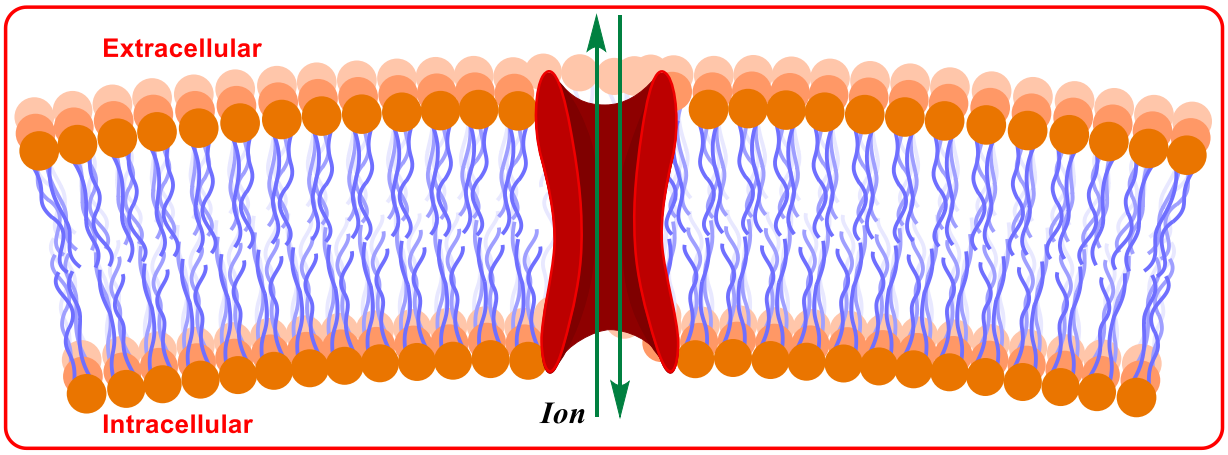

1.1. INTRODUCTION:

The immense biodiversity on the planet earth, whether a small prokaryotic cell or a multicellular giant organism, are all composed of a small basic unit cell. The cell is considered to be the basic functional, structural and biological unit of life. The cells grow and differentiate to form different kinds of tissues, which in turn form different organs with complex functional and structural aspects, in a multicellular organism. The cells perform important biological tasks like transfer of the genetic information, energy production, signaling to perform different functions, etc. A typical eukaryotic cell consists of the protoplasm and a double layered cell membrane. The protoplasm forms the basis of life and consists of the cytosol and other sub-cellular organelles like mitochondria, endoplasmic reticulum, lysosomes, nucleus, ribosomes, etc. The cell membrane is made up of phospholipids which contain a hydrophilic head group (phosphate head group) and two hydrophobic tails (alkyl tails), which are assembled in such a way to give rise to bilayer structure as per the fluid mosaic model of the cell membrane (Figure 1.1). This lipid bilayer membrane, which has typically 3-4 nm thick hydrophobic cores, covers most of the intracellular organelles, and the outer periphery of the cell to form cell membrane or plasma membrane, which covers the protoplasm and ensures its confinement and protection from the outer environment. The amphiphilic nature of the cell membrane makes it selectively permeable; meaning it only allows certain molecules to pass through, which maintains the homeostasis of the cell.

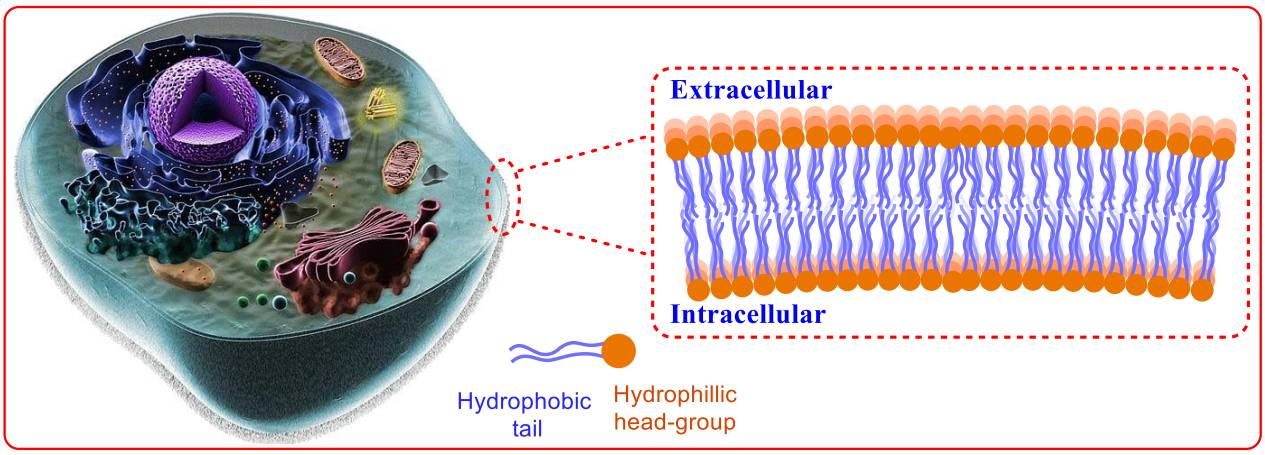

Figure 1.1. Schematic representation of eukaryotic cell and structure of lipid bilayer. The image has been adapted from https://biologydictionary.net/animal-cell/

1.2. Membrane Transport:

As discussed above, the cell serves as the basic structural and functional unit of life, there is a need for continuous production and exchange of energy by cells to perform important life processes like biosynthesis, cell signaling, cell division, and other bio-processes. These processes are achieved by continuous uptake of raw materials from the external environment and removal

of the metabolite wastes produced during biochemical transformations. However, this exchange across the cell membrane is not a freely feasible process due to the selectively permeable nature of the cell membrane. This nature allows small non-polar molecules, e.g. O_2, CO_2 and N_2, water, ethanol, and small hydrophobic molecules to easily diffuse along the concentration gradient across it. However, the small charged ions and large polar molecules like sugars and amino acids, which are biologically very vital, are not diffused freely due to the thermodynamic barrier provided by the lipophilic part of the membrane (Figure 1.2).

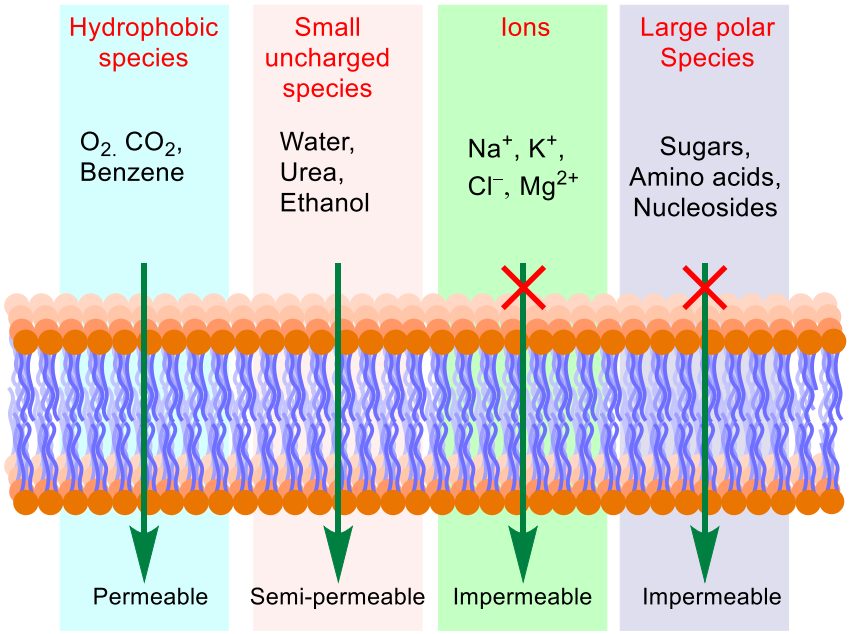

Figure 1.2. Representation of the transport processes across the cell membrane for different solutes.

So to overcome this thermodynamic barrier, nature has endowed the cells with special machineries in the form of membrane-embedded proteins which allow the passage of hydrophilic species across the cell membrane. These proteins lower the free energy of diffusion for these polar species by providing a static hydrophilic pathway through the lipophilic part of the cell membrane.

1.3. Ion Transport across the Cell Membrane:

The ion transport across the cell membrane is a very vital biological phenomenon which maintains the ionic homeostasis of the cells. The ion transport process helps in signal transduction, regulation of cellular pH, osmotic stress, apoptosis, etc. The ion transport systems are broadly classified into two categories as ion carriers and ion channels. The ion carriers are small protein molecules that can bind to an ion on one side of the membrane through non-covalent interactions and undergo a change in the conformation to release the same ion on the other side of the membrane (Figure 1.3 A). The other class includes ion channels that are transmembrane proteins which form a static hydrophilic path for the movement of ions across the

membrane via diffusion (Figure 1.3 B). However, larger polar biomolecules are allowed to pass through the membrane by larger proteins which form bigger cavities (typically more than 10 Å) known as pores (Figure 1.3 C). All these processes are collectively called as passive transport because the transport process occurs along the concentration gradient. On the other hand, there are special ion channels that allow the ion transport process to occur against the concentration gradient. These ion channels are called ion pumps, and these transporters utilize the energy generated from the ATP to ADP reaction to pump the ions against the concentration gradient (Figure 1.3 D).

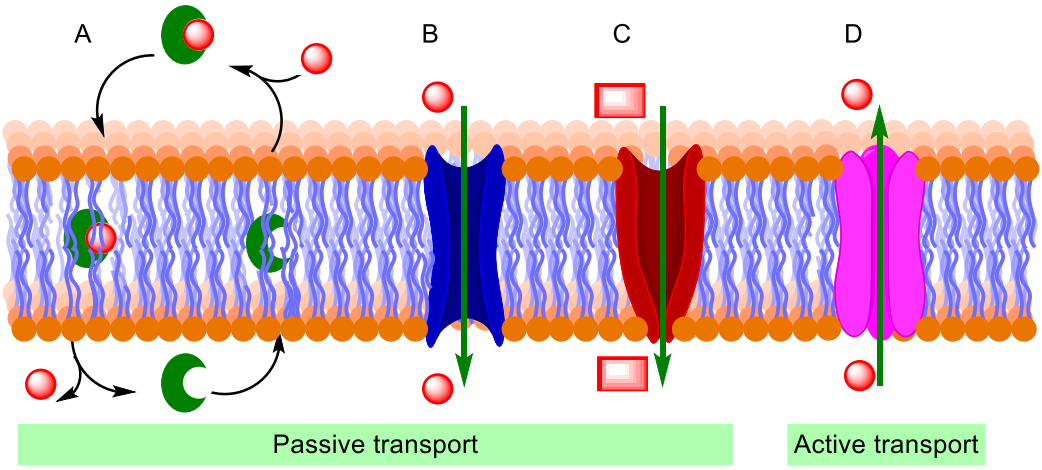

Figure 1.3. Schematic representation of transport process by ion carriers (A), ion channels (B), pores (C) and ion pumps (D).

Depending upon the number and nature of species of the transported ions and direction of transport, the transporters may be classified as Uniporters - transporting a single species in a single direction or Cotransporters - which transport two or more species together. The Cotransporters include Symporters, which transport two species in the same direction and Antiporters which transport two species of same type of charge in the opposite direction.

1.4. Ion Transport and Membrane Potential:

The establishment of definite ionic homeostasis in cells on both the sides of the plasma membrane as well as across the subcellular organelles maintains a definite potential due to such ionic concentrations. The equilibrium membrane potential for any ion can be calculated by Nernst equation:

$$Vm = (RT/F)\ \ln(\frac{[ion]out}{[ion]in}) \qquad \text{Equation 1.1}$$

where, V_m = membrane potential; R = ideal gas constant (joules/ kelvin /mole); T = temperature (kelvin); F = Faraday's constant (coulomb per mol); $[ion]_{out}$ = concentration of ions outside cell; $[ion]_{in}$ = concentration of ions inside cell.

The membrane potential of any biological membrane is mainly controlled by ion flux through the ion channels, and the potential at which there is no net ion flow is called resting potential. The resting potential due to chloride channels in mammalian cells is 30-60 mV which arises due to chloride gradient across the cell membrane (5-10 mM inside and 110-150 mM outside). Similarly, the mitochondrial membrane maintains a potential of 150-220 mV.

1.5. Classification of Ion Transport Systems:

The ion transport systems are mainly classified into two types based on the mode of action – ion carriers and ion channels. The ion channels are further classified into various categories depending upon the selectivity, direction of ion flux and gating activity (Figure 1.4).

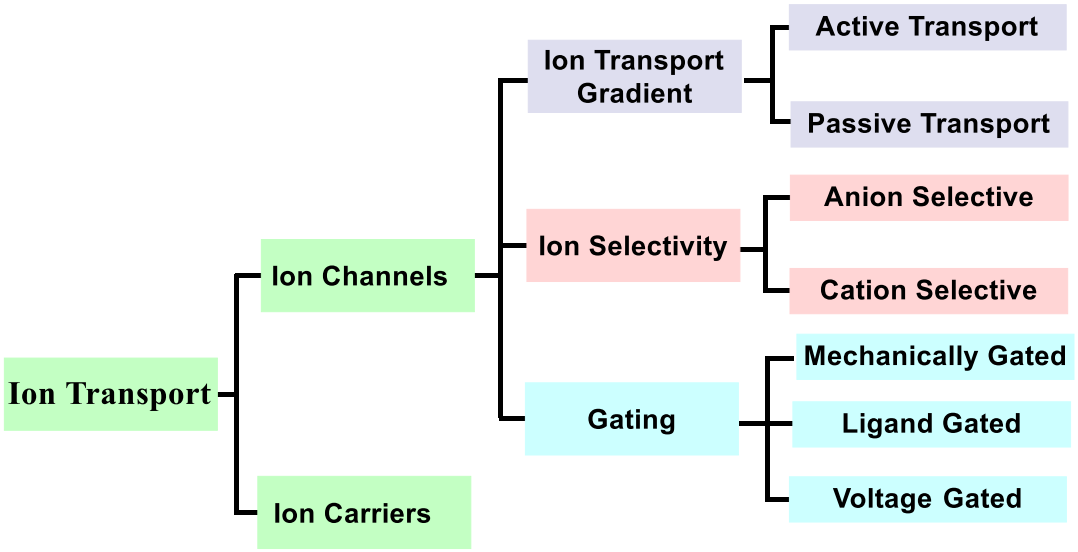

Figure 1.4. Categories of ion transport systems.

The transport gradient decides whether the active transport (against the gradient) or passive transport (along the gradient) is taking place. Depending upon the ion selectivity the ion channels can be classified either as cation channels, like Kcs and gramicidin, or anion selective like CLC family of chloride channels. On the other hand, the opening and closing of a channel to facilitate the movement of ions in response to any stimuli are termed as gating and depending upon the stimuli, there are three major categories of ion channels as discussed below.

I. Mechanically-Gated Ion channels: The ion channels which are opened and closed by electrical membrane potential near the channel. These channels respond to the depolarization and hyperpolarization of the respective membranes to open up and close (Figure 1.5 A). The typical examples include voltage – dependent anion channel (VDAC) and potassium channel Kcs A.

II. Ligand-Gated Ion channels: The ion channels whose activity is being regulated by specific ligand binding, which leads to the conformational changes for opening and closing the channel,

are called as ligand-gated ion channels (Figure 1.5 B). The examples include the release of Ca^{2+} ions from the endoplasmic reticulum to cytosol by calcium channel which is governed by inositol triphosphate (IP_3) ligand.[1]

III. Voltage-Gated Ion channels: The ion channels whose activity is regulated by the membrane stress are called as mechanically-gated ion channels or mechanosensitive ion channels (MSCs). The membrane tension triggers conformational changes of MSCs to open the channel and flow ions or small signaling molecules, which releases osmotic stress and activates signaling cascades.[2] The example includes TRPC6 cation channel which is expressed in cardiovascular system.[3]

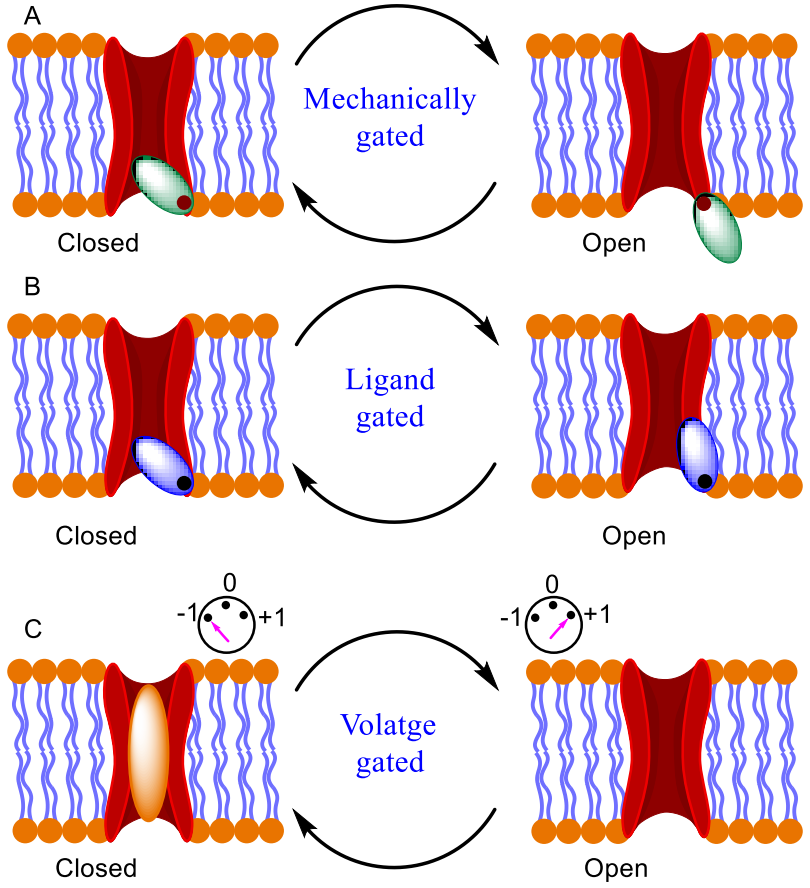

Figure 1.5. Representation of mechanically-gated (A), ligand-gated (B) and voltage-gated (C) ion channels.

1.6. Importance of Ion Transport

The transmembrane ion transport is a very crucial process for regulating the fundamental biological processes like sensory transduction,[4] cell proliferation,[5,6] osmotic stress,[7] etc. The natural ion channels allow the transport of specific ions through the channel lumen, with various binding sites, across the cell membrane.[8,9] Among the different ion channels, the chloride ion channels are relatively poorly explored, probably due to the involvement of cation channels in

the excitable cells. However, after the discovery of the involvement of chloride channels in stabilizing the membrane potential, the area gained more importance and after a decade the discovery of cystic fibrosis due to defective CFTR made the chloride channels a hot field among the structural biologists.

The chloride ion is the most abundant anion in the physiological systems, so are the chloride channels. The naturally occurring chloride ion channels include the CLC family, CFTR, CLIC, CLCA, etc. The selective transport of chloride ion is involved in the maintenance of physiological pH of intracellular compartments, regulation of cell volume, transepithelial salt transport, cell cycle, and apoptosis.[7,10,11] The chloride ion transport is a very crucial process in cancer cells which has unveiled very important observations. The CLC–3 channel, which is a member of the voltage–gated chloride ion channel family, is highly expressed in cancer cells which lead to cell proliferation, drug resistance, and apoptosis. The increased uptake of chloride ions by CLC–3 leads to an increase in cell volume which facilitates the G1 to S phase transition in the cell cycle, hence, increased cell proliferation and formation of tumors. However, the activation of CLC–3 channels in nasopharyngeal carcinoma cells inhibits the signaling pathway P13K / Akt / mTOR, resulting in apoptosis induction. The other interesting fact is that the overexpression of CLC–3 channels in late endosomes and lysosomes enhance the internal acidity, which leads to the deactivation of the chemically basic drugs and ultimately enhances the drug resistance of cancer cells. So the proper functioning of CLC–3 channels is very vital for normal physiological working of living organisms.

The other aspect includes the dysfunctions of the ion channels, which are due to genetic or acquired mutations, called channelopathies.[12,13] For example, the dysfunctions of CFTR lead to loss of lung immune system and cause a dreadful disease known as cystic fibrosis.[14,15] The complete treatment of cystic fibrosis (CF) is currently a challenge and new strategies are being tried to cure CF.[16,17] Other diseases include Myotonia congenita, which occurs due to defects in the CLC–1 channel and causes skeletal muscle problems.[18] Similarly, other renal disorders which arise due to dysfunctions of chloride ion channels include Barters syndrome, Dent's disease etc.[19]

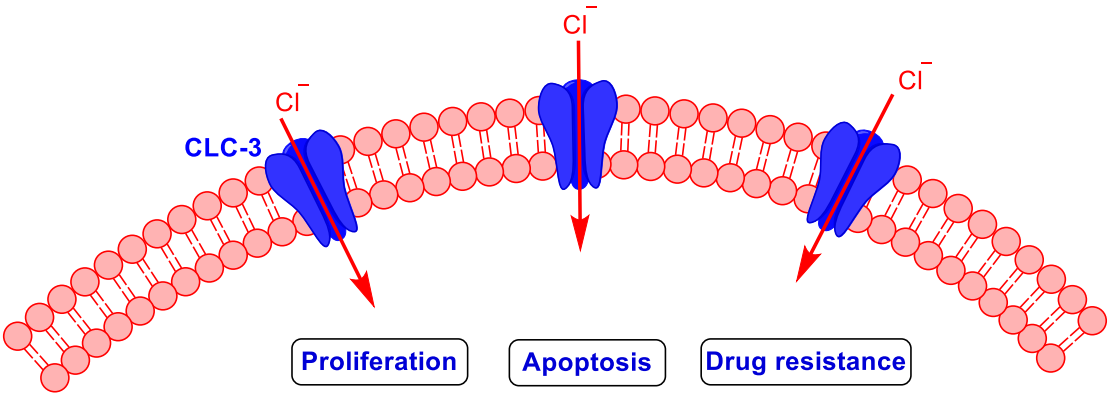

Figure 1.6. Schematic representation of effects of CLC–3 channel in cancer cells.

1.7. Artificial Ion Transport Systems:

The above findings have compelled scientists to make more efforts to understand the various aspects of the naturally occurring ion transport systems owing to their vital and diverse roles. In this realm of science, supramolecular chemists are contributing a lot by designing the artificial mimics of these naturally occurring transport systems to unveil various non-covalent interactions that are operating, which is otherwise a very complex job, in such complex systems. The selectivity filter, ion binding and energetics related to ion hopping through channel lumen are all being addressed by designing chemically robust systems as compared to very delicate biomolecules. The enormous progress has been made by this field of research and the progress continues. However, the general principle for designing such artificial systems remains the same, *i.e*., there has to be a hydrophilic cavity with various ion binding sites which will favor the ion recognition and ion flux, and a hydrophobic surface that will interact with the hydrophobic tails of the membrane.

The above findings have lead scientists to develop various strategies to develop artificial ion channels. These strategies include unimolecular, barrel stave, barrel hoop and barrel rosette ion channels (Figure 1.7).

A. Unimolecular Ion Channels: The unimolecular ion channels are composed of a single molecular unit that provides the transmembrane pathway for the movement of ions from one side of the membrane to another. The typical examples are cyclodextrins and calixarene derivatives connected with properly substituted hydrophobic tails.[20-22] Similarly, the peptide-based nanostructures are known to form the unimolecular ion channels.[23]

B. Barrel Hoop Ion Channels: The barrel hoop ion channels are formed by the preorganized macrocyclic scaffolds which assemble to form columnar stacks inside the lipid bilayer membrane. The typical examples are being provided by Ghadiri and coworkers, who reported a class of peptide macrocycles that self-assemble to form ion channels in lipid membranes.[24-26]

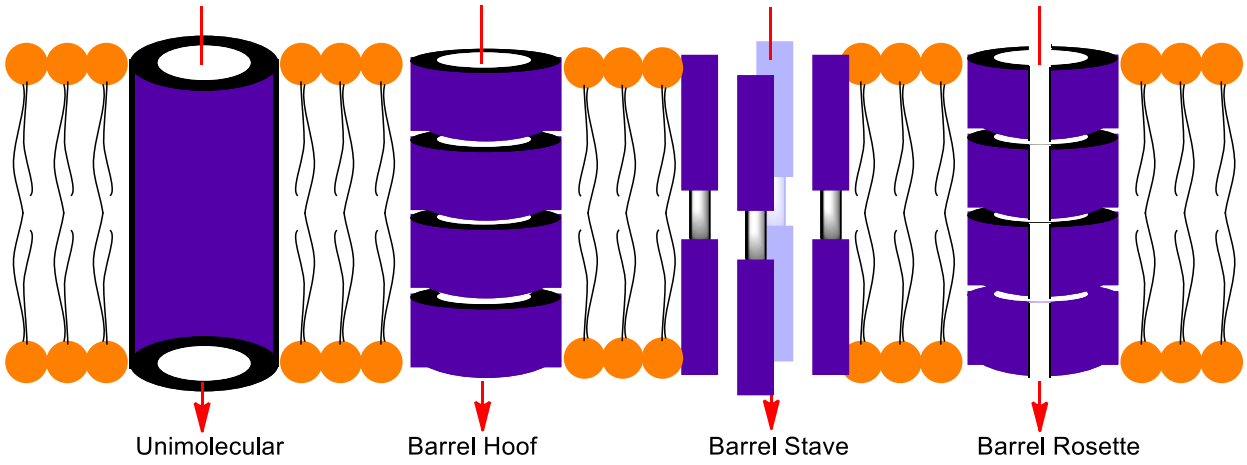

Figure 1.7. Schematic representation of various ion channel designs.

C. Barrel Stave Ion Channels: The barrel stave ion channels are formed by the self-assembly of few transmembrane staves to give rise to a cylindrical scaffold with a well-defined hydrophilic pathway for the movement of ions across the membrane. The typical examples are being provided by bolaamphiphiles[27] and bischolic acid derivatives.[28]

D. Barrel Rosette Ion Channels: The barrel rosette ion channels are formed by the self-assembly of very discrete molecules into supramolecular macrocyclic structures, which in turn self-assemble into columnar stacks to form transmembrane ion channels. The earlier examples include the self-assembly of G-quartets into effective ion channels by Matile and coworkers.[29] The other examples include the self-assembled ion channels formed by adequately substituted mannitol[30] and vicinal diol moieties[31] to form effective chloride ion channels.

Artificial Ion Carriers:

The development of small-molecule ion carriers for selective ion recognition and transport has been exploited in recent years and a lot of strategies have been developed for the successful design of synthetic ion carriers. The inspiration for the design of artificial ion carriers comes from the naturally occurring valinomycin, a selective K^+ ion transporter[32] and prodigiosin, which act as Cl^- ion transporter as well as H^+/Cl^- symporter.[33] The general principle for the design of an ion carrier is that there should be a rigid scaffold with multiple ion binding sites for ion recognition. The examples include cholapod based transporters,[34,35] *trans*-decalins,[36-38] tripodal anion carriers,[39-42] squaramides[43-45] etc. Most of these systems use hydrogen bonding interactions through amide hydrogen atoms as ion recognition forces. However, Matile and coworkers have recently reported the halogen bond,[46] chalcogen bond,[47] and pnictogen bond[48] mediated anion transport by the small molecule ion carriers.

1.8. Artificial Ion Transport Systems as Next Generation Therapeutics:

The development of synthetic ion transport systems has been an emerging field of research in the realm of supramolecular chemistry from the past decades. These synthetic ion transport systems have been used in sensing, catalysis, as well as organic porous materials.[49-53] However, the introduction of the concept of "ion channel replacement therapy" has instigated renewed interests in the development of new ion transport systems for the treatment of diseases related to channelopathies, *i.e.*, dysfunction of natural ion channels.[54,55] The chloride channel-forming peptides have been applied to restore the chloride transport in cystic fibrosis. The addition of these peptides to the apical surface of cystic fibrosis airway tissues enhances the anion secretion along with surface hydration, which increases the potential of such systems in the therapeutics. Similarly, the bis-(*p*-nitrophenyl)ureidodecalin system was introduced by Davis and coworkers as efficient and non-toxic chloride carrier in cells, which could find a suitable place in the therapeutics (Figure 1.8 A).[38] However, the recent work by Burke and coworkers further enhanced the interest in the ion channel replacement therapy. The group used the amphotericin B, which forms non-selective ion channels, in the cystic fibrosis cells from the patients and found that these systems can restore host defenses in cystic fibrosis airway epithelia via a mechanism that is independent of CFTR and is therefore independent of genotype.[15] However, the cytotoxicity of the system remains an issue that needs to be worked out.

Similarly, these artificial ion transport systems have been reported to be associated with the apoptosis inducing activity in cancer cells, which raises new hope for anticancer drug development. The naturally occurring prodigiosin (Figure 1.8 B) is known to act as an H^+/Cl^- carrier and is associated with inducing apoptosis in cancer cells by destroying the pH of intracellular organelles as well as ion homeostasis.[56,57] Similarly the bis-sulfanamides[58] (Figure 1.8 C) and tambjamine analogues[59] have also shown the potential anticancer activities (Figure 1.8 D). Similarly, the vicinal diols[31] which form the chloride selective transmembrane ion channels have also shown potential anticancer activities (Figure 1.8 E). However, the detailed mechanistic pathway of small molecule ion carriers was revealed by Shin and coworkers for the first time using calix[4]pyrrole systems (Figure 1.8 F), which showed the activation of the caspase-dependent pathway was operative during apoptosis induction.[60] The same group showed that the squaramide based carriers (Figure 1.8 G), disrupts the autophagy and induces apoptosis by perturbing cellular chloride concentrations in cells.[61] However, along with the cancer cells, all these systems show toxicity to the healthy cells as well, and there is a need to develop the methodologies by which these systems can differentiate the healthy cells from cancer cells. Addressing the problem of selectivity towards cancer cells will take these ion transport systems to the next stage of their potential as therapeutic agents.

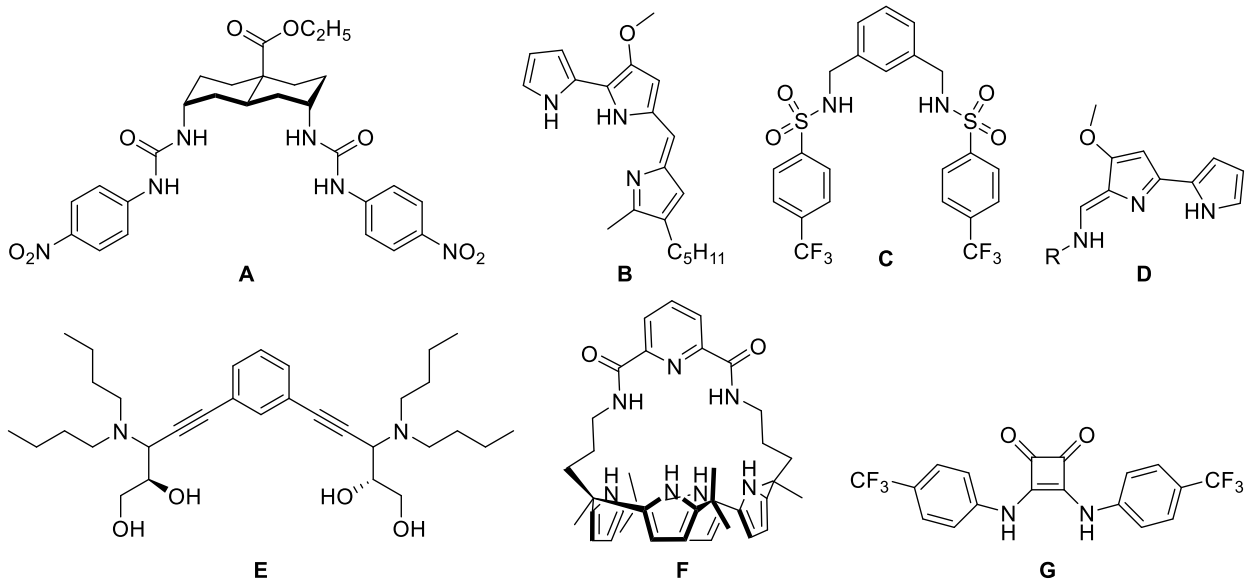

Figure 1.8. Structures of bioactive artificial ion transport systems.

1.9. Techniques Used to Study Synthetic Ion Transport Systems:

The study of synthetic ion transport systems is done by using the model cell membrane in the form of either spherical membranes (vesicles) or planar bilayer membranes (in BLMs), which are composed of lipids. A brief discussion about the techniques used in the study of ion transport process across bilayer membranes is given as under.

1.9.1. Ion Transport Study in Spherical Bilayers:

The spherical bilayer membranes are formed from the commercially available lipids like 1-palmitoyl-2-oleoyl-sn-glycero-3-phosphocholine (POPC) or egg yolk phosphatidylcholine (EYPC) by the standardized freeze and thaw methods to form the unilamellar vesicles. These vesicles are extruded through a polycarbonate membrane of desired pore size (100 – 200 nm) with the help of an extruder assembly (Avanti Polar Lipids) and purified by size exclusion column chromatography over sehphadex-G50 using an adequate buffer. These vesicles are then used to study the ion transport experiments by fluorescence assays, ion selective electrodes and NMR methods.

A. Fluorescence Based Assays: In fluorescence assays, the vesicles are prepared by entrapping 8-hydroxypyrene–1,3,6–trisulfonate (HPTS) (Figure 1.9), which is a pH sensitive dye. The HPTS (λ_{ex} = 450nm and λ_{em} = 510 nm) shows enhancement in the fluorescence above pH 7.2. The pH gradient is applied in extravesicular media by NaOH, and then the ion transporter molecules are added. If there is influx of OH^- or efflux of H^+ ions, the pH inside the vesicles will increase, leading to the enhanced fluorescence emission intensity at 510 nm of HPTS dye when the dye is excited at 450 nm. The change in the emission intensity gives an idea about the

transport ability of a respective system. Similarly, lucigenin dye (full form), whose fluorescence gets quenched in the presence of chloride. The dye can be used to study the chloride transport across the respective vesicles by studying the changes in the fluorescence intensity of the dye. In addition, the other fluorescent dyes like Carboxyfluorescein (CF), ANTS-DPX and calcein can also be used to monitor the ion transport by using the standardized protocols. The CF and ANTS-DPX are used to distinguish the ion channels from transmembrane pores (with diameter more than 10 nm) as well as to study the effect of compounds on the integrity of lipid bilayer membrane.

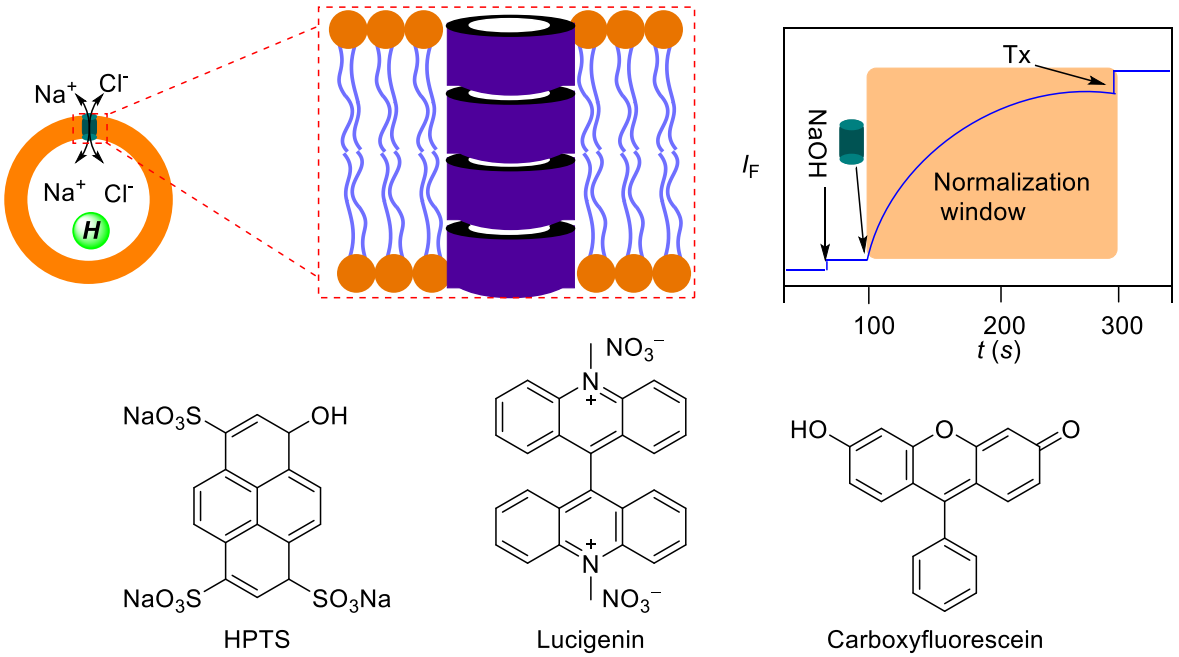

Figure 1.9. Representation of fluorescence-based ion transport assay in spherical vesicles, and the structure of the different dyes used.

B. Ion Selective Electrode based Assays: The ion selective electrodes are used to study the efflux of respective ions entrapped in the vesicles by measuring the changes in conductivity of solution. Typically for a chloride selective electrode, the vesicles are encapsulated by NaCl and these vesicles are suspended in $NaNO_3$ buffer. The rate of Cl^- ion efflux from the vesicles in the presence of a chloride transporter is measured by the chloride selective electrode (Figure 1.10 A).

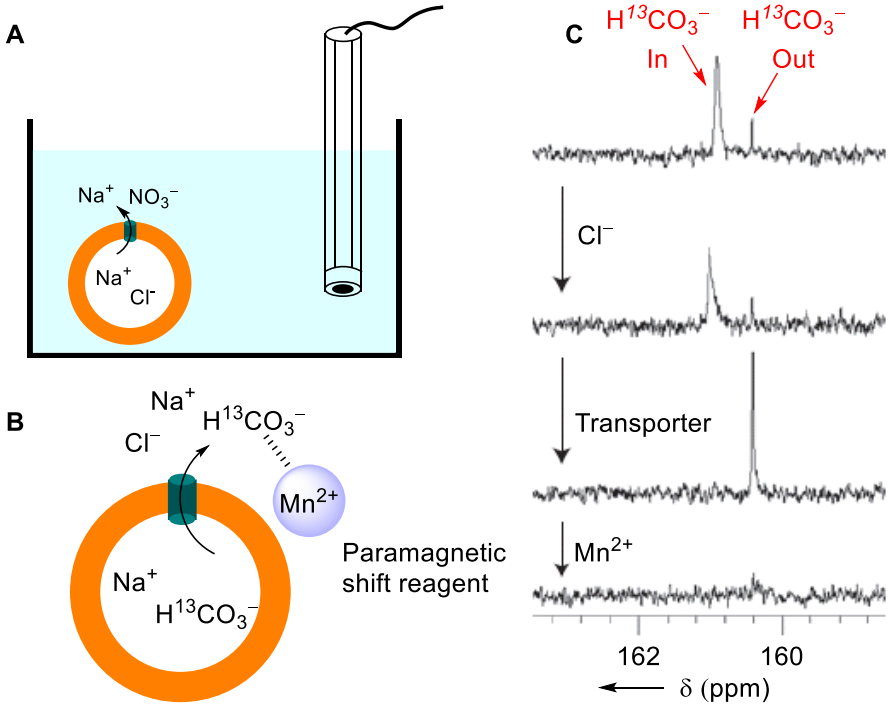

Figure 1.10. Schematic representation of ion transport study using ion selective electrode (A). Representatiion of bicarbonate transport across vesicles by ^{13}C NMR study (B and C)

C. NMR based Assays: The NMR based method to study the ion transport is applicable for only NMR active species. In a typical experiment for monitoring anion transport, the unilamellar vesicles entrapping with NaA (where, A is a NMR-active anionic species) are prepared and an NMR inactive anion along with a paramagnetic shift reagent like Mn^{2+} are added in the extravesicular buffer. The shift reagent enhances the chemical shift values or line-broadening of the peaks corresponding to inta– and extravesicular anions (Figure 1.10 B, C). So in the presence of an anion transporter, the intensity or broadening of the corresponding peaks can be monitored to study the anion transport by the respective transporter.[62]

1.9.2. Ion Transport Study in Planar Bilayers:

The planar bilayer membranes are used to study the ion transport ability of a transport system by measuring the ion conductance across the planar lipid bilayers membrane (BLMs). The typical set up consists of an electrolyte chamber which is consists of two chambers, as *cis* and *trans*– chamber, separated by a Teflon barrier with a tiny aperture of 150 – 250 μm, which is used to connect the two chambers (Figure 1.11 A). A planar lipid bilayer is formed on this aperture by painting the lipid (usually 1,2-diphytanoyl-sn-glycero-3-phosphocholine, DPhPc) which insulates the two chambers. This bilayer acts as an insulator so that no ion can flow from one chamber to another, and consequently no current flow can be observed. However, upon addition of channel forming molecule, the connection between two chambers gets re-established

by the so formed channel which allows the ionic flow and gives rise to the observed conductance across the circuit.

The working principle of such planar bilayer conductance measurement can be rationalized based on parallel plate capacitor, where by applying a voltage across the membrane will result in the current generation which is a measure of ion channel behavior. The periodic fluctuation of current values (pico ampere values) is the characteristic signature of opening and closing events of the channel.

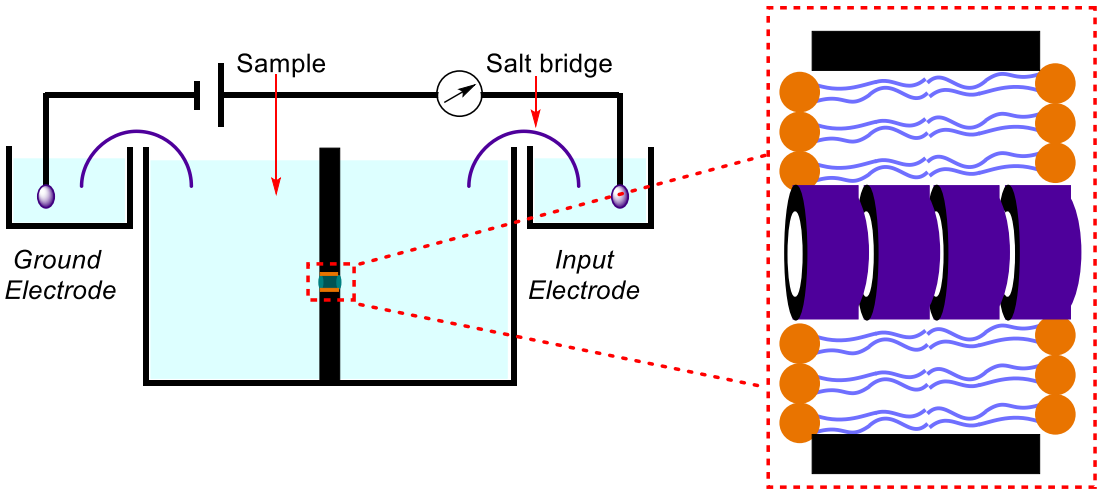

Figure 1.11. Schematic representation of planar bilayer conductance measurement technique.

1.10. REFERENCES:

(1) Hucho, F.; Weise, C. *Angew. Chem. Int. Ed.* **2001**, *40*, 3100.

(2) Muraoka, T.; Umetsu, K.; Tabata, K. V.; Hamada, T.; Noji, H.; Yamashita, T.; Kinbara, K. *J. Am. Chem. Soc.* **2017**, *139*, 18016.

(3) Peyronnet, R.; Nerbonne, J. M.; Kohl, P. *Circ. Res.* **2016**, *118*, 311.

(4) Legutko, B.; Staufenbiel, M.; Krieglstein, K. *Int. J. Dev. Neurosci.* **1998**, *16*, 347.

(5) Chiu, S. Y.; Wilson, G. F. *J. Physiol.* **1989**, *408*, 199.

(6) Nowak, L.; Bregestovski, P.; Ascher, P.; Herbet, A.; Prochiantz, A. *Nature* **1984**, *307*, 462.

(7) Lange, K. *J. Cell. Physiol.* **2000**, *185*, 21.

(8) Gouaux, E.; Mackinnon, R. *Science* **2005**, *310*, 1461.

(9) B. Hille, *Ion Channels of Excitable Membranes* (Sinauer Associates, Sunderland, MA, ed.) *3*, **2001.**

(10) Wang, B.; Xie, J.; He, H.-Y.; Huang, E.-W.; Cao, Q.-H.; Luo, L.; Liao, Y.-S.; Guo, Y. *Oncotarget* **2017**, *8*, 63788.

(11) Benz, R.; Hancock, R. E. *J. Gen. Physiol*. **1987**, *89*, 275.

(12) Kim, J.-B. *Korean J. Pediatr*. **2014**, *57*, 1.

(13) Kasianowicz, J. J. *Chem. Rev.* **2012**, *112*, 6215.

(14) Quinton, P. M. *Nature* **1983**, *301*, 421.

(15) Muraglia, K. A.; Chorghade, R. S.; Kim, B. R.; Tang, X. X.; Shah, V. S.; Grillo, A. S.; Daniels, P. N.; Cioffi, A. G.; Karp, P. H.; Zhu, L.; Welsh, M. J.; Burke, M. D. *Nature* **2019**, *567*, 405.

(16) Davies, J. C.; Moskowitz, S. M.; Brown, C.; Horsley, A.; Mall, M. A.; McKone, E. F.; Plant, B. J.; Prais, D.; Ramsey, B. W.; Taylor-Cousar, J. L.; Tullis, E.; Uluer, A.; McKee, C. M.; Robertson, S.; Shilling, R. A.; Simard, C.; Van Goor, F.; Waltz, D.; Xuan, F.; Young, T.; Rowe, S. M. *N. Engl. J. Med.* **2018**, *379*, 1599.

(17) Keating, D.; Marigowda, G.; Burr, L.; Daines, C.; Mall, M. A.; McKone, E. F.; Ramsey, B. W.; Rowe, S. M.; Sass, L. A.; Tullis, E.; McKee, C. M.; Moskowitz, S. M.; Robertson, S.; Savage, J.; Simard, C.; Van Goor, F.; Waltz, D.; Xuan, F.; Young, T.; Taylor-Cousar, J. L. *Engl. J. Med.* **2018**, *379*, 1612.

(18) Pusch, M.; Steinmeyer, K.; Koch, M. C.; Jentsch, T. J. *Neuron* **1995**, *15*, 1455.

(19) Dworakowska, B.; Dolowy, K. *Acta. Biochim. Pol.* **2000**, *47*, 685.

(20) Tabushi, I.; Kuroda, Y.; Yokota, K. *Tetrahedron Lett.* **1982**, *23*, 4601.

(21) Madhavan, N.; Robert, E. C.; Gin, M. S. *Angew. Chem. Int. Ed.* **2005**, *44*, 7584.

(22) Maulucci, N.; De Riccardis, F.; Botta, C. B.; Casapullo, A.; Cressina, E.; Fregonese, M.; Tecilla, P.; Izzo, I. *Chem. Commun.* **2005**, 1354.

(23) Biron, E.; Otis, F.; Meillon, J.-C.; Robitaille, M.; Lamothe, J.; Van Hove, P.; Cormier, M.-E.; Voyer, N. *Bioorg. Med. Chem.* **2004**, *12*, 1279.

(24) Fernandez-Lopez, S.; Kim, H. S.; Choi, E. C.; Delgado, M.; Granja, J. R.; Khasanov, A.; Kraehenbuehl, K.; Long, G.; Weinberger, D. A.; Wilcoxen, K. M.; Ghadiri, M. R. *Nature* **2001**, *412*, 452.

(25) Sánchez-Quesada, J.; Isler, M. P.; Ghadiri, M. R. *J. Am. Chem. Soc.* **2002**, *124*, 10004.

(26) Ghadiri, M. R.; Granja, J. R.; Buehler, L. K. *Nature* **1994**, *369*, 301.

(27) Eggers, P. K.; Fyles, T. M.; Mitchell, K. D. D.; Sutherland, T. *J. Org. Chem.* **2003**, *68*, 1050.

(28) Yoshii, M.; Yamamura, M.; Satake, A.; Kobuke, Y. *Org. Biomol. Chem.* **2004**, *2*, 2619.

(29) Sakai, N.; Kamikawa, Y.; Nishii, M.; Matsuoka, T.; Kato, T.; Matile, S. *J. Am. Chem. Soc.* **2006**, *128*, 2218.

(30) Saha, T.; Dasari, S.; Tewari, D.; Prathap, A.; Sureshan, K. M.; Bera, A. K.; Mukherjee, A.; Talukdar, P. *J. Am. Chem. Soc.* **2014**, *136*, 14128.

(31) Saha, T.; Gautam, A.; Mukherjee, A.; Lahiri, M.; Talukdar, P. *J. Am. Chem. Soc.* **2016**, *138*, 16443.

(32) Daniele, R. P.; Holian, S. K. *Proc. Natl. Acad. Sci. U. S. A.* **1976**, *73*, 3599.

(33) Darshan, N.; Manonmani, H. K. *J. Food Sci. Technol.* **2015**, *52*, 5393.

(34) Edwards, S. J.; Valkenier, H.; Busschaert, N.; Gale, P. A.; Davis, A. P. *Angew. Chem. Int. Ed.* **2015**, *54*, 4592.

(35) Davis, A. P. *Coord. Chem. Rev.* **2006**, *250*, 2939.

(36) Hussain, S.; Brotherhood, P. R.; Judd, L. W.; Davis, A. P. *J. Am. Chem. Soc.* **2011**, *133*, 1614.

(37) Valkenier, H.; Judd, L. W.; Li, H.; Hussain, S.; Sheppard, D. N.; Davis, A. P. *J. Am. Chem. Soc.* **2014**, *136*, 12507.

(38) Li, H.; Valkenier, H.; Judd, L. W.; Brotherhood, P. R.; Hussain, S.; Cooper, J. A.; Jurček, O.; Sparkes, H. A.; Sheppard, D. N.; Davis, A. P. *Nat. Chem.* **2015**, *8*, 24.

(39) Mondal, D.; Sathyan, A.; Shinde, S. V.; Mishra, K. K.; Talukdar, P. *Org. Biomol. Chem.* **2018**, *16*, 8690.

(40) Roy, A.; Saha, D.; Mukherjee, A.; Talukdar, P. *Org. Lett.* **2016**, *18*, 5864.

(41) Roy, A.; Saha, D.; Mandal, P. S.; Mukherjee, A.; Talukdar, P. *Chem.: Eur. J.* **2017**, *23*, 1241.

(42) Busschaert, N.; Gale, P. A.; Haynes, C. J. E.; Light, M. E.; Moore, S. J.; Tong, C. C.; Davis, J. T.; Harrell, J. W. A. *Chem. Commun.* **2010**, *46*, 6252.

(43) Bao, X.; Wu, X.; Berry, S. N.; Howe, E. N. W.; Chang, Y.-T.; Gale, P. A. *Chem. Commun.* **2018**, *54*, 1363.

(44) Busschaert, N.; Kirby, I. L.; Young, S.; Coles, S. J.; Horton, P. N.; Light, M. E.; Gale, P. A. *Angew. Chem. Int. Ed.* **2012**, *51*, 4426.

(45) Zhang, S.; Wang, Y.; Xie, W.; Howe, E. N. W.; Busschaert, N.; Sauvat, A.; Leduc, M.; Gomes-da-Silva, L. C.; Chen, G.; Martins, I.; Deng, X.; Maiuri, L.; Kepp, O.; Soussi, T.; Gale, P. A.; Zamzami, N.; Kroemer, G. *Cell. Death Dis.* **2019**, *10*, 242.

(46) Vargas Jentzsch, A.; Emery, D.; Mareda, J.; Metrangolo, P.; Resnati, G.; Matile, S. *Angew. Chem. Int. Ed.* **2011**, *50*, 11675.

(47) Benz, S.; Macchione, M.; Verolet, Q.; Mareda, J.; Sakai, N.; Matile, S. *J. Am. Chem. Soc.* **2016**, *138*, 9093.

(48) Lee, L. M.; Tsemperouli, M.; Poblador-Bahamonde, A. I.; Benz, S.; Sakai, N.; Sugihara, K.; Matile, S. *J. Am. Chem. Soc.* **2019**, *141*, 810.

(49) Steller, L.; Kreir, M.; Salzer, R. *Anal. Bioanal. Chem.* **2012**, *402*, 209.

(50) Natarajan, R.; Bridgland, L.; Sirikulkajorn, A.; Lee, J.-H.; Haddow, M. F.; Magro, G.; Ali, B.; Narayanan, S.; Strickland, P.; Charmant, J. P. H.; Orpen, A. G.; McKeown, N. B.; Bezzu, C. G.; Davis, A. P. *J. Am. Chem. Soc.* **2013**, *135*, 16912.

(51) Travaglini, L.; Bridgland, L. N.; Davis, A. P. *Chem. Commun.* **2014**, *50*, 4803.

(52) Busschaert, N.; Caltagirone, C.; Van Rossom, W.; Gale, P. A. *Chem. Rev.* **2015**, *115*, 8038.

(53) Blake, S.; Capone, R.; Mayer, M.; Yang, J. *Bioconjug.Chem.* **2008**, *19*, 1614.

(54) Cossu, C.; Fiore, M.; Baroni, D.; Capurro, V.; Caci, E.; Garcia-Valverde, M.; Quesada, R.; Moran, O. *Front. Pharmacol.* **2018**, *9*, 852.

(55) Broughman, J. R.; Shank, L. P.; Takeguchi, W.; Schultz, B. D.; Iwamoto, T.; Mitchell, K. E.; Tomich, J. M. *Biochemistry* **2002**, *41*, 7350.

(56) Cheung, S.; Wu, D.; Daly, H. C.; Busschaert, N.; Morgunova, M.; Simpson, J. C.; Scholz, D.; Gale, P. A.; O'Shea, D. F. *Chem* **2018**, *4*, 879.

(57) Sessler, J. L.; Eller, L. R.; Cho, W.-S.; Nicolaou, S.; Aguilar, A.; Lee, J. T.; Lynch, V. M.; Magda, D. J. *Angew. Chem. Int. Ed.* **2005**, *44*, 5989.

(58) Saha, T.; Hossain, M. S.; Saha, D.; Lahiri, M.; Talukdar, P. . *J. Am. Chem. Soc.* **2016**, *138*, 7558.

(59) Hernando, E.; Soto-Cerrato, V.; Cortés-Arroyo, S.; Pérez-Tomás, R.; Quesada, R. *Org. Biomol.r Chem.* **2014**, *12*, 1771.

(60) Ko, S.-K.; Kim, S. K.; Share, A.; Lynch, V. M.; Park, J.; Namkung, W.; Van Rossom, W.; Busschaert, N.; Gale, P. A.; Sessler, J. L.; Shin, I. *Nat. Chem.***2014**, *6*, 885.

(61) Busschaert, N.; Park, S. H.; Baek, K. H.; Choi, Y. P.; Park, J.; Howe, E. N. W.; Hiscock, J. R.; Karagiannidis, L. E.; Marques, I.; Felix, V.; Namkung, W.; Sessler, J. L.; Gale, P. A.; Shin, I. *Nat. Chem.* **2017**, *9*, 667.

(62) Davis, J. T.; Gale, P. A.; Okunola, O. A.; Prados, P.; Iglesias-Sánchez, J. C.; Torroba, T.; Quesada, R. *Nat. Chem.* **2009**, *1*, 138.

Chapter 2

Anion Selective Ion Channel Constructed from Self-Assembly of Bis-Cholate Substituted Fumaramide

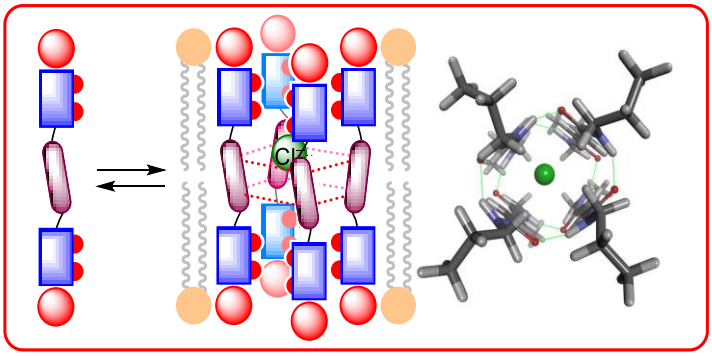

2.1. INTRODUCTION

The design of biomimetic ion transport systems has emerged as a very attractive field of research in the past decades. The primary aim and inspiration of these synthetic transport systems are to address the problems related to the channelopathies. The development of artificial ion channels and carriers started with the development of the first ion channel by Tabushi et. al. based on a cyclodextrin scaffold, which acted like a unimolecular ion channel in the lipid bilayer membrane.[1] Then onwards, this research field continued to evolve and new design strategies came into the limelight. The design of a synthetic ion channel demands perfection in the selectivity filter and the activity of the respective channel. In the case of unimolecular ion channels, the selectivity filter is usually static and so the selectivity cannot be modulated. However, in the case of supramolecular channels, the selectivity filter can be tuned by the summation of different binding sites available in monomeric structures. Among the different supramolecular designs, the barrel stave ion channels have been explored and along with the almeticin[2] and amphotericin[3] a lot of molecules (Figure 2.1) were assumed to adopt the barrel stave structure.[4,5] Further, the new interest in the field emerged after the findings that these synthetic channels can be used to switch the cancer cells to apoptosis.[6] However, this strategy has crucial limitations because, these channels cannot differentiate the cancer cells from the healthy cells, so the undesirable damage to the healthy cells is one of the major drawbacks of using these systems as therapeutics. To address this issue the stimulus-responsive systems are being developed so that upon applying a specific stimulus the ion transporters can be activated selectively in cancer cells and the damage to healthy cells can be avoided to a large extent. In this regard, some works have been reported for the regulation of ion transport (cation transport) by using the light modulated ion channels based on crown ethers.[7,8] However, such modulation has not been materialized for the synthetic chloride ion channels.

We wished to address the problem of the selectivity filter and activity modulation in the same system. For such a design, the fumaramide caught our attention. The fumaramide is a very attractive chemical moiety for self-assembly due to its specific conformation and directional intermolecular hydrogen bonding ability. [9] The moiety offers two hydrogen bond donors and two hydrogen bond acceptors, which results in the efficient self-assembly. On the other hand, its maleamide isomer is a poor self-assembling moiety due to intramolecular hydrogen bonding which locks it in the folded conformation. Therefore, the photo-isomerization of fumaramide to maleamide and the reverse thermal isomerization [10] has been very useful in constructing different kinds of molecular machines,[11,12] drug delivery system,[13] peptide helicity control,[14] etc. However, such an efficient hydrogen bonding ability of fumaramides has received the least attention in the field of synthetic mimics of transmembrane ion transport. Our lab has recently reported that N^1,N^4-dihexylfumaramide system prefers the typical flat-ribbon self-assembly through hydrogen bonding in the solid state.[15] In this assembly, each pair of consecutive molecules is connected by two hydrogen bonds. However, when the side arms are changed to cyclohexyl groups, the solid state structure of N^1,N^4-dicyclohexylfumaramide showed that

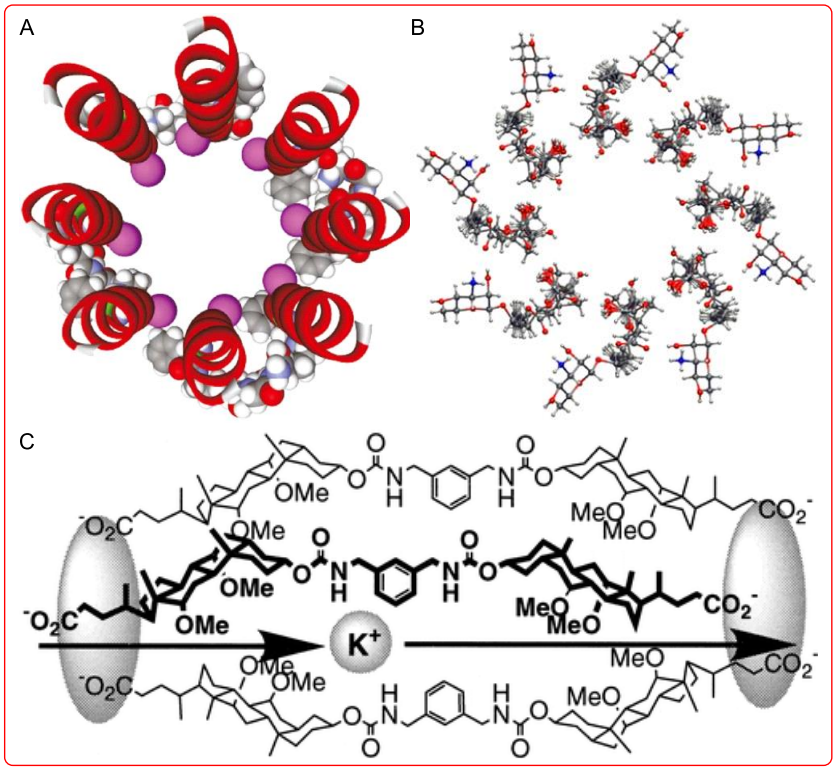

Figure 2.1. Barrel stave ion channel model for almethicin (A), amphotericin B (B) and bis Cholic acid derivatives (C).

each pair of consecutive molecules is connected through a single hydrogen bonded interaction and these molecules are orthogonally oriented to each other due to the presence of sterically bulky groups at terminals. This specific orientation of consecutive molecules leads each molecule to form hydrogen bonds with four neighboring molecules, which helped in the formation of a stable supramolecular barrel rosette ion channel in the lipid bilayer membrane. Now, it can be anticipated that if the steric crowding is moved away from the central fumaramide core, the flat-ribbon type of consecutive molecules can be regained successfully, and if the steric moiety can offer distinct hydrophobic and hydrophilic faces, a supramolecular barrel-stave ion channel can be obtained.[16] So, we thought to initiate the formation of anion selective barrel-stave ion channel by a fumaramide system that is bis-functionalized with a cholic acid derived amine. The cholic acid backbone was used as side arms due to the distinct hydrophobic β-face for the van der Waals interaction with the membrane and a hydrophilic α-face (three –OH groups are present on the α-face) surface which provides the polar interior of the channel.[17,18] There are multiple reports about ion channel formation utilizing properly functionalized cholate moieties (with either methylated [18,19] or free[4] hydroxyl groups); however, all these channels are reported to be cation selective. We thought that the free hydroxyl groups of each cholic acid part would help in the anion recognition, through O−H•••anion interactions through hydrogen bonding. In addition, the alkene C=C of the fumaramide unit would participate in the anion recognition by anion-π interactions.[15] The structure of the designed fumaramide **1a** is shown in Figure 2.2. The

corresponding maleamide **1b** was also designed as a negative control to appreciate the importance of flat-ribbon self-assembly.

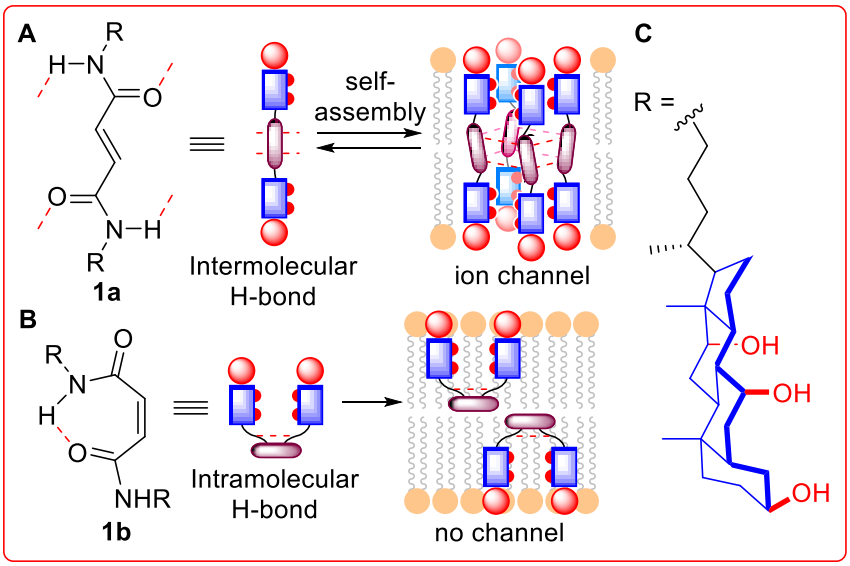

Figure 2.2. Structure and self-assembly processes of fumaramide **1a** (A), and that of maleamide **1b** (B). Description of the R group (C).

2.2 RESULTS AND DISCUSSION:

2.2.1. Synthesis:

The syntheses of **1a** and **1b** was started from the cholic acid, which involves the conversion of the terminal acid group (**3**) to the corresponding amine (**5**) by a reported protocol.[17] The cholic acid derived amine (**5**) was then coupled to fumaryl chloride **2a** to give **1a** in 41% yield (Scheme 1). The reaction of the same amine with the maleic acid **2b** in presence of EDC•HCl provided **1b** in 36% yield. The compounds were purified column chromatography and all the newly synthesized compounds were characterized by ^{1}H NMR, ^{13} C NMR, HRMS, IR spectroscopy and melting point data.

2.2.2. Solution Phase Self-Assembly Studies:

To study whether the self-assembly process is functional in solution phase, the morphological characterization of **1a** was done using atomic force microscopy (AFM). The multiple solutions of compound **1a** with concentrations of 50 µM, 100 µM and 150 µM were prepared in THF and these solutions were subjected to sonication for fifteen minutes. Then, these solutions were

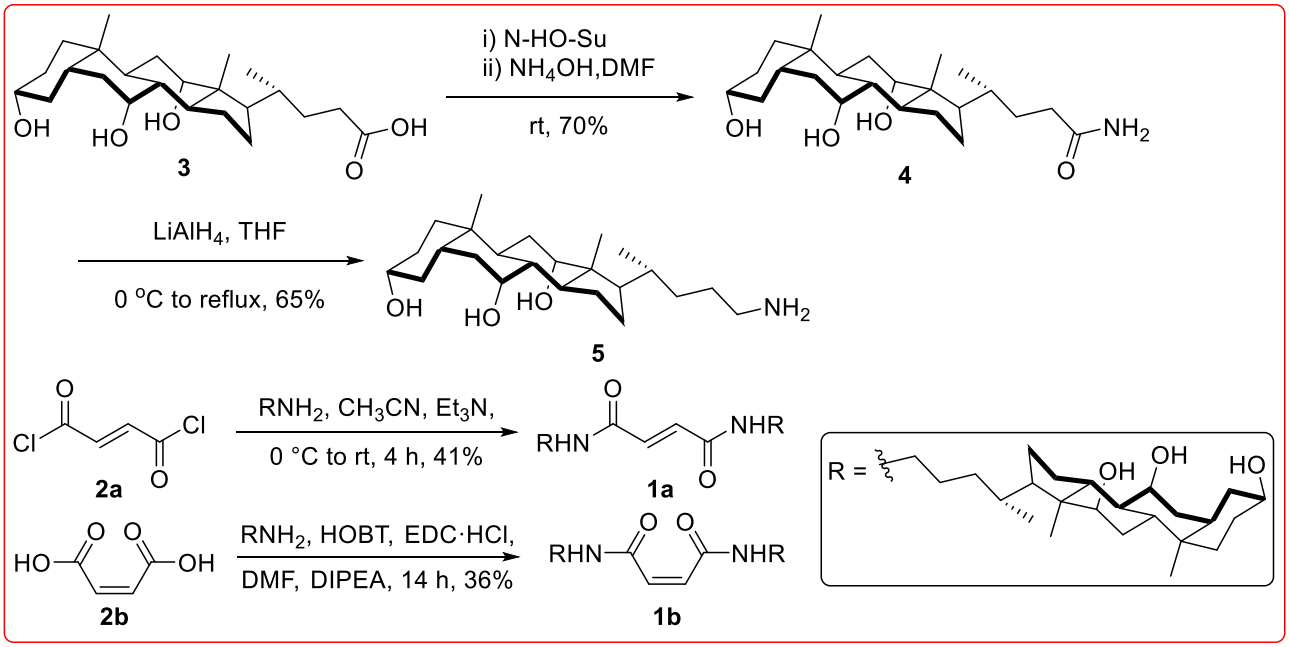

Scheme 1. Synthesis of fumaramide **1a** and maleamide **1b.**

filtered through fine filters (HPLC filters) and 1 µL of each solution was placed on a mica sheet and dried in a vacuum desiccator using high vacuum pump for two days. The AFM data were recorded using Nano Wizard Atomic Force Microscopy and the samples were analyzed by AFM.

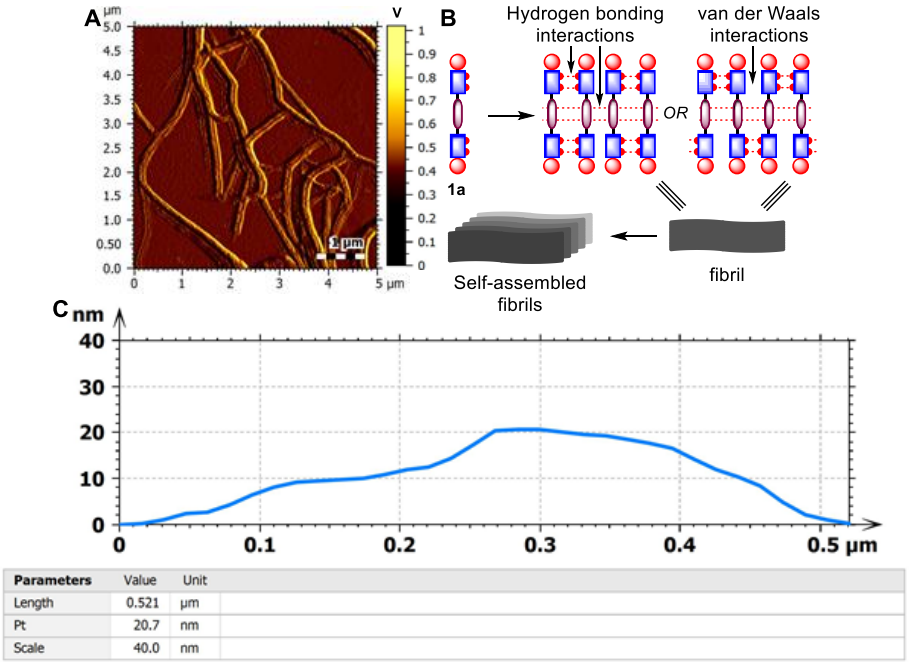

Figure 2.3. AFM image of **1a** in THF at 100 µM concentration (**A**). Possible modes of self-assembly in solution phase by **1a** (**B**) and height profile (**C**).

The solution prepared in THF (100 μM), showed efficient self-assembled fibril formation (Figure 2.3 A). These observations can be rationalized based on C=O•••H-N (among fumaramides) and C-O•••H-O (among hydroxyl groups present on α-face of cholates) hydrogen bond interactions, and van der Waals interactions (among β-faces of cholates) resulting in the fibrils (Figure 2.3B). These fibrils can further self-assemble, to form hierarchical self-assembled structures.[20,21]

2.2.3. Ion Transport Studies:

To study the ion transport activity of **1a** and **1b**, the model lipid bilayer membrane composed of egg-yolk phosphatidylcholine (EYPC) was formed prepared in the form of large unilamellar vesicles (LUVs). The EYPC-LUVs were prepared by entrapping the pH-sensitive fluorescent dye, 8-hydroxy-1,3,6-pyrenetrisulfonate (HPTS) and then the pH gradient of 0.8 unit (pH_{in} = 7.0 and pH_{out} = 7.8) was applied using 0.5 M NaOH, which enhances the fluorescence intensity of HPTS dye if the ion transport process is operating.[22] The activity of compound **1a** (6 μM) was much higher than of 1b (6 μM) was (Figure 2.4A) when compared under identical conditions. Interestingly, the ion transport activity of compound **1a** was lost and matched to that of compound **1b** (Figure 2.4 A), when it was subjected to the photo-isomerization of the C=C bond. This data supports the fact that the *trans* conformation of the C=C bond provides efficient self-assembly to form the active ion transport system. When the conformation of the C=C bond was changed to the *cis*, the self-assembly of was disturbed due to the intramolecular hydrogen bond of each isomerized molecule. So this result suggested that the channel activity can be switched off upon photoisomerization of fumaramide to maleamide. Although, this switching off of ion transport property was remarkable, the use of UV light for photoisomerization and lack of reverse photoisomerization condition limited the applicability of this system in biological applications.

The dose-responsive ion transport activity of **1a** and **1b**, followed by Hill analysis provided the half-maximal activity, EC_{50} = 3.1 μM (Figure 2.4B, C) and 9.8 μM (Figure 2.4D, E), respectively. The fumaramide derivative showed much better activity than the corresponding maleamide derivative, which is expected due to the formation of an efficient ion transport system by the former. The Hill coefficient n = 4 for **1a** indicated that the formation of the active transporter is most probably involving four fumaramide molecules.[23] For the less active isomer **1b**, n = 5.82 suggested the involvement of six molecules in the active structure formation.

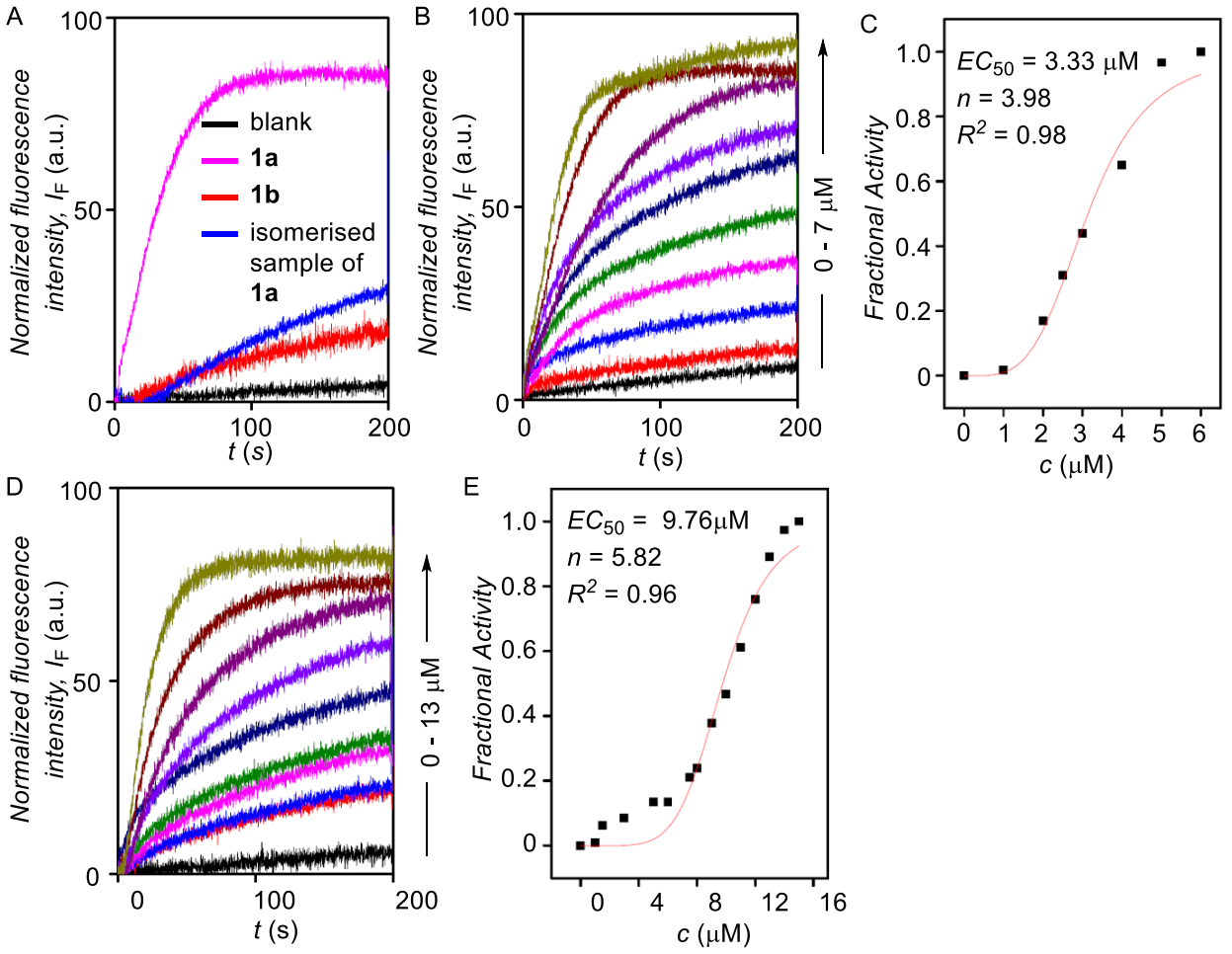

Figure 2.4. Comparison of activities of **1a** and **1b** at 6 μM concentration and photo-isomerization of **1a** to **1b** 6 μM concentration (A). Dose-response curve of fumaramide **1a** (B) and corresponding Hill analysis at 100 s (C) and dose-response curve (D) and corresponding Hill analysis at 100 s (E) of maleamide derivative **1b**.

2.2.4. Ion Selectivity studies:

The results of the ion transport activity assays of the fumaramide derivative **1a** encouraged us to evaluate the ion selectivity and mechanism of ion transport through the channel formed by **1a**. To evaluate ion selectivity through the channel, the HPTS assay was used and the transport activity was studied by varying the extravesicular ions. Firstly, the ion transport of **1a** was evaluated across EYPC-LUVs entrapping HPTS dye, in the presence of intravesicular NaCl and extravesicular isoosmolar MCl (M^+ = Li^+, K^+, Rb^+, and Cs^+).[24] When the transport activity of **1a** was checked in the presence of different external cations, there was no significant difference in the transport activity (Figure 2.5A). This result suggests that there is no involvement of any cation (i.e. H^+/M^+ antiport or M^+/OH^- symport) in the ion transport process of **1a**. Next, the anion selectivity of **1a** was evaluated by varying the intravesicular[25] (method A), as well as extravesicular anions[26] (method B), and the change in the ion transport rate was checked upon

applying pH gradient of 0.8 (pH_{in} = 7.0 and pH_{out} = 7.8). There were considerable changes in the ion transport rate for different NaX salts (X^- = Cl^-, Br^-, I^-, NO_3^- and ClO_4^-) varied under both the conditions (Figure 2.5 B, C). The results suggested that the compound **1a** forms a Cl^- ion selective ion transport system in the lipid bilayer membrane.

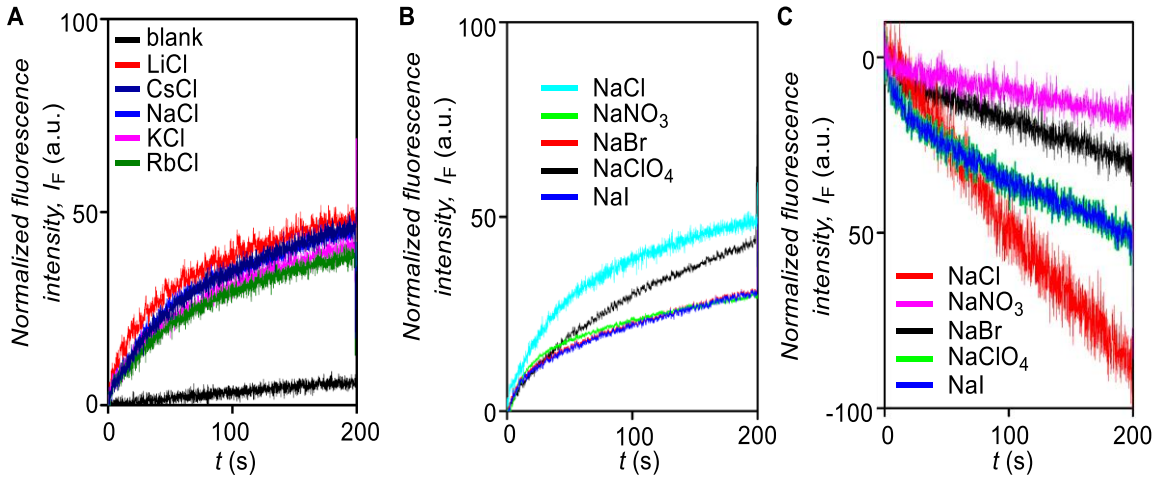

Figure 2. 5. Cation selectivity of **1a** (A); Anion selectivity of **1a** by method A (B) and method B (C).

When the ion selectivity sequence was analyzed, it seems that the anion selectivity order seems to be controlled by both radius and hydration energy of anions (Figure 2.6).[27,28] The ion selectivity studies suggested anion participation in the transport mechanism. The selectivity filter of the channel could be possibly due to the hydrogen bonding interactions of an anion with the hydroxyl groups of cholate and anion-π interactions of the ion with the fumaramide moieties.

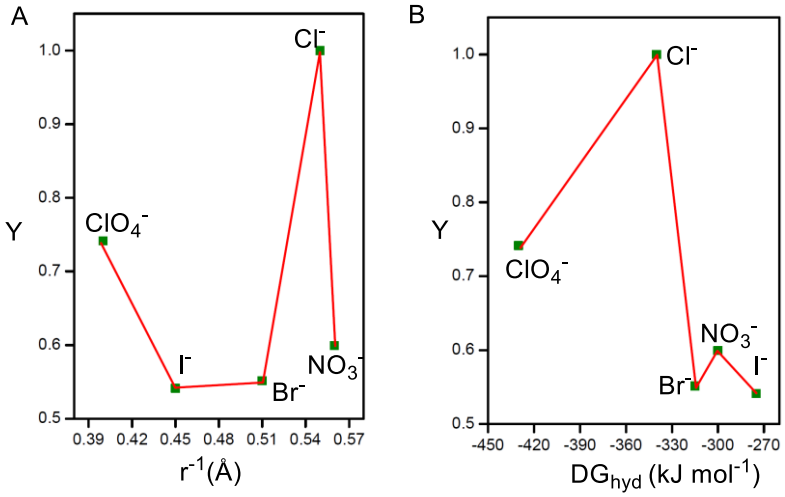

Figure 2.6. Fractional activity *Y* (relative to Cl^-) as a function of the reciprocal anion radius (A) and fractional activity *Y* (relative to Cl^-) as a function of the anion hydration energy (B).

2.2.5. Chloride transport Assay:

As the ion selectivity studies by HPTS assay suggested that the compound **1a** is selective for chloride ions, so to reconfirm the Cl^- ion selectivity of the channel, the influx of Cl^- ions into vesicles (EYPC- LUVs) entrapped with lucigenin dye (chloride sensitive) was monitored by lucigenin fluorescence assay by the reported method.[29] When the ion transport activity of **1a** was checked, the structure of ion transporter formed showed a dose-dependent quenching of lucigenin fluorescence, confirming the Cl^- influx during transport (Figure 2.7 A), confirming the chloride selectivity of the channel.

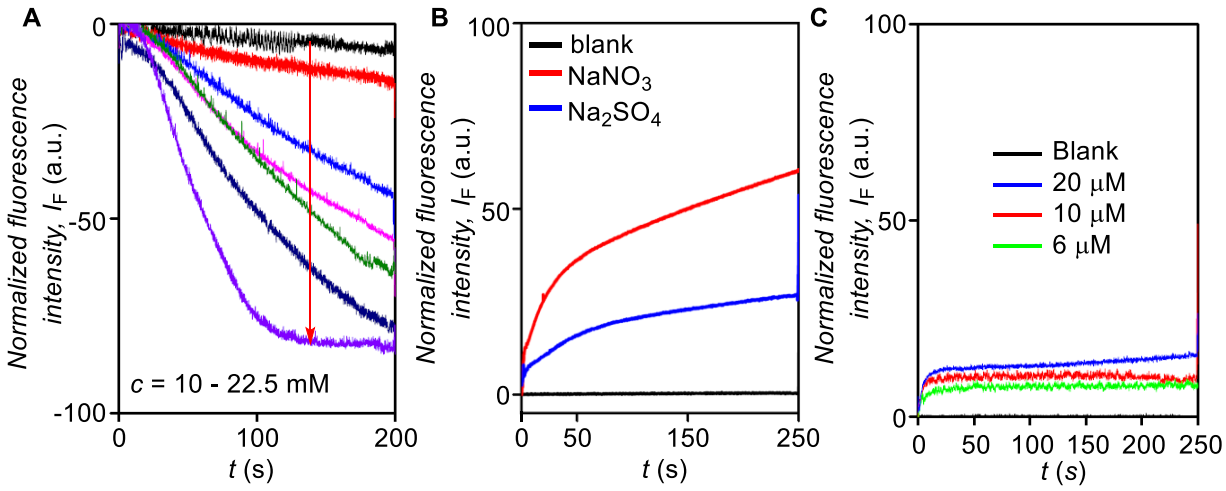

Figure 2.7. Dose-dependent Cl^- influx by compound **1a** (A) across EYPC-LUVs⊃lucigenin. Cl^- ion efflux by **1a** (8 μM) in the presence of either extravesicular SO_4^{2-} or extravesicular NO_3^- ion with isoosmolar intravesicular Cl^- (B) and ANTS–DPX leakage assay in presence of compound **1a** with variable concentrations (C).

Next, the mechanism of ion transport by **1a** was evaluated by using the lucigenin assay with a modified protocol. The EYPC liposomes were prepared by entrapping NaCl (200 mM) and 1 mM of lucigenin dye[30] which keeps the lucigenin fluorescence in the quenched state. Then, the isoosmolar Na_2SO_4 was added to the extravesicular solution and Cl^- efflux was monitored with time. A similar experiment was performed with isoosmolar $NaNO_3$ as extravesicular buffer. The results indicated that the SO_4^{2-} ion, being highly hydrophilic, is not transported easily by **1a** (Figure 2.7 B). However, the relatively more lipophilic NO_3^- ion is easily transported into the vesicles by **1a** with the concomitant efflux of Cl^-. These results suggest that the antiport mechanism of ion transport is operating through the structure formed by **1a**.

To confirm that the compound **1a** forms an efficient transport system rather than membrane damage, the ANTS-DPX coupled assay was used. The ANTS is a fluorescent dye (λ_{em} = 520 nm with λ_{ex} = 353 nm), whereas the DPX is the quencher of this fluorescence. The EYPC-LUVs⊃ANTS-DPX were prepared according to the known procedure.[31] Upon adding the compound **1a**, there was no significant leakage of the dye from vesicles, which confirmed that

the compound neither destroys the integrity of the lipid bilayer membrane nor large transmembrane pores are formed by the compound (Figure 2.7 C).

2.2.6. Plannar Bilayer Conductance Studies:

To study whether the ion transport is facilitated by transmembrane channels or mobile carriers formed by **1a**, conductance measurements across the planar lipid bilayer membrane was done. In a typical experiment, the two compartments (*cis* and *trans* chambers) containing 1 M KCl solution were separated by a planar lipid bilayer composed of diphytanoyl phosphatidylcholine (diPhyPC) lipid.[6,27] The compound **1a** (20 μM) was added to the *trans*-chamber and stirred for around 30 minutes. Distinct single channel opening and closing events were observed at different holding potentials, which indicated the formation of single ion channels by compound **1a** in the lipid bilayer membrane (Figure 2.8A, B). The single-channel conductance was calculated to be 40.06 ± 0.9 pS in 1 M KCl solution. The diameter of the channel formed by **1a** was calculated from the single channel conductance values by using equation 1 to be as 4.1 ± 0.12 Å which is close to the diameter of Cl^- ion (3.6 Å).

$$1/g = (l + \pi d/4) \times (4\rho / \pi d^2) \qquad \text{(Equation 1)}$$

where, g = corrected conductance, l = length of the ion channel = 34 Å, and ρ = resistivity of the 1 M KCl solution = 9.47 Ω·cm).

The plot showing the variation of current versus voltage (*I-V*) showed a linear relation in the range of –90 mV to +90 mV both in symmetrical as well as unsymmetrical concentrations of KCl (Figure 2.8C) in *cis* and *trans* chambers, with the reversal potential to be -15 ± 2 mV. The ohmic behavior of the channel is anticipated due to the non-dipolar nature of channel forming molecules.

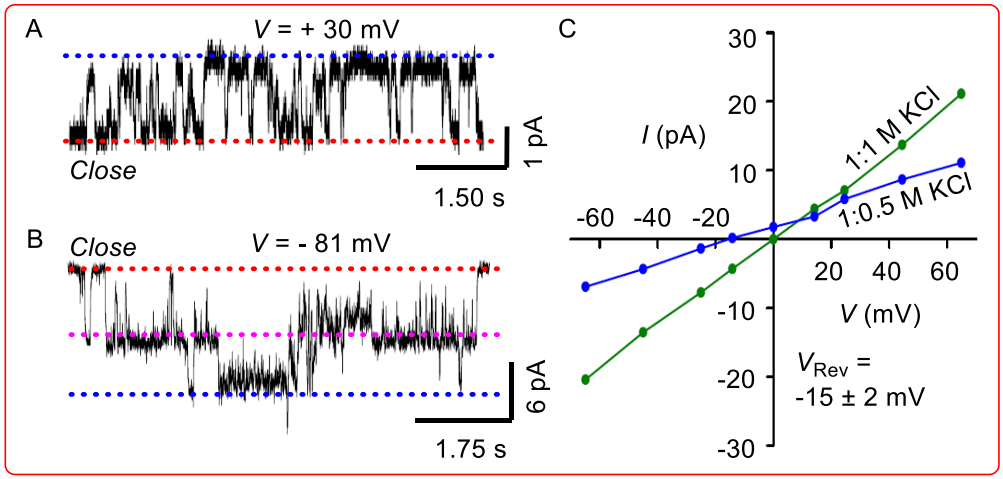

Figure 2.8. Single-channel conductance of compound **1a** (20 μM) recorded at +30 mV (A) and at −100 mV (B) under symmetrical KCl solutions. *I-V* plots of **1a** under symmetrical and unsymmetrical concentrations of KCl (C).

2.2.7. Molecular Modelling of Ion channel:

The data obtained for the channel formed by **1a** inspired us to get more insights about the binding filter and the overall picture of the channel. So we performed the geometry optimization studies to construct a theoretical model of the proposed channel. At first, an equivalent all-atom model of the channel was constructed using four fumaramide molecules, where the cholate moieties were replaced (in order to make the calculations easy) with the propyl groups, as a barrel stave supramolecular structure. The resulting supramolecular structure was optimized using MOPAC201223[32] software with the PM6-DH+24[33] method. The outcome of the results suggested that the individual fumaramide molecules are interlocked via intermolecular C=O•••H-N hydrogen bonding interactions and Cl^- ion the recognition within the cavity occurs through anion-π interactions[34] (Figure 2.9 A, B). After getting the initial picture of the channel, a model of the full-channel was constructed using four molecules of **1a** and three Cl^- ions were placed within the lumen of the channel (one Cl^- near the fumaramide core moieties and two Cl^- either

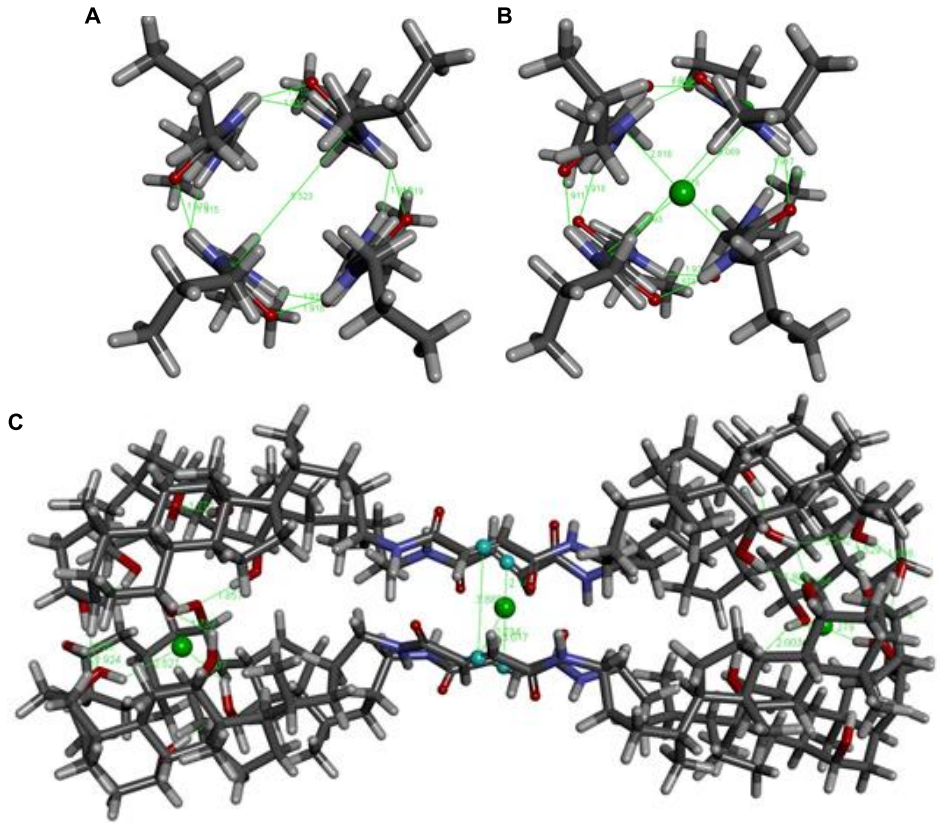

Figure 2.9. Top views of the geometry optimized tetrameric N^1,N^4-dipropylfumaramide channel. Side with (A) and without chloride ion (B). Side view of the optimized full-channel with non-covalent interactions among fumaramides and anion–π with two chloride ions (green) placed near the end and one at centre of the channel. Cyan colored dots represent the centroids of C=C bonds.

side, near the cholates). The reason for adding more than one Cl^- ions simultaneously within the lumen of the channel was motivated by the literature reports, which demonstrate the presence of multiple ions within the lumen of the natural channels[35,36] when more than one ion binding sites are present and to reduce the time of optimization. The all-atom model was also optimized using the same method (Figure 2.9 C). The resulting supramolecular barrel stave structure showed that many of the hydroxyl groups of cholate moieties are participating in the inter-stave hydrogen bonding interactions, (O···H-O distance 1.7 Å to 1.9 Å), which stabilize the overall channel structure, whereas other hydroxyl groups form hydrogen bonds with the Cl^- ions (*i.e.* OH···Cl^- bond distances are 2.0 Å to 2.5 Å). The interactions of the Cl^- with surrounding fumaramides were also evident.

2.3. CONCLUSION:

In summary, we have reported the design of a bis-cholate substituted fumaramide barrel-stave supramolecular anion channel formation. The positioning of the steric and rigid cholate moieties away from the fumaramide core favored their intermolecular hydrogen-bonded barrel-stave self-assembly in the lipid bilayer membrane. The hydroxyl groups of cholate moieties and alkene π-electron cloud of fumaramides leads to the formation of the lumen with polar channel interior, which is suitable for anion binding. Fluorescence-based ion transport experiments across the large unilamellar vesicles (LUVs) indicated the formation of a supramolecular ion channel by fumaramide molecule **1a**. Such a channel favors the antiport mechanism of anion transport with the highest selectivity towards the chloride ion. The planar bilayer conductance measurements confirmed the formation of ion channels of diameter 4.1 ± 0.12 Å and provided an additional support to chloride selectivity. The geometry optimized structure of the proposed channel with internal chloride ions confirmed the formation of C=O•••H-N hydrogen-bonded channel and anion recognition by anion-π interactions from electron-deficient C=C moieties and hydrogen bonding from hydroxyl groups.

2.4. EXPERIMANTAL SECTION:

2.4.1. General Methods.

All reactions were carried out under the nitrogen (inert) atmosphere. All the chemicals were purchased from commercial sources and were used as received unless stated otherwise. Solvents were dried by standard methods prior to use or purchased as dry. Thin layer chromatography (TLC) was carried out with E. Merck silica gel 60-F_{254} plates and column chromatography was performed over silica gel (100-200 mesh) obtained from commercial suppliers. Egg yolk phosphatidylcholine (EYPC) lipid was purchased from Avanti Polar Lipids as a solution dissolved in chloroform (25 mg/mL). HEPES buffer, HPTS dye, ANTS-DPX system, Triton X-100, NaOH and all inorganic salts of molecular biology grade were purchased from Sigma. Size exclusion chromatography was done on column packed with sephadex G-50. Large unilamellar vesicles (LUVs) were prepared from EYPC lipid by using mini extruder, equipped with a

polycarbonate membrane either of 100 nm or 200 nm pore size, obtained from Avanti Polar Lipids.

2.4.2. Physical Measurements.

The ^{1}H and ^{13}C NMR spectra were recorded on 400 MHz Bruker (or 100 MHz for ^{13}C) spectrometers using either residual solvent signals as an internal reference or from internal tetramethylsilane on the δ scale relative to chloroform (δ 7.26), dimethylsulphoxide (δ 2.50 ppm), acetone (δ 2.05) for ^{1}H NMR and chloroform (δ 77.20 ppm), dimethylsulphoxide (δ 39.50 ppm), acetone (δ 29.84 and 206.26) for ^{13}C NMR. The chemical shifts (δ) are reported in ppm and coupling constants (J) in Hz. The following abbreviations are used: s (singlet), d (doublet) m (multiplet), td (triplet of doublet) while describing ^{1}H NMR signals. High-resolution mass spectra (HRMS) were obtained from MicroMass ESI-TOF MS spectrometer. Fluorescence spectra were recorded by using Fluoromax-4 from Jobin Yvon Edison equipped with an injector port and a magnetic stirrer. 10 mM HEPES (with 100 mM NaCl or other salts as per necessity) buffer solutions were used for fluorescence experiment and the pH of the buffers were adjusted to 7.0 or 8.0 by NaOH and pH of the buffer solutions were measured using Helmer pH meter. FT-IR spectra were obtained using NICOLET 6700 FT-IR spectrophotometer as KBr disc and reported in cm^{-1}. Melting points of all the compounds were measured using a VEEGO Melting point apparatus. All melting points were measured in open glass capillary and values are uncorrected. All fluorescence data were processed either by Origin 8.5 or KaleidaGraph and finally all data were processed through Chem Draw Professional 15.

2.4.3. Synthesis.

Synthesis of compound 4: Synthesis of compound **2** was done according to known protocol.[17] Cholic acid **3** (1.07 g, 2.62 mmol), DCC (590 mg, 2.86 mmol), and *N*-hydroxysuccinimide (430 mg, 3.78 mmol) were dissolved in anhydrous THF and CH_3CN (10:1 mL). After 8 h at room temperature, the white solid formed was filtered out and the filtrate was concentrated *in vacuo* to give a white foam (88% yield). A portion of this solid (350 mg, 0.700 mmol) was dissolved in anhydrous DMF and NH_4OH (27% aqueous solution) was added. After 12 h of stirring at 50 °C, the mixture was poured into brine. The precipitate was collected by suction filtration, washed with water (2 × 10 mL), and purified with column chromatography over silica gel using CH_2Cl_2/CH_3OH (8:1) as the eluent to give a white powder (213 mg, 75% yield). ^{1}H NMR spectrum was matched with the data of the reported compound.

Synthesis of compound 5: Synthesis of compound **5** was also done according to known protocol.[17] Compound **4** (310 mg, 0.76 mmol) was dissolved in anhydrous THF under N_2. $LiAlH_4$ (288 mg, 7.6 mmol) was added slowly. The reaction mixture was heated to reflux for 12 h. A small amount of ethyl acetate was added slowly to quench the $LiAlH_4$, which was the filtered and the filtrate was collected and concentrated *in vacuo*. The residue was purified with

column chromatography over silica gel using CH_2Cl_2/CH_3OH (10:1) and CH_3OH/Et_3N (50:1) as the eluents to give a white solid (194 mg, 65% yield). ^{1}H NMR spectrum of the synthesized compound was matched with reported data.

Synthesis of compound 1a: In a 25 mL round bottom flask, a solution of amine **5** (200 mg, 0.51mmol) and Et_3N (178 µL, 1.27 mmol) in CH_3CN (4 mL) were taken and cooled to 0 ^oC. A solution of fumaryl chloride (~18 µL, 0.17 mmol) in CH_3CN (2 mL) was added drop wise during a period of 1 h at the same temperature. The reaction mixture was stirred for additional 1 h at room temperature. White precipitate was observed in the reaction mixture. After completion of reaction, solvent was removed under reduced pressure. The obtained residue was partially dissolved in EtOAc (2 × 100 mL) and transferred to a separatory funnel. The organic layer was washed first with water (2 × 100 mL) and then with brine (2 × 50 mL) solution. The organic layer was then evaporated under reduced pressure to obtain light brown to white solid, which was further purified by column chromatography over silica gel. Expected product was obtained as white solid with 45% (66 mg) yield. **M.p.:** 175-177 ^oC; **IR (KBr):** ν/cm^{-1} 3418, 2930, 2864, 1713, 1635, 1552, 1461, 1378, 1304, 1167, 977; **^{1}H NMR (400 MHz, DMSO-d_6, δ):** 8.31 (m, 2H), 6.80 (s, 2H), 4.33 (d, 2H, *J* = 4.3 Hz), 4.11 (d, 2H, *J* = 3.5 Hz), 4.01 (d, 2H, *J* = 3.3 Hz), 3.79 (s, 2H), 3.61 (s, 2H), 3.11 (m, 4H), 2.26–0.81 (m, 64H), 0.59 (s, 6H) ppm; **^{13}C NMR (100 MHz, DMSO-d_6):** δ 164.1 , 133.0, 71.5, 70.9, 66.7, 46.6, 46.2, 45.7, 42.0, 41.7, 35.8, 35.6, 35.3, 34.9, 33.3, 30.9, 29.0, 27.8, 27.7, 26.7, 26.0, 23.3, 23.1, 22.2, 14.5, 12.; **HRMS (ESI):** Calc. for $C_{52}H_{86}N_2O_8$ $[M+H]^+$: 867.6462; Found: 867.6475.

Synthesis of compound 1b: In a 25 mL round bottom flask, maleic acid (30 mg, 0.26 mmol), amine **3** (245 mg, 0.63 mmol) and HOBT (97 mg, 0.63 mmol) were dissolved in DMF (12 mL) and cooled to 0 ^oC. Then EDC·HCl (150 mg, 0.78 mmol) was added in portions to the above reaction mixture. The reaction mixture was stirred at room temperature for 18 h. After completion of reaction, THF was removed under reduced pressure and obtained residue was extracted with ethyl acetate (2 × 100 mL) and water (2 × 100 mL). Organic layer was washed with brine solution (2 × 50 mL) and then evaporated under *vacuo* to give light brown residue. Column chromatography was performed over silica gel to get the expected compound (dirty white solid) with 39% (87 mg) yield. **M.p.:** 125-127 ^oC; **IR (KBr):** ν/cm^{-1} 3435, 2925, 2854, 1744, 1630, 1460, 1381, 1184, 1083, 1031, 909. **^{1}H NMR (400 MHz, DMSO d_6, δ):** 9.33 (m, 2H), 6.09 (s, 2H), 4.32 (d, 2H, *J* = 4.2 Hz), 4.11 (d, 2H, *J* = 3.4 Hz), 4.0 (d, 2H, *J* = 3.2 Hz), 3.79 (s, 2H), 3.61 (s, 2H), 3.08 (m, 4H), 2.28–0.81 (m, 64H), 0.59 (s, 6H); **^{13}C NMR (100 MHz, DMSO-d_6):** δ 164.8, 132.4, 71.5, 70.9, 66.7, 49.0, 46.7, 46.2, 42.0, 41.7, 35.7, 35.5, 35.3, 34.8, 33.2, 30.8, 29.0, 27.8, 27.7, 26.6, 25.9, 23.2, 23.0, 17.6, 13.9, 12.8. **HRMS (ESI):** Calc. for $C_{52}H_{86}N_2O_8$ $[M+H]^+$: 867.6462; Found: 867.6461.

2.4.4 Atomic Force Microscopy (AFM) studies.

The different solutions of compound **1a** with concentrations 50 µM, 100 µM and 150 µM were was prepared in THF and this solution was sonicated for 15 minutes. Then 1 µL of these

solutions were placed on mica sheet and dried under the vacuum desiccators using high vacuum pump for 2 days. AFM data were recorded using Nano Wizard Atomic Force Microscopy.

2.4.5. Ion Transport Studies.

Buffer and stock solution preparation : HEPES buffer (10 mM) was prepared by dissolving solid HEPES in autoclaved water, then NaCl (100 mM) was added and followed by adjustment of pH = 7.0 by adding NaOH solution. Stock solutions of all compounds were prepared in either HPLC grade DMSO (for HPTS assay) and in 1:1 MeOH/THF (for Lucigenin assay). [22,24]

Preparation of EYPC-LUVs⊃HPTS: 1 mL egg yolk phosphatidylcholine (EYPC) (25 mg/mL in $CHCl_3$) was taken in a 10 mL clean and dry small round bottomed flask. A thin transparent film of lipid was prepared by purging nitrogen with continuous rotation. The resulting transparent film was kept in high vacuum for at least 5 h to remove all trace of $CHCl_3$ for drying. After that transparent film was hydrated with 1 mL of aforementioned buffer (1 mM HPTS, 10 mM HEPES, 100 mM NaCl, pH = 7.0) for 1 h with occasional vortexing of 4-5 times and then subjected to freeze-thaw cycle (≥ 15 times). Extrusions were done 19 times (must be an odd number) by a Mini-extruder equipped with a polycarbonate membrane (pore diameter of 100 nm). All extravesicular dyes were removed by gel filtration with Sephadex G-50 with buffer (10 mM HEPES, 100 mM NaCl, pH = 7.0) and obtained vesicle was diluted to 6 mL with buffer (10 mM HEPES, 100 mM NaCl, pH = 7.0) to give EYPC-LUVs⊃HPTS: ~ 5.0 mM EYPC, inside: 1 mM HPTS, 10 mM HEPES, 100 mM NaCl, pH = 7.0 and outside: 10 mM HEPES, 100 mM NaCl, pH = 7.0.

Ion transport activity: 1975 μL of HEPES buffer (10 mM HEPES, 100 mM NaCl, pH = 7.0) was taken in a clean fluorescence cuvette followed by addition of 25 μL of EYPC-LUVs⊃HPTS in the same cuvette and was placed on the fluorescence instrument (at t = 0 s) equipped with magnetic stirrer. Fluorescence emission intensity of HPTS dye, F_t was monitored at λ_{em} = 510 nm (λ_{ex} = 450 nm) with time. After that a pH gradient between the intra and extra vesicular system was created by adding 20 μL of 0.5 M NaOH to the same cuvette at t = 20 s (Figure 2.10). All compounds were added at t = 100 s in different concentrations and finally at t = 300 s, 25 μL of 10% Triton X-100 was added to destroy all vesicles which resulted in destruction of pH gradient (Figure 2.10) which resulted in saturation in fluorescence emission intensity.

The time axis was normalized according to Equation 2:

$$t = t - 100 \qquad \text{(Equation 2)}$$

The time of compound addition can be normalized to t = 0 s and time of Triton-X 100 addition was normalized to t = 200 s.

Fluorescence intensities (F_t) were normalized to fractional emission intensity I_F using Equation 3:

$$I_F = [(F_t - F_0)/(F_\infty - F_0)] \times 100 \qquad \text{(Equation 3)}$$

Where F_0 = Fluorescence intensity just before the compound addition (at t = 0 s). F_∞ = Fluorescence intensity at saturation after complete leakage (at t = 330 s). F_t = Fluorescence intensity at time t.

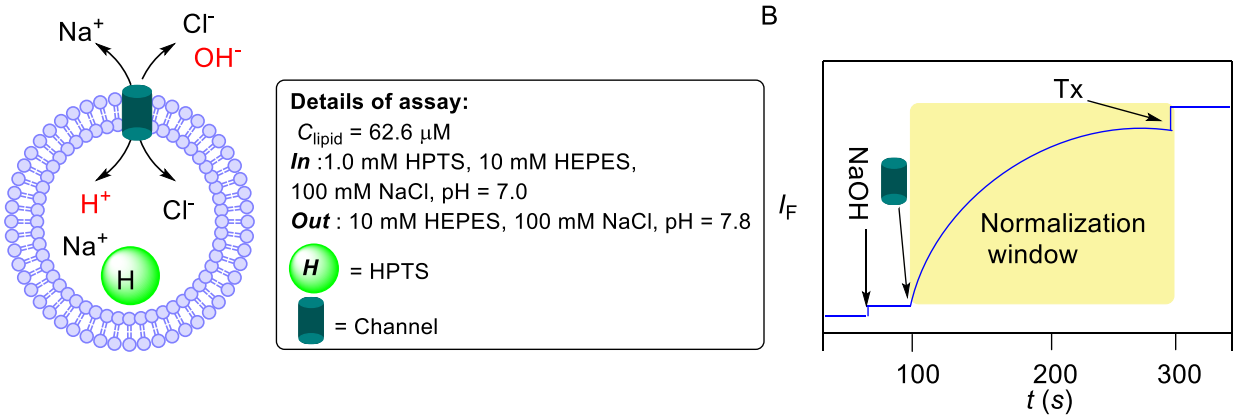

Figure 2.10. Representation of ion transport activity assay using EYPC-LUVs⊃HPTS.

Ion transport kinetics was studied at different concentrations for each compound. Change of HPTS emission intensity in this process was monitored with time. The concentration profile data were analyzed by Hill Equation (Equation 4) to get the Effective concentration (EC_{50}) and Hill coefficient (n),

$$Y = Y_\infty + (Y_0 - Y_\infty) / [1 + (c / EC_{50})^n] \qquad \text{(Equation 4)}$$

Where, Y_0 = Fluorescence intensity just before the channel addition (at 0 s). Y_∞ = Fluorescence intensity with excess channel concentration, c = concentration of channel forming molecule.

Determination of Ion Selectivity by HPTS assay:

Buffer and Stock Solution Preparation: HEPES buffers with all salts were prepared by dissolving solid HEPES (10 mM) followed by addition of appropriate salt (100 mM) in autoclaved water and adjustment of pH (pH = 7.0) was done by drop wise addition of NaOH solution.

Preparation of EYPC-LUVs⊃HPTS for Cation Selectivity: EYPC-LUVs⊃HPTS (~ 5.0 mM EYPC, inside: 1 mM HPTS, 10 mM HEPES, 100 mM NaCl, pH = 7.0 and outside: 10 mM HEPES, 100 mM NaCl, pH = 7.0) were prepared following reported protocol.

Cation Selectivity Assay: In a clean fluorescence cuvette 1975 μL of different HEPES buffer solutions (10 mM HEPES, 100 mM MCl, pH = 7.0; where, M^+ = Li^+, Na^+, K^+, Rb^+ and Cs^+) were taken followed by addition of 25 μL of EYPC-LUVs⊃HPTS vesicle in slowly stirring condition by a magnetic stirrer equipped with the fluorescence instrument (at t = 0 s). The time course of HPTS fluorescence intensity, F_t was monitored at λ_{em} = 510 nm (λ_{ex} = 450 nm). At t = 20 s, 20 μL of 0.5 M NaOH was added to the cuvette to make the pH gradient between the intra and extra vesicular system. The compound **1a** was added at t = 100 s and at t = 300 s, 10% Triton X-100 (25 μL) was added to lyze all vesicles for complete destruction of pH gradient. For data analysis and comparison, time (X-axis) was normalized between the point of channel addition (*i.e.* t = 100 s was normalized to t = 0 s) and end point of experiment (*i.e.* t = 300 s was normalized to t = 200 s). Fluorescence intensities (F_t) were normalized to fractional emission intensity I_F using Equation 3.

Anion selectivity Assay. The anion selectivity was evaluated by two methods as given below.

Method 1.

Preparation of EYPC-LUVs⊃HPTS for Anion Selectivity: EYPC-LUVs⊃HPTS (~ 5.0 mM EYPC, inside: 1 mM HPTS, 10 mM HEPES, 100 mM NaX, pH = 7.0 and outside: 10 mM HEPES, 100 mM NaX, pH = 7.0) were prepared following reported protocol. [25]

Anion Selectivity Assay: In a clean fluorescence cuvette 1975 μL of HEPES buffer (10 mM HEPES, 100 mM NaX, at pH = 7.0; where, X^- = Cl^-, Br^-, ClO_4^-, NO_3^- and I^- was added followed by addition of 25 μL of EYPC-LUVs⊃HPTS vesicle in slowly stirring condition by a magnetic stirrer equipped with the fluorescence instrument (at t = 0 s). HPTS fluorescence emission intensity (F_t) was monitored with time at λ_{em} = 510 nm (λ_{ex} = 450 nm). 20 μL of 0.5 M NaOH was added to the cuvette at t = 20 s to make the pH gradient between the intra and extra vesicular system. The compound **1a** was added at t = 100 s and at t = 300 s, 25 μL of 10% Triton X-100 was added to lyze all vesicles for complete destruction of pH gradient. For data analysis and comparison, time (X-axis) was normalized between the point of transporter addition (*i.e.* t = 100 s was normalized to t = 0 s) and end point of experiment (*i.e.* t = 300 s was normalized to t = 200 s) using Equation S1. Fluorescence intensities (F_t) were normalized to fractional emission intensity I_F using Equation 3.

Method 2.

Preparation of EYPC-LUVs⊃HPTS for Anion Selectivity: EYPC-LUVs⊃HPTS (~ 5.0 mM EYPC, inside: 1 mM HPTS, 10 mM HEPES, pH = 7.0 and outside: 25 mM HEPES, 2 N NaX, pH = 7.0) were prepared following reported protocol. [26]

Anion Selectivity Assay: : In a clean fluorescence cuvette 1.6 mL of 10 mM HEPES buffer with pH 7.0 was added followed by addition of 80 μL EYPC-LUVs⊃HPTS vesicle in slowly stirring condition by a magnetic stirrer equipped with the fluorescence instrument (at t = 0 s). HPTS

fluorescence emission intensity (F_t) was monitored with time at λ_{em} = 510 nm (λ_{ex} = 450 nm). 50 µL of 2 N NaX salt solution was added at 30 s to create the ion gradient across the lipid bilayer. The compound **1a** was added at t = 100 s and at t = 300 s, 25 µL of 10% Triton X-100 was added to lyze all vesicles for complete destruction of ion gradient.

Determination of chloride ion selectivity by lucigenin assay:[30]

Preparation of EYPC-LUVs⊃Lucigenin for concentration dependent assay and symport assay: 1 mL solution of EYPC (25 mg) lipid dissolved in $CHCl_3$ was taken in a clean and dry small round bottom flask. The solvents were evaporated slowly by a stream of nitrogen, followed by drying under vacuum for at least 5 h. After that 1 mL of 1 mM *N*,*N*′-Dimethyl-9,9′-biacridinium dinitrate (lucigenin) in 200 mM $NaNO_3$ (dissolved in water) was added, and the suspension was hydrated for 1 h with occasional vortexing of 4-5 times and then subjected to freeze-thaw cycle (≥ 15 times). The vesicle solution was extruded through a polycarbonate membrane with 200 nm pores for minimum 19 times (must be an odd number), to give vesicles with a mean diameter of ~ 200 nm. The extracellular lucigenin was removed from the vesicles by size exclusion column chromatography (Sephadex G-50) using 200 mM $NaNO_3$ as eluent. The obtained vesicles were diluted to 4 mL with 200 mM $NaNO_3$.

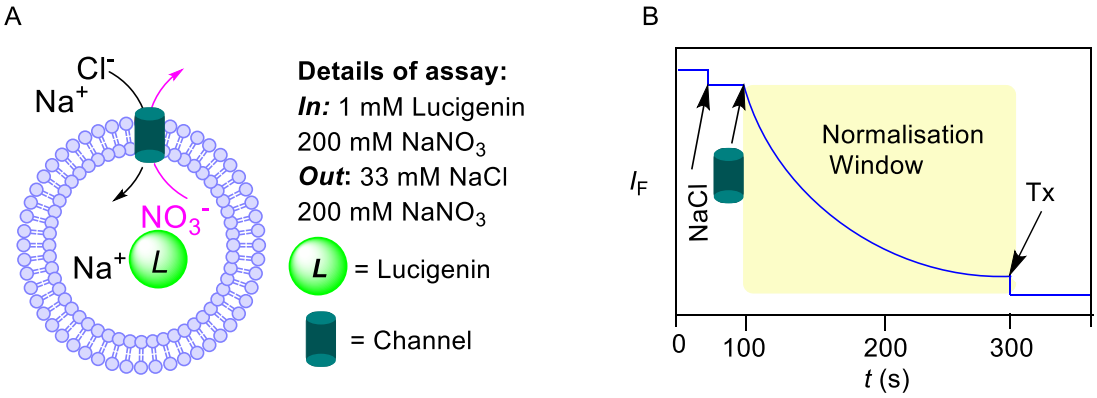

Figure 2.11. Schematic illustration of chloride influx assay using EYPC-LUVs⊃Lucigenin (A) and representative fluorescence kinetics experiment of corresponding assay (B).

Determination of chloride ion selectivity by lucigenin assay: In a clean and dry fluorescence cuvette 50 µL of above lipid solution and 1950 µL of 200 mM $NaNO_3$ solution was taken and kept in slowly stirring condition by a magnetic stirrer equipped with the fluorescence instrument (at t = 0 s). In this assay, the time course of lucigenin fluorescence emission intensity, Ft was observed at λ_{em} = 535 nm (λ_{ex} = 450 nm). 25 µL of 2 N NaCl was added to the cuvette at t = 50 s to make the salt gradient between the intra and extra vesicular system. Compound **1a** was added at t = 100 s and finally at t = 300 s, 25 µL of 10% Triton X-100 was added to lyse all vesicles for 100% chloride influx. Fluorescence intensities (F_t) were normalized to fractional emission intensity I_F using Equation 5.

Normalized Fl Intensity (I_F) = [(Ft - F_0) / (F_∞ - F_0)] × (-100) (Equation 5)

Preparation of EYPC-LUVs⊃Lucigenin for antiport study: A solution of EYPC (25 mg) dissolved in $CHCl_3$ was taken in a clean and dry small round bottom flask. The solvents were evaporated slowly by a stream of nitrogen, followed by drying under vacuum for at least 4 hour. After that 1 mL of 1 mM *N*,*N*′-dimethyl-9,9′-biacridinium dinitrate (lucigenin) in 200 mM NaCl (dissolved in water) was added, and the suspension was hydrated for 1 h with occasional vortexing of 4-5 times and then subjected to freeze-thaw cycle (≥ 15 times). The vesicle solution was extruded through a polycarbonate membrane with 200 nm pores 19 times (must be an odd number), to give vesicles with a mean diameter of ~ 200 nm. The extracellular lucigenin was removed from the vesicles by size exclusion column chromatography (Sephadex G-50) using 200 mM NaCl as eluent. The vesicles were diluted to 4 mL with 200 mM NaCl.

Determination of antiport mechanism by lucigenin assay: In a clean and dry fluorescence cuvette 50 μL of above lipid solution and 1950 μL of iso-osmolar solution of different NaX salts were taken and kept in slowly stirring condition by a magnetic stirrer equipped with the fluorescence instrument (at t = 0 s). The time course of lucigenin fluorescence emission intensity, Ft was monitored at λ_{em} = 535 nm (λ_{ex} = 450 nm). Compound **1a** was added at t = 100 s and finally at t = 300 s, 25 μL of 10% Triton X-100 was added to lyse all vesicles for 100% chloride efflux. Fluorescence intensities (F_t) were normalized to fractional emission intensity I_F using Equation 5.

Evaluation of membrane stability and channel nature by ANTS-DPX assay: [31]EYPC LUVs were loaded with anionic fluorophore ANTS (8-aminonaphthalene-1,3,6-trisulfonic acid disodium salt) and cationic quencher DPX (1,1-[1,4-phenylenebis(methylene)]bis[pyridinium]bromide) (Figure 2.12 A). Efflux of either ANTS or DPX through pores formed by **1a** was followed by an increase in ANTS emission intensity.
EYPC LUVs were loaded with anionic fluorophore ANTS (8-aminonaphthalene-1,3,6-trisulfonic acid disodium salt) and cationic quencher DPX (1,1-[1,4-phenylenebis(methylene)]bis[pyridinium]bromide) (Figure 2.12 B). Efflux of either ANTS or DPX through pores formed by **1a** was followed by an increase in ANTS emission intensity.

The following buffers were prepared by known method. [37]

Buffer A: 12.5 mMANTS, 45.0 mM DPX, 5 mM TES, 20 mM KCl, pH = 7.0
Buffer B: 5 mM TES, 100 mM KCl, pH = 7.0

Prepartion of EYPC-LUVs⊃ ANTS/DPX vesicles: A thin film of EYPC (25 mg) was prepared by evaporating a solution of EYPC in $CHCl_3$ and MeOH (1 mL each) on a rotary evaporator and then in vacuo (6 h), and then hydrated with 1 mL buffer A, followed by vortex treatment (4 times). The resulting suspension was subjected to > 5 freeze-thaw cycles (using liquid N_2 to

freeze and a warm water bath to thaw), and 19 times extruded using a Mini-Extruder through a 100 nm polycarbonate membrane (Avanti). External ANTS/DPX was removed by gel filtration (Sephadex G-50) using buffer B and diluted with the same buffer to 3 mL to give EYPC-LUVs⊃ ANTS/DPX stock solution.

ANTS/DPX-assay: In a clean and dry fluorescence cuvette 50 µL of above lipid solution and 1950 µL buffer B were added. The compound **1a** was added at 50 seconds and kept in slowly stirring condition by a magnetic stirrer equipped with the fluorescence instrument (at t = 0 s). The time course of fluorescence emission intensity, Ft was monitored at λ_{em} = 520 nm (λ_{ex} = 353 nm). Finally at t = 300 s, 25 µL of 10% Triton X-100 was added to lyse all vesicles for 100% dye efflux. Fluorescence intensities (Ft) were normalized to fractional emission intensity I_F using Equation 3.

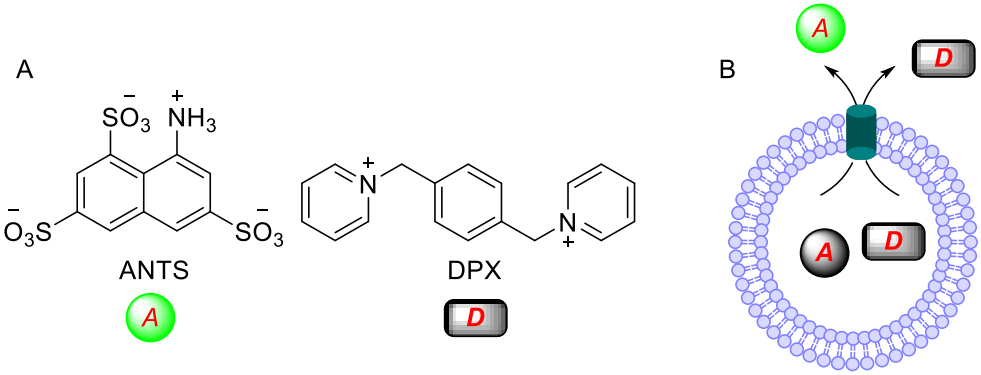

Figure 2.12. Structure of ANTS and DPX dyes and representation of ANTS–DPX assay.

2.4.6. Planar Bilayer Conductance Measurements.[27]

Bilayer membrane (BLM) was formed across an aperture of 150 µM diameter in a polystyrene cup (Warner Instrument, USA) with lipid diphytanoylphosphatidylcholine (Avanti Polar Lipids), dissolved in *n*-decane (18 mg/mL). Both chambers (*cis* and *trans*) were filled with symmetrical solution, containing 1 M KCl. The *trans* compartment was held at virtual ground and the *cis* chamber was connected to the BC 535 head-stage (Warner Instrument, USA) via matched Ag-AgCl electrodes. Compound **1a** (20 µM) was added to the *trans* chamber and the solution was stirred with magnetic stirrer for 30 min. Channel formation was confirmed by the distinctive channel opening and closing events after applying voltages. Currents were low pass filtered at 1 kHz using pClamp9 software (Molecular probes, USA) and analog-to-digital converter (Digidata 1440, Molecular probes). All data were analyzed by the software pClamp 9. The complete data trace observed for ten minutes contained a series of opening and closing events at some indefinite intervals. The average current was calculated from this trace and then conductance and other calculations were made accordingly.

Determination of anion selectivity permeability ratio by Planar Bilayer Conductance Measurements: The *cis* and *trans* chambers were filled with unsymmetric solutions of KCl. The *cis* chamber was filled with 1.0 M KCl solution and *trans* chamber was filled with 0.5 M KCl. The compound **1d** (2 μM) was added to the *trans* chamber and stirred for 5 minutes. The reversal potential was calculated to be 10 ± 2 mV (Figure 2.8 C).

The permeability ratio (P_{Cl-}/P_{K+}) was calculated by using Goldman-Hodgkin-Katz equation (Equation 6).

$$\frac{P_{Cl^-}}{P_{K^+}} = \frac{a_{K^+cis} - a_{K^+trans} \times \exp\left(-\frac{V_{rev} \times F}{R \times T}\right)}{a_{Cl^-cis} \times \exp\left(-\frac{V_r \times F}{R \times T}\right) - a_{Cl^-trans}} \qquad \text{(Equation 6)}$$

where, P_{Cl^-}/P_{K^+} = anion/cation permeability ratio; a_{K^+cis} = K^+ activity in the *cis* chamber; a_{K^+trans} = K^+ activity in the *trans* chamber; a_{Cl^-cis} = Cl^- activity in the *cis* chamber; a_{Cl^-trans} = Cl^- activity in the *trans* chamber; V_{rev} = reversal potential; F = Faraday constant; R = gas constant; T = temperature (K).

2.4.7. Theoretical Studies.

The theoretical calculations were carried out using MOPAC2012[S7] software with the PM6-DH+[S8] method to get more insights about the pattern of intermolecular hydrogen bonding among the fumaramide units. The bulky cholate units were replaced with small propyl units to make the calculations easy and simple. The optimized structure generated showed that the cavity is formed by intermolecular hydrogen bonding among four fumaramide units where each fumaraimde unit is slightly tilted from z-axis (z-axis parallel to transmembrane orientation) to allow efficient hydrogen bond formation. Each fumaramide moiety got marginally deviated from the transmembrane orientation to form stable hydrogen bonds (Figure 2.9). In the free form, similar hydrogen bond distances (i.e. O-N distance = 1.9 Å) were calculated and the channel generated a cavity size of approximately 5.6 Å. However, in the Cl^- bound form, the cavity size increased to almost 5.9 Å. A marginal expansion of the cavity size by approximately 0.3 Å was observed as result of Cl^- binding. The smaller channel diameter (4.1 ± 0.12 Å), determined by the conductance measurement, may be attributed to the narrowing of the channel near rigid and bulky cholate moieties. Further, an all-atom model of the channel was built involving four molecules and three chloride ions (one Cl^- near the fumaramide moieties and two Cl^- either side, near the cholates), and the resulting structure was optimized using same method. The optimized model showed that several hydroxyl groups of cholate moieties are participating in inter-stave O···H-O hydrogen bonding interactions with bond length varying from 1.7 Å to 1.9 Å. Further, some of the hydroxyl groups form hydrogen bonds with chloride ion with bond distance varying from 2.0 to 2.5 Å.

2.4.7. NMR SPECTRA.

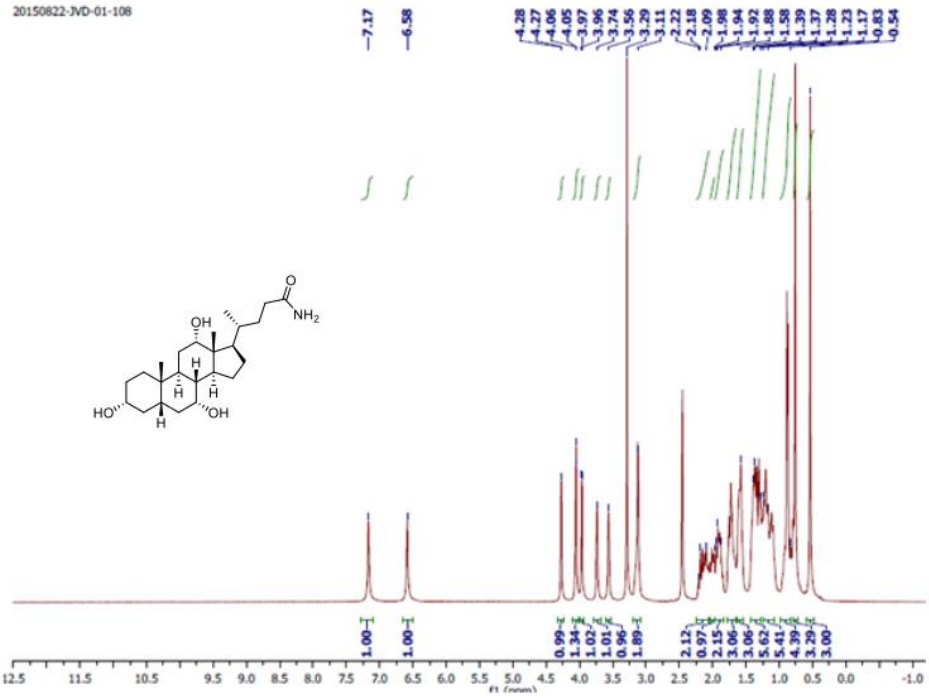

Figure 2.13. ^{1}H NMR spectrum of **4** in DMSO-d_6.

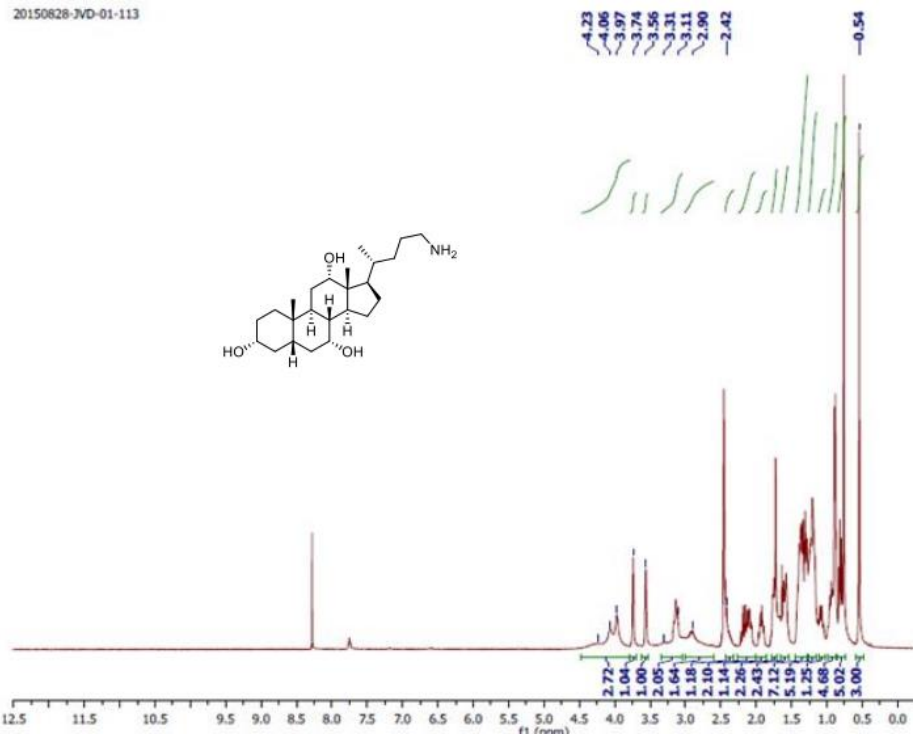

Figure 2.14. ^{1}H NMR spectrum of **5** in DMSO-d_6.

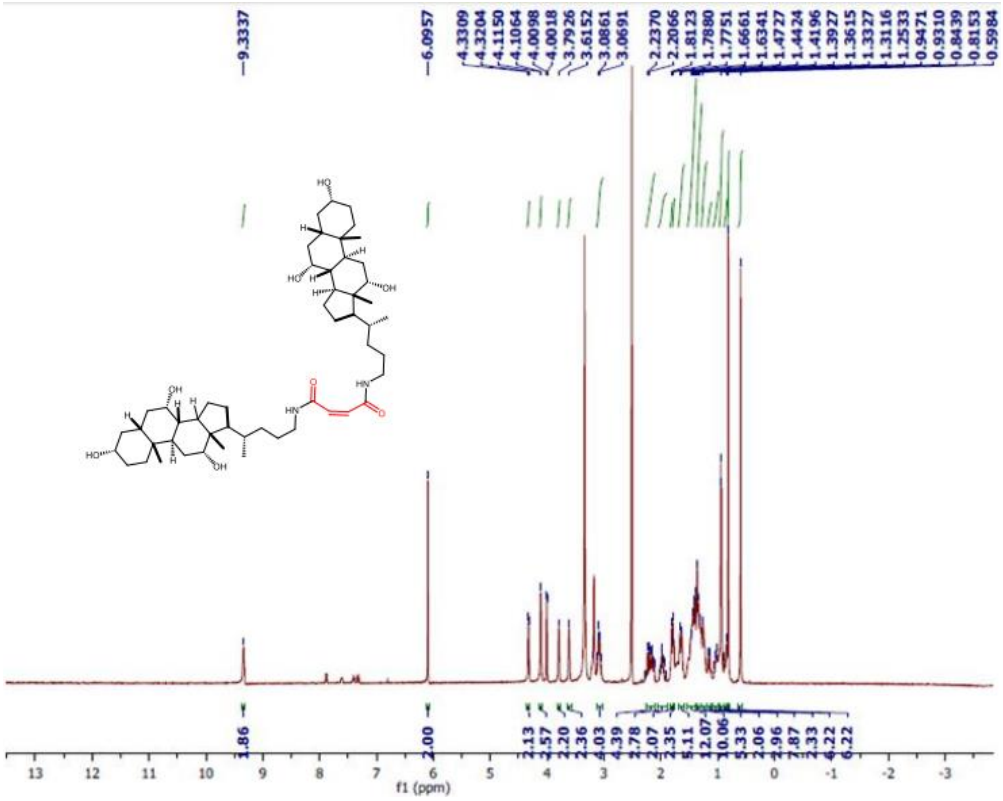

Figure 2.15. ^{1}H NMR spectrum of **1b** in DMSO-d_6.

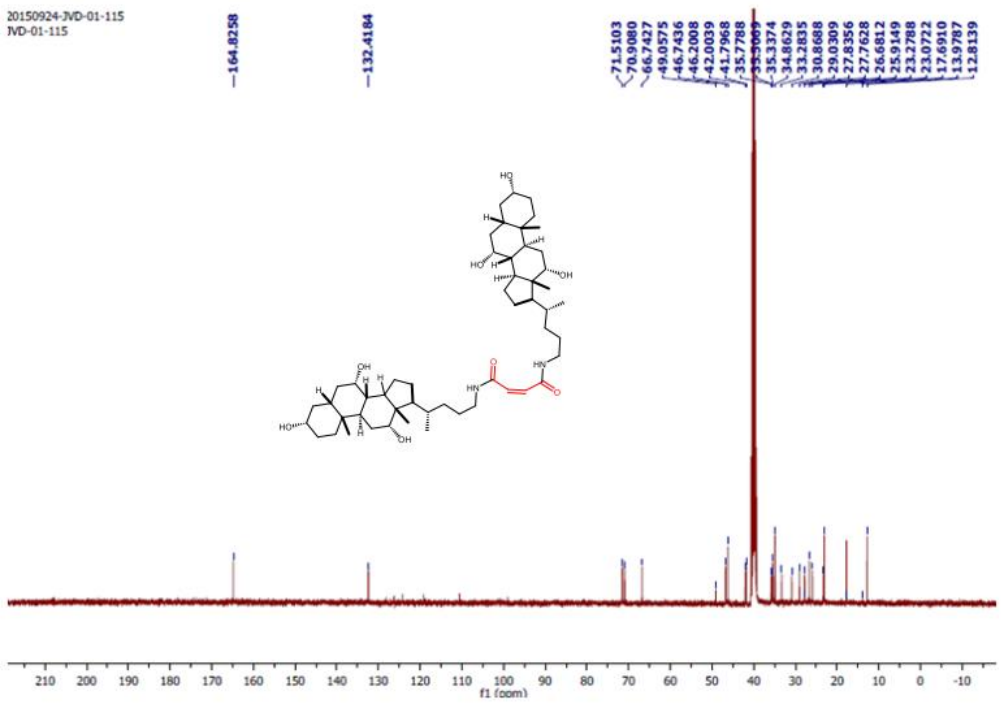

Figure 2.16. ^{13}C NMR spectrum of **1b** in DMSO-d_6.

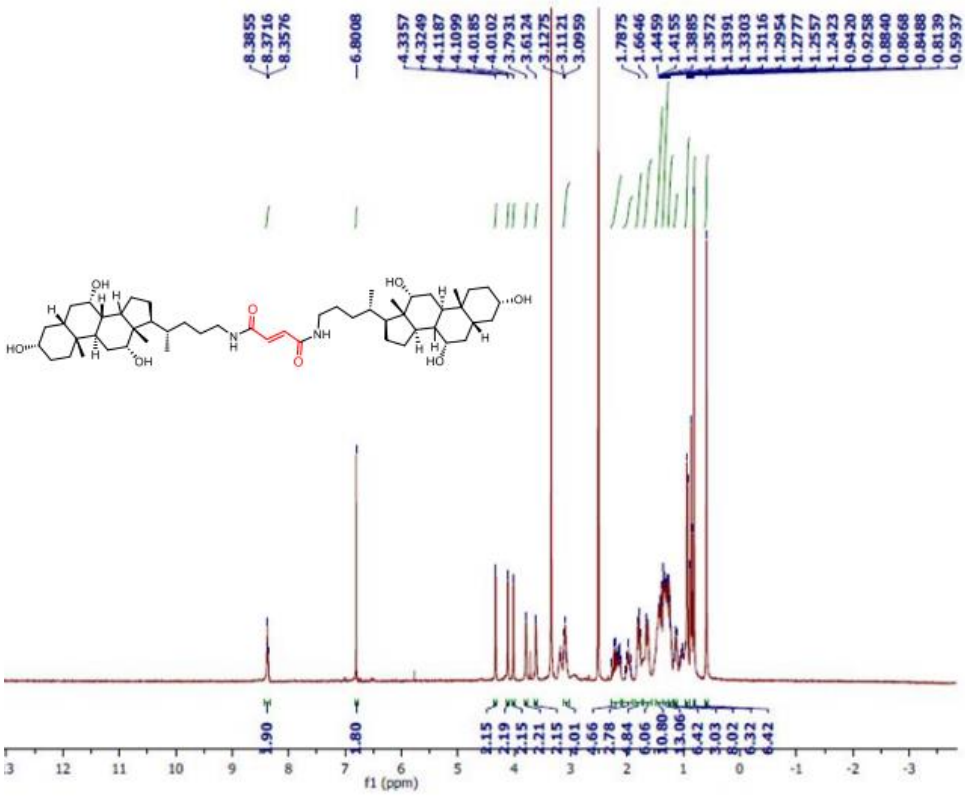

Figure 2.17. ^{1}H NMR spectrum of **1a** in DMSO-d_6.

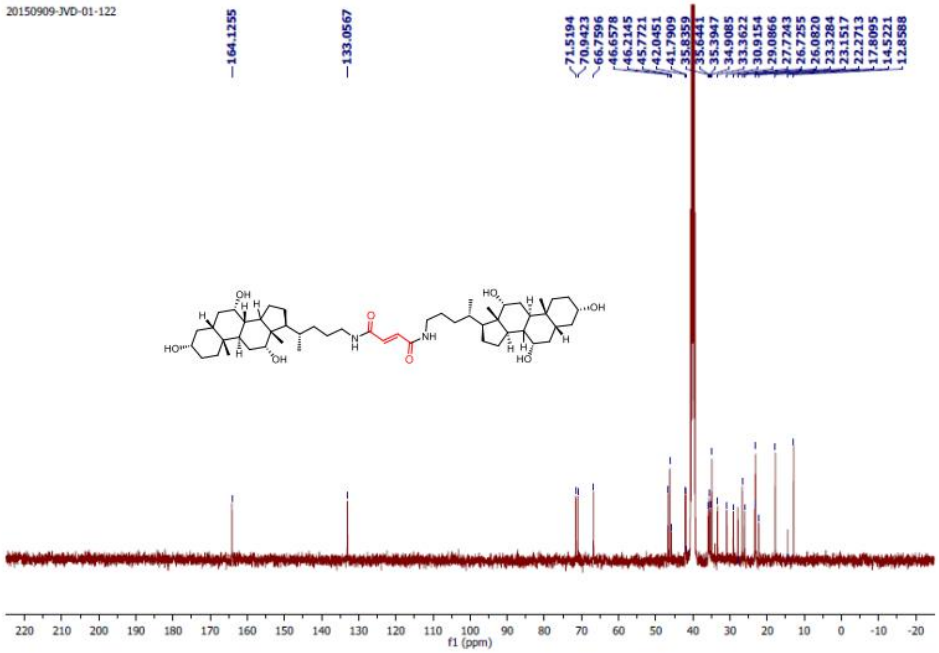

Figure 2.17. ^{13}C NMR spectrum of **1a** in DMSO-d_6.

2.5. REFERENCES:

(1) Tabushi, I.; Kuroda, Y.; Yokota, K. *Tetrahedron Lett.* **1982**, *23*, 4601.

(2) Lougheed, T.; Zhang, Z.; Andrew Woolley, G.; Borisenko, V. *Bioorg. Med. Chem.***2004**, *12*, 1337.

(3) Palacios, D. S.; Dailey, I.; Siebert, D. M.; Wilcock, B. C.; Burke, M. D. *Proc. Nat. Acad. Sci. U. S. A.* **2011**, *108*, 6733.

(4) Yoshii, M.; Yamamura, M.; Satake, A.; Kobuke, Y. *Org. Biomol. Chem.* **2004**, *2*, 2619.

(5) Bandyopadhyay, P.; Janout, V.; Zhang, L.-h.; Sawko, J. A.; Regen, S. L. *J. Am. Chem. Soc.* **2000**, *122*, 12888.

(6) Saha, T.; Gautam, A.; Mukherjee, A.; Lahiri, M.; Talukdar, P. *J. Am. Chem. Soc.* **2016**, *138*, 16443.

(7) Liu, T.; Bao, C.; Wang, H.; Lin, Y.; Jia, H.; Zhu, L. *Chem. Commun.* **2013**, *49*, 10311.

(8) Zhou, Y.; Chen, Y.; Zhu, P.-P.; Si, W.; Hou, J.-L.; Liu, Y. *Chem. Commun.* **2017**, *53*, 3681.

(9) Biscarini, F.; Cavallini, M.; Leigh, D. A.; León, S.; Teat, S. J.; Wong, J. K. Y.; Zerbetto, F. *J. Am. Chem. Soc.* **2002**, *124*, 225.

(10) Leigh, D. A.; Pérez, E. M. *Chem. Commun*. **2004**, 2262.

(11) Kay, E. R.; Leigh, D. A.; Zerbetto, F. *Angew. Chem Int. Ed.* **2007**, *46*, 72.

(12) Hernandez, J. V.; Kay, E. R.; Leigh, D. A. *Science* **2004**, *306*, 1532.

(13) Martinez-Cuezva, A.; Valero-Moya, S.; Alajarin, M.; Berna, J. *Chem. Commun*. **2015**, *51*, 14501.

(14) Mazzier, D.; Crisma, M.; De Poli, M.; Marafon, G.; Peggion, C.; Clayden, J.; Moretto, A. *J. Am. Chem. Soc*. **2016**, *138*, 8007.

(15) Roy, A.; Gautam, A.; Malla, J. A.; Sarkar, S.; Mukherjee, A.; Talukdar, P. *Chem. Commun*. **2018**, *54*, 2024.

(16) Matile, S. *Chem. Soc. Rev.* **2001**, *30*, 158.

(17) Zhou, Y.; Ryu, E.-H.; Zhao, Y.; Woo, L. K. *Organometallics* **2007**, *26*, 358.

(18) Bandyopadhyay, P.; Janout, V.; Zhang, L.-h.; Regen, S. L. *J. Am. Chem. Soc*. **2001**, *123*, 7691.

(19) Ma, L.; Harrell, W. A.; Davis, J. T. *Org. Lett.* **2009**, *11*, 1599.

(20) Restuccia, A.; Seroski, D. T.; Kelley, K. L.; O'Bryan, C. S.; Kurian, J. J.; Knox, K. R.; Farhadi, S. A.; Angelini, T. E.; Hudalla, G. A. *Chem. Commun*. **2019**, *2*, 53.

(21) Gerbelli, B. B.; Vassiliades, S. V.; Rojas, J. E. U.; Pelin, J. N. B. D.; Mancini, R. S. N.; Pereira, W. S. G.; Aguilar, A. M.; Venanzi, M.; Cavalieri, F.; Giuntini, F.; Alves, W. A. *Macromol. Chem. Phys.* **2019**, *220*, 1900085.

(22) Roy, A.; Saha, D.; Mandal, P. S.; Mukherjee, A.; Talukdar, P. *Chem. Eur. J.* **2017**, *23*, 1241.

(23) Litvinchuk, S.; Bollot, G.; Mareda, J.; Som, A.; Ronan, D.; Shah, M. R.; Perrottet, P.; Sakai, N.; Matile, S. *J. Am. Chem. Soc*. **2004**, *126*, 10067.

(24) Saha, T.; Roy, A.; Gening, M. L.; Titov, D. V.; Gerbst, A. G.; Tsvetkov, Y. E.; Nifantiev, N. E.; Talukdar, P. *Chem. Commun.* **2014**, *50*, 5514.

(25) Ren, C.; Ding, X.; Roy, A.; Shen, J.; Zhou, S.; Chen, F.; Yau Li, S. F.; Ren, H.; Yang, Y. Y.; Zeng, H. *Chem. Sci.* **2018**, *9*, 4044.

(26) Benke, B. P.; Aich, P.; Kim, Y.; Kim, K. L.; Rohman, M. R.; Hong, S.; Hwang, I.-C.; Lee, E. H.; Roh, J. H.; Kim, K. *J. Am. Chem. Soc.* **2017**, *139*, 7432.

(27) Saha, T.; Dasari, S.; Tewari, D.; Prathap, A.; Sureshan, K. M.; Bera, A. K.; Mukherjee, A.; Talukdar, P. *J. Am. Chem. Soc* **2014**, *136*, 14128.

(28) Marcus, Y. *J. Chem. Soc. Faraday Trans.* **1991**, *87*, 2995.

(29) McNally, B. A.; Koulov, A. V.; Smith, B. D.; Joos, J.-B.; Davis, A. P. *Chem. Commun.* **2005**, 1087.

(30) Roy, A.; Saha, D.; Mukherjee, A.; Talukdar, P. *Org. Lett.* **2016**, *18*, 5864.

(31) Sordé, N.; Matile, S. *J. Supramol. Chem.* **2002**, *2*, 191.

(32) Stewart, J. J. P. *MOPAC**2012***; Stewart Computational Chemistry: Colorado Springs, CO, USA, 2012.

(33) Korth, M. *J. Chem. Theory Comput.* **2010**, *6*, 3808.

(34) Gorteau, V.; Bollot, G.; Mareda, J.; Matile, S. *Org. Biomol. Chem.* **2007**, *5*, 3000.

(35) Tao, X.; Avalos, J. L.; Chen, J.; MacKinnon, R. *Science* **2009**, *326*, 1668.

(36) Mindell, J. A.; Maduke, M.; Miller, C.; Grigorieff, N. *Nature* **2001**, *409*, 219.

(37) Talukdar, P.; Sakai, N.; Sordé, N.; Gerard, D.; Cardona, V. M. F.; Matile, S. *Bioorg. Med. Chem.* **2004**, *12*, 1325.

Chapter 3

Apoptosis-Inducing Activity of a Fluorescent Barrel Rosette M^+/Cl^- Channel

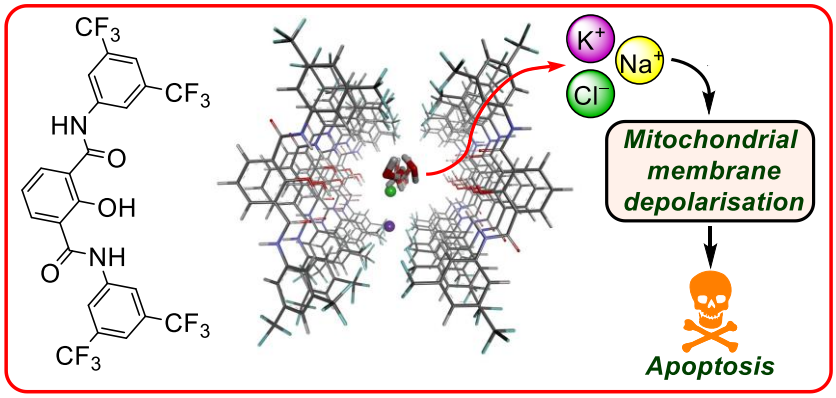

3.1. INTRODUCTION:

The ion selectivity of the naturally occurring ion channels makes them very specific for different ions, and the specific selectivity of a channel can be attributed to the presence of multiple ion binding sites. The lumen of the channel offers multiple binding sites for the specific ions, which allows the passage of the ions across the lipophilic domains of the cell membrane. This can be exemplified by reviewing the structure of the naturally occurring potassium channel KcsA, where the ion selectivity is formed by the sequential orientation of the carbonyl units along a single uniform row, forming the hydrophilic lumen of the channel. In this channel which was isolated from *S. lividians*, four identical α-helical subunits are self-assembled to form a large channel filled with water molecules in which the ion selectivity is determined by the special region called as selectivity filter.[1] The some of the main chain carbonyl oxygen atoms, from each subunit of the channel, are exposed along the line of the selectivity filter, which helps in K^+ ion

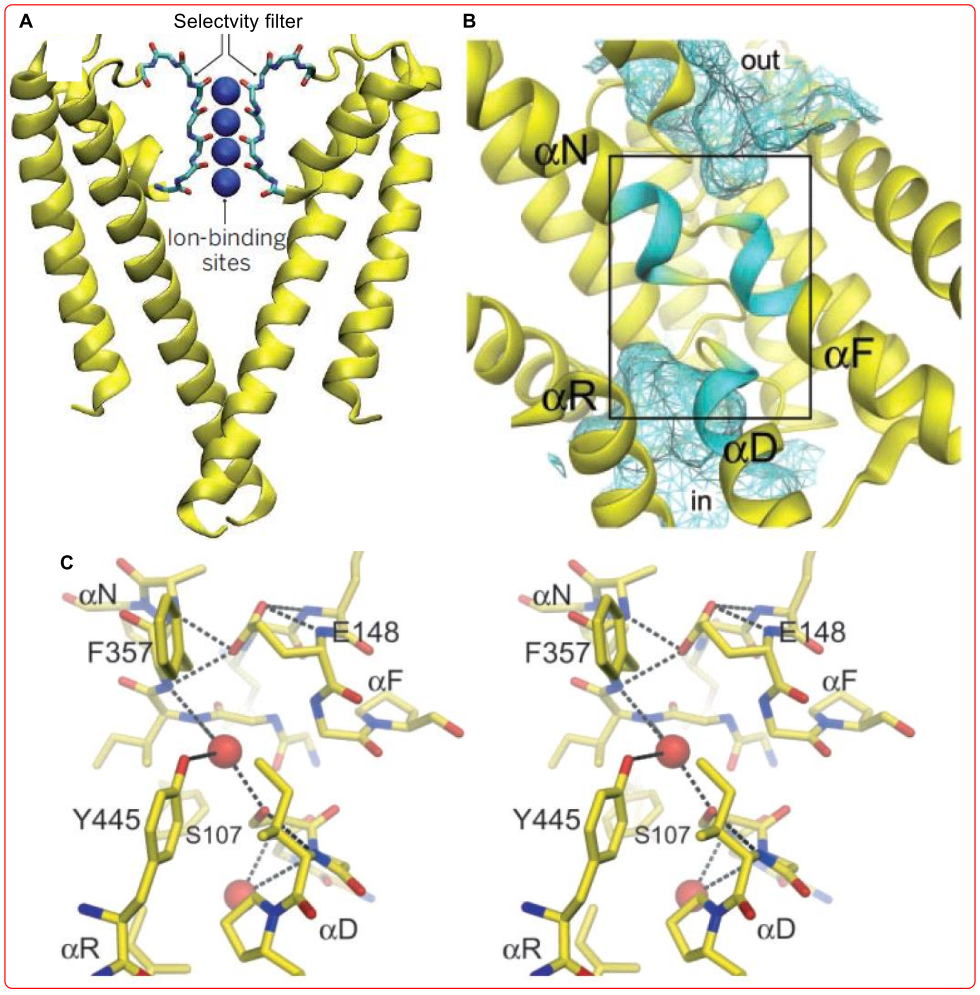

Figure 3.1. A section of the KcsA potassium channel with the ion-binding sites (blue) in the selectivity filter (A); View of the ion-conducting pore of the ClC subunit (B), and the view of the selectivity filter of the EcCLC channel with bound Cl ions as red spheres.

recognition and its transport across the cell membrane (Figure 3.1 A).

Similarly, the chloride selective channels the CLCs are well known for their selective Cl^- ion transport across the cell membranes. The crystal structure of CLC channel isolated from *E. coli* shows the presence of three ion-binding sites generating the selectivity filter that forms a bridge between the extra- and intracellular solutions (Figure 3.1 B).[2] The Cl^- ions bind to three distinct sites in the selectivity filter through the non-covalent interactions with the hydroxyl groups of amino-acid side chains and backbone amide NH groups, most of which are located at the N-terminus of α-helices (Figure 3.1 C). These three ion binding sites are occupied simultaneously by the chloride ions, although there is a close proximity. In resemblance to K^+ channels, ions permeate through the CLC channel as a single file, and the mutual repulsion among the ions leads to the rapid conduction of the ions through the lumen of the channel across the cell membrane.

Considering the aforementioned facts, it can be anticipated that imposing the multiple selectivity filters in the synthetic ion channels can considerably enhance the selectivity and activity of these channels. In this regard, there are multiple reports in the literature. Matile[3-5] and Barboiu[6] have reported the design of such channels with multiple binding filters, however, all these channels were found to be cation selective (Figure 3.2).

Apart from the cation selective channels, the challenge to impose the single-file ion selectivity filter with multiple anion binding sites of synthetic anion selective channels has now been addressed to a good extent. Matile and coworkers reported the oligonaphthalene dimide[7] and oligoperylendiimide[8] based rigid-rod scaffolds (Figure 3.3) which lead to the formation of anion channels through anion-π interactions. However, the data of these channels were not available in planar bilayers. Our group reported the mannitol[9] and corresponding 1,3-phenylene tetrol[10] based chloride ion channels which transport the chloride ions across the lipid bilayer membrane via hydrogen bonding interactions of Cl^- ion with the hydroxyl groups in the channel lumen. The formation of the rosette ion channels was proved through theoretical studies, and proved by fluorescence and planar bilayer conductance measurements. The later was found to induce apoptosis in cancer cells. This was followed by another report from Zeng and coworkers[11] which showed that adequately substituted leucine derivatives form anion channels in the lipid bilayer membranes.

Considering the above reports, we thought of inducing the membrane filter in the form of amide linkages and hydroxyl groups within a single molecular scaffold, which can self-assemble in the lipid bilayer membrane to form the barrel rosette kind of ion channel which can induce the selectivity for both anions and cations simultaneously. In this work, we report a series of inherently fluorescent molecules that form self-assembled barrel-rosette ion channels to facilitate the symport of M^+ and Cl^- across liposomes and cell membranes. The design of the molecular scaffold contains a central core of 2-hydroxy-N^1,N^3-diarylisophthalamide connected to two

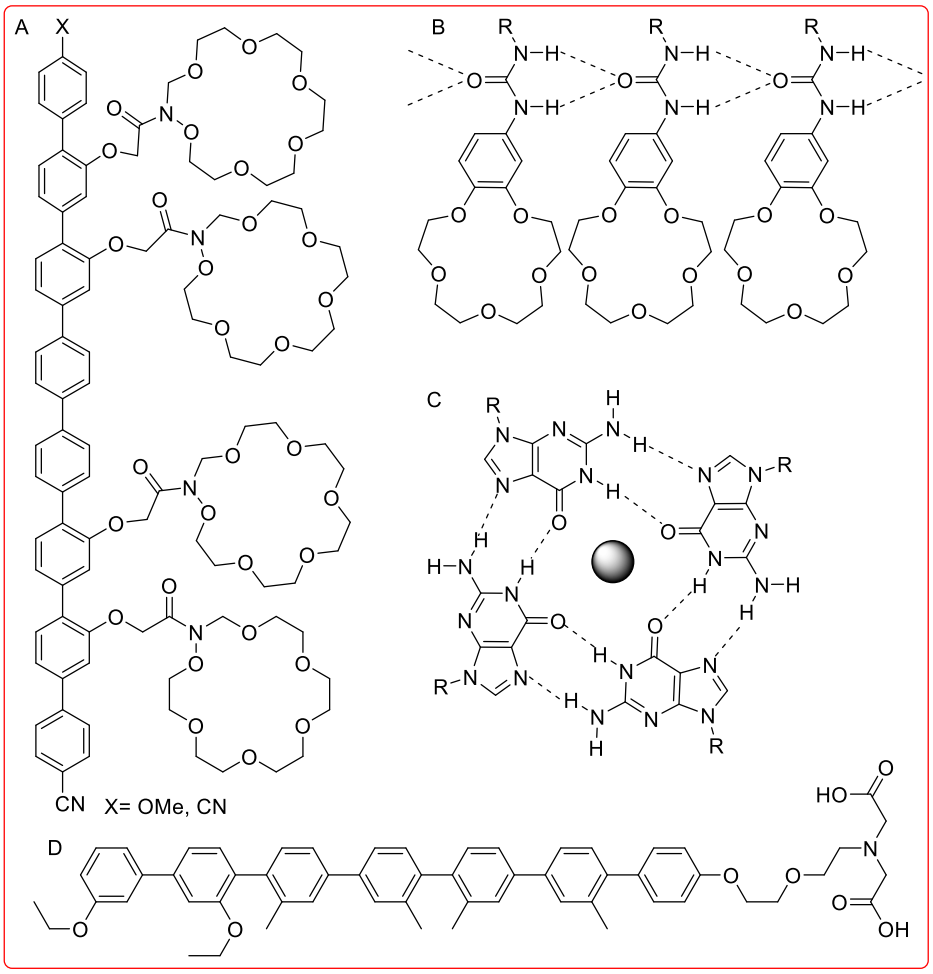

Figure 3.2. Structure of different cation channels with single-file ion selectivity filters.

identical aromatic side arms as phenyl, 4-methylphenyl, 4-trifluoromethylphenyl or 3,5-bis(trifluoromethyl) phenyl to get molecules **1a**−**1d** respectively (Fig. 3.4 A). We envisaged that the intramolecular C=O•••H–O, and C–O•••H–N interactions in the central core would provide a preorganized geometry of individual monomers, a conformation which may favor the desired ion selectivity. The π-π stacking interactions among aromatic rings and intermolecular hydrogen bonding interactions among amide moieties would lead to the efficient self-assembly of the individual monomers in the lipid bilayer membrane to form an active channel (Fig. 3.4 B). The theoretical calculations with the calculator plugins of the Marvin Sketch program,[12] indicated that the variation of terminal aromatic groups would change the pK_a of both amide protons (Figure 3.4 D). Estimated pK_a = 6.42 for the 2-hydroxyl group of each compound indicated that in the supramolecular channel, one or more hydroxyl groups may get deprotonated at physiological pH providing cation binding site. The cation recognition sites can also be provided by either C–F or C=O moiety via cation-dipole interactions in the lumen of the channel. The 2-hydroxyl group is anticipated to generate the inherent fluorescence of these molecules via the push-pull effect.

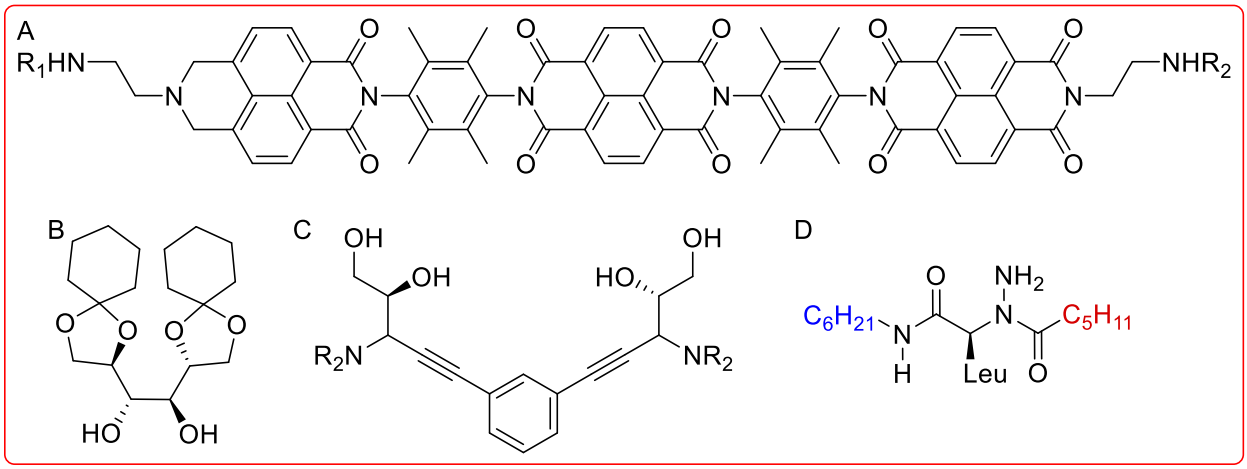

Figure 3.3. Structure of different anion channels with single-file ion selectivity filters.

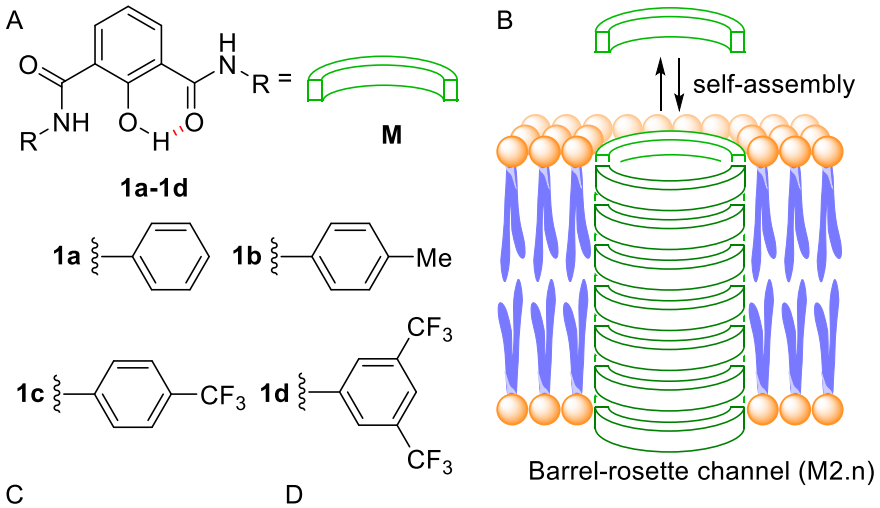

Compound	pK_a			log P
	proton a	proton b	proton c	
1a	12.77	12.00	6.42	3.85
1b	12.95	12.17	6.42	4.88
1c	12.41	11.63	6.42	5.61
1d	11.27	10.50	6.42	7.36

Figure 3.4. Structure of designed channel-forming compounds **1a**−**1d** (A); self-assembly of individual monomers **M** into rosette channel $\mathbf{M_{2.n}}$ in lipid bilayer membrane (B); labeling of different hydrogen atoms in the core structure (C), and the table displaying the effect of aromatic substitution on the p*K*a values and log P values (D).

3.2. RESULTS AND DISCUSSION:

3.2.1. Synthesis.

The synthesis of compounds **1a–1d** was started from the protected acid **4** by converting it to the acid chloride using oxalyl chloride,[13] which was then coupled with the respective

aromatic amine to get the corresponding amide **5a−5d** (Scheme 1). The product was treated with 1 M BBr_3 in dichloromethane for the O-methyl deprotection[14] to get the corresponding final compounds **1a−1d** with a free hydroxyl group. All the newly synthesized compounds were purified by column chromatography, and characterized by ^{1}H NMR, ^{13}C NMR, HRMS, IR, and melting point.

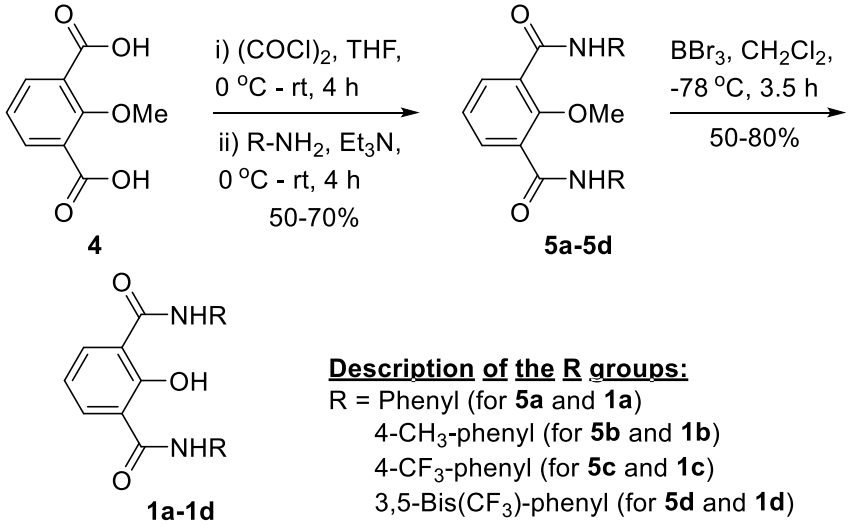

Scheme 3.1. Synthetic route for the synthesis of **1a–1d**.

3.2.2. Ion Transport Activity.

The ion transport activity of the compounds **1a−1d** was checked by fluorescence based assays across egg yolk phosphatidylcholine unilamellar vesicles (EYPC−LUVs).[15-18] At first, the large EYPC−LUVs were prepared by entrapping the pH-sensitive dye 8-hydroxypyrene-1,3,6-trisulfonate (HPTS, pK_a = 7.2), and 0.5 M NaOH was added in the extravesicular buffer to create a pH gradient (i.e., ΔpH = 0.8) across the membrane. The change in the rate of fluorescence intensity was monitored after the addition of **1a−1d**, in each experiment and finally, the Triton X-100 was added to lyse the vesicles for the complete leakage of the HPTS dye.[19] The comparison of the ion transport activities showed the sequence as **1a** < **1b** < **1c** << **1d**, inferring **1d** is forming the most efficient ion transport system (Figure 3.5). This ion transport activity sequence of **1a−1d** infers that the pK_a values of the amide protons as the major factor to control transport rate as compared to logP values.[20,21] The Hill analysis provided the EC_{50} value, i.e., the concentration required to reach half of the maximum activity, to be 0.48 μM (compound to lipid ratio = 0.58 mol%), and the Hill coefficient, *n* to be almost equal to 2 (Figure 3.5 C). From this data obtained after Hill analysis, it can be inferred that a noncovalent dimer of the compound is the active structure for the supramolecular nanochannel assembly.[22] The Hill analysis could not be performed with the dose-dependent activity data of **1a** due to its precipitation at higher concentrations.

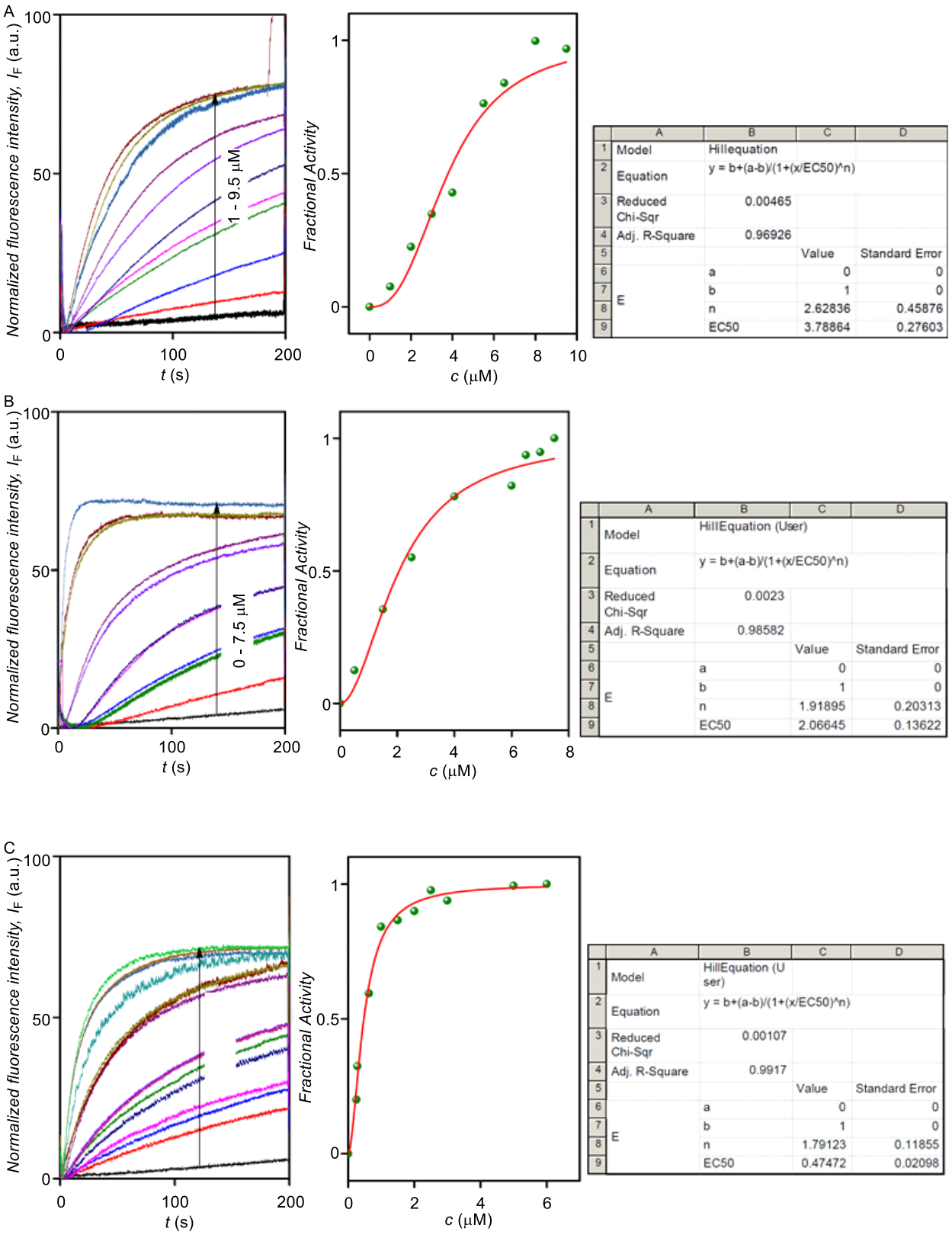

Figure 3.5. Dose-response ion transport curves and Hill analysis of compound **1b** (A), **1c** (B), and **1d** (C).

3.2.3. Ion Selectivity and Mechanism of Ion Transport.

The excellent ion transport activity of **1d** further encouraged us to evaluate the ion selectivity of this channel forming molecule. First, the cation selectivity of the channel was evaluated across EYPC-LUVs⊃HPTS by entrapping the vesicles NaCl and an isoosmolar extravesicular MCl (where, M^+ = Li^+, Na^+, K^+, Rb^+, and Cs^+) was used as external buffer.[23-25] The results of this assay provided the cation selectivity sequence as $K^+ \approx Rb^+ > Cs^+ > Na^+ > Li^+$ (Fig. 3.6 A). After getting the cation selectivity of the channel, we next evaluated anion selectivity of the channel by varying the intravesicular as well as extravesicular anions of NaX salts (X^- = Cl^-, Br^-, I^-, NO_3^-, and ClO_4^-), and the rate of ion transport was monitored by applying a pH gradient of 0.8 (pH_{in} = 7.0 and pH_{out} = 7.8).[11,23,26] Interestingly, the results confirmed a considerable selectivity of the channel towards Cl^- compared to the other anions (Figure 3.6 B). These selectivity studies suggested that the channel formed by **1d** transports both cations and anions across the lipid bilayer membrane.

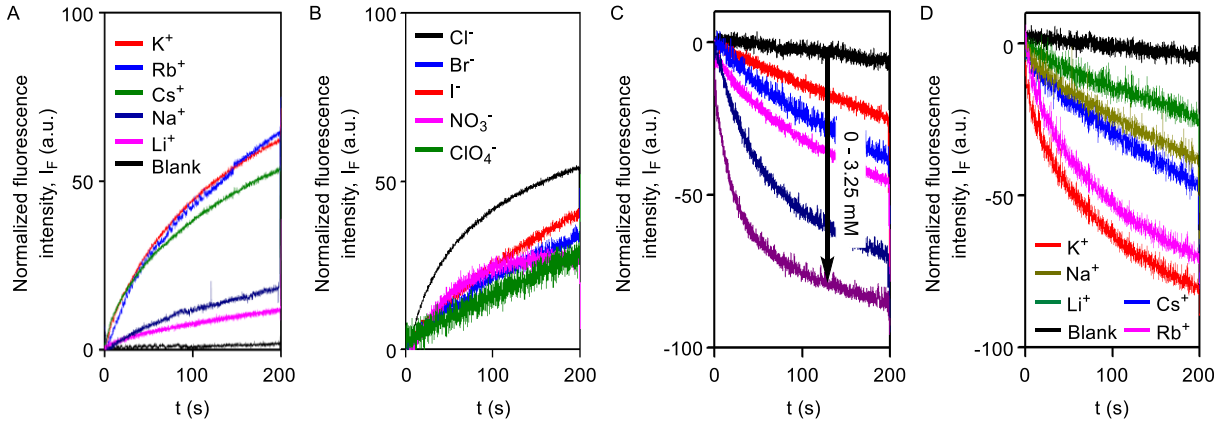

Figure 3.6. Cation selectivity of **1d** (0.1 μM) across EYPC-LUVs⊃HPTS (A); anion selectivity of **1d** (0.5 μM) across EYPC-LUVs⊃HPTS (B); Cl^- ion influx across EYPC-LUVs⊃lucigenin upon addition of **1d** (0 - 3.25 μM) (C); cation dependent Cl^- ion influx across EYPC-LUVs⊃lucigenin upon addition of **1d** (1.5 μM) (D).

After getting the idea of ion selectivity of the channel, the Cl^- ion selectivity of **1d** was again assessed by transport activity across EYPC-LUVs⊃lucigenin, which were prepared by entrapping the lucigenin dye and $NaNO_3$ salt. The transport rate of **1d** was investigated in detail by monitoring the fluorescence intensity of intravesicular lucigenin dye at λ_{em} = 535 nm (λ_{ex} = 450 nm)[27,28] by applying a Cl^-/NO_3^- gradient in the extravesicular buffer. The results showed a concentration-dependent quenching of lucigenin fluorescence upon addition of channel forming compound **1d** (Figure 3.6 C). This data shows that the supramolecular channel formed by the compound can allow the influx of Cl^- across liposomes.

The ion selectivity sequence of **1d** suggests that the channel conducts M^+/Cl^- cotransport across the lipid bilayer membrane. To prove this cotransport process, the cation selectivity was checked

in the lucigenin assay. When the extravesicular cations were varied in the above mentioned lucigenin assay, the results corroborated with cation selectivity as obtained by HPTS assay (Figure 3.6 D). This data supports that the channel is M^+/Cl^- symport process is operating through the channel. To confirm this symport mechanism of ion transport, the valinomycin coupled assay was used.[29] The KCl solution was added to the extravesicular buffer to create the Cl^-/NO_3^- gradient across the vesicles. Then, the valinomycin was added along with compound **1d** and the transport rate was checked. There was no enhancement of the ion transport rate, which suggests that there is no cooperative transport of valinomycin and **1d** (Figure 3.7 A), thereby, confirming that the symport mechanism is operating. To further confirm our results, the EYPC liposomes were prepared by entrapping NaCl (200 mM) and 1.0 mM of lucigenin dye. Then, isoosmolar Na_2SO_4 was added to the extravesicular solution and Cl^- efflux was monitored by monitoring the fluorescence intensity of the lucigenin dye. A similar experiment was also performed with extravesicular isoosmolar $NaNO_3$. The results indicate that there is no difference in the transport rate of two ions by **1d** (Figure 3.7 B), suggesting that the symport mechanism of ion transport is operative.[30]

Next, we investigated whether the membrane integrity is intact after the addition of **1d** or there is a formation of supramolecular pores in the membrane, the carboxyfluorescein (CF) leakage was monitored across EYPC-LUVs⊃CF.[31] The CF molecules at high concentration inside the liposomes lead to the fluorescence quenching of the dye due to collisions among the molecules. However, leakage of these molecules from the liposomes into the external buffer restores their fluorescence (λ_{em} = 517 nm, λ_{ex} = 492 nm). When compound **1d** was added to the liposomes, there was no significant enhancement in fluorescence intensity of CF (Fig. 3.7 C), suggesting that neither the membrane is getting damaged, nor the larger pores are being formed by **1d**.

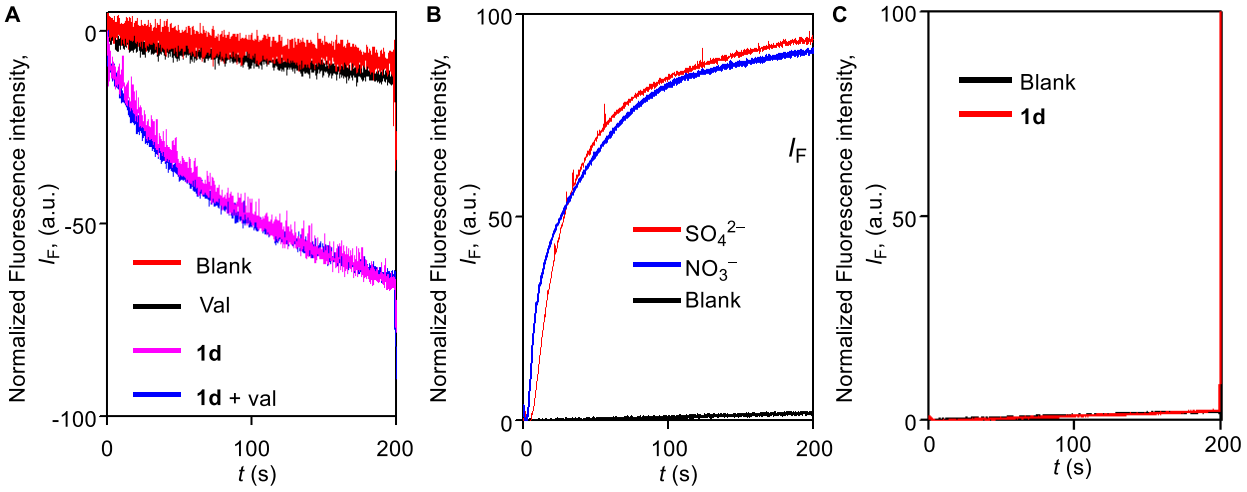

Figure 3.7. Comparison of transport activity of **1d** (1.5 μM) in the presence and absence of valinomycin (0.125 μM) (A); Cl^- efflux across EYPC-LUVs⊃lucigenin by **1d** (2.5 μM) in the presence of SO_4^{2-} and NO_3^- as extravesicular anions (B) and carboxyfluorescein efflux assay for compound **1d** (10 μM).

3.2.4. Planar Bilayer Conductance Studies.

To confirm the channel formation by compound **1d** in the lipid membrane, the ionic conductance across the planar lipid bilayer membrane was measured.[32] The two compartments (*cis* and *trans* chambers) containing KCl solution (1.0 M) were separated by a planar lipid bilayer membrane made from diphytanoyl phosphatidylcholine (diPhyPC) lipid.[33,34] The addition of **1d** (2.0 μM) to the system led to the distinct channel openings and closing at different holding potentials, confirming the formation of ion channels (Fig. 3.8 A, B). The single-channel conductance was found to be 100 ± 2 pS, and the channel diameter = 5.06 ± 0.16 Å was calculated by Hill equation (Equation 1)

$$1/g = (l + \pi d/4) \times (4\rho/ \pi d^2) \qquad \text{(Equation 1)}$$

where, g = corrected conductance (obtained by multiplying measured conductance with the Sansom's correction factor), l = thickness of the membrane (34 Å), and ρ = resistivity of the recording solution (ρ = 9.44 Ω•cm).

The current versus voltage *(I-V)* plot in the presence of the symmetric solution of KCl (1.0 M each) showed ohmic behavior, which confirms the non-dipole nature of the channel. The ion selectivity of the channel was checked using unsymmetric solutions of KCl in two chambers (i.e., 1.0 M in *cis* and 0.5 M KCl in *trans*), which showed that the rate of Cl^- transport is considerably higher than the rate of K^+ transport with a permeability ratio P_{Cl^-}/P_{K^+} = 8.29 ± 1 (Fig. 3.8 C). This data suggests that the electrogenic transport of Cl^- gives the current signals during the recordings.

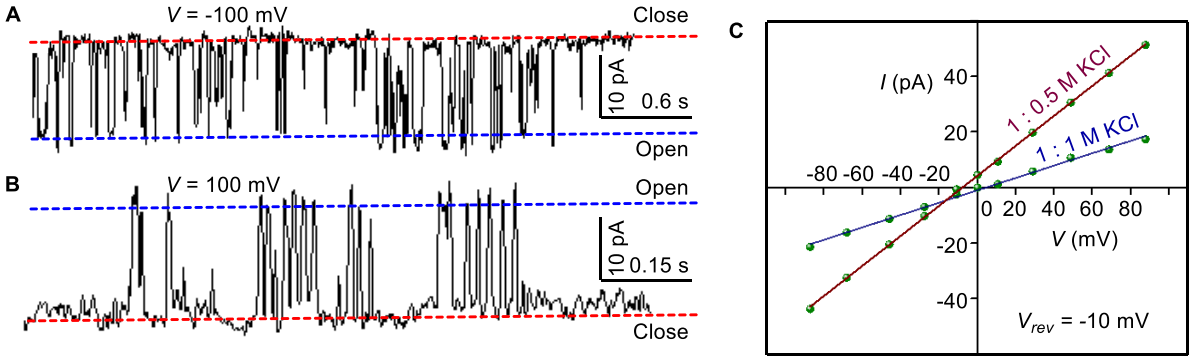

Figure 3.8. Single-channel conductance of **1d** (2.0 μM) recorded at -100 mV (A) and at 100 mV (B) under symmetrical KCl solutions. *I-V* plots of **1d** under symmetrical and unsymmetrical concentrations of KCl (C).

3.2.5. Molecular Modeling of the Channel.

To gain more insights about the channel structure and the corresponding selectivity filter, the theoretical model of the channel was proposed. The crystal structure of **compound 1c** (Figure 3.9 A, B) provided the evidence that the 2-hydroxy-N^1,N^3-diarylisophthalamide molecules exist predominantly in an intramolecularly C=O•••H–O and C–O•••H–N hydrogen bonded preorganized geometry. The conformational study of the molecule **1d** using Conflex 8 program[35,36] supported this fact where a similar conformation set **Conf-1** is favored according to the determined Boltzmann populations (Figure 3.10). At first, eleven molecules of **1d** in the **Conf-1a** were placed on top of another to form one side of the channel. Subsequently, the other side of the channel was constructed in the same way and the two halves of the channel were arranged face-to-face to form the barrel-rosette channel. The constructed channel was further optimized using MOPAC2012[37] software with the PM6-DH+[38] method to get the final channel (Figure 3.11 A). This optimized channel was then placed in the POPC lipid bilayer membrane, and molecular dynamics (MD) simulations were carried out (see methods). The equilibrated channel is shown in Figure 3.11 B . Figure 3.11 C shows the densities of various constituents of the channel indicating the proper formation of the channel. The top view of the channel with pore diameter is shown in Figure 3.11 D. Figure 3.11 E shows that the variation in pore diameter is minimal around an average of 5.3 Å during the simulation, in excellent agreement with the experiment. In the simulated channel, upon inspection at various time frames (Figure 3.11 F-I) multiple noncovalent interactions were found to stabilize the channel structure and recognition of the ions. The stacking interactions among aromatic rings (among successive central phenyl rings, and among successive aromatic arms), as well as the hydrophobic interactions among CF_3 groups were found to be present. Moreover, intermolecular C=O···H–$O_{(phenolic)}$ and C–O···H–N interactions were also evident in the channel. The water molecules inside the channel formed a continuous array with multiple intermolecular H–O···H–O interactions with neighboring water molecules. The water molecules were also involved in hydrogen bonding with C–F and C=O groups of the channel forming molecules. The K^+ ion was involved in cation-dipole interactions with neighboring F-centres of the channel forming molecules and with O-centres of neighboring water molecules (Table 2). The Cl^- ion was involved in C–O–H···Cl^- interactions with the channel forming molecules and O–H···Cl^- interactions with neighboring water molecules (Table 3). Interestingly, the permeation of K^+ and Cl^- in the channel took place with an interionic distance within 5 Å, confirming the presence of electrostatic interaction (Figure 3.11 J, K). However, in the bulk water, the ions got separated due to hydration.

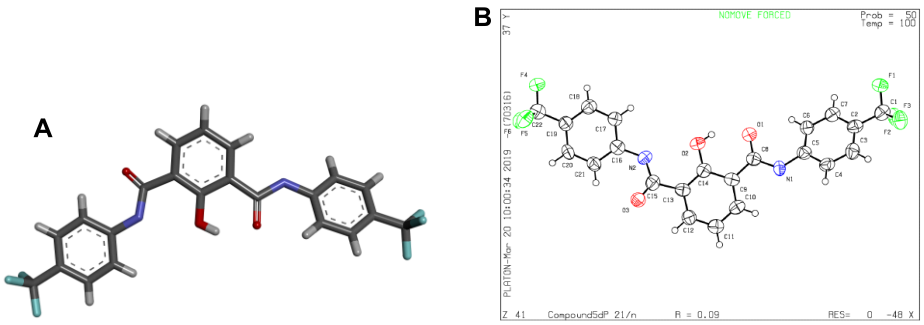

Figure 3.9. Single crystal X-ray structure of **1c** (A), and ORTEP diagram of **1c** (B)

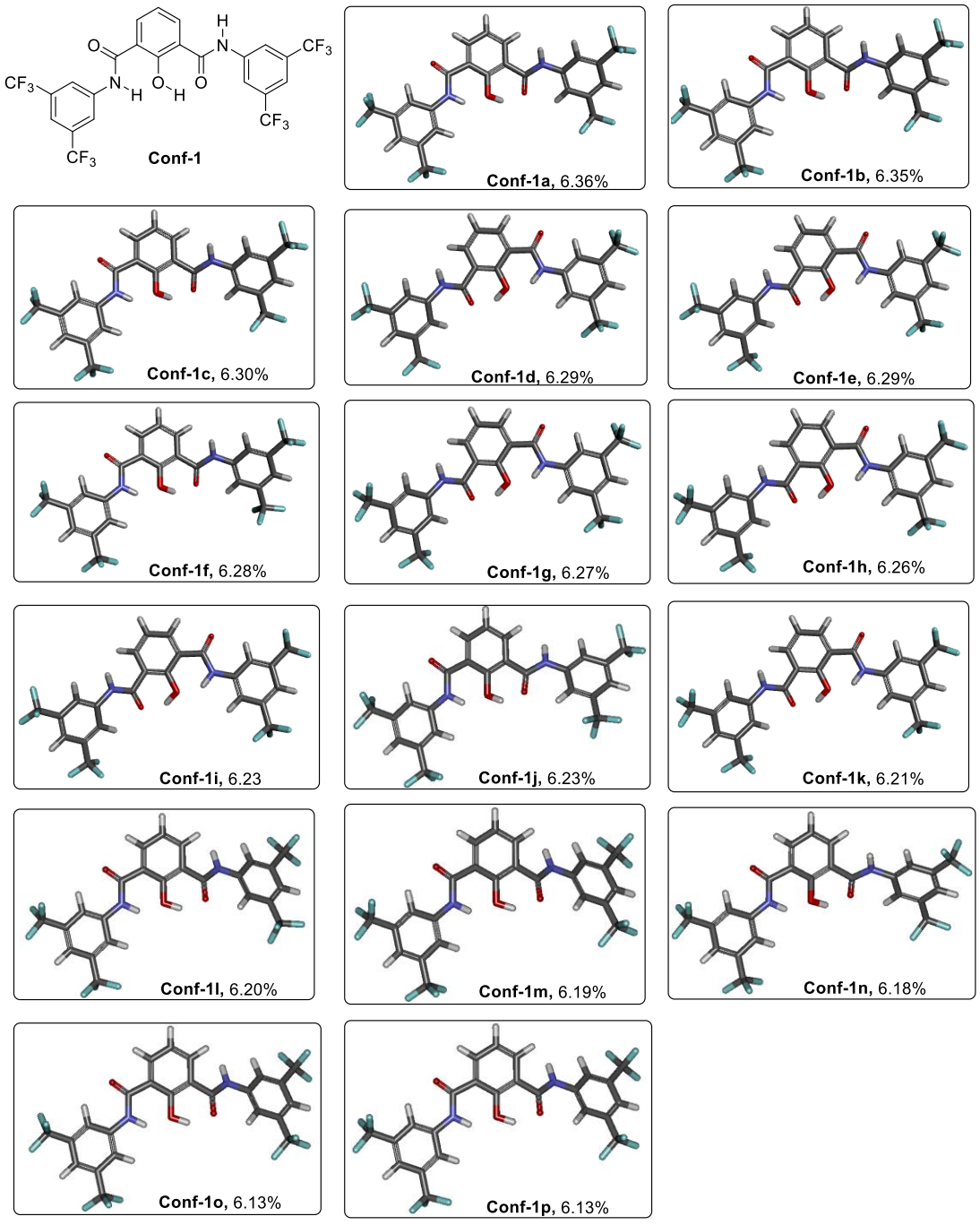

Figure 3.10. Geometry optimized structures of the most probable conformations of **1d** along with the Boltzmann distribution of populations for the formation of Channel **A** (**Conf-1a - Conf-1p**)

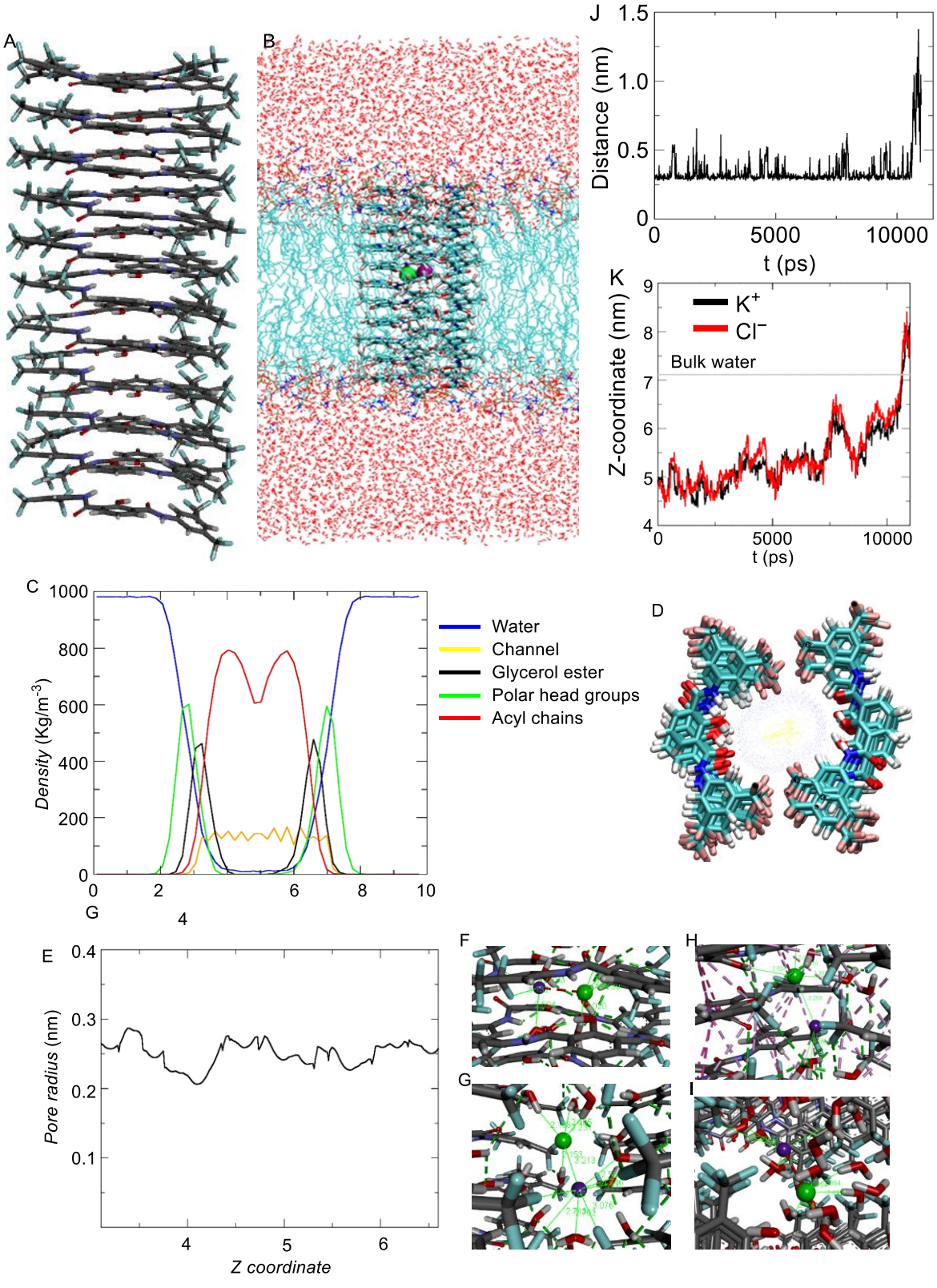
A
B
J
Distance (nm)
t (ps)
K
Z-coordinate (nm)
K+
Cl−
Bulk water
t (ps)
C
Density (Kg/m-3)
Water
Channel
Glycerol ester
Polar head groups
Acyl chains
D
E
Pore radius (nm)
Z coordinate
F
G
H
I

Figure 3.11.; (Side view of the geometry optimized channel formed by **1d** in **Conf-1a** (A); equilibrated channel−POPC/water system (B); mass density profile of the channel in POPC membrane (C), top view of the pore (D), and variation of pore radius during the simulation (E);; zoomed view of snapshots of the frames taken at start (F), at 3ns (G), at 7.5 ns (H), at 10 ns (I); variation of distance between K^+ and Cl^- ions during production run (J) ;positions of ions inside the channel during the simulation (K).

Table 2. Average interaction energy between potassium ion and polar atoms of the channel residues.

Atom/s	Total energy (kJ/mol)
Fluorine atoms (red)	-72.5
Amide nitrogen (green)	-5.9
Hydroxyl oxygen (blue)	-9.4
Carbonyl oxygen (black)	-22.0

Table 3. Average interaction energy between the chloride ion and polar atoms in the channel residues.

Atom/s	Total energy (kJ/mol)
Phenyl hydrogen	-34.9
Hydroxyl hydrogen	-45.5
Amide hydrogen	-19.9

3.2.6. UV-Visible Absorption and Fluorescence Emission Studies.

Since the compound **1d** is inherently fluorescent, so we recorded the absorption spectrum using SHIMADZU, UV-2600, UV-vis spectrophotometer. The absorption spectrum was recorded in commercially available 1X phosphate saline buffer (DPBS) buffer from Lonza. The compound **1d** gives absorption band at 335 nm (Figure 3.12 A). The steady State fluorescence experiments were carried out in a micro fluorescence cuvette (Hellma, path length 1.0 cm) on a Fluoromax 4 instrument (Horiba Jobin Yvon) in Dulbecco's Phosphate-Buffered Saline (DPBS) as well as in lipid phase, which showed am emission peak at 460 nm (Figure 3.12 B).

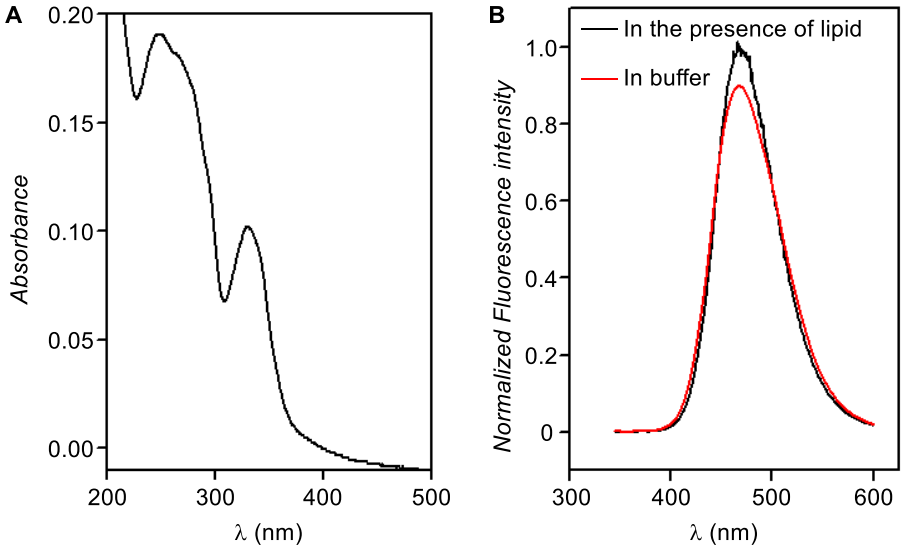

Figure 3.12. UV-Visible absorbance of **1d** (20 μM) in buffer (A), and normalized fluorescence emission spectra of **1d** (20 μM) in buffer and in the presence of lipid (B).

3.2.7. Biological Studies.

To study the biological impact of ion transport by **1d**, we first carried out the live cell imaging studies to investigate whether the molecules of the compound stay only in the membrane or can permeate inside the cell as well. The live cell imaging of **1d** was carried out in the human epithelial breast cancer cell line, MCF7, and the results suggested that the compound does not remain confined to cell membrane only, but also permeate into the cytosolic part as well. (Figure 3.13 A, B, C).[39] Afterwards, the time of insertion of the compound **1d** in the cells was studied using real-time analysis. The results indicated that the compound **1d** gets inserted into the cytosolic part of the cells within a few seconds of incubation. Interestingly, the real-time analysis also showed a change in the cell morphology within a few minutes and a decrease in the cell volume was observed. This type of morphological change is indicative of the apoptotic volume decrease (AVD), which is a well-known initial event of apoptosis.[40,41]

The results encouraged us to go further to study the cell viability in the presence of compounds **1a**−**1d**. A single-point screening of the cell viability upon incubation **1a**−**1d** in MCF7 cells for 24 hours was evaluated by MTT assay[10] showed that the compound **1d** displayed maximum cell killing activity (Figure 3.13 D). Next, the dose-dependent effect of compound **1d** on MCF7 cells was studied which showed a concentration dependent decrease in the cell viability, providing the IC_{50} value of approximately 7.50 μM (Figure 3.13 E). Next, the effect of ion transport on the cell viability was studied. The effect of chloride ions in mediating the cell death was studied by comparing the cell viability both in the presence and absence of chloride ions in the culture medium. The chloride mediated apoptosis is well studied in the literature.[10,19,42] So, two different types of HBSS (Hanks balanced salt solution) were prepared, with and without Cl^- ions to be

used as the culture media. The MCF7 cells were cultured in both the media separately and incubated with compound **1d** at different concentrations around IC_{50} value. As expected, the compound showed more cell death with chloride ions present in the extracellular buffer compared to that without chloride ions (Figure 3.13 F). This experiment clearly demonstrates that the chloride-mediated cell death is taking place. As the compound is M^+/Cl^- symporter, so we decided to evaluate the effect of K^+ ions as well as Na^+ ion in the cell death. Since the concentration of Na^+ ions is very high outside the cell compared to K^+ ions, we expected a better involvement of Na^+ ions, if the symport process is taking place. So to evaluate the effect of cations, we again prepared HBSS buffer without both K^+ and Na+ ions and used as the culture media. The compound **1d** showed higher cell viability without the presence of K^+ and Na^+ ions in the culture media in comparison to that when studied in the presence of normal HBSS buffer (containing Na^+, K^+, and Cl^- ions) (Figure 3.13 G). These results confirm that the cell death is mediated by M^+/Cl^- symport across the cell membrane.

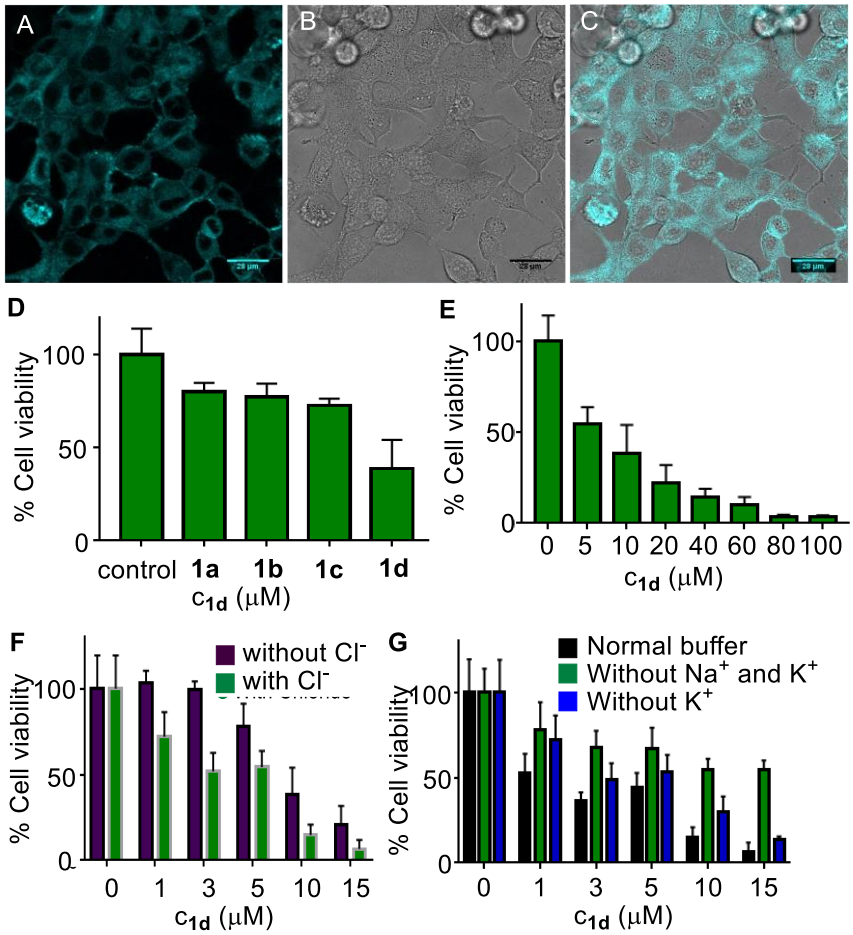

Figure 3.13. Live cell imaging of **1d** at 10 μM in MCF7 cell line Fluorescence (A), DIC image (B) and overlay image (C). Cyan color was given for better contrast. Scale bar = 80 μm. Cell viability obtained from single-point screening of compounds **1a–1d** (10 μM each) by MTT assay after 24 h incubation (D); dose-dependent cell viability in the presence of **1d** (E); cell viability of MCF7 cells in the presence and absence

of Cl^- ions incubated with **1d** at different concentrations (F); and in the presence and absence of Na^+ and K^+ ions (G).

The above results indicated that the compound **1d** is inducing the ion mediated cell death in MCF7 cells. Next we evaluated the path of cell death, *i.e.*, whether cell death is being mediated by necrosis or apoptosis. To evaluate the apoptosis mechanism, the events involved in the apoptotic pathway were evaluated in detail. Apoptosis is also evidenced by the disruption of mitochondrial membrane potential (MMP),[43,44] which subsequently results in cytochrome c release. The release of cytochrome c in the cytoplasm switches on the apoptotic signalling cascade.[45-47] Firstly, we monitored the change in mitochondrial membrane potential (MMP) by using the MMP sensitive JC-1 dye. This dye exhibits red fluorescence emission due to the formation of J-aggregates in the healthy mitochondrial membrane. However, in the damaged mitochondria the depolarization of the mitochondrial membrane leads to dispersion of the dye in the cytosol, resulting in green fluorescence emission. The MCF7 cells were incubated with compound **1d** (10 μM), followed by the treatment with JC-1 dye by the reported protocol. The cells were analysed under a confocal microscope (leica sp8) to monitor the changes in the red and green fluorescence in the treated cells. The study showed a significant decrease in the red fluorescence and a concomitant increase in the green emission (Figure3.14 A, B).[46,48] The quantification of the pixel intensity ratio (green/red = 2.57)[10] in treated cells compared to the control (green/red = 0.263) confirmed the enhancement in the depolarization of MMP due to the change in ionic homeostasis of cells.

This change in MMP of cells leads is known to cause the disturbance in the electron transport chain in the mitochondrial respiratory cycles, which ultimately results in generation of reactive oxygen species (ROS).[49,50] Thus, 2',7'-dichlorodihydrofluorescein diacetate (H_2DCFDA),[44,51] was used as an ROS probe to monitor ROS generation in cells. This probe is non-fluorescent in nature when protected as diacetate. However, upon cellular internalization, the hydrolysis of the ester groups by the cellular esterases followed by the ROS-mediated oxidation generates a green fluorescent 2',7'-dichlorofluorescein (DCF), whose fluorescence can be used to monitor the ROS generation in cells. The MCF7 cells were treated with **1d** and then stained with H_2DCFDA, in a time dependent manner followed by the analysis of cells under a fluorescence microscope. A significant enhancement in the green fluorescence was observed, which clearly demonstrates the generation of ROS as a result of ion transport by **1d** (Figure 3.14 C-F).

It is well known that the elevated ROS levels in the cells cause the stress and open up the mitochondrial permeability transition pores (PTP),[52,53] which are formed by naturally occurring voltage gated ion channels present in the mitochondrial membrane. This opening of the PTP results in the disruption of the mitochondrial outer membrane which in turn leads to the release of cytochrome c from the mitochondrial membrane into cytosol.[54,55] Therefore, to monitor the release of cytochrome c into the cytosol, we used the technique of immunostaining using the specific antibody. The MCF7 cells were treated with compound **1d** and then, processed for immunofluorescence to monitor the release of cytochrome c. The results showed a significant

enhancement in the fluorescence intensity of the dispersed signal over cytosol (Figure 3.14 G, H) indicates the release of cytochrome c.

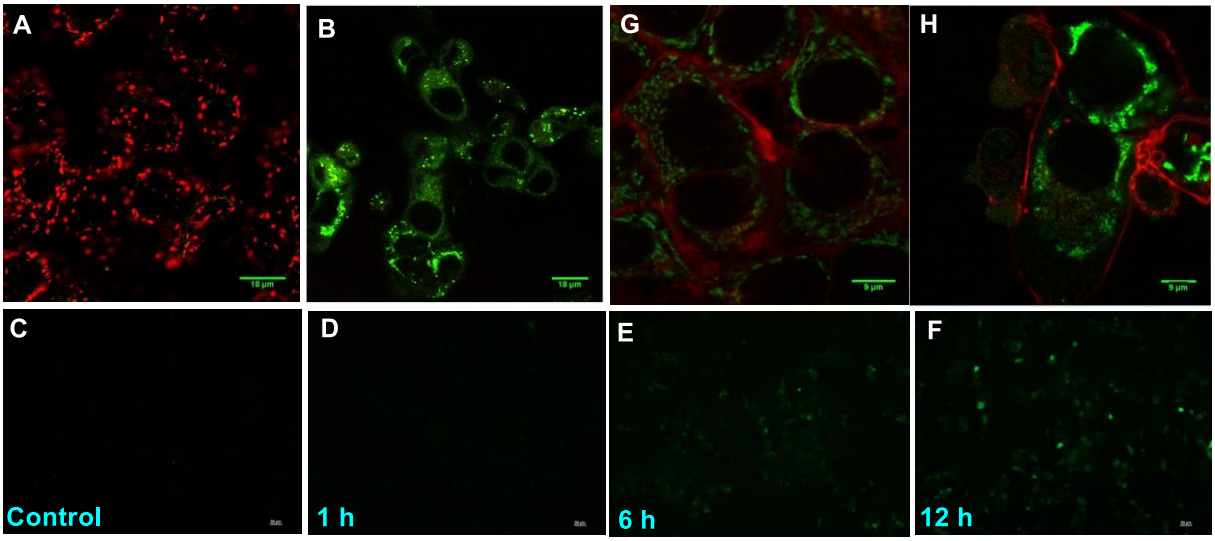

Figure 3.14. Live cell imaging of MCF7 cells upon treatment with 0 μM (A) and 10 μM (B) of **1d** for 24 h followed by staining with JC-1 dye. Red and green channel images were merged to generate the displayed image. MCF7 cells treated first with 0 μM (C) and 10 μM (D) of **1d** for 8 h and then fixed and analyzed for cytochrome c release by immunostaing with cytochrome c specific primary antibody (green). Phalloidin (red) co-staining was used to mark the boundaries. Live cell images of MCF-7 cells incubated with compound **1d**, and H_2DCFDA as ROS probe (scale bar = 50 μm) in a time dependent manner (E - F).

In the intrinsic apoptotic pathway which gets initiated from the mitochondria, the released cytochrome c binds to the Apaf-1 to form an apoptosome. Then, this cytochrome c/Apaf-1 complex activates caspase 9 pathway, which then activates the other downstream signaling pathways to switch the cells to apoptosis.[45,56-58] Therefore, we analyzed the activation of caspase 9 pathway using the immunoblot analysis of cleaved caspase 9 levels in MCF7 cells upon treatment with compound **1d**. The incubation of the cells with **1d** led to a significant increase in the expression of cleaved caspase 9 (Figure 3.15 A). The increase in the levels of caspase 9 was quantified with respect to the GAPDH as the loading control. Thus, the expression of cleaved caspase 9 confirms the activation of the intrinsic pathway of apoptosis. To get further support for the activation of apoptotic pathway, the expression of cleaved poly(ADP-ribose) polymerase (PARP) was checked. The PARP cleavage by endogenous caspases is a very well-known phenomenon[59,60] which prevents the DNA repair and facilitates the apoptosis. The significant amount of degradation of full-length PARP-1 (116 kDa) with a concomitant increase of cleaved PARP-1 (86 kDa) was observed upon immunoblot analysis of MCF7 cells incubated with 10 μM concentrations of **1d** (Figure 3.15 B), supporting the caspase 9 pathway of apoptosis.

As a final validation for the overall process, the propidium iodide (PI) assay was used. The PI dye binds to the nuclear constituents of the cell, typically DNA and RNA, of the damaged cells,

however, it is impermeable to the healthy cells.[61] So the MCF7 cells were treated with **1d** for 24 h and then stained with PI. The live cell imaging of the treated cells clearly showed that the PI uptake is very prominent compared control cells (Figure 3.15 C, D). So this data finally validates that the cells have been damaged by treatment with **1d**.

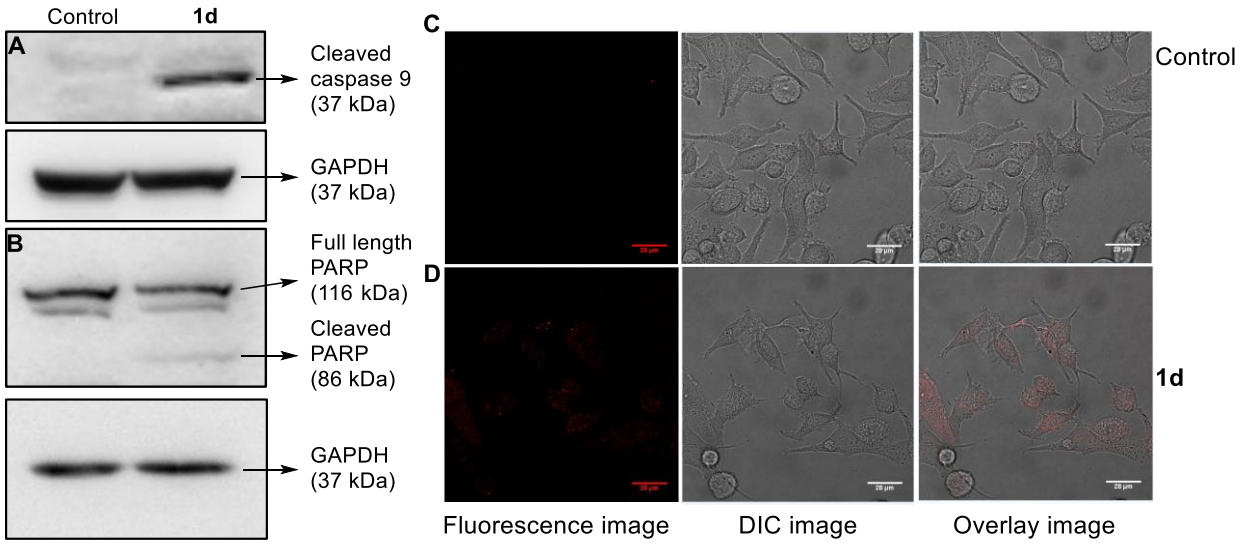

Figure 3.15. Immunoblot assay for active caspase 9 (A) in MCF7 cells and PARP cleavage (B) after 24 h incubation with 0 μM and 10 μM of **1d**. Live cell images of MCF-7 cells incubated with compound 0 μM (C) and 10 μM of 1d (D), and propidium iodide (PI; red) probe.

3.3. CONCLUSION:

In summary, we have introduced the concept of inducing the selective membrane filter for M^+/Cl^- transport across the lipid bilayer membrane, through the inherently fluorescent 2-hydroxy-N^1,N^3- diarylisophthalamides which form efficient ion channels in the lipid bilayer membranes. The variation of the aromatic side arms indicated that the compound with two 3,5-bis(trifluoromethyl)phenyl arms (**1d**) was the most active among the entire series when ion transport activity was measured across large unilamellar vesicles. The study also confirmed the M^+/Cl^- symport as the operating mechanism of ion transport by fluorescence assays. The channel formation was also validated by planar bilayer conductance measurements studies, which gave ion conductance of 100 ± 2 pS. The permeability ratio, P_{Cl^-}/P_{K^+} = 8.29 ± 1, indicates higher selectivity for Cl^- compared to K^+. The inherent fluorescence of the compound **1d** was used for the live cell imaging in MCF7 cells, which indicated the presence of the compound in the cell membrane as well as in the cytosolic content of the cell. The channel facilitates the transport of chloride, potassium, and sodium across the cellular membrane, and the process resulted in the perturbation of the ionic homeostasis of cells leading to significant cell death. The apoptotic pathway of cell death was confirmed by the mitochondrial membrane depolarization and reactive oxygen species generation. These processes resulted in the cytochrome c release, which activated the activation of caspase 9 pathway, PARP cleavage. The staining of nuclear contents by

propidium iodide in the treated cells confirmed that the membrane integrity has been compromised in treated cells compared to control. These results will help to in future to envision new developments in field of synthetic ion transport systems for their therapeutic applications.

3.4. EXPERIMENTAL SECTION:

3.4.1. General Methods.

All reactions were carried out under the nitrogen atmosphere. All the chemicals were purchased from commercial sources and were used as received unless stated otherwise. Solvents were dried by standard methods prior to use or purchased as dry. Thin layer chromatography (TLC) was carried out with E. Merck silica gel 60-F_{254} plates and column chromatography was performed over silica gel (100-200 mesh) obtained from commercial suppliers. Egg yolk phosphatidylcholine (EYPC) lipid was purchased from Avanti Polar Lipids as a solution dissolved in chloroform (25 mg/mL). HEPES buffer, HPTS dye, Carboxyfluorescein (CF) system, Triton X-100, NaOH and all inorganic salts of molecular biology grade were purchased from Sigma. Size exclusion chromatography was performed on a column of SephadexG-50. Large unilamellar vesicles (LUV) were prepared from EYPC lipid by using mini extruder, equipped with a polycarbonate membrane either of 100 nm or 200 nm pore size, obtained from Avanti Polar Lipids. The JC1 dye was the generous gift from Dr. Shilpy Sharma at Savitribai Phule Pune University. The H_2DCFDA was purchased from Sigma Aldrich.

3.4.2. Physical measurements.

The ^{1}H and ^{13}C NMR spectra were recorded on 400 MHz Jeol ECS-400 (or 100 MHz for ^{13}C) spectrometers using either residual solvent signals as an internal reference or from internal tetramethylsilane on the δ scale relative to chloroform (δ 7.26), dimethylsulphoxide (δ 2.50 ppm), acetone (δ 2.05) for ^{1}H NMR and chloroform (δ 77.20 ppm), dimethylsulphoxide (δ 39.50 ppm), acetone (δ 29.84 and 206.26) for ^{13}C NMR. The chemical shifts (δ) are reported in ppm and coupling constants (J) in Hz. The following abbreviations are used: s (singlet), d (doublet) m (multiplet), and td (triplet of doublet) while describing ^{1}H NMR signals. High-resolution mass spectra (HRMS) were obtained from MicroMass ESI-TOF MS spectrometer. All the FT-IR spectra were taken and reported in wave numbers (cm^{-1}) using a solution of compound in 30% MeOH/$CHCl_3$. Fluorescence spectra were recorded by using Fluoromax-4 from Jobin Yvon Edison equipped with an injector port and a magnetic stirrer. 10 mM HEPES (with 100 mM NaCl or other salts as per necessity) buffer solutions were used for fluorescence experiment and the pH of the buffers were adjusted to 7.0 or 8.0 by NaOH and pH of the buffer solutions was measured using Helmer pH meter. Melting points of all the compounds were measured using a VEEGO Melting point apparatus. All melting points were measured in open glass capillary and values are uncorrected. All fluorescence data were processed either by Origin 8.5 or KaleidaGraph and finally, all data were processed through ChemDraw Professional 15. The conductance measurements were carried out in planar bilayer membrane (BLM) workstation

obtained from the Warner Instruments consisting of a head stage and its corresponding amplifier BC-535, 8 pole Bessel filter LPF-8, Axon CNS Digidata 1440A and pClamp 10 software.The conductance data was analyzed by clampfit 10 software. MTT assay was recorded in a microplate reader (Varioskan Flash). Western blot was visualized in ImageQuant LAS 4000 (GE Healthcare). Cell images were taken using Leica sp8 confocal microscope and Nikon Eclipse TS 100 fluorescence microscope. The cell images were processed by image j software. The Grapgpad Prism 7 was used for plotting the data from biological assays.

3.4.3. Synthesis.

Synthesis of compound 4: Synthesis of compound **4** was also done according to the known protocol.[62]

General method for synthesis of 1a–1d.

The compound **4** was converted to corresponding acid chloride by using oxalyl chloride at 0 ^{o}C for four hours. Then, the respective amine was added at 0 ^{o}C and the reaction mixture was allowed to come to room temperature and stirred for four hours to get **5a-5d**. The compound so formed was directly treated with boron tribromide in CH_2Cl_2 (1 M BBr_3 in CH_2Cl_2) at -78 ^{o}C. The reaction mixture was allowed to come to room temperature and stirred for three hours. Then, the reaction mixture was washed with sodium bicarbonate and organic layer was collected in dichloromethane and dried using sodium sulfate and solvent was removed *in vacuo*. The purification was done using silica gel chromatography to get the desired compounds **1a-1d** with 50% to 80% yields.

Compound 1a: Pale yellow solid (75% yield); **M.p.:** 183.0–185.0 ^{o}C; **IR** (ν/cm^{-1}) 3322, 3062, 2929, 2832, 1652, 1594, 1535, 1485, 1337, 1151, 748; **^{1}H NMR (400 MHz, $CDCl_3$)** δ 14.35 (s, 1H), 9.30 (t, 2H), 8.14 (d, *J* = 7.8 Hz, 2H), 7.69 (d, *J* = 8.7 Hz, 4H), 7.42 (t, *J* = 7.9 Hz, 4H), 7.22 (t, *J* = 7.9 Hz, 2H), 7.08 (t, *J* = 7.8 Hz, 1H); **^{13}C NMR (100 MHz, $CDCl_3$):** δ 165.92, 160.30, 137.19, 133.58, 129.11, 125.19, 121.33, 119.05, 118.48; **HRMS (ESI):** Calc. for $C_{20}H_{16}N_2O_3$ $[M+H]^+$: 333.1239; Found: 333.1278.

Compound 1b: White solid (65% yield); **M.p.:** 204.0–206.0 ^{o}C; **IR** (ν/cm^{-1}) 3342, 2951, 2839, 1651, 1605, 1437, 1352, 1112, 1017, 751; **^{1}H NMR (400 MHz, $CDCl_3$):** δ 9.20 (s, 2H), 8.08 (d, *J* = 7.8 Hz, 2H), 7.52 (d, *J* = 8.4 Hz, 4H), 7.18 (dd, *J* = 8.0 Hz, 4H), 7.02 (t, *J* = 7.9 Hz, 1H), 2.34 (s, 6H); **^{13}C NMR (100 MHz, $CDCl_3$):** δ 165.60, 160.28, 134.90, 134.58, 133.31, 129.64, 121.14, 119.07, 20.97; **HRMS (ESI):** Calc. for $C_{22}H_{20}N_2O_3$ $[M+H]^+$: 361.1552; Found: 361.1578.

Compound 1c: White solid (58% yield); **M.p.:** 213.0–215.0 ^{o}C; **IR** (ν/cm^{-1}) 3310, 2947, 2835, 1657, 1547, 1414, 1326, 1101, 1018, 753; **^{1}H NMR (400 MHz, DMSO):** δ 10.95 (s, 2H), 8.11 (d, J = 7.8 Hz, 2H), 7.98 (d, J = 8.5 Hz, 4H), 7.77 (d, J = 8.7 Hz, 4H), 7.14 (t, J = 7.7 Hz, 1H) **^{13}C NMR (100 MHz, DMSO):** δ 167.08 (s), 142.35 (s), 133.52 (s), 126.52 (q, J = 7.4, 3.6 Hz), 126.13 (s), 124.61 (d, J = 31.8 Hz), 123.44 (s), 121.06 (d, J = 10.5 Hz), 120.63 (s).; **^{19}F NMR**

(377 MHz, DMSO): δ -60.44 (s); **HRMS (ESI):** Calc. for $C_{22}H_{14}F_6N_2O_3$ $[M+H]^+$: 469.0987; Found: 469.0987.)

Compound 1d: White solid (50% yield); **M.p.:** 217.0–219.0 °C; **IR** (ν/cm^{-1}) 3344, 2942, 2832, 1658, 1550, 1454, 1220, 1115, 1022, 749; **^{1}H NMR (400 MHz, CD_3OD:$CDCl_3$):** δ 14.10 (s, 1H), 9.57 (s, 2H), 8.22 (s, 6H), 7.72 (s, 2H), 7.19 (t, *J* = 7.9 Hz, 1H). **^{13}C NMR (100 MHz, CD_3OD:$CDCl_3$):** δ 170.70 (s), 143.24 (s), 138.43 (s), 136.11 (q, J = 33.4 Hz), 131.13 (s), 128.42 (s), 125.71 (s), 124.76 (s), 123.14 (d, J = 28.6 Hz), 121.71 (q, J = 13.6, 10.1 Hz); **^{19}F NMR (377 MHz, $CDCl_3$):** δ -63.02 (s); **HRMS (ESI):** Calc. for $C_{24}H_{12}F_{12}N_2O_3$ $[M+H]^+$: 605.0735; Found: 605.0743.

3.4.4. Ion Transport Studies.

The ion transport studies were performed as discussed in the previous chapter.

Preparation of EYPC-LUVs⊃CF: A thin lipid film was prepared by evaporating a solution of 12.5 mg EYPC in 0.5 ml $CHCl_3$ in vacuo for 4 h. After that lipid film was hydrated with 0.5 mL buffer (10 mM HEPES, 10 mM NaCl, 50 mM CF, pH 7.0) for 1 h with occasional vortexing of 4-5 times and then subjected to freeze-thaw cycle (≥ 20 times). The vesicle solution was extruded through a polycarbonate membrane with 100 nm pores 19 times (has to be an odd number), to give vesicles with a mean diameter of ~ 100 nm. The extracellular dye was removed size exclusion chromatography (Sephadex G-50) with 10 mM HEPES buffer (100 mM NaCl, pH 7.0. Final) Final concentration: ~ 2.5 mM EYPC lipid; intravesicular solution: 10 mM HEPES, 10 mM NaCl, 50 mM CF, pH 7.0; extravesicular solution: 10 mM HEPES, 100 mM NaCl, pH 7.0.

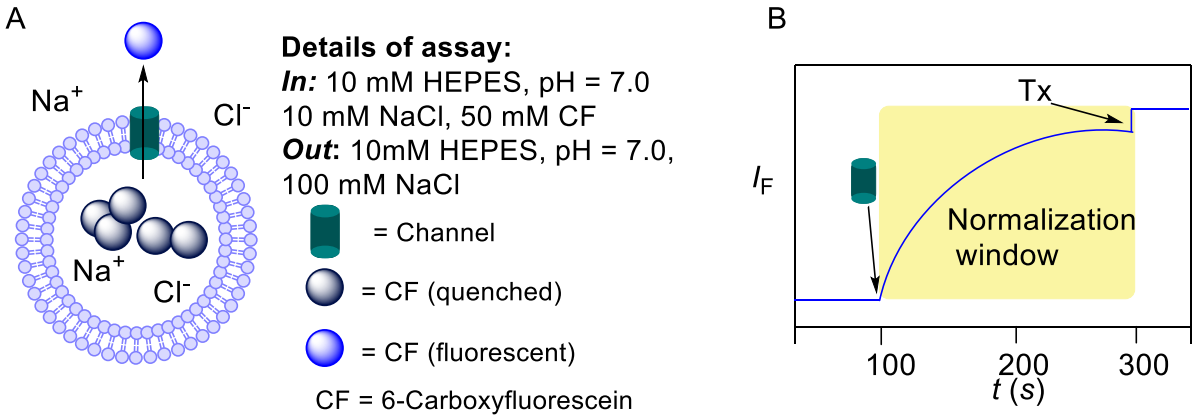

Figure 3.16. Schematic illustration of CF leakage assay using EYPC-LUVs⊃HPTS, CF (**A**) and representative fluorescence kinetics experiment of corresponding assay (**B**).

CF leakage assay: In a clean and dry fluorescence cuvette 25 µL of above lipid solution and 1975 µL of 10 mM HEPES buffer (100 mM NaCl, pH 7.0) was taken and kept in slowly stirring condition by a magnetic stirrer equipped with the fluorescence instrument (at *t* = 0 s). The time

course of CF fluorescence emission intensity, F_t was observed at λ_{em} = 517 nm (λ_{ex} = 492 nm). Compound **1d** was added at t = 100 s and finally at t = 300 s, 25 μL of 10% Triton X-100 was added to lyse those vesicles for 100% chloride influx. Fluorescence intensities (F_t) were normalized to fractional emission intensity I_F according methods described in previous chapter. This study confirmed that neither the bilayer membranes are defected nor large transmembrane pores are formed by **1d**.

3.4.5. Planar Bilayer Conductance measurements.

The bilayer membrane (BLM) was formed across an aperture of 150 μM diameter in a polystyrene cup (Warner Instrument, USA) with lipid diphytanoylphosphatidylcholine (Avanti Polar Lipids), dissolved in *n*-decane (20 mg/mL). Both compartments (*cis* and *trans*) were filled with symmetrical solution, containing 1 M KCl. The *trans* compartment was held at virtual ground and the *cis* chamber was connected to the BC 535 head-stage (Warner Instrument, USA) via matched Ag-AgCl electrodes. Compound **1a** (20 μM) was added to the *trans* chamber and the solution was stirred with magnetic stirrer for 30 min. Channel formation was confirmed by the distinctive channel opening and closing events after applying voltages. Currents were low pass filtered at 1 kHz using pClamp9 software (Molecular probes, USA) and analog-to-digital converter (Digidata 1440, Molecular probes). All data were analyzed by the software pClamp 9. The complete data trace observed for ten minutes contained a series of opening and closing events at some indefinite intervals. The average current was calculated from this trace and then conductance and other calculations were made accordingly.

Determination of anion selectivity permeability ratio by Planar Bilayer Conductance Measurements:

The *cis* and *trans* chambers were filled with unsymmetric solutions of KCl. The *cis* chamber was filled with 1.0 M KCl solution and *trans* chamber was filled with 0.5 M KCl. The compound **1d** (2 μM) was added to the *trans* chamber and stirred for 5 minutes. The reversal potential was calculated to be 10 ± 2 mV (Figure 3.8 C)

The permeability ratio (P_{Cl^-}/P_{K^+}) was calculated by using Goldman-Hodgkin-Katz equation (Equation S5).

$$\frac{P_{Cl^-}}{P_{K^+}} = \frac{a_{K^+cis} - a_{K^+trans} \times \exp\left(-\frac{V_{rev} \times F}{R \times T}\right)}{a_{Cl^-cis} \times \exp\left(-\frac{V_r \times F}{R \times T}\right) - a_{Cl^-trans}} \qquad \text{(Equation 2)}$$

where, P_{Cl^-}/P_{K^+} = anion/cation permeability ratio; a_{K^+cis} = K^+ activity in the *cis* chamber; a_{K^+trans} = K^+ activity in the *trans* chamber; a_{Cl^-cis} = Cl^- activity in the *cis* chamber; a_{Cl^-trans} = Cl^- activity in the *trans* chamber; V_{rev} = reversal potential; F = Faraday constant; R = gas constant; T = temperature (K).

3.4.6. Single Crystal X-Ray Diffraction Study.

The single crystals of **1c** were grown from mixture of acetonitrile and *n*-decane and allowing slow evaporation of the solvents. Single-crystals data were collected on a Bruker SMART APEX four-circle diffractometer equipped with a CMOS photon 100 detector (Bruker Systems Inc.) and with a Cu Kα radiation (1.5418 Å). The incident X-ray beam was focused and monochromated using Micro focus (IμS). Crystal of **1c** was mounted on nylon Cryo loops with Paratone-N oil. Data was collected at 100(2) K. Structure was solved by Intrinsic Phasing module of the direct methods and refined using the SHELXTL 2014 software suite.

Details of the crystal 1c: CCDC 1904396; C_{22} H_{12} F_6 N_2 O_3; M = 466.34; Rod shaped; Colorless; Monoclinic; space group P 2_1/n; Cell: a = 10.7749(11), b = 15.2475(15), c = 12.3140(13); Cell volume =1918.36 $Å^3$, Angles α = 90, β = 108.515(8), γ = 90; GoF = 0.996, Z = 4, T = 100(2), θ_{max} = 59.85^o

3.4.7. Molecular Modeling Studies:

To have a clear picture about the channel formation by **1d**, we constructed a theoretical model by predicting the most probable conformation using Conflex 8 program (Figure 3.10). This conformation was used to generate the supramolecular channel model (Figure 3.11 A). Afterwards, the MD simulations were carried out by using an explicit preequilibrated phospholipid bilayer of 128 POPC (1-palmitoyl-2-oleoyl-sn-glycero-3-phosphocholine) molecules obtained from P. Tieleman's University of Calgary website (http://moose.bio.ucalgary.ca). The optimized channel was inserted in a box of 128 POPC molecules using inflategro methodology at the proper density (area per lipid) of ~ 0.66 nm^2. To solvate the system, 7544 SPC model water molecules were added to the system. GROMOS-53a6 united atom force field was used for POPC molecules. The automated topology builder created by Malde, *et al.* was used to create the all-atom topology parameters of the channel with GROMOS-53a6 force field. The parameter for potassium ion suitable for GROMOS force field was obtained from the literature. The GROMACS 2018.5 software was used for molecular dynamics to carry out all the simulations.

3.4.7. Biological Studies.

A. Cell culture protocol.

The cells were grown in High Glucose Dulbecco's Modified Eagle Medium (DMEM; Invitrogen or Lonza) containing 10% fetal bovine serum (FBS; Invitrogen), 2 mM L-glutamine (Invitrogen) and 100 units/mL penicillin-streptomycin (Invitrogen). Cells were maintained in 100 mm tissue culture treated dishes (Corning) at 37 °C in humidified 5% CO_2 incubator (Thermo Scientific).

B. Live cell imaging.

The MCF 7 cells were seeded in glass bottom 35 mm dishes at the concentration of 5 x 10^5 cells per plate. After attaining the confluency, the cells were focused in Lieca sp8 confocal

microscope and then the DMEM media containing 10 μM of **1d** was added. The blue fluorescent compound was seen in DAPI region using blue LASER. The time course to enter the cell was monitored using real time analysis.

C. MTT-based cytotoxicity assay.

Cells were dispersed in a 96-well flat bottom tissue culture treated plates (Corning) at density of 10^4 cells/well (per 100 μL) and incubated at 37 ^oC in a 5% CO_2 incubator for 16 h. Compounds were added to each well in different concentration by maintaining maximum amount of DMSO at 2 μL and incubated for 24 h. DMEM solution containing compounds in each well were replaced with 110 μL of MTT-DMEM mixture (0.5 mg MTT/mL of DMEM) and incubated for 4 h in identical condition. After 4 h, MTT solution was removed and 100 μL of DMSO was added in each well to dissolve the formazan crystals. The absorbance was recorded in a microplate reader (Varioskan Flash) at the wavelength of 570 nm. All experiments were performed in triplicates, and the relative cell viability (%) was expressed as a percentage of cells treated with DMSO

D. Sodium, potassium and chloride mediated cell death studies.

HBSS buffer solution: Hank's balanced salt solution (HBSS with Cl^-) was prepared with the following compositions: 136.9 mM NaCl, 5.5 mM KCl, 0.34 mM Na_2HPO_4, 0.44 mM KH_2PO_4, 0.81 mM $MgSO_4$, 1.25 mM $CaCl_2$, 5.5 mM D-glucose, 4.2 mM $NaHCO_3$ and 10 mM HEPES (pH 7.4). Chloride free HBSS was prepared by mixing 136.9 mM Na-gluconate, 5.5 mM K-gluconate, 0.34 mM Na_2HPO_4, 0.44 mM KH_2PO_4, 0.81 mM $MgSO_4$, 1.25 mM Ca-gluconate, 5.5 mM D-glucose, 4.2 mM $NaHCO_3$ and 10 mM HEPES (pH 7.4). For the Hank's balanced salt solution without Na^+ and K^+, the corresponding salts were replaced with choline salts of the respective ions.

HBSS buffers (all the categories) were mixed with 10% FBS and 1% penicillin-streptomycin before using as extracellular media. Cells were dispersed in a 96-well flat bottom tissue culture treated plates (Corning) at density of 10^4 cells/well (per 100 μL) and incubated at 37 ^oC in 5% CO_2 for 24 h. Cellular media was replaced by respective HBSS buffers containing 10% FBS. Compound **1d** was added to each well in different concentration by maintaining maximum amount of DMSO at 1 μL and incubated for 24 h. HBSS buffer solution of compounds in each well was replaced by 100 μL of MTT-DMEM mixture (0.5 mg MTT/mL of HBSS) and incubated for 4 h in identical condition. Excess MTT solution was removed after 4 h and 100 μL of DMSO was added in each well to dissolve the formazan crystals. The absorbance was recorded in a microplate reader (Varioskan Flash) at the wavelength of 570 nm.

E. Mitochondrial membrane depolarization.

The MCF 7 cells were seeded in glass bottom 35 mm dishes at the concentration of 5 x 10^5 cells per plate. Cells were incubated with 10μM of **1d** for 24 h. After that cells were washed thoroughly and incubated with JC-1 at the final concentration of 50 nM for 30 min. Fluorescence

images were acquired after washing with PBS in both red and green channel using Lieca sp8 confocal microscope. The ratio of pixel intensities (red/green) from 7 different images of each set of cells (by using Image J software).

F. ROS generation.

The MCF 7 cells were seeded in glass bottom 35 mm dishes at the concentration of 5×10^5 cells per plate. Cells were incubated with 10 μM of **1d** for 24 h. After that cells were washed thoroughly and incubated with DCFDA at the final concentration of 0.5 μM for 20 min. The cell images were acquired after washing with PBS in time dependent manner using green channel with Nikon Eclipse TS 100 fluorescence microscope.

G. Immunofluorescence analysis for cytochrome *c* release:

Cells were seeded at a density of 1×10^5 cells per well on top of glass cover slips (Micro-Aid, India). Following **5d** treatment, cells were fixed using 4% formalin (Macron Chemicals) and were permeabilised using 0.5% Triton X-100 for 10 min at 4 ^{o}C. Cells were blocked with 10% (v/v) FBS (Invitrogen), stained with primary antibody (cytochrome *c* antibody) and then incubated with secondary antibody (goat anti-rabbit AlexaFluor-488). Cells were then counterstained with phallogen to stain the cell boundaries and mounted on glass slides (Micro-Aid, India). Cell images were taken in were taken using Leica sp8 confocal microscope. Microscopy images were captured using 63 X oil-immersion objective.

H. Immunoblot analysis.

MCF-7 cells were seeded at a density of 6 x 10^5 cells per well in 6-well tissue culture treated plates (Corning) and maintained at 37 °C for 24 h. Cells were then treated with 10 μM of **1d** by direct addition of drug to the culture medium for 24 h . Control cells were treated with equivalent volume of DMSO. After 24 h treatment, medium containing **1d** was aspirated and cells were washed once with 1X phosphate buffered saline (PBS; PAN-Biotech GmbH). Cells were lysed in sample buffer containing 60 mM Tris (pH 6.8), 6% glycerol, 2% sodium dodecyl sulfate (SDS), 0.1 M dithiothreitol (DTT) and 0.006% bromophenol blue and lysates were stored at - 40 °C.

Cell lysates were resolved using sodium dodecyl sulfate polyacrylamide gel electrophoresis (SDS-PAGE) and transferred to Immobilon–P polyvinylidene difluoride (PVDF) membrane (Millipore). Blocking was performed in 5% (w/v) skimmed milk (SACO Foods, USA) prepared in 1X Tris buffered saline containing 0.1% Tween 20 (1X TBS-T) for 1 h at room temperature. Blots were incubated for 16 h at 4 ^{o}C temperature in primary antibody solution. Following washes, blots were incubated with peroxidase-conjugated secondary antibody solution prepared in 5% (w/v) skimmed milk in 1X TBS-T for 1 h at room temperature following which blots were developed using Immobilon Western Detection Reagent kit (Millipore) and visualized using ImageQuant LAS 4000 (GE Healthcare).

I. Propidium iodide staining.

The MCF 7 cells were seeded in glass bottom 35 mm dishes at the concentration of 5×10^5 cells per plate. Cells were incubated with 10 μM of **1d** for 24 h. The cell plate was washed thoroughly with Phosphate buffer saline (PBS) 2 to 3 times. Then, propidium iodide dye (10 μg/mL) was added to the plate in dark and the plate was incubated for 15 minutes at 37 ^{o}C in CO_2 incubator. After 15 minutes, plates were removed from incubator, dye was removed and the scaffolds were washed thoroughly with PBS to remove the excess stain. 1 mL of fresh PBS was added to the scaffolds, and then analyzed for cell under confocal fluorescence microscope.

3.5. NMR Spectra.

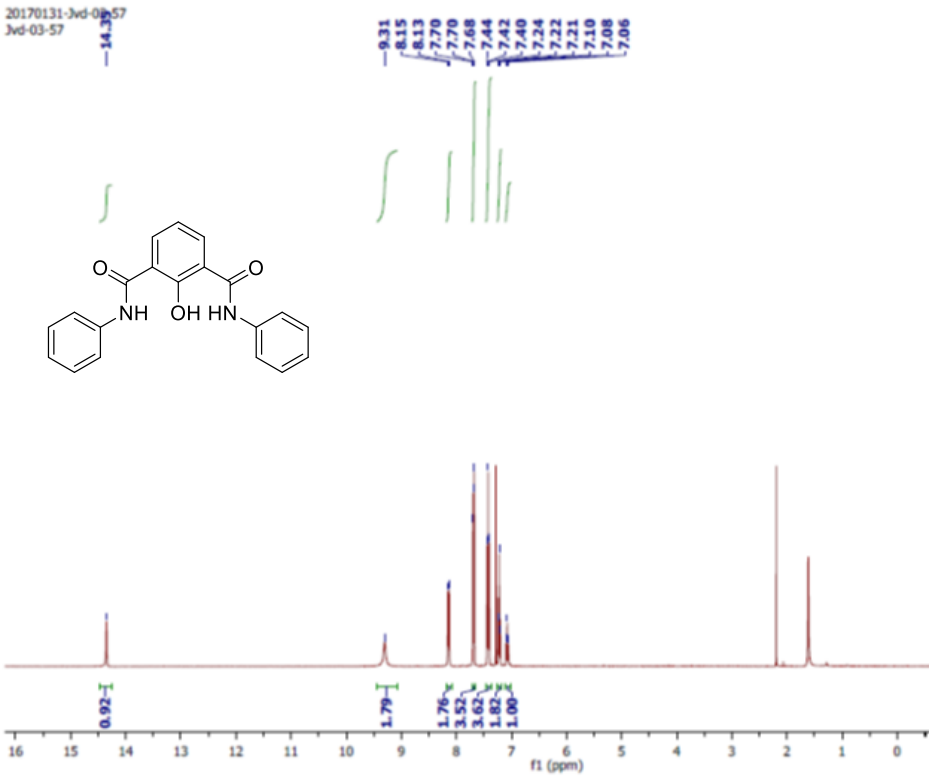

Figure 3.17. ^{1}H NMR spectrum of **1a** in $CDCl_3$.

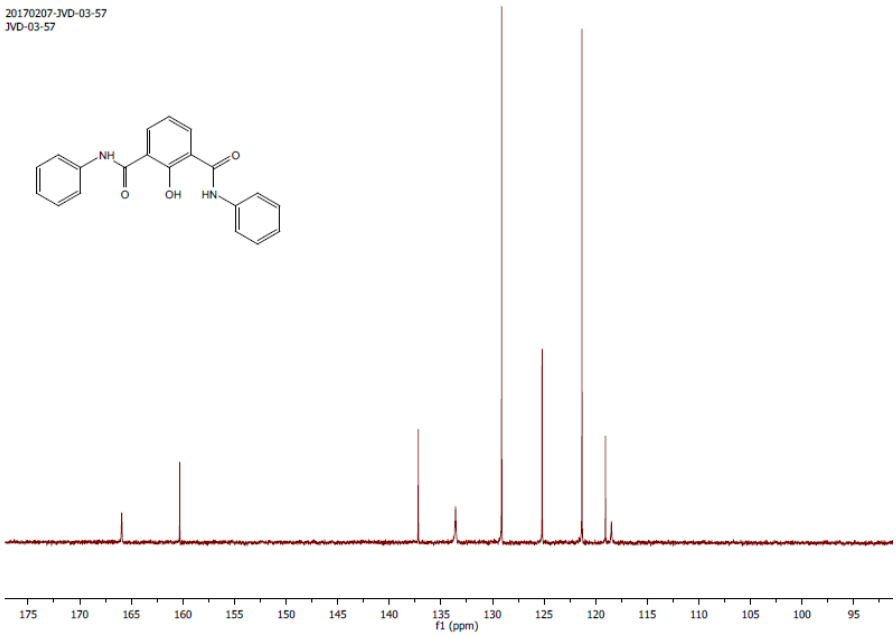

Figure 3.18. ^{13}HC NMR spectrum of **1a** in $CDCl_3$.

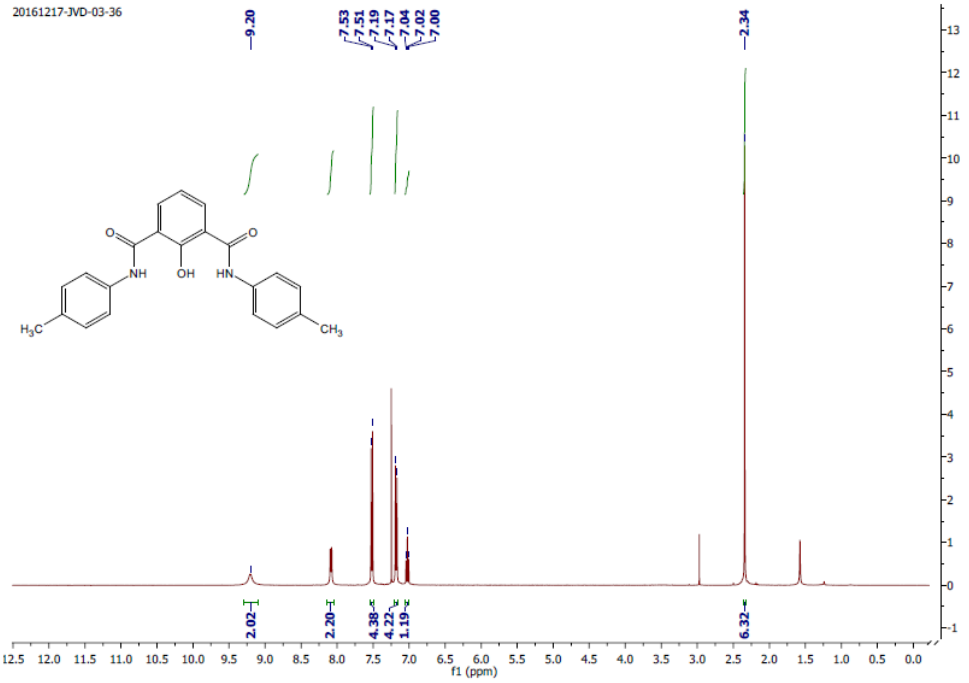

Figure 3.19. ^{1}H NMR spectrum of **1b** in $CDCl_3$.

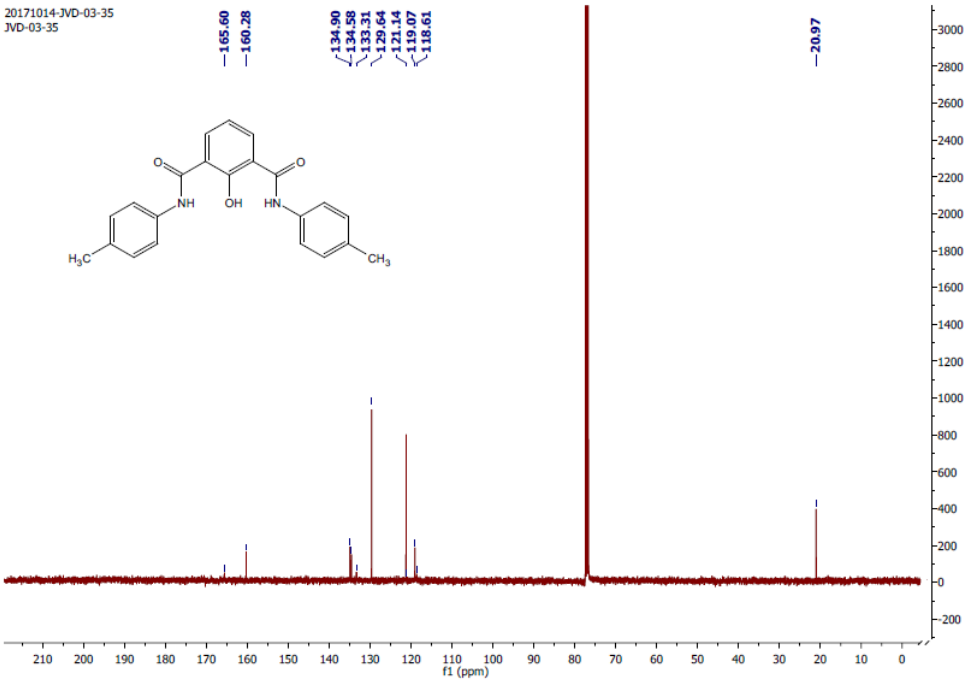

Figure 3.20. ^{13}C NMR spectrum of **1b** in $CDCl_3$.

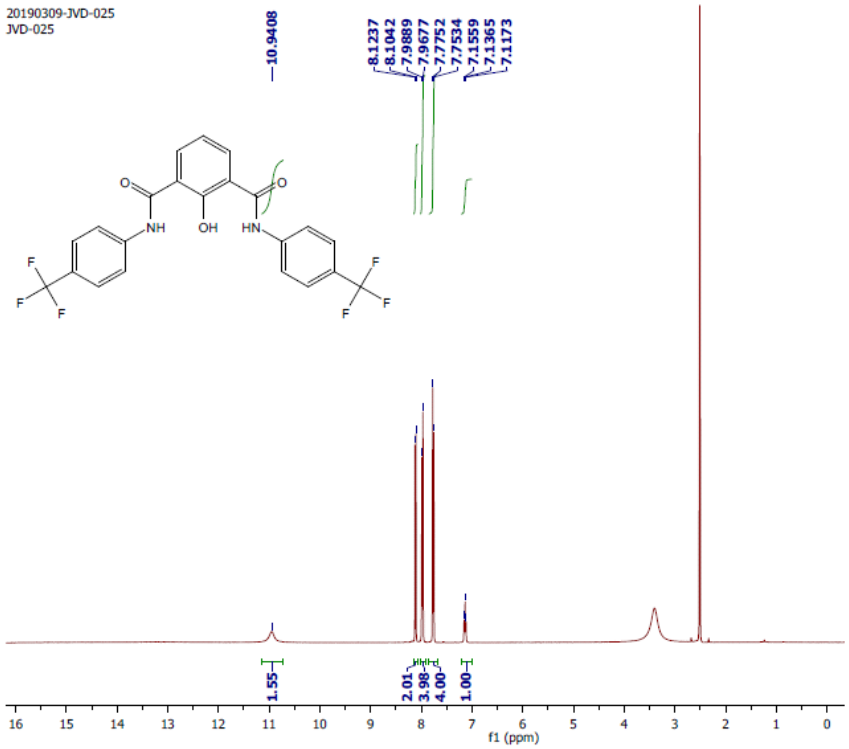

Figure 3.21. ^{1}H NMR spectrum of **1c** in DMSO-d_6.

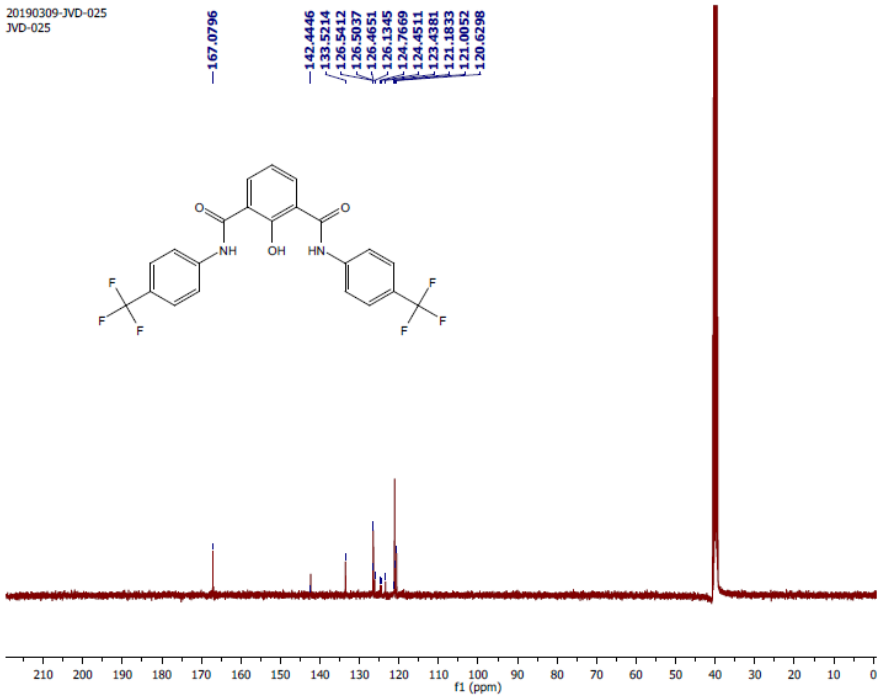

Figure 3.22. ^{13}C NMR spectrum of **1c** in DMSO-d_6.

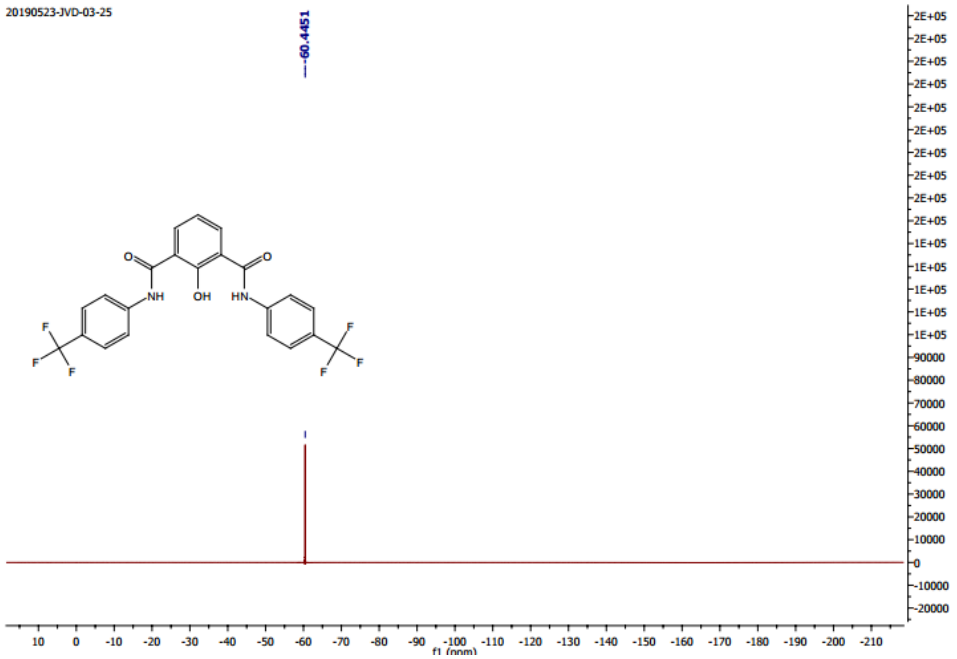

Figure 3.23. ^{19}F NMR spectrum of **1c** in DMSO-d_6

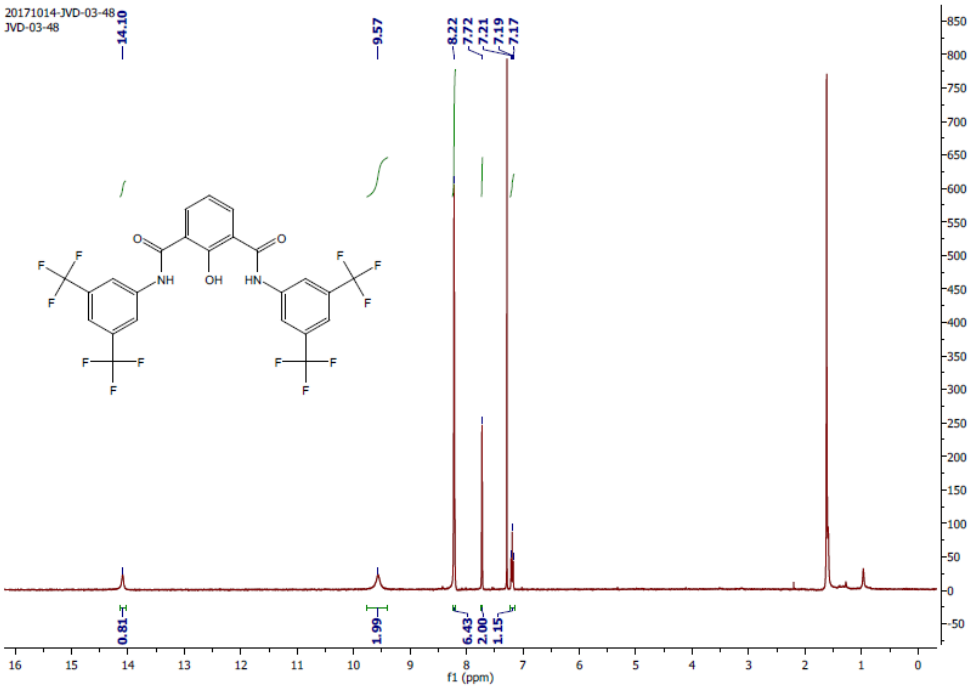

Figure 3.24. ^{1}H NMR spectrum of **1d** in CD_3OD:$CDCl_3$.

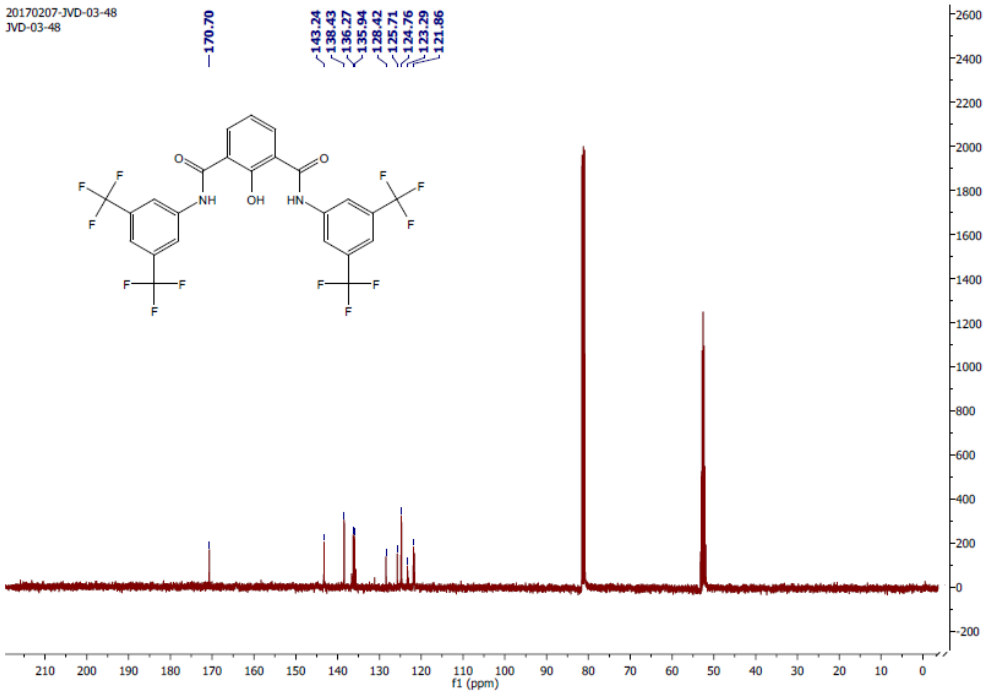

Figure 3.25. ^{13}C NMR spectrum of **1d** in CD_3OD:$CDCl_3$.

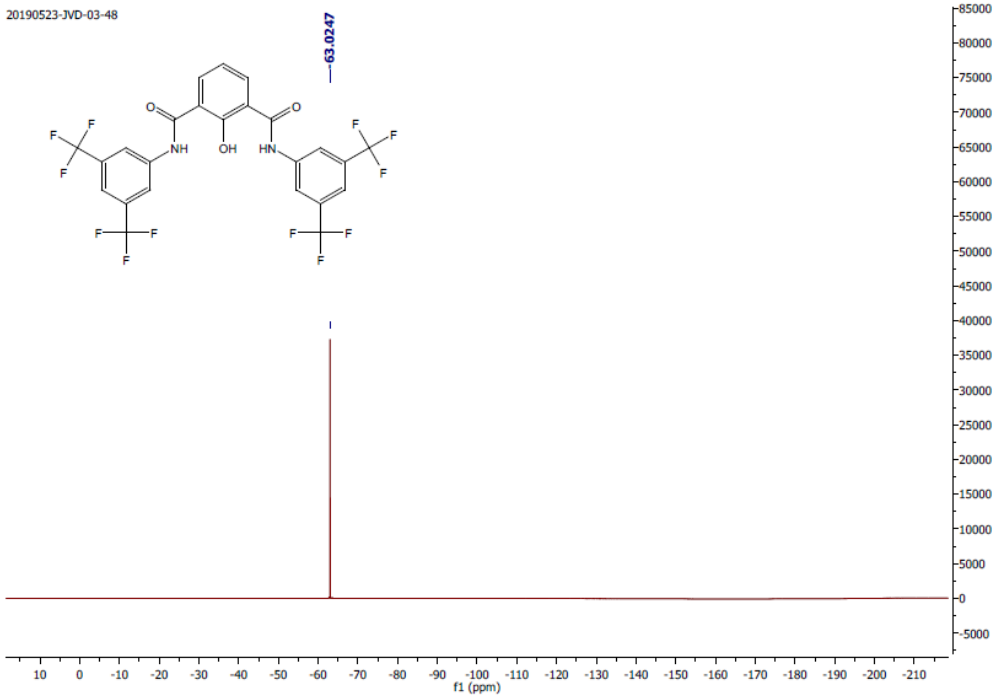

Figure 3.26. ^{19}FNMR spectrum of **1d** in CD_3OD:$CDCl_3$.

3.6. REFERENCES:

(1) Hummer, G. *Science* **2014**, *346*, 303.

(2) Dutzler, R.; Campbell, E. B.; MacKinnon, R. *Science* **2003**, *300*, 108.

(3) Tedesco, M. M.; Ghebremariam, B.; Sakai, N.; Matile, S. *Angew. Chem. Int. Ed.* **1999**, *38*, 540.

(4) Forman, S. L.; Fettinger, J. C.; Pieraccini, S.; Gottarelli, G.; Davis, J. T. *J. Am. Chem. Soc.* **2000**, *122*, 4060.

5) Winum, J.-Y.; Matile, S. *J. Am. Chem. Soc.* **1999**, *121*, 7961.

(6) Cazacu, A.; Tong, C.; van der Lee, A.; Fyles, T. M.; Barboiu, M. *J. Am. Chem. Soc.* **2006**, *128*, 9541.

(7) Gorteau, V.; Bollot, G.; Mareda, J.; Perez-Velasco, A.; Matile, S. *J. Am. Chem. Soc.* **2006**, *128*, 14788.

(8) Perez-Velasco, A.; Gorteau, V.; Matile, S. *Angew. Chem. Int. Ed.* **2008**, *47*, 921.

(9) Saha, T.; Dasari, S.; Tewari, D.; Prathap, A.; Sureshan, K. M.; Bera, A. K.; Mukherjee, A.; Talukdar, P. *J. Am. Chem. Soc.* **2014**, *136*, 14128.

(10) Saha, T.; Gautam, A.; Mukherjee, A.; Lahiri, M.; Talukdar, P. *J. Am. Chem. Soc.* **2016**, *138*, 16443.

(11) Ren, C.; Zeng, F.; Shen, J.; Chen, F.; Roy, A.; Zhou, S.; Ren, H.; Zeng, H. *J. Am. Chem. Soc.* **2018**, *140*, 8817.

(12) Marvin 5.8.0, ChemAxon, 2012 (http://www.chemaxon.com)

(13) Trifonov, A. L.; Levin, V. V.; Struchkova, M. I.; Dilman, A. D. *Org. Lett.* **2017**, *19*, 5304.

(14) Routasalo, T.; Helaja, J.; Kavakka, J.; Koskinen, A. M. P. *Eur. J. Org. Chem.* **2008**, *2008*, 3190.

(15) Sisson, A. L.; Shah, M. R.; Bhosale, S.; Matile, S. *Chem. Soc. Rev.* **2006**, *35*, 1269.

(16) Talukdar, P.; Bollot, G.; Mareda, J.; Sakai, N.; Matile, S. *J. Am. Chem. Soc.* **2005**, *127*, 6528.

(17) Shinde, S. V.; Talukdar, P. *Chem. Commun.* **2018**, *54*, 10351.

(18) Roy, A.; Gautam, A.; Malla, J. A.; Sarkar, S.; Mukherjee, A.; Talukdar, P. *Chem. Commun.* **2018**, *54*, 2024.

(19) Saha, T.; Roy, A.; Gening, M. L.; Titov, D. V.; Gerbst, A. G.; Tsvetkov, Y. E.; Nifantiev, N. E.; Talukdar, P. *Chem. Commun.* **2014**, *50*, 5514.

(20) Lipinski, C. A.; Lombardo, F.; Dominy, B. W.; Feeney, P. J. *Adv. Drug Deliv. Rev.* **1997**, *23*, 3.

(21) Saggiomo, V.; Otto, S.; Marques, I.; Félix, V.; Torroba, T.; Quesada, R. *Chem. Commun.* **2012**, *48*, 5274.

(22) Litvinchuk, S.; Bollot, G.; Mareda, J.; Som, A.; Ronan, D.; Shah, M. R.; Perrottet, P.; Sakai, N.; Matile, S. *J. Am. Chem. Soc.* **2004**, *126*, 10067.

(23) Malla, J. A.; Roy, A.; Talukdar, P. *Org. Lett.* **2018**, *20*, 5991.

(24) Gilles, A.; Barboiu, M. *J. Am. Chem. Soc.* **2016**, *138*, 426.

(25) Ren, C.; Shen, J.; Zeng, H. *J. Am. Chem. Soc.* **2017**, *139*, 12338.

(26) Ren, C.; Ding, X.; Roy, A.; Shen, J.; Zhou, S.; Chen, F.; Yau Li, S. F.; Ren, H.; Yang, Y. Y.; Zeng, H. *Chem. Sci.* **2018**, *9*, 4044.

(27) Benke, B. P.; Aich, P.; Kim, Y.; Kim, K. L.; Rohman, M. R.; Hong, S.; Hwang, I.-C.; Lee, E. H.; Roh, J. H.; Kim, K. *J. Am. Chem. Soc.* **2017**, *139*, 7432.

(28) Yamnitz, C. R.; Negin, S.; Carasel, I. A.; Winter, R. K.; Gokel, G. W. *Chem. Commun.* **2010**, *46*, 2838.

(29) Saha, T.; Hossain, M. S.; Saha, D.; Lahiri, M.; Talukdar, P. *J. Am. Chem. Soc.* **2016**, *138*, 7558.

(30) Busschaert, N.; Wenzel, M.; Light, M. E.; Iglesias-Hernández, P.; Pérez-Tomás, R.; Gale, P. A. *J. Am. Chem. Soc.* **2011**, *133*, 14136.

(31) Langton, M. J.; Scriven, L. M.; Williams, N. H.; Hunter, C. A. *J. Am. Chem. Soc.* **2017**, *139*, 15768.

(32) Jung, M.; Kim, H.; Baek, K.; Kim, K. *Angew. Chem. Int. Ed.* **2008**, *47*, 5755.

(33) Sakai, N.; Matile, S. *Langmuir* **2013**, *29*, 9031.

(34) Jentzsch, A. V.; Emery, D.; Mareda, J.; Nayak, S. K.; Metrangolo, P.; Resnati, G.; Sakai, N.; Matile, S. *Nat. Commun.* **2012**, *3*, 905.

(35) H. Goto, S. Obata, N. Nakayama and K. Ohta, CONFLEX 8, CONFLEX Corporation, Tokyo, Japan, 2012.

(36) Goto, H.; Osawa, E. *J. Am. Chem. Soc.* **1989**, *111*, 8950.

(37) Stewart, J. J. P. *MOPAC**2012***; Stewart Computational Chemistry: Colorado Springs, CO, USA, 2012.

(38) Korth, M. *J. Chem. Theory Comput.* **2010**, *6*, 3808.

(39) Berry, S. N.; Soto-Cerrato, V.; Howe, E. N. W.; Clarke, H. J.; Mistry, I.; Tavassoli, A.; Chang, Y.-T.; Pérez-Tomás, R.; Gale, P. A. *Chem. Sci.***2016**, *7*, 5069.

(40) Bortner, C. D.; Cidlowski, J. A. *Cell Death Differ.* **2002**, *9*, 1307.

(41) Model, M. A. *Am. J. Physiol. Cell Physiol.* **2014**, *306*, C417.

(42) Busschaert, N.; Park, S. H.; Baek, K. H.; Choi, Y. P.; Park, J.; Howe, E. N. W.; Hiscock, J. R.; Karagiannidis, L. E.; Marques, I.; Felix, V.; Namkung, W.; Sessler, J. L.; Gale, P. A.; Shin, I. *Nat. Chem.* **2017**, *9*, 667.

(43) Sakamuru, S.; Attene-Ramos, M. S.; Xia, M. *Methods Mol. Biol.***2016**, *1473*, 17.

(44) Patil, S.; Kuman, M. M.; Palvai, S.; Sengupta, P.; Basu, S. *ACS Omega* **2018**, *3*, 1470.

(45) Ashkenazi, A. *Nat. Rev. Drug Discov.* **2008**, *7*, 1001.

(46) Smiley, S. T.; Reers, M.; Mottola-Hartshorn, C.; Lin, M.; Chen, A.; Smith, T. W.; Steele, G. D.; Chen, L. B. *Proc. Nat. Acd. Sci. U.S. A.* **1991**, *88*, 3671.

(47) Poncet, D.; Boya, P.; Métivier, D.; Zamzami, N.; Kroemer, G. *Apoptosis* **2003**, *8*, 521.

(48) Cossarizza, A.; Baccarani-Contri, M.; Kalashnikova, G.; Franceschi, C. *Biochem. Biophys. Res. Commun.* **1993**, *197*, 40.

(49) Sabharwal, S. S.; Schumacker, P. T. *Nat. Rev. Cancer* **2014**, *14*, 709.

(50) Liou, G. Y.; Storz, P. *Free Radic. Res.* **2010**, *44*, 479.

(51) Wu, D.; Yotnda, P. *J. Vis. Exp.* **2011**.

(52) Halestrap, A. P. *J Mol. Cell Cardiol.* **2009**, *46*, 821.

(53) CROMPTON, M. *Biochem. J.* **1999**, *341*, 233.

(54) Madesh, M.; Hajnoczky, G. *J. Cell Biol.* **2001**, *155*, 1003.

(55) Skulachev, V. P. *Apoptosis* **2006**, *11*, 473.

(56) Cullen, S. P.; Martin, S. J. *Cell Death Differ.* **2009**, *16*, 935.

(57) Wu, J.; Liu, T.; Xie, J.; Xin, F.; Guo, L. *Cell. Mol. Life Sci.* **2006**, *63*, 949.

(58) Shi, Y. *Mol. cell* **2002**, *9*, 459.

(59) Park, S.-H.; Choi, Y. P.; Park, J.; Share, A.; Francesconi, O.; Nativi, C.; Namkung, W.; Sessler, J. L.; Roelens, S.; Shin, I. *Chem. Sci.* **2015**, *6*, 7284.

(60) Chaitanya, G. V.; Alexander, J. S.; Babu, P. P. *Cell Commun. Signal.* **2010**, *8*, 31.

(61) Suzuki, T.; Fujikura, K.; Higashiyama, T.; Takata, K. *J. Histochem. Cytochem.* **1997**, *45*, 49.

(62) Li, F.; Basile, V. M.; Pekarek, R. T.; Rose, M. J. *ACS Appl. Mater. Interfaces* **2014**, *6*, 20557.

Chapter 4

A Glutathione Activatable Ion Channel Induces Apoptosis in Cancer Cells by Depleting Intracellular Glutathione Levels

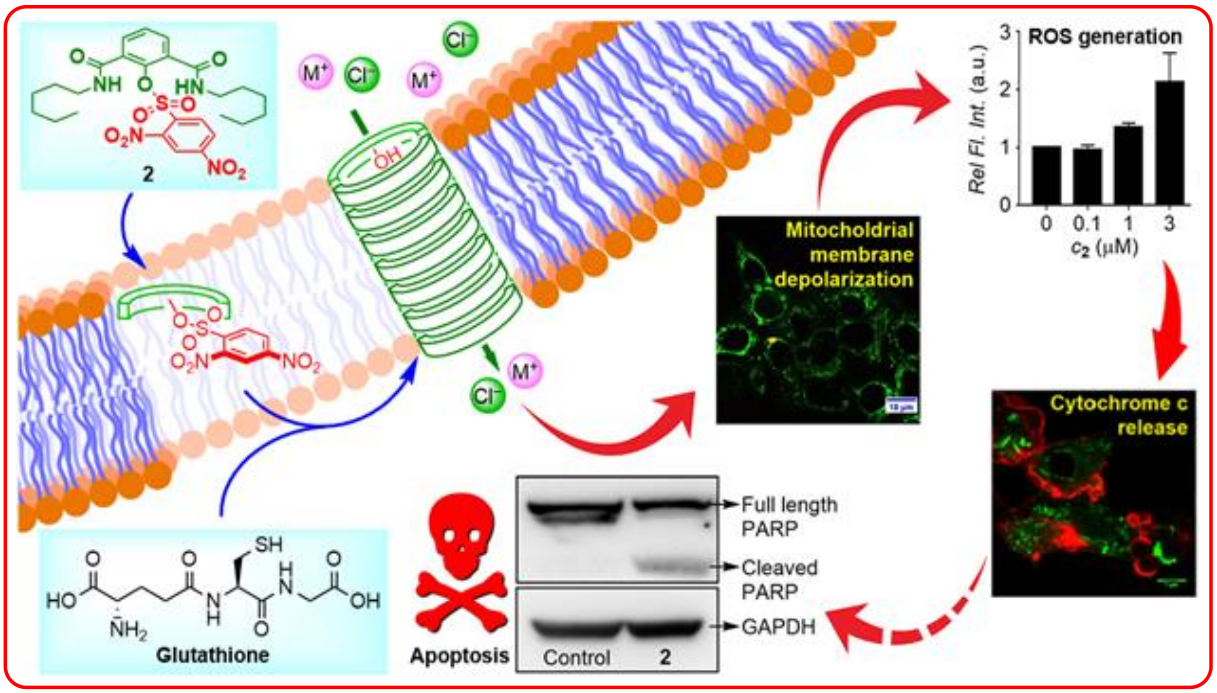

4.1. INTRODUCTION:

As discussed in chapter 3, the designed ion channel can switch the cells to undergo ion mediated apoptosis. However, the system can't differentiate between healthy cells and cancer cells, along with the cancer cells the innocent healthy cells have to be sacrificed. Therefore, to overcome the problem there is a need to develop stimulus responsive systems which can be activated by a suitable signal. In this regard, various studies have been reported in literature for the design of such ion transport systems which can be activated by specific stimuli. As an example, it is well known that the cancer cells in tumor tissues have slightly decreased extracellular pH compared to the healthy cells due to the anaerobic glucose metabolism.[1] Therefore, to overcome the limitation of the innocent death of healthy cells and to specifically target cancer cells, recent studies have been done by exploiting the acidic microenvironment of solid tumor tissues. For example, prodigiosin – a secondary metabolite from Serratia marcescens – and its analogs work both as a Cl^-/anion antiporter and H^+/Cl^- symporter, and induce cytotoxicity in cancer cells majorly by altering the pH of cellular organelles.[2-4] This acidic microenvironment also acts as an external defense system for cancer cells wherein acidification of basic anticancer drugs occurs which inhibits their permeation into the cells.[5]

Similarly, our group has recently developed a photodynamic therapeutic approach to induce apoptosis in cancer cells by introducing photocleavable procarrier that can be activated in cancer cells using a specific wavelength of light.[6] However, both these strategies are far from the real demands since light can be used for only surface phenomenon and pH gradient may not be sufficient enough for obtaining remarkable results *in vivo*. Therefore, there exists a great demand to develop new ion transport systems, which can be activated within the cells without the aid of external factors.

In this regard, intracellular glutathione (GSH) levels of cancer cells, owing to the multiple roles in cancer cells, can be used as stimulus to activate the ion transport process selectively in cancer cells and induce the apoptosis. The cancer cells are under constant genomic instability, oncogenic stress, cellular hypoxia, and oxidative stress – conditions that favor apoptosis,[7] yet cancer cells often avoid these cellular responses by disabling the apoptotic pathways using the internal defense mechanism. As an example, oxidative stress has been characterised by the increased production of reactive oxygen species (ROS; H_2O_2, O_2^-, OH^-, etc.), which can in turn affect the metabolism and induce mitochondrial dysfunction in cells.[8,9] However, cancer cells possess the ability to combat oxidative stress via enzymatic[10,11] and nonenzymatic[12] antioxidant mechanisms. Amongst the different cellular antioxidants, the tripeptide – glutathione (L-γ-glutamyl-L-cysteinyl-glycine, GSH) – is the most abundant intracellular thiol that nonenzymatically detoxifies ROS and helps prevent oxidative stress induced apoptosis in cancer cells.[13] Moreover, elevated levels of GSH in cancer cells (e.g. in breast, colon, lung, etc.) is also linked to the development of resistance to several chemotherapeutic drugs.[14,15] Such a dual-process model of defense by GSH has caused serious limitations to the use of several anticancer

drugs. Therefore, the development of new treatment modalities are warranted that target this GSH mediated internal defense mechanism to induce cytotoxicity in cancer cells.

Considering the higher intracellular GSH levels in cancer cells when compared to the healthy cells, we envisioned that ion transport systems that can be activated by the higher GSH concentrations could take advantage of the internal GSH defense of cancer cells to release ion transporting molecules, which then would induce apoptosis in these cells selectively by perturbing the ion homeostasis. Along these lines, Liu and coworkers have reported selenium containing organic nanoparticles as thiol sensitive ion carriers; however, these studies were confined only to artificial membranes.[16] Manna and coworkers recently reported the GSH mediated chloride transport by small ionophores; however, their system did not show significant cytotoxicity in Hela cells.[17]

Li and coworkers reported a chloride channel based on the isophthalamide core by connecting it to two α-aminoxy acid units.[18] We hypothesized that the introduction of a bulky group at the C-2 position of the isophthalamide would not allow efficient self-assembly of the monomers thereby restricting the ion channels formation; and the selection of a thiol cleavable bulky group would allow its removal at high GSH concentrations. Thus, we introduced a hydroxyl group at the C-2 position of isophthalamide moiety as the group is amenable to its linking to thiol cleavable groups (Figure 4.1A). The 2,4-dinitrobenzene sulfonyl (DNS) group was selected as thiol cleavable group,[19] as its cleavage is known to generate GS-2,4-dinitrobenzene conjugate (SG-DNB) and SO_2 as by-products. Although, low levels of SO_2 may be harmless or even beneficial to cells; exposure to high doses of SO_2 have been known to generate high levels of ROS and thereby induce apoptosis.[20-22] Moreover, ROS production and apoptosis inducing activity of synthetic ion channels is already discussed above. Therefore, the levels of GSH would be affected not only during the release of the ion channel forming molecule, but, would also be reduced significantly due to the ROS generated. Alkyl groups such as n-butyl, n-hexyl, and n-octyl were attached at each end of the 2-hydroxyisophthalamide moiety to design **1a-1c** with different lipophilicity values, so that the resultant ion transport efficiency can be optimized, and a DNS-protected compound **2** was designed as the protransporter (Figure 4.1B). A 2,4-dinitrobenzene (DNB) protected compound **3** was also designed as the DNB group is known to be inert to GSH and only gets activated by the higher content of hydrogen sulfide (Figure 1B).[23] Thus, compound **3** is expected to act as a negative control for all our studies.

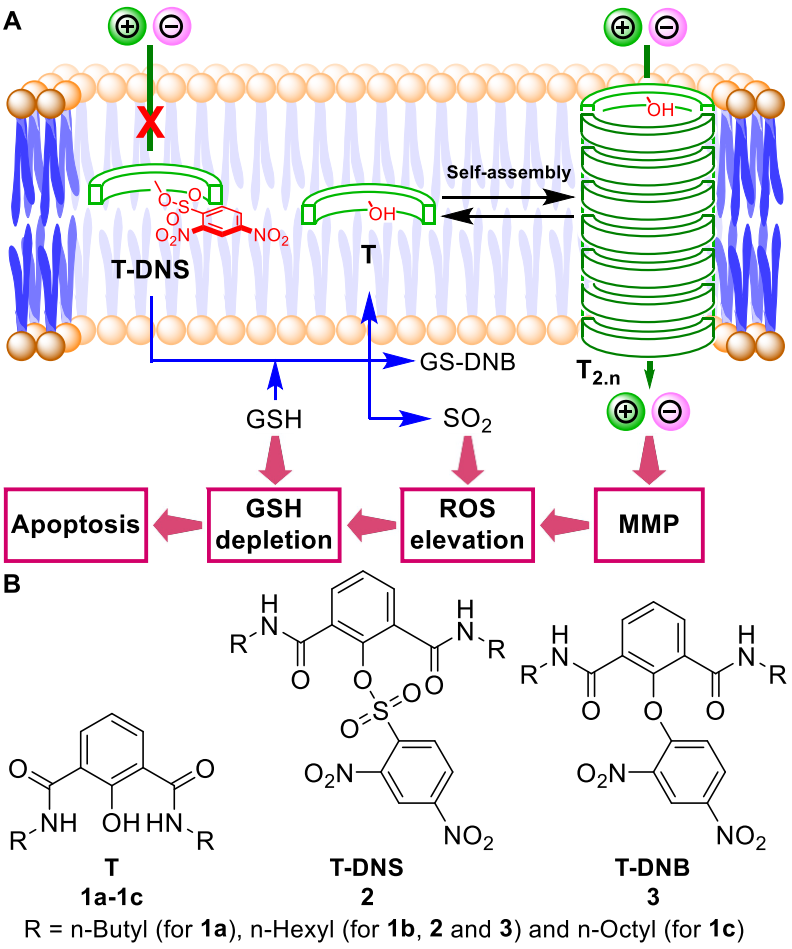

Figure 4.1. Schematic representation of the channel activation inside the cell by intracellular GSH, and the self-assembly of individual monomer **T** into rosette channel $\mathbf{T_{2.n}}$ in cell membrane (**A**). Different processes involved in the depletion of intracellular GSH and induction of apoptosis have been depicted. The structures of the active transporters **1a-1c**, 2,4-dinitrosulfonyl protected protransporter **2,** and 2,4-dinitrophenyl protected protransporter **3** have been shown (**B**). The description of R groups in **1**, **2** and **3** have also been provides below.

4.2. RESULTS AND DISCUSSION:

4.2.1. Synthesis.

The compounds **1a–1c** were synthesized from 2-methoxybenzene-1,3-dicarboxylic acid **6** by converting it to the acid chloride using oxalyl chloride,[24] which was then coupled with the respective amines to get the di-carboxyamides **7a−7c**.[25] These products were then subjected to O-methyl deprotection using 1 M BBr_3 in dichloromethane to get the final compounds **1a−1c**, each containing a free hydroxyl group (Scheme 4.1).[26] The DNS-protected compound **2** and DNB-protected compound **3** were synthesized by reacting compound **1b** with 2,4-dinitrobenzenesulfonyl chloride[19] and 2,4-dinitrochlorobenzene,[23] respectively. All compounds were purified by column chromatography, and the structures were confirmed by ^{1}H NMR, ^{13}C NMR, and HRMS data.

A

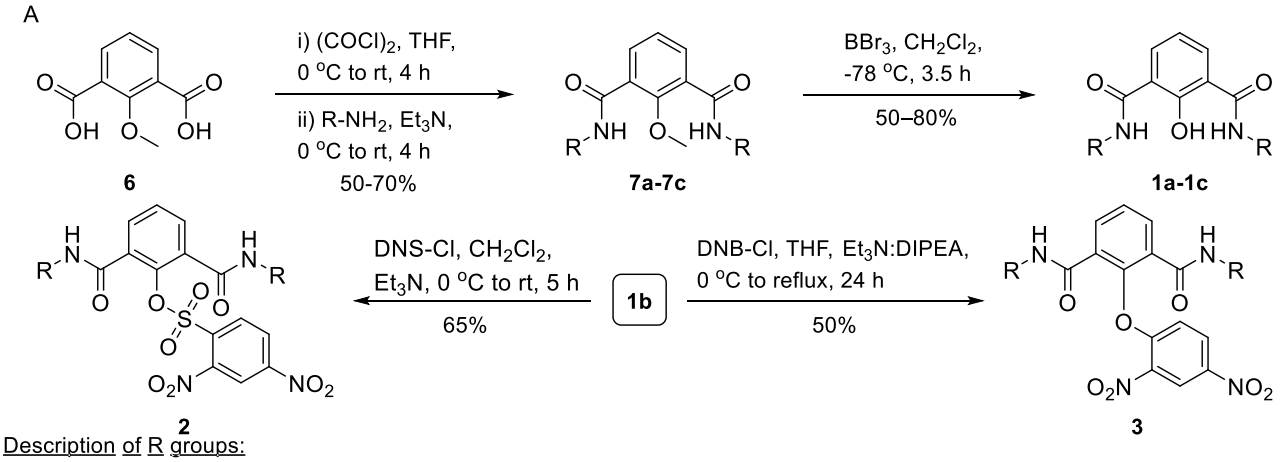

Description of R groups:
R = n-butyl (for **7a** and **1a**), n-hexyl (for **7b**, **1b**, **2** and **3**) and n-octyl (for **7c** and **1c**)

B

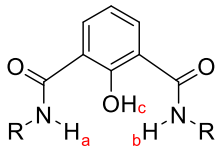

Compound	R	pK_a			log P
		proton a	proton b	proton c	
1a	n-Butyl	16.07	15.02	6.94	3.77
1b	n-Hexyl	16.07	15.02	6.94	5.54
1c	n-Octyl	16.07	15.02	6.94	7.32

Scheme 4.1. General scheme for the synthesis of **1a**–**1c**, **2**, and **3** (A). Table displaying the effect of substitution on the p*K*a values and log P values (B).

4.2.2. Ion Transport Studies.

Ion transport activities of compounds **1a−1c**, **2**, and **3** were evaluated across large unilamellar vesicles consisting of egg yolk phosphatidylcholine (EYPC−LUVs⊃HPTS) by 8-hydroxypyrene-1,3,6-trisulfonate (HPTS) based fluorometric methods.[27] The EYPC vesicles, entrapping the pH-sensitive HPTS dye (pK_a = 7.2), were prepared with internal and external pH = 7.0, and a pH gradient was then applied by addition of NaOH (i.e., ΔpH = 0.8) in the extravesicular buffer.[28] The collapse of the pH gradient upon the addition of **1a−1c**, **2** and **3** was monitored by the change in the dye fluorescence intensity at λ_{em} = 510 nm (λ_{ex} = 450 nm).The comparison of activities provided the activity sequence: **1a** < **1c** < **1b**, inferring that the compound **1b** works as the most efficient ion transporter (Figure 4.2 A). This result corroborates to the logP = 5.54 of the compound (Scheme 4.1 B), which has been reported to be optimum for efficient permeation of the molecules across biological membranes.[29]

The DNS-protected compound **2** and DNB-protected compound **3** were almost inactive at identical concentrations (Figure 4.2 A). The addition of GSH to **2** was associated with an efficient transmembrane ion transport, similar to that observed for **1b**, thereby confirming the thiol-mediated activation of ion transport process (Figure 4.2 A).[30] The addition of GSH to **3**, on the other hand, did not show any significant increase in the ion transport rate (Figure 4.2 A). These results confirmed the importance of SO_2 group in thiol-mediated cleavage of the DNS protecting group (Figure 4.2 B). The dose-dependent activity data of compound **1b** (Figure 4.2

C), upon Hill analysis, provided the effective concentration at 50% activity, EC_{50} = 6.54 μM and Hill coefficient, *n* = 2.2 (Figure 4.2 D, E). The determined Hill coefficient (EC_{50}) value corroborates to the supramolecular dimer **T_2** formed by monomers of **1b** as the active rosette structure for the supramolecular nanochannel assembly.

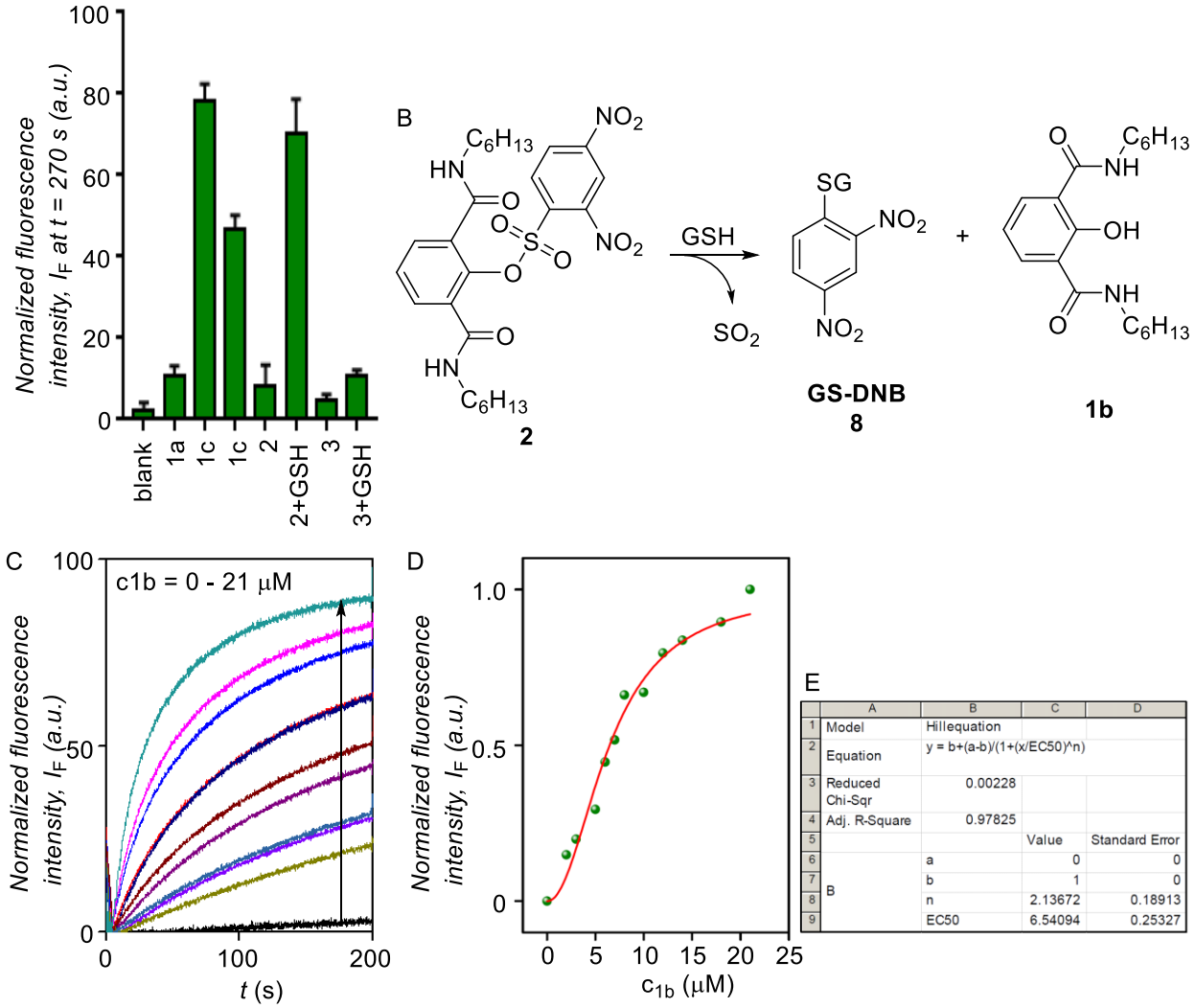

Figure 4.2. Comparative ion transport activities of **1a-1c**, **2** and **3** and GSH activation of **2** and **3** (A) (normalized fluorescence at 170 s after the sample addition); GSH mediated cleavage of the DNS group from **2** to release **1b**, SO_2 and **8** (B); dose-dependent transport activity of **1b** (C). Hill analysis of compound **1b** (D, E).

4.2.3. Ion Selectivity and Mechanism of Ion Transport.

The appreciable ion transport activity observed for compound **1b** led us to investigate the ion selectivity of the compound. Initially, the ion transport activity across EYPC-LUVs⊃HPTS was measured with intravesicular NaCl and an isoosmolar extravesicular M^+/Cl^- salt (where, M^+ = Li^+, Na^+, K^+, Rb^+, and Cs^+) were used to investigate the possible selectivity among the different cations.[31] The data provided the selectivity sequence as $K^+ > Rb^+ > Cs^+ > Na^+ \approx Li^+$ when the

collapse of the applied pH gradient was monitored (Figure 4.3 A). These results indicated the participation of these metal cations in the ion transport process.

To determine the role of anions in the transport process, the anion selectivity study was performed by varying the intravesicular as well as the extravesicular anions of NaX salt (X^- = Cl^-, Br^-, I^-, NO_3^-, and ClO_4^-),[32] and the collapse of rates of the applied pH gradient was compared in the presence of **1b**. The results from this experiment provided the selectivity sequence as $Cl^- > ClO_4^- > Br^- > I^- > NO_3^-$ that confirmed the highest selectivity was present for Cl^- (Figure 4.3 B). These studies suggested the major involvement of alkali metal cations and inorganic anions in the transport process.

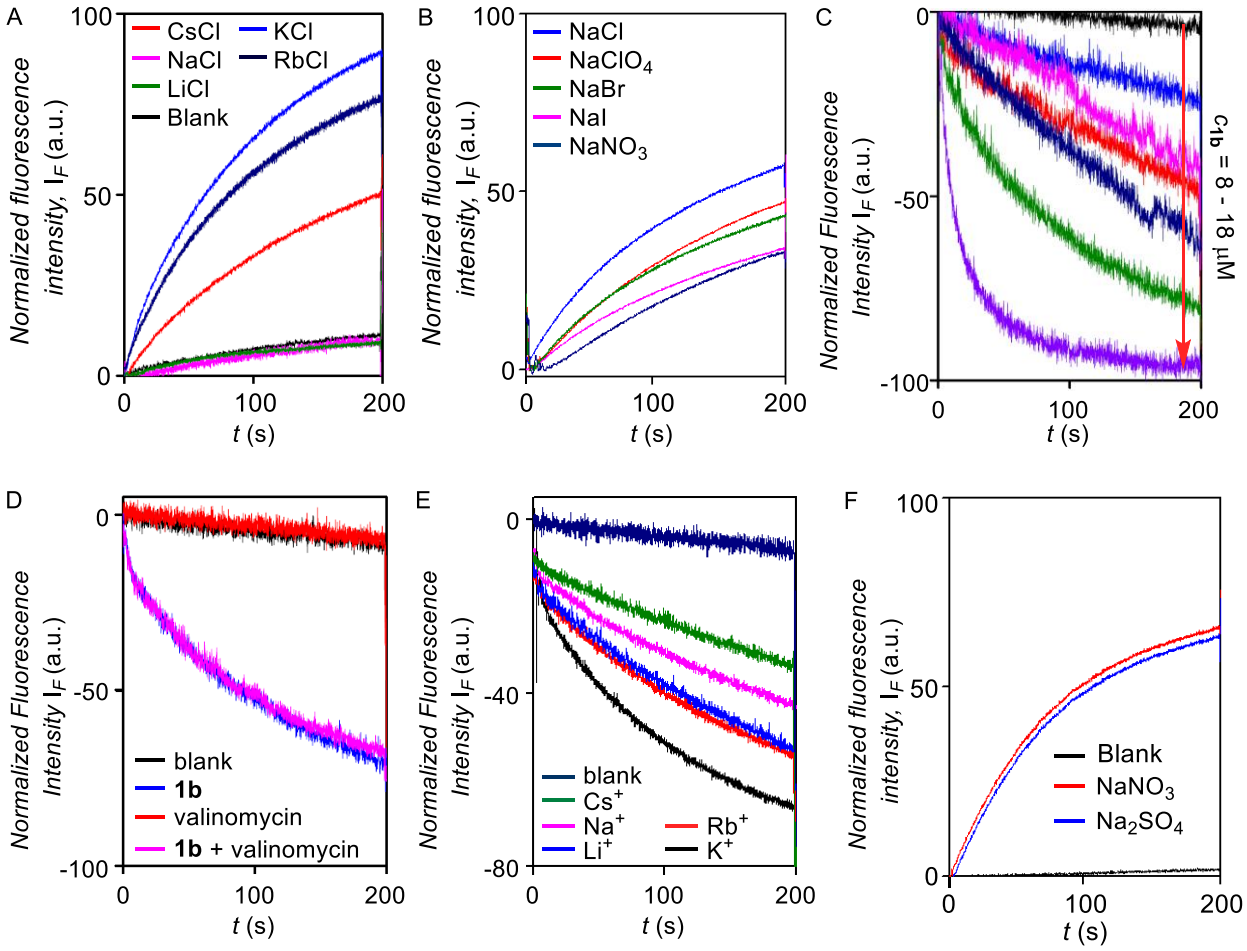

Figure 4.3. Cation selectivity of **1b** (0.3 μM) (A) and anion selectivity of **1b** (7.0 μM) (B). Cl^- ion influx across EYPC-LUVs⊃lucigenin upon addition of **1b** (8-18 μM) (C). Comparison of Cl^- influx across EYPC-LUVs⊃lucigenin for **1b** (10 μM) in presence and absence of valinomycin (0.125 μM) (D). Effect of cations on the Cl^- influx across EYPC-LUVs⊃lucigenin (E). Cl^- efflux across EYPC-LUVs⊃lucigenin by **1b** (12 μM) in the presence of intravesicular Cl^- and either SO_4^{2-} or NO_3^- as isoosmolar extravesicular anion (F).

To further confirm the Cl^- ion transport activity of **1b**, the EYPC-LUVs were prepared by entrapping lucigenin dye (i.e. EYPC-LUVs⊃lucigenin) and $NaNO_3$ salt, and a Cl^-/NO_3^- gradient was applied by adding NaCl (2 M) in the extravesicular buffer. The influx of the Cl^- was measured by monitoring the fluorescence intensity of intravesicular dye at λ_{em} = 535 nm (λ_{ex} = 450 nm).[33] A dose-dependent quenching of lucigenin fluorescence was observed upon addition of the compound **1b**. These data indicated that the supramolecular channel formed by the compound **1b** can allow the influx of Cl^- across liposomes (Figure 4.3 C).

To get further support for the cotransport mechanism, valinomycin (a known K^+ transporter)[34] was coupled with **1b** and the ion transport rate was monitored. KCl was added to the extravesicular buffer to create the Cl^-/NO_3^- gradient. Then valinomycin was added along with **1b** to monitor their cooperative effect.[6] The ion transport rate in the absence and presence were comparable (Figure 4.3 D) that suggests the lack of cooperative transport by valinomycin and **1b**. In addition to this, the effect of different cations on the chloride efflux was also checked by varying the external cations,[35] which also supported KCl cotransport mechanism (Figure 4.3 E). To reassure that the M^+/Cl^- symport mechanism is operating in the transport process, the EYPC liposomes, entrapping NaCl (200 mM) and 1.0 mM of lucigenin dye, were prepared. Then, the isoosmolar Na_2SO_4 was added to the extravesicular solution and Cl^- efflux was monitored with time. A similar experiment was also performed with extravesicular isoosmolar $NaNO_3$. The results indicate that there is no difference in the transport rate of two ions by **1b** (Figure 4.3 F), suggesting that the symport mechanism of ion transport is operative.

4.2.4. Planar Bilayer Conductance Studies.

The formation of the transmembrane ion channel by the compound **1b** was proved by planar bilayer conductance measurements, where the ionic conductance across the planar lipid bilayer membrane was measured.[36] As already discussed in previous chapters, planar lipid bilayer membrane composed of diphytanoyl phosphatidylcholine (diPhyPC) lipid was used to insulate the two chambers (*cis* and *trans* chambers) containing KCl solution (1.0 M). The addition of **1b** (10.0 μM) to the system showed up distinct channel openings and closing at different holding potentials, confirming the formation of ion channel (Figure 4.4 A, B). The single-channel conductance was found to be 160 ± 2 pS, and channel diameter was calculated to be 6.6 ± 0.16 Å. The variation of current with voltage (*I-V* plot) in the presence of the symmetric solution of KCl (1.0 M each) showed a linear variation, i.e., ohmic behavior (Figure 4.4 C), which is expected for the non-dipolar nature of the channel. When the ion selectivity of the channel was checked using unsymmetric solutions of KCl in two compartments (i.e., 0.5 M in *trans* and 1.0 M KCl in *cis*), it was observed that the rate of Cl^- transport is slightly higher than the rate of K^+ transport with a permeability ratio P_{Cl^-}/P_{K^+} = 50 ± 1 (Figure 4.4 C).

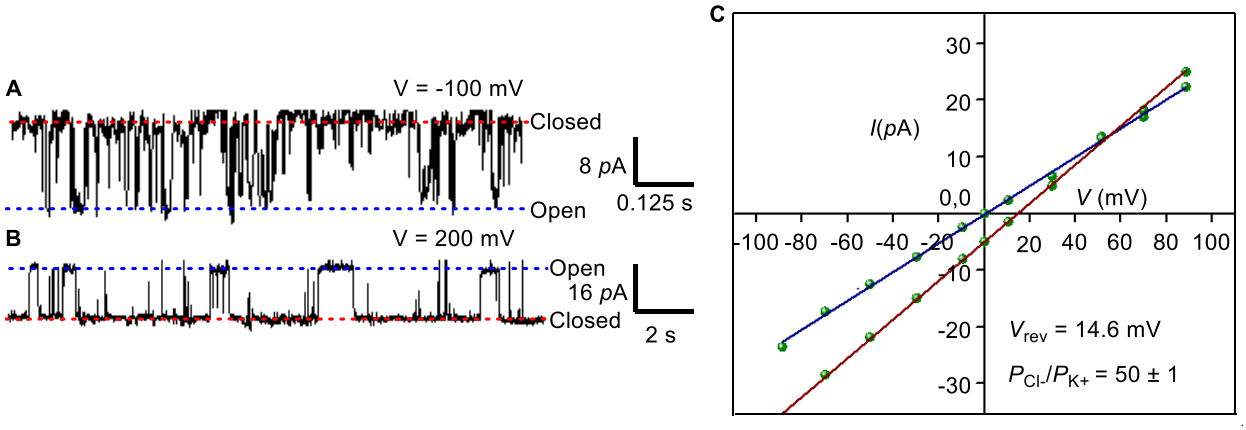

Figure 4.4 Single-channel conductance of **1b** (10.0 μM) recorded at -100 mV (**A**) and at 100 mV (**B**) under symmetrical KCl solutions. *I-V* plots of **1b** under symmetrical and unsymmetrical concentrations of KCl (**C**).

4.2.5. Molecular Modeling of the Channel.

From the literature reports it is evidenced that in 2-hydroxy-N^1,N^3-dialkylylisophthalamide the phenolic oxygen forms hydrogen bond with one of the amide hydrogens (C–O···H–N) and phenolic hydrogen forms hydrogen bond with one of the amide oxygens (C=O···H–O) thereby preferring the **Conf-1** (Figure 4.5 A).[37,38] Hence, this conformation of **1b** was considered for generating the ion channel model. At first, two molecules of **1b** in the **Conf-1** were placed face-to-face to form a dimeric rosette and then seven units of such rosettes were placed in a coaxial manner to generate the channel. Subsequently, the channel was optimized using MOPAC2012[39] software with the PM6-DH+[40] method. In the optimized supramolecular nanotubular assembly, intramolecular C–O···H–N and C=O···H–O interactions were still evident (Figure 4.5 B). Moreover, the intermolecular C–O···H–N interactions and π-π stacking interactions among aromatic rings were observed, giving stability to the assembly. In the geometry-optimized channel, eleven water molecules were placed in the lumen, along with one K^+ ion above and one Cl^- ion below sixth water molecule. The whole system was then optimized using the above stated method. In the optimized structure (Figure 4.5 C, D), the water molecules formed a continuous array through intermolecular H–O···H–O interactions. In the channel lumen, the K^+ ion showed electrostatic interaction with the Cl^- ion and dipole-cation interaction with the carbonyl oxygen (Figure 4.5 E). The anion was further involved in O–H···Cl^- interactions with two neighboring water molecules.

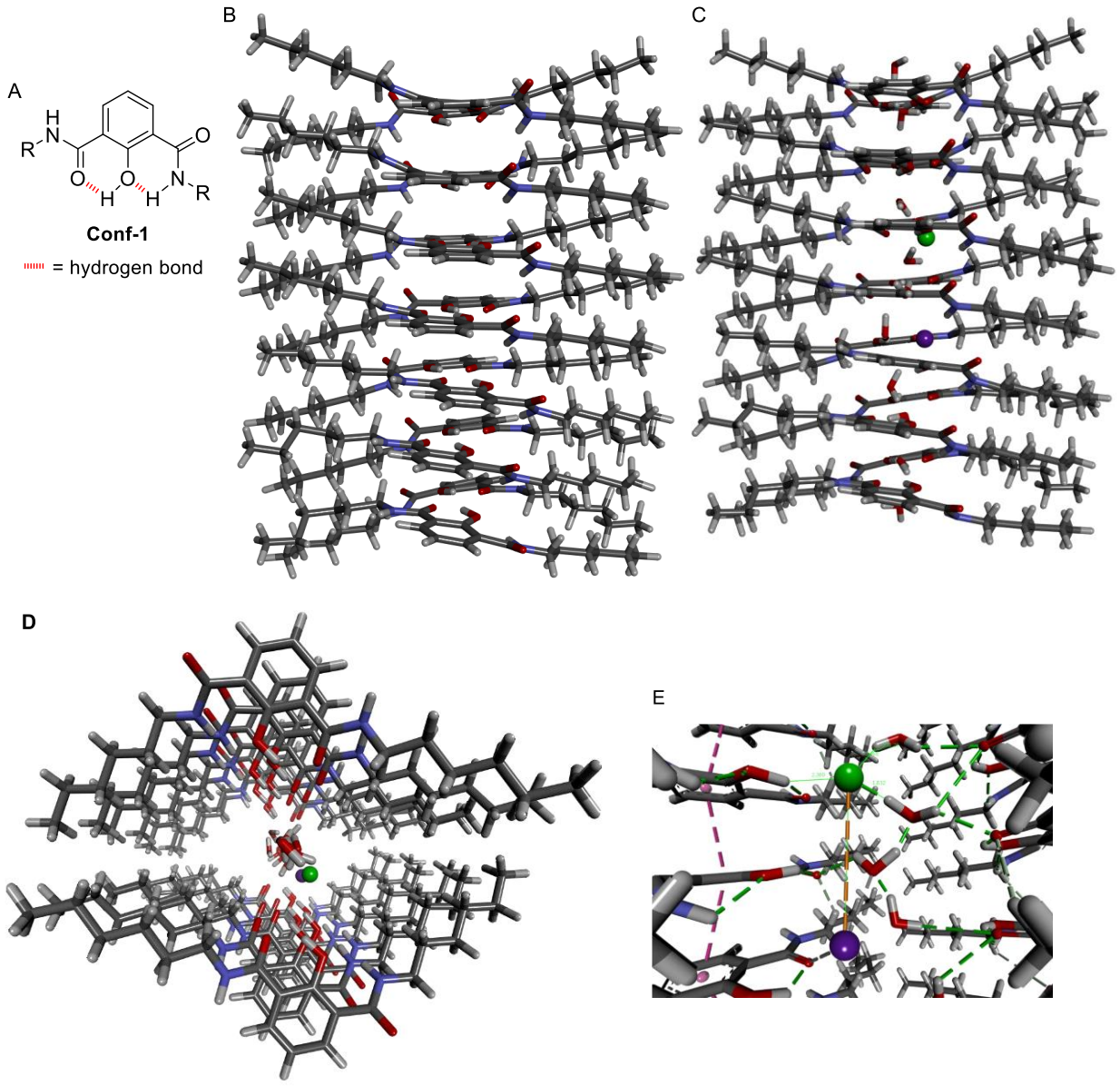

Figure 4.5. Intramolecular hydrogen bonded **Conf-1** of the molecule **1b** (A). Side view of the geometry optimized channel formed by **1b** (B). Side view (C) and top view (D) of the geometry optimized channel formed by **1b** filled with eleven water molecules, one K^+ and one Cl^-. Close view of the geometry optimized channel formed by **1b** with eleven water molecules, one K^+ and one Cl^- in showing the different ion binding interactions (E).

4.2.6. UV-Visible Absorption and Fluorescence Emission Studies.

The UV-visible spectrum of **1b** (10.0 μM) was recorded in Dulbecco's Phosphate-Buffered Saline (DPBS) buffer (pH 7.2), which showed an absorption band at 300 − 375 nm with the λ_{max} at 330 nm (Figure 4.6 A). When the compounds **1b**, **2** and **3** (10.0 μM each) were excited with 330 nm light, an intense fluorescence emission band centered at 410 nm was observed for **1b**, whereas **2** and **3** were nonfluorescent due to quenching of fluorescence by DNS[41] and DNB

groups[23] (Figure 4.6 B). Further, the release of compound **1b** from **2** (10.0 µM) was monitored in the presence of GSH (5 molar equivalents) by measuring the fluorescence intensity at λ = 410 nm (λ_{ex} = 330 nm) with time. The increase in fluorescence upon addition of the thiol undoubtedly demonstrated the release of **1b** (Figure 4.6 C). Similar study with **3** did not show any time-dependent increase of fluorescence.[42]

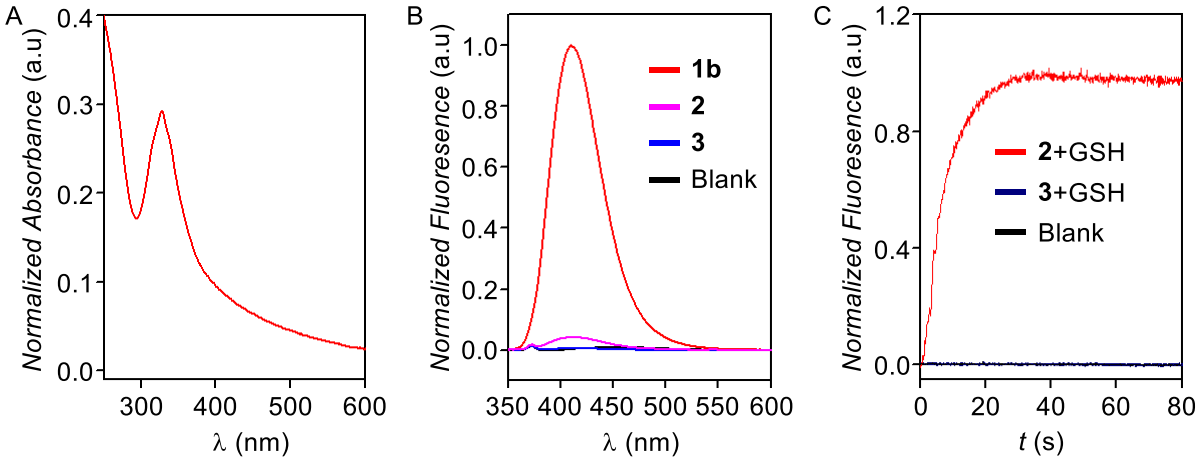

Figure 4.6. UV-Visible absorbance of 1b (A); and normalized fluorescence emission spectra of 1b, 2 and 3 in buffer (B), and fluorescence recovery of 2 and 3 in the presence of GSH (C).

4.2.7. Biological Studies.

Cell viability studies: The cell viability of MCF 7 cells was checked in presence of the compounds **1b**, **2** and **3**. The viability of MCF-7 cells was monitored using the MTT assay after incubating these cells with **1b**, **2** and **3** (0 – 100 µM each) for 24 hours. The addition of compound **2** was found to be associated with highest cytotoxicity, with IC_{50} value around 0.5 – 1.0 µM (Figure 4.7 A; blue) as compared compound **3** (red). On the other hand, the IC_{50} obtained for compound **1b** was ~ 50 µM and was found to be relatively less toxic when compared to compound **2** (Figure 4.7 A, green). The higher permeation of propidium iodide, a dye known to easily cross the compromised cell membranes to bind with nuclear constituents,[43] was observed in MCF-7 cells treated with compound **2** (1.0 µM) for 24 h (Figure 4.7 B, C), thereby, confirming that the compound **2** has induced the cell death to the treated cells.

Next, to rationalize the differences in the cytotoxicity, live cell imaging of MCF-7 cells was performed to study the membrane permeability and cytoplasmic abundance of the compounds under study. The MCF-7 cells were incubated with the compounds for 30 minutes and observed under a confocal microscope (Leica Sp8). Interestingly, a marked enhancement in blue fluorescence was observed in MCF-7 cells treated cells treated with **2** (Figure 4.7 F) when compared to **1b** (Figure 4.6 E) or the untreated/control cells (Figure 4.7 D). Based on these observations, we propose that the proactive channel molecule **2** is more permeable compared to

active channel **1b**.[6] These results are supported by the fact that compound **2** contain a sulfonyl group – known to have better membrane permeability. These results can be rationalized based on the reactivity of **2** with GSH. Since MCF-7 cells have elevated GSH[44,45] content, the DNS group upon entering the cells reacts with GSH; hence, compound **2** gets cleaved to subsequently release **1b** (measured by blue fluorescence intensity quantitation as depicted in Figure 4.7), thereby leading to increased cytotoxicity. On the other hand, the DNB group responds poorly to GSH;[23] hence, its cleavage is poor and therefore, causing less cell death.

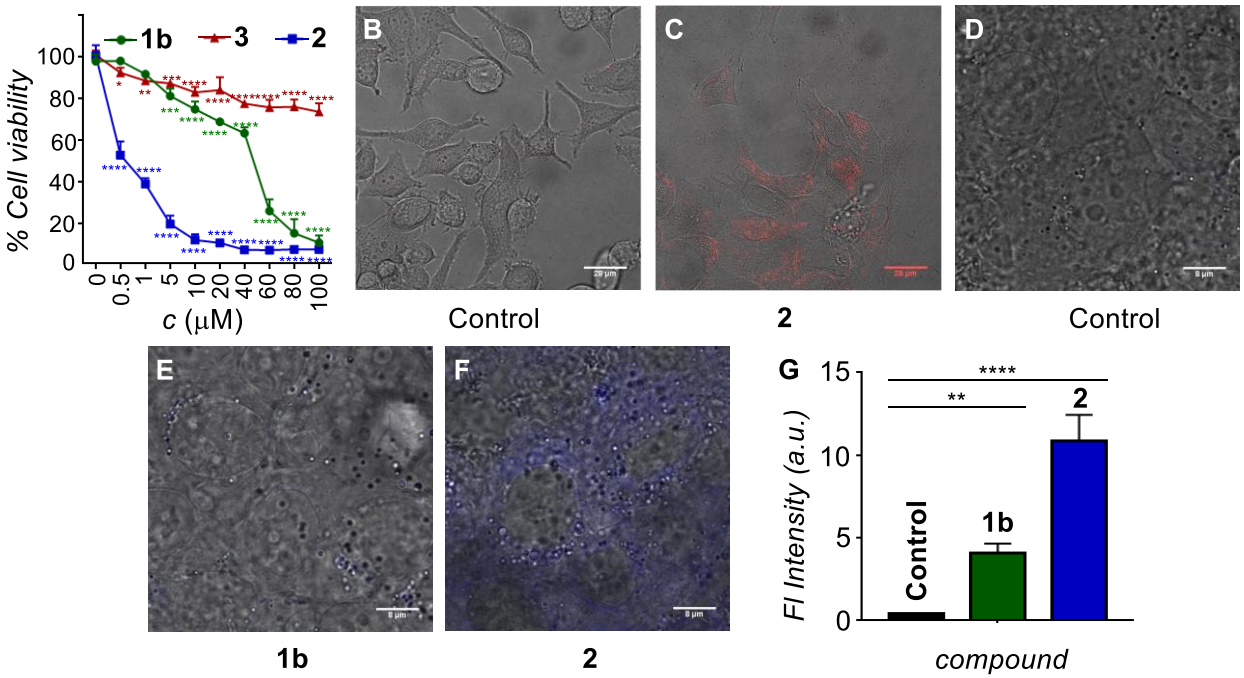

Figure 4.7. Dose-dependent cell viability of MCF-7 cells incubated with **1b**, **2** and **3** (0 – 100 μM each) for 24 hours (A); live cell images of MCF-7 cells upon treating with 0 μM (B) and 1.0 μM of compound **2** (C) for 15 minutes followed by staining with propidium iodide; live cell imaging of control (D), **1b** (5 μM, E) and **2** (5 μM, F) in MCF-7 cell line after 30 minutes of incubation; quantification of fluorescence inside the cells (G). * represents $p < 0.05$, **, $p < 0.01$ and *** for $p < 0.001$ using Tukey HSD tests.

As shown in figure 4.2 B, the observed cytotoxicity for compound **2** can also be due to the bye-products SO_2 and **8**. In order to exclude this, the cytotoxicity of MCF-7 cells was evaluated in the presence of compound **9** (Figure 4.8 A), which upon reaction with thiol, releases benzylamine, **8** and SO_2;[46] and compound **10** (Figure 4.8 B), which in the presence of intracellular esterases, is known to release SO_2 and other non-toxic bi-products.[47] Both compounds **9** (green) and **10** (blue) showed significantly lesser cytotoxity when compared to **2** (purple) at identical concentrations, thereby, indicating that the observed cytotoxicity is mainly associated with compound **1b** formed from **2** (Figure 4.8 C)

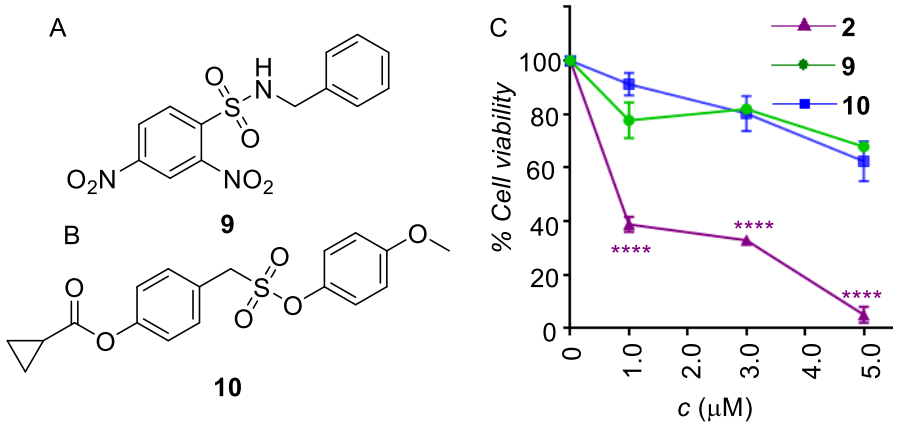

Figure 4.8. Chemical structure of compounds **9** (A) and **10** (B). Dose-dependent cell viability of MCF-7 cells incubated with **2**, **9** and **10** (0 – 5.0 μM each) for 24 hours (C). * represents $p < 0.05$, **, $p < 0.01$ and *** for $p < 0.001$ using Tukey HSD tests.

To further investigate the importance of intracellular GSH in activating compound **1b**, viability assays were performed in the rat insulinoma cells – *INS-1E*. A recent study has shown that the GSH-content in these cells can be modulated by varying the glucose concentration in the media without significantly affecting the cellular viability.[48] The cytotoxicity mediated by compound **2** (0 – 20.0 μM) was significantly higher in *INS-1E* cells cultured in low glucose media (i.e., high GSH levels) when compared to those in high glucose media (i.e., low GSH levels) (Figure 4.9 A, B). As we had hypothesized, compound **3** (0 – 20.0 μM) did not induce considerable cytotoxicity in both low and high GSH containing cells, thereby proving that the release of **1b** does not take place from **3**.

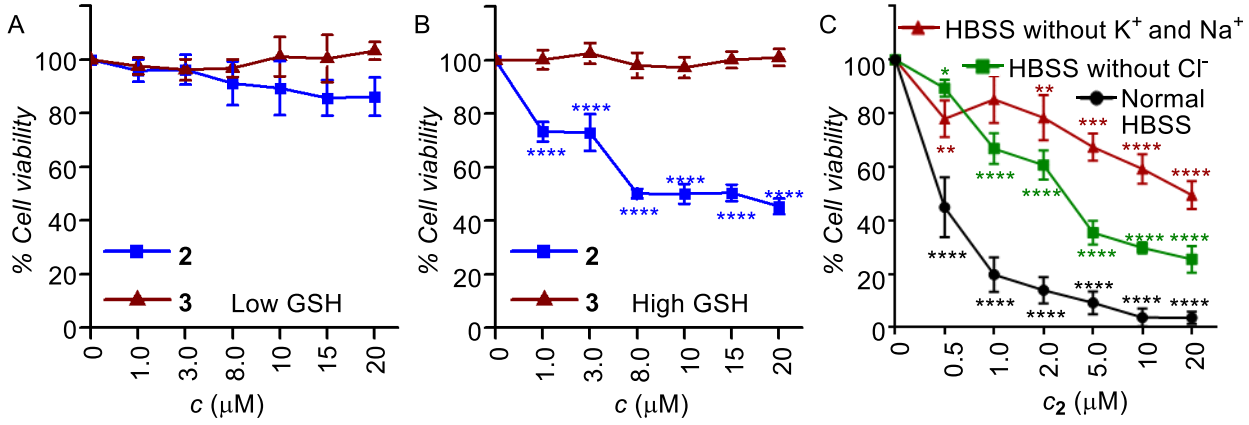

Figure 4.9 Dose-dependent cell viability of *INS-1E* cells in incubated with **2** and **3** (0 – 20.0 μM each) for 24 hours under low (A) and high GSH (B) concentrations. Cell viability of MCF-7 cells in presence and absence of Na^+ and K^+ and Cl^- ions incubated with **2** at different concentrations (**K**). * represents $p < 0.05$, **, $p < 0.01$ and *** for $p < 0.001$ using Tukey HSD tests.

As discussed in previous chapter, reports from our lab[49,50] and others[51,52] have shown that the perturbation of Cl^- ion homeostasis by means of synthetic channels and carriers mediate apoptosis in cells. Therefore, to gain insight about Cl^- mediated cytotoxicity, viability in MCF-7 cells was performed with compound **2** (0 – 20.0 μM) in the presence of HBSS (Hanks balanced salt solution) buffer with and without Cl^- ions.[53] Interestingly, cells cultured in HBSS with Cl^- showed enhanced cytotoxicity (Figure 4.9 C; Black) compared to HBSS without Cl^- (Figure 4.9 C; Green) thereby demonstrating that cell death is mediated via Cl^- transport. In addition to Cl^-, the import of cations such as K^+ and Na^+ also triggers the apoptosis process. We have already shown above that the compound **1b** is a symporter of M^+/Cl^- across the lipid bilayer. Therefore, the effect of M^+ ions (K^+ and Na^+) on cellular viability was assessed.The MCF-7 cells were incubated with compound **2** (0 – 20.0 μM) in HBSS buffer with and without M^+ ions. A higher cytotoxicity was observed with compound **2** in presence of K^+ and Na^+ ions (Figure 4.9 C, brown), thereby confirming the K^+ and Na^+ ions also play a role in mediating cytotoxicity.

Chloride channel formation triggers apoptosis in cancer cells: Mitochondrial apoptosis generally involves the disruption of mitochondrial membrane potential (MMP),[54,55] which subsequently results in the release of cytochrome c from the mitochondrial membrane into the cytoplasm – one of the switches that trigger apoptosis.[56,57] The change in MMP was investigated using MMP sensitive JC-1 dye,[58] which shows red fluorescence emission due to the formation of J-aggregates in the healthy mitochondrial membranes. However, the depolarization of MMP leads to dispersion of the formed aggregates, resulting in green fluorescence emission.[59] Interestingly, MCF-7 cells treated with compound **2** (1.0 μM) for 24 hours showed a significant decrease in the red fluorescence and a simultaneous enhancement in the green emission (Figure 4.10 B) when compared to the control cells (Figure 4.10 A). The quantification of the red/green ratio (Figure 4.10 C for **2** and D for **1b**) in treated cells compared to the control confirmed the enhancement in the MMP depolarization.[49,55]

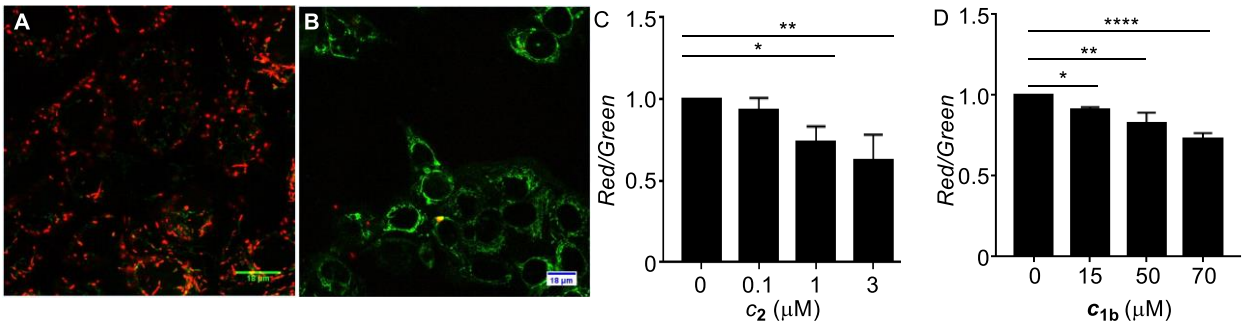

Figure 4.10. Live cell images of MCF-7 cells upon treating with 0 μM (**A**) and 1.0 μM (B) of compound **2** for 24 h followed by staining with JC-1 dye, red and green channel images were merged to generate the given image (Scale bar = 18 μm). Quantification of change in the red/green ratio with concentration of **2** in MCF-7 cells incubated with **2** (C) * represents $p < 0.05$, **, $p < 0.01$ and *** for $p < 0.001$ using Tukey HSD tests.

This was associated with increased generation of both mitochondrial (Figure 4.11 B for **2** and 4.11 C for **1b** , green) and cellular ROS (Figure 4.11 A, B for **2** and 4.11C for **1b**, brown) as detected by the mitosox[48] and 2',7'-dichlorodihydrofluorescein diacetate (H_2DCFDA)[55,60] dyes, respectively.

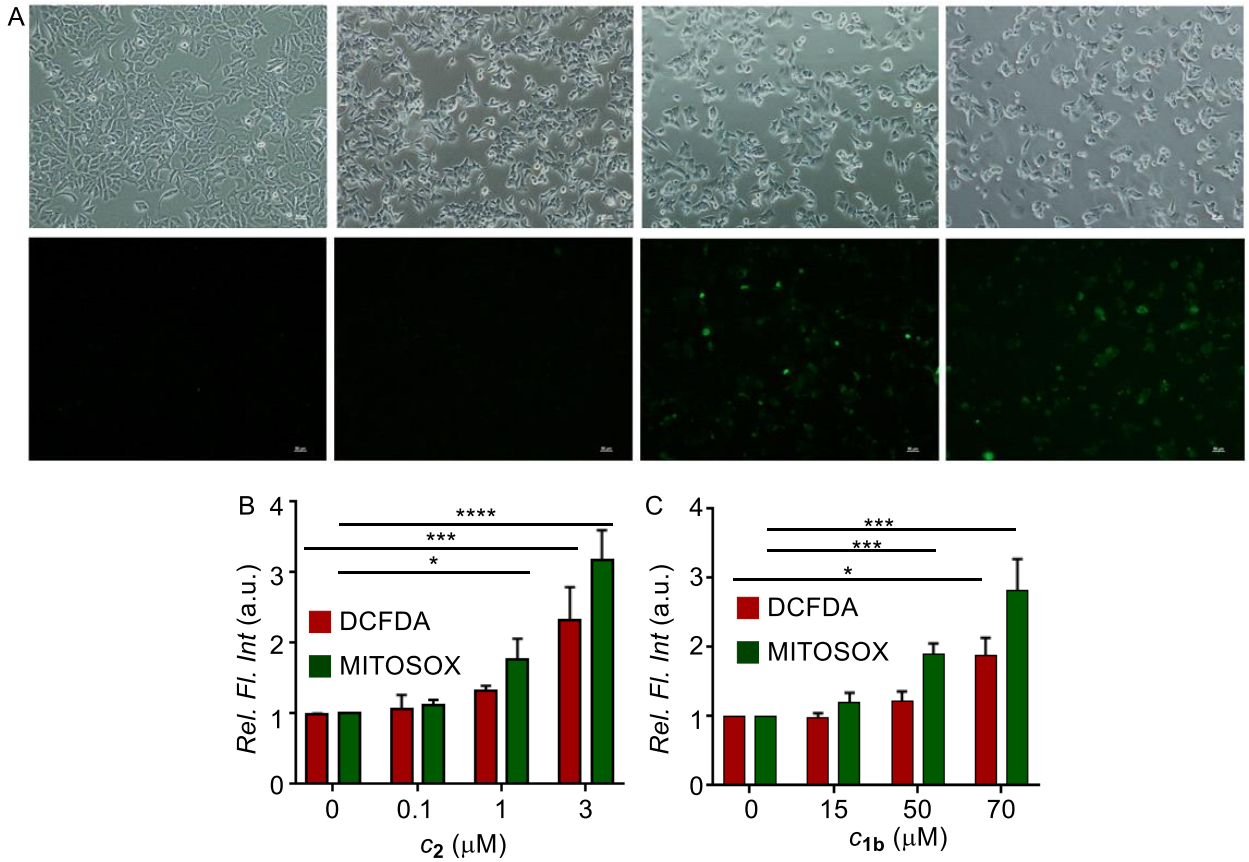

Figure 4.11. Live cell images of MCF-7 cells incubated with compound **2** and DCFDA as ROS probe (scale bar 50 μm) in a time dependent manner (A).Quantification of dose-dependent mitochondrial and cellular ROS generation in MCF-7 cells incubated with **2** and **1b** by mitosox dye and H_2DCFDA dye (B, C). * represents $p < 0.05$, **, $p < 0.01$ and *** for $p < 0.001$ using Tukey HSD tests.

It is well-documented in the literature that abnormally high ROS levels lead to the increased apoptosis in cancer cells by reducing the GSH levels.[61] We had hypothesized that compound **2** works as a double-edged sword to reduce the intracellular GSH levels by (i) getting activated into **1b** by reacting with GSH (Figure 2 B), and (ii) increasing the ROS levels as a consequence of perturbation in ion homeostasis. Indeed, the GSH levels (as measure by ^{1}H NMR) in MCF-7 cells treated with compound **2** (green) were significantly reduced when compared with the control cells (Figure 4.12 A; red), thereby proving our hypothesis.

The enhancement in levels of ROS is well known to open up the mitochondrial permeability transition pores (PTP),[62,63] which releases the cytochrome c from the mitochondrial membrane into the cytosol.[64,65] Indeed, MCF-7 cells incubated with 1.0 μM (Figure 4.12 C) of compound **2**

showed significantly enhanced fluorescence intensity depicting the release of cytochrome c release into the cytoplasm when compared to the control cells (Figure 4.12 B).

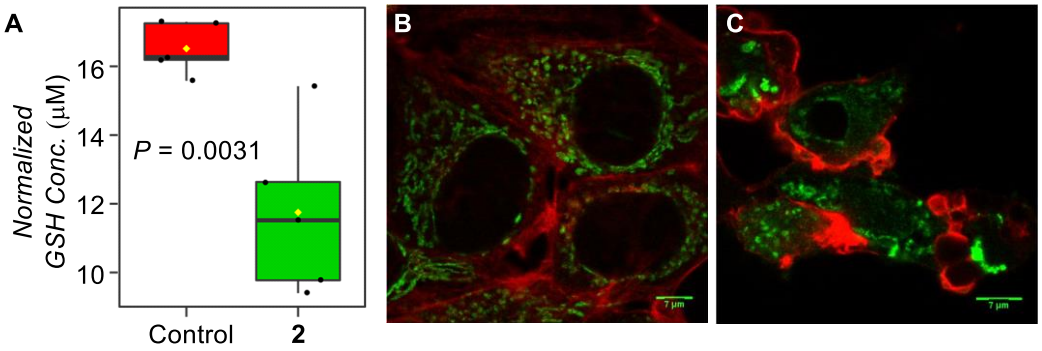

Figure 4.12 Quantification of glutathione levels in untreated MCF cells and those treated with Compound **2** (1 μM) by ^{1}H NMR (A); Release of Cytochrome c from MCF-7 cells upon treating with 0 μM (B) and 1.0 μM (C) of compound **2**. Immunostaining was performed with cytochrome c specific primary antibody (green). Phalloidin (red) co-staining was used to mark the boundaries.

AS is already reported that the released cytochrome c binds to the Apaf-1 to form the cytochrome c/Apaf-1 apoptosome complex and switches on the apoptotic pathway by caspase 9 activation;[59,60] the immunoblot analysis was performed to evaluate the expression of caspase 9 in MCF-7 cells incubated with compound **2** (1.0 μM) which showed a statistically significant increase in the expression of cleaved caspase 9 when compared to the control cells (Figure 4.13 B). As a prominent evidence of the apoptotic pathway, the expression level of cleaved poly (ADP-ribose) polymerase (PARP) was also monitored using immunoblot analysis. PARP cleavage by endogenous caspases is a very well-known phenomenon.[65-67] PARP-1 cleavage avoids DNA repair to facilitate apoptosis. The cleavage of full-length PARP-1 (116 kDa) to generate cleaved PARP-1 (86 kDa) was observed upon incubation of MCF-7 cells with **2** (1.0 μM) (Figure 4.13 A, B). These data clearly indicate that the mitochondrial/intrinsic apoptotis pathway is getting activated in MCF-7 cells upon treated with compound **2**.

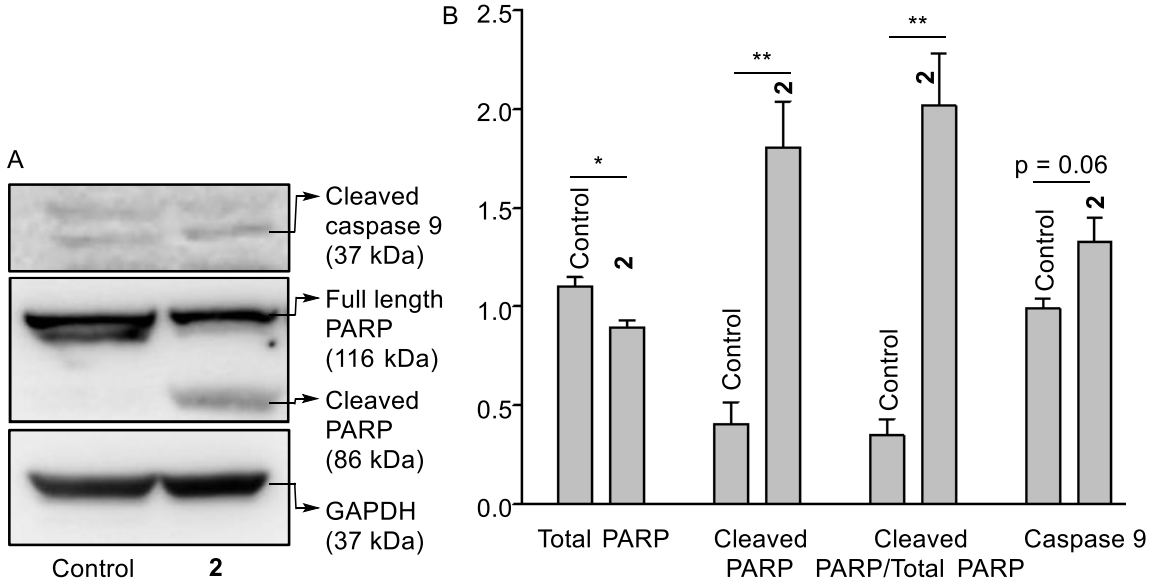

Figure 4.13. Immunostaining was performed with cytochrome c specific primary antibody (green). Phalloidin (red) co-staining was used to mark the boundaries; Expression of cleaved caspase 9, full length and cleaved PARP-1 in MCF-7 cells, after 24 h incubation with **2** (0 and 1.0 μM) (H) as determined by immunoblot analysis. * represents $p < 0.05$, **, $p < 0.01$ and *** for $p < 0.001$ using Tukey HSD tests.

Effect of compound 2 on the growth and proliferation of 3D spheroids: It is already reported in literature that Doxorubicin (DOX) works as a potent inhibitor of MCF-7 cells when grown in 2D and 3D culture models.[68] It has been demonstrated that DOX at concentrations between 0.8-1.0 μM significantly affects the proliferation of the cells. After gaining insights into the mechanism of action of compound **2** in 2D cultures, we further tested if it could inhibit 3D cultures of MCF-7 cells. A seven-day protocol was developed wherein the drugs (DOX or compound **2**) were administered to the developing 3D cultures on days 4, 5 and 6 (Figure 4.14 A). Immunofluorescence staining done using Phalloidin and Hoechst 33258 clearly indicates that the compound **2** (Figure 4.14 B) significantly reduces the surface area (Figure 4.14 C), surface volume (Figure 4.14 E) and the number of cells per spheroid (Figure 4.14 D) when compared to the control. Interestingly the results were similar to those obtained using DOX, thereby indicating the potential of compound **2** to inhibit tumor growth *in vivo*.

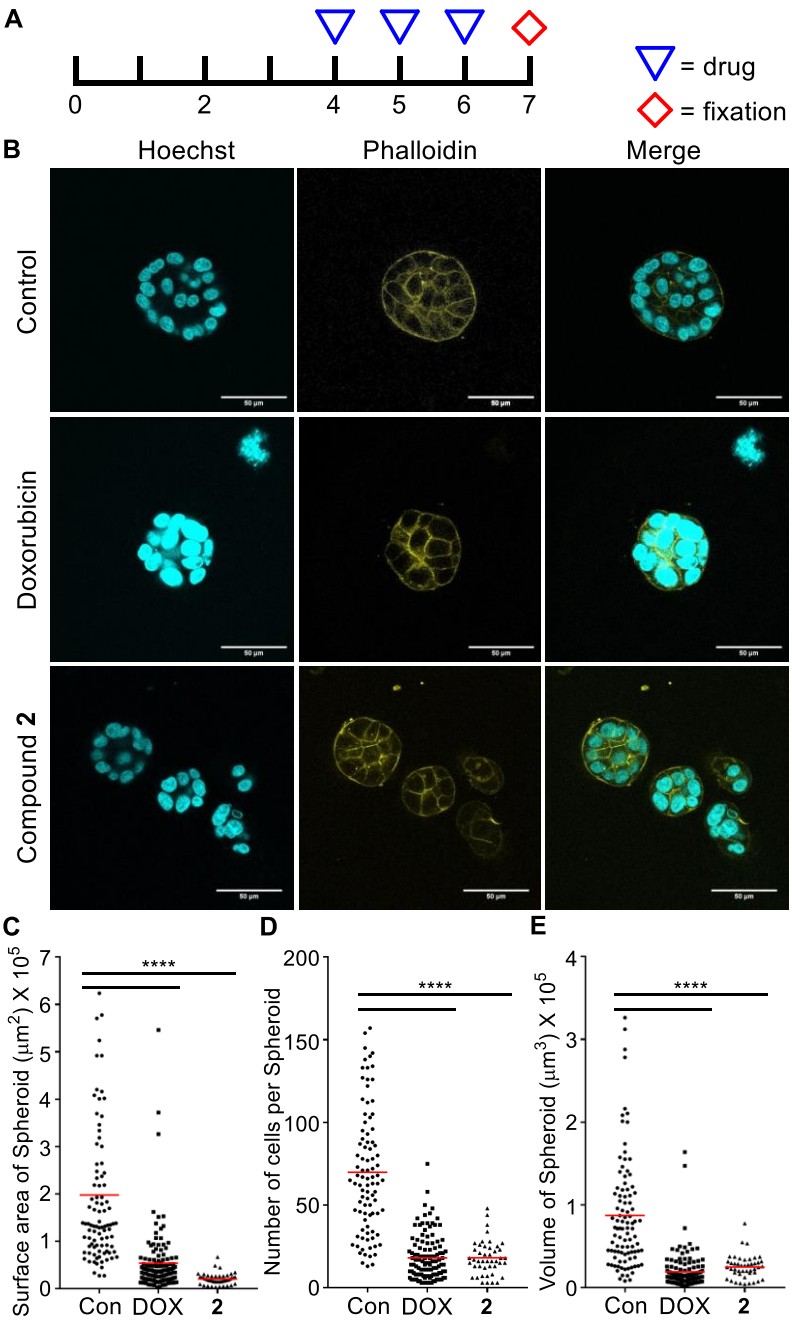

Figure 4.14. Representation of the protocol for induction of 3D cultures in MCF-7 cells. The drug intervention was done on days 4, 5, and 6, using compound **2** (2 µM) and doxorubicin (positive control, 0.8 µM). DMSO was used in control wells (A). Immunofluorescence for 3D cultures using Phalloidin (stains actin filaments) and Hoechst 33258 (B). Quantitation of surface area (μm^2) (C); number of cells per spheroid (D); and spheroid volume (μm^3) (E) under different experimental conditions were performed using Image J software. Con = control and DOX = doxorubicin. * Represents $p < 0.05$, **, $p < 0.01$ and **** for $p < 0.001$ using Tukey HSD tests.

4.3. CONCLUSION:

In summary, we have developed a novel glutathione-activatable synthetic ion channel system that induces the caspase-dependent apoptosis in MCF-7 cells. The intracellular glutathione releases the channel-forming N^1,N^3-dialkyl-2-hydroxyisophthalamide system (**1b**) from its 2,4-nitrobenzenesulfonyl (DNS) protected protransporter **2**, which forms transmembrane ion channels capable of conducting M^+/Cl^-symport across biological membranes. This symport is associated with increased ROS levels which in turn reduced intracellular GSH levels; altered mitochondrial membrane permeability (MMP); mediated cytochrome c release associated with activation of caspase 9 and PARP cleavage – the major inducers of apoptosis. These results were further confirmed using a 3D model of MCF-7 cells wherein the addition of compound **2** was able to restrict growth and proliferation of the spheroids, similar to those reported for DOX – a standard drug used for breast cancer treatment. These studies will provide attractive approaches to explore the application of synthetic ion transport systems for therapeutic approaches.

4.4. EXPERIMENTAL SECTION:

4.4.1.General Methods.

All reactions were carried out under the nitrogen atmosphere. All the chemicals were purchased from commercial sources and were used as received unless stated otherwise. Solvents were dried by standard methods prior to use or purchased as dry. Thin layer chromatography (TLC) was carried out with E. Merck silica gel 60-F_{254} plates and column chromatography was performed over silica gel (100-200 mesh) obtained from commercial suppliers. Egg yolk phosphatidylcholine (EYPC) lipid was purchased from Avanti Polar Lipids as a solution dissolved in chloroform (25 mg/mL). HEPES buffer, HPTS dye, Triton X-100, NaOH and all inorganic salts of molecular biology grade were purchased from Sigma. Size exclusion chromatography was performed on a column of SephadexG-50. Large unilamellar vesicles (LUV) were prepared from EYPC lipid by using mini extruder, equipped with a polycarbonate membrane either of 100 nm or 200 nm pore size, obtained from Avanti Polar Lipids. The JC1 dye was the generous gift from Dr. Shilpy Sharma at Savitribai Phule Pune University. The H_2DCFDA was purchased from Sigma Aldrich.

4.4.2. Physical measurements.

The ^{1}H and ^{13}C NMR spectra were recorded on 400 MHz Jeol ECS-400 (or 100 MHz for ^{13}C) spectrometers using either residual solvent signals as an internal reference or from internal tetramethylsilane on the δ scale relative to chloroform (δ 7.26), dimethylsulphoxide (δ 2.50 ppm), acetone (δ 2.05) for ^{1}H NMR and chloroform (δ 77.20 ppm), dimethylsulphoxide (δ 39.50 ppm), acetone (δ 29.84 and 206.26) for ^{13}C NMR. The chemical shifts (δ) are reported in ppm and coupling constants (J) in Hz. The following abbreviations are used: s (singlet), d (doublet) m

(multiplet), and td (triplet of doublet) while describing ^{1}H NMR signals. High-resolution mass spectra (HRMS) were obtained from MicroMass ESI-TOF MS spectrometer. All the FT-IR spectra were taken and reported in wave numbers (cm^{-1}) using a solution of compound in 30% MeOH/$CHCl_3$. Fluorescence spectra were recorded by using Fluoromax-4 from Jobin Yvon Edison equipped with an injector port and a magnetic stirrer. 10 mM HEPES (with 100 mM NaCl or other salts as per necessity) buffer solutions were used for fluorescence experiment and the pH of the buffers were adjusted to 7.0 or 8.0 by NaOH and pH of the buffer solutions was measured using Helmer pH meter. Melting points of all the compounds were measured using a VEEGO Melting point apparatus. All melting points were measured in open glass capillary and values are uncorrected. All fluorescence data were processed either by Origin 8.5 or KaleidaGraph and finally, all data were processed through ChemDraw Professional 15. The conductance measurements were carried out in planar bilayer membrane (BLM) workstation obtained from the Warner Instruments consisting of a head stage and its corresponding amplifier BC-535, 8 pole Bessel filter LPF-8, Axon CNS Digidata 1440A and pClamp 10 software.The conductance data was analyzed by clampfit 10 software. MTT assay was recorded in a microplate reader (Varioskan Flash). Western blot was visualized in ImageQuant LAS 4000 (GE Healthcare). Cell images were taken using Leica sp8 confocal microscope and Nikon Eclipse TS 100 fluorescence microscope. The cell images were processed by image j software. The Grapgpad Prism 7 was used for plotting the data from biological assays.

4.4.3. Synthesis.

General method for synthesis of 1a – 1c: The compounds **1a–1c** were synthesized from 2-methoxybenzene-1,3-dicarboxylic acid **6**, which was prepared following reported protocols.[69,70] The compound **6** (200 mg, 1.0 m mol.) was taken in 25 mL round bottom flask and 5 mL of dry tetrahydrofuran (THF) was added, followed by addition of catalytic amount (3-4 drops) of dry dimethylformamide (DMF). This reaction mixture was cooled to 0 ^{o}C and then, the oxalyl chloride (200 µL, 3.16 mmol) was added slowly. The reaction mixture was stirred for 4 hours at 0 ^{o}C and then allowed to come to room temperature. The solvent was evaporated and the corresponding bis(acid chloride) was subjected directly for amide formation. The bis(acid chloride) (200 mg, 0.86 m mol) was dissolved in 5 mL of dry tetrahydrofuran (THF) and cooled to 0 ^{o}C. Then, the respective amine (3 mmol) was added followed by addition of triethyl amine (10 mmol) at to 0 ^{o}C. The reaction mixture was allowed to stir at room temperature for 3 hours and filtered under pressure. The filtrate was collected and the solvent was evaporated under pressure to get corresponding amide (**7a - 7c**). The resulting compound (**7a - 7c,** 100 mg) was dissolved in 3 mL of dry dichloromethane (DCM) was directly treated with boron tribromide in dry dichloromethane (1 M BBr_3 in DCM) (1 mL) at -78 ^{o}C. The reaction was quenched by addition of saturated solution of sodium bicarbonate, and the organic layer was collected in dichloromethane (DCM) and dried using sodium sulfate and solvent was removed *in vacuo*. The purification was done using silica gel chromatography using hexane: ethyl acetate system to get the desired compound with 60% to 70% yields.

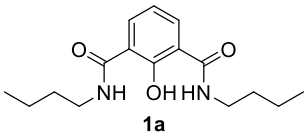

1a

Compound 1a: White solid (65 mg, 70% yield); **M.p.:** 99.0 – 100.0 ^{o}C; **^{1}H NMR (400 MHz, $CDCl_3$):** δ 7.92 (d, J = 7.7 Hz, 2H), 7.44 (s, 2H), 6.93 (t, J = 8.0, 1H), 3.46 (td, J = 7.1, 5.8 Hz, 4H), 1.68 – 1.60 (m, 2H), 1.59 – 1.56 (m, 2H), 1.52 – 1.26 (m, 4H), 0.95 (t, J = 7.3 Hz, 6H); **^{13}C NMR (100 MHz, $CDCl_3$):** δ 167.63, 160.47, 132.84, 118.51, 117.99, 39.69, 31.54, 20.26, 13.85; **HRMS (ESI):** Calc. for $C_{16}H_{24}N_2O_3$ $[M+H]^+$: 293.1865; Found: 293.1869.

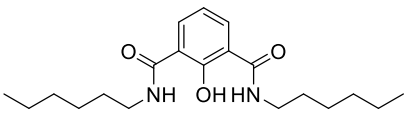

1b

Compound 1b: White solid (61 mg, 65% yield); **M.p.:** 82.5 – 83.5 ^{o}C; **^{1}H NMR (400 MHz, $CDCl_3$):** δ 14.44 (s, 1H), 7.96 (d, J = 7.5 Hz, 2H), 7.44 (s, 2H), 6.98 (t, J = 7.8 Hz, 1H), 3.49 (td, J = 7.1, 5.8 Hz, 4H), 1.66 (dt, J = 14.9, 7.4 Hz, 4H), 1.42 (dd, J = 8.8, 7.0 Hz, 4H), 1.38 – 1.32 (m, 8H), 0.92 (t, J = 7.0 Hz, 6H); **^{13}C NMR (400 MHz, $CDCl_3$):** δ 192.96, 167.58, 160.46, 132.74, 118.53, 39.99, 31.56, 29.46, 26.92, 22.63, 14.10; **HRMS (ESI):** Calc. for $C_{20}H_{32}N_2O_3$ $[M+H]^+$: 349.2491; Found: 349.2489.

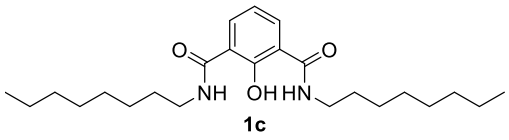

1c

Compound 1c: White solid (48 mg, 52% yield); **M.p.:** 77.0 – 78.0 ^{o}C; **^{1}H NMR (400 MHz, $CDCl_3$):** δ 14.46 (s, 1H), 7.96 (d, J = 7.7 Hz, 2H), 7.47 (s, 2H), 6.97 (t, J = 7.8 Hz, 1H), 3.49 (dd, J = 12.9, 7.1 Hz, 4H), 1.66 (dd, J = 14.4, 7.0 Hz, 4H), 1.47 – 1.36 (m, 4H), 1.37 – 1.20 (m, 16H), 0.90 (t, J = 6.9 Hz, 6H); **^{13}C NMR (400 MHz, $CDCl_3$):** δ 167.58, 160.39, 132.67, 118.42, 118.12, 39.93, 31.79, 29.70, 29.42, 29.27, 29.20, 27.04, 22.64, 14.08; **HRMS (ESI):** Calc. for $C_{24}H_{41}N_2O_3$ $[M+H]^+$: 405.3117; Found: 405.3113.

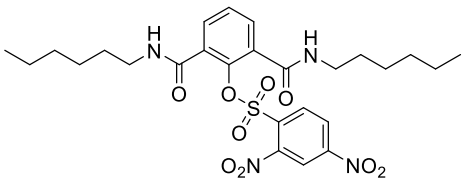

2

Compound 2: To a solution of compound **1b** (100 mg, 0.28 mmol) in dry dichloromethane (5 mL) was added trimethylamine (80 µL, 0.56 mmol) and then cooled to 0 ^{o}C. To this reaction mixture was added a solution of 2,4-dinitrobenzenesulphonylchloride (DNS-Cl) (115 mg, 0.42 mmol) in dichloromethane at 0 ^{o}C. The reaction mixture was allowed to come to room temperature and stirred for 5 hours. The TLC showed complete consumption of **1b**. The reaction mixture was extracted in ethyl acetate after washing with saturated solution of ammonium chloride and the brine. The organic layer was dried using sodium sulfate. The compound was purified using silica gel column chromatography with 40% ethyl acetate : hexane mixture to obtain **2** as yellowish solid (105 mg, 65% yield). **M.p.:** 131.5 – 132.0 ^{o}C; **^{1}H NMR (400 MHz, $CDCl_3$):** δ 8.72 (d, J = 7.7 Hz, 1H), 8.56 (dd, J = 8.7, 2.2 Hz, 1H), 8.21 (d, J = 8.7 Hz, 1H), 7.77 (d, J = 7.7 Hz, 2H), 7.49 (t, J = 7.7 Hz, 1H), 6.22 (t, J = 5.6 Hz, 2H), 3.22 (dd, J = 13.1, 7.2 Hz, 4H), 1.55 (m, 4H), 1.39 – 1.28 (m, 12H), 0.91 (t, J = 6.9 Hz, 6H).; **^{13}C NMR (400 MHz, $CDCl_3$):** δ 167.63, 160.47, 132.84, 118.51, 117.99, 39.69, 31.54, 20.26, 13.85; **HRMS (ESI):** Calc. for $C_{26}H_{35}N_4O_9S$ $[M+H]^+$: 579.2125; Found: 579.2119.

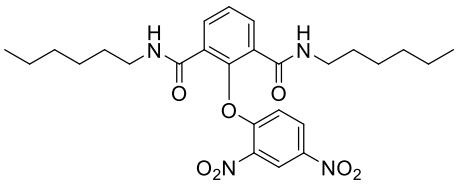

3

Compound 3: To the solution of compound **1b** (100 mg, 0.28 mmol) in dry tetrahydrofuran (THF) was added triethylamine (80 µL, 0.56 mmol) and DIPEA (27 µL, 0.56 mmol). To this reaction mixture was added a solution of 1-chloro-2,4-dinitrobenzene (DNB) (85 mg, 0.42 m mol) at 0 ^{o}C. The reaction mixture was refluxed for 24 hours. The TLC showed almost complete consumption of **1b**. The reaction mixture was extracted in ethyl acetate after washing with saturated solution of ammonium chloride and the brine. The organic layer was dried using sodium sulfate. The compound was purified using preparative HPLC with 40% ethyl acetate : hexane mixture as eluent, to obtain **3** as yellow solid (72 mg, 50% yield); **M.p.:** 151.0 – 152.0 ^{o}C; **^{1}H NMR (400 MHz, DMSO-*d6* at 120 ^{o}C):** δ 8.75 (d, J = 22.8 Hz, 1H), 8.54 (dd, J = 8.8, 1.7 Hz, 1H), 8.36 (d, J = 2.1 Hz, 1H), 7.80 (d, J = 8.7 Hz, 2H), 7.58 (s, 2H), 6.96 (d, J = 9.3 Hz, 1H), 3.65 (s, 4H), 1.54 – 1.44 (m, 4H), 1.24 – 1.08 (m, 12H), 0.81 (t, J = 7.0 Hz, 6H).**^{13}C NMR (400 MHz, DMSO-*d6* at 120 ^{o}C):** δ 147.11, 146.77, 142.32, 130.83, 130.36, 129.16, 128.83, 128.60, 121.58, 121.30, 119.72, 51.15, 31.02, 27.84, 26.16, 22.0, 13.80; **HRMS (ESI):** Calc. for $C_{26}H_{35}N_4O_9S$ $[M+H]^+$: 515.2506 ; Found: 515.3083. $[M+H]^+$: 515.2506; Found: 515.2500.

Note: Due to the aggregation behavior of **3**, the NMR spectra were recorded at 120 ^{o}C in DMSO-*d6*.

4.4.4. Ion Transport Studies.

The ion transport studies were performed as discussed in the previous chapters.

4.4.5. Planar Bilayer Conductance measurements.

The studies were performed by same methods as discussed in the previous chapters.

4.4.6. Molecular Modeling of the Channel.

The molecular modeling was started with geometry optimization of **1b** by conflex software to get the idea about the most stable conformation. Then, the dimeric rosettes of **1b** were used to form a channel, which was optimized by MOPAC2012 software using PM6-DH^{+} method.

4.4.6. Biological Studies.

In Vitro Studies using 2D and 3D Models:

General: All tissue culture treated plastic wares used in this study were purchased from Eppendorf and Thermo scientific, unless mentioned otherwise. DMEM, PBS and Penicillin-Streptomycin were purchased from Lonza. RPMI, Fetal bovine serum, and Trypsin were purchased from Invitrogen. MTT dye was purchased from Sigma Aldrich. The antibodies were

purchased from Jackson Immuno Research and Millipore as mentioned for each. The 3D culture was done using on matrigel using DMEM media.

Cell culture protocol: MCF-7 cells were grown in High Glucose Dulbecco's Modified Eagle Medium (DMEM; Invitrogen or Lonza) containing 10% fetal bovine serum (FBS; Invitrogen), 2 mM L-glutamine (Invitrogen) and 100 units/mL penicillin and 100 µg/ml streptomycin (Invitrogen). Cells were maintained as monolayer cultures in 100 mm tissue culture treated dishes (Corning) at 37 °C in humidified 5% CO_2 incubator (Thermo Scientific).
INS-1E cells between passages 62 and 72 were grown in monolayer cultures in a humidified 5% CO2 atmosphere at 37°C in RPMI 1640 media supplemented with 10 mM HEPES, 1 mM pyruvate, 50 µM 2-mercaptoethanol, 10% (v/v) heat-inactivated FBS, 100 units/ml penicillin and 100 µg/ml streptomycin.

Induction of 3D cultures: MCF-7 cells were cultured using the "on-top" method of 3D culturing. Briefly MCF-7 (3500 cells/well) were re-suspended in DMEM supplemented with 10% FBS, 1X Penicillin-Streptomycin solution containing 5% Matrigel® (Corning®). This cell suspension was seeded on an 8-well chamber coverglass (Nunc Lab tek; Thermo Scientific) pre-coated with 55µL Matrigel®. The culture was maintained at 37 °C with 5% CO_2 in a humidified incubator for seven days. The media was changed every two days for the next seven days.

Live cell imaging: MCF-7 cells were seeded in glass bottom 35 mm dishes at a density of 5×10^5 cells per plate. After attaining the confluency, the cells were focused in Lieca sp8 confocal microscope and then the DMEM media containing IC_{50} concentration (1 µM) of **2** was added. A blue fluorescence was observed for the compound **2** when excited with the DAPI laser. The time course to enter the cell was monitored using real time analysis.

MTT-based cytotoxicity assay:[50] The viability of the MCF-7 cells under the influence of different compounds was determined using the MTT assay. Briefly, cells were resuspended in a 96-well flat bottom tissue culture plates (Corning) at density of 1×10^4 cells/well (per 100 µL) and incubated at 37 ^oC in a 5% CO_2 incubator for 24 h. Compounds were added to each well in increasing concentration while maintaining maximum amount of DMSO added (solvent) at 2% (2 µL) and incubated further for 24 h. Statistical analysis was done using one-way analysis of variance (ANOVA).

For *INS-1E*, cells were seeded onto 96-well plates (Corning) at an initial density of 1×10^4 cells/well and were allowed to adhere at 37 °C for 24 h. Subsequently, the medium was replaced with fresh culture medium (100 µL) containing 5 mM glucose (basal glucose media) and the plates were further incubated for 24 h. Post-incubation, in one set of plates, the glucose concentration was increased to 16 mM glucose (referred to as low GSH) while the other set was maintained in basal glucose media (referred to as high GSH) for another 24 hours. The cells were exposed to increasing concentration of the compounds for another 24 hours.

Post-incubation, the media in each well was replaced with 110 µL of MTT-DMEM mixture (0.5 mg MTT/mL of DMEM) and incubated for 4 h at 37 °C. The solution was then replaced with 100 µL DMSO to dissolve the formazan crystals. The absorbance was measured in a microplate reader (Varioskan Flash) at the wavelength of 570 nm. All experiments were performed in triplicate. The reduction in cell viability was expressed as the percentage for each treatment relative to the control wells (set as 100%).

Cytotoxicity of SO_2 and by-products. To evaluate the effect of sulfur dioxide and the other byproduct **8**, we evaluated the cytotoxicity of compound **9** which releases compound **8** along with SO_2, and that of compound **10** which releases SO_2 and a non-toxic 4-methoxyphenol in presence of esterase enzyme. The effects of both compounds **9** and **10** were similar and negligible as compared to compound **2** at the same concentrations. Statistical analysis was done using one-way analysis of variance (ANOVA).

Mitochondrial membrane depolarization: MCF-7 cells were seeded in glass bottom 35 mm dishes at the concentration of 1×10^6 cells per plate. Cells were incubated with IC_{50} concentration (1 µM) of compound **2** for 24 h. Post-incubation, cells were washed twice with 1X PBS and incubated with JC-1 (Himedia) at the final concentration of 50 nM for 30 min. Fluorescence images were acquired after washing with PBS in both red and green channel using Lieca sp8 confocal microscope.

For quantification, MCF-7 cells were resuspended in a 96-well flat bottom tissue culture plates (Corning) at a density of 10^4 cells/well (per 100 µL) and incubated at 37 ^oC in a 5% CO_2 incubator for 24 h. Post-incubation, the media was replaced with fresh media. Then, the compounds were added after four hours to each well in increasing concentration by maintaining maximum amount of DMSO at 1.5% (1.5 µL per 100 µL) and were incubated further for 24 h. The cells were again washed twice with PBS and the JC1 dye (50 nM) was added in DMEM and incubated for 30 minutes. Finally the cells were washed with PBS and 100 µL of PBS was added and the plates were read with a multi-mode plate reader (Perkin Elmer) at 529 nm (green) and at 590 nm (red). All experiments were performed in triplicates, and the ratio of red/green was expressed as a percentage of untreated cells. Statistical analysis was done using one-way analysis of variance (ANOVA).

Mitosox assay: The MCF-7 cells were dispersed in a 96-well flat bottom tissue culture treated plates (Corning) at density of 10^4 cells/well (per 100 µL) and incubated at 37 ^oC in a 5% CO_2 incubator for 24 h. Fresh media was added to the cells. Then, the compounds were added to each well in different concentration by maintaining maximum amount of DMSO at 1.5 % (1.5 µL) and incubated for 24 h. The cells were washed with PBS and mitosox (5 µM) in PBS was added to each well and incubated for 20 minutes. The cells were again washed twice with PBS and then 100 µL of PBS was added and the cells were read with plate reader at 580 nm (λ_{ex} = 510 nm). All experiments were performed in triplicates, and the relative ROS (%) was expressed as a

percentage of untreated cells. Statistical analysis was done using one-way analysis of variance (ANOVA).

ROS generation:[71] The MCF-7 cells were seeded in glass bottom 35 mm dishes at the concentration of 1×10^6 cells per plate. Cells were incubated with 1 μM of **2** for 24 h. After that cells were washed thoroughly and incubated with DCFDA at the final concentration of 0.5 μM for 20 min. The cell images were acquired after washing with PBS in time dependent manner using green channel with Nikon Eclipse TS 100 fluorescence microscope.

For quantification, the MCF-7 cells were resuspended in a 96-well flat bottom tissue culture treated plates (Corning) at density of 10^4 cells/well (per 100 μL) and incubated at 37 ^oC in a 5% CO_2 incubator for 24 h. The cells were washed with PBS and a fresh media was added to the cells. Then, the compounds were added after four hours to each well in different concentration by maintaining maximum amount of DMSO at 1.5 % (1.5 μL) and incubated for 24 h. The cells were again washed twice with PBS and the DCFDA in PBS was added and incubated for 20 minutes. Finally the cells were washed with PBS and 100 μL of PBS was added and the cells were read with plate reader at 535 nm ($\lambda_{ex} = 488$ nm). All experiments were performed in triplicates, and the relative ratio (%) was expressed as a percentage of untreated cells. Statistical analysis was done using one-way analysis of variance (ANOVA).

Metabolite extraction and NMR Spectroscopy: MCF-7 cells (N = 5) were exposed to the compound **2** and DMSO (solvent control) for 24 hours and were harvested by centrifugation for 5 mins at 100 *g* at 4°C. The cell pellets were processed immediately for metabolite extraction using ice-cold methanol. Briefly, MCF-7 cells were seeded in 100 mm plates (in duplicate) at a density of 3 x 10^6 and were given different treatments as described above. Post-incubation, the cells were harvested by centrifugation for 5 min at 100 *g* at 4°C and washed twice with 1X PBS. The cell culture pellets were re-suspended in 300 μL of pre-chilled 1X PBS and 25 μl was kept separately for protein isolation and estimation using BCA reagent (ThermoFisher Scientific). The cell suspension was mixed with two volumes of ice-cold methanol, vortexed briefly and incubated at -20°C for 30 min. Post-incubation, the samples were centrifuged at 13,000 *g* for 30 min at 4°C. The supernatant was frozen into liquid nitrogen and lyophilized to remove residual water and methanol. The final extracts were stored at -80°C until NMR acquisition. The lyophilized extracts were allowed to thaw on ice before reconstituting into 580 μL 100% NMR buffer (20 mM sodium phosphate, pH 7.4 in D_2O containing 0.4 mM DSS (2,2-dimethyl-2-silapentane-5-sulfonic acid)). Briefly, 17.46 ± 0.01 mg of DSS was weighed (Mol wt. 218.32 g/mol) and dissolved in 2000 μL ± 2 μL of phosphate buffer. This stock solution was then diluted to 100 fold resulting in a final buffer solution containing 87.30 ± 0.16 mg/L of DSS in solution, which corresponds to 399.9 ± 0.7 μM of DSS in buffer. The samples were vortexed for 2 min at room temperature and centrifuged at 4000 *g* for 2 min. The supernatants were transferred to 5 mm NMR tubes for NMR measurements.

All NMR data were measured at 298 K using a Bruker AVANCE III HD Ascend NMR spectrometer operating at 14.1 Tesla equipped with a quad-channel ($^{1}H/^{13}C/^{15}N/^{31}P/^{2}H$) cryogenic probe. Water suppression pulse sequence noesygppr1d from Bruker library was used to record ^{1}H NMR spectra, where an inter-scan delay of 5 s, a mixing time of 100 ms, and the data acquisition period of 6.95 s/scan was used. For each spectrum, a total of 64 transients and 16 dummy scans were collected with 32K data points in a spectral width of 7200 Hz. For ^{1}H-^{1}H total correlation spectroscopy (TOCSY) experiment (mixing time = 80 ms), a total of 2048 × 1024 data points with 64 transients per increment in the indirect dimension were recorded spanning a spectral width of 6000 Hz in both the dimensions.

Metabolite identification and quantification: All of the ^{1}H NMR spectra were manually phased and baseline-corrected using Topspin (v3.5) software (www.bruker.com/bruker/topspin). ^{1}H NMR raw data was multiplied with exponential function and zero-filled to 64K data points before Fourier transformation. All the ^{1}H chemical shifts were directly referenced with respect to 4,4-dimethyl-4-silapentane-1-sulphonic acid (DSS; 400 μM). The chemical shift values, J-values, line shape, and multiplicity information were used in combination with BMRB [72] and HMDB [73] databases using Chenomx NMR Suite 8.1 software to carry out the ^{1}H resonance assignment for GSH. A chemical shift tolerance of 0.05 ppm was used while comparing the data with BMRB/HMDB. The absolute concentrations (μM) were normalized with respect to the protein concentration obtained using the BCA assay to account for the cell number variability among replicates. Statistical analysis was done using one-way analysis of variance (ANOVA).

Immunofluorescence analysis for cytochrome *c* release: MCF-7 cells were seeded at a density of 1×10^{6} cells per well on top of glass cover slips (Micro-Aid, India). Following treatment, cells were fixed using 4% formalin (Macron Chemicals) and were permeabilised using 0.5% Triton X-100 for 10 min at 4 ^{o}C. Cells were blocked with 10% (v/v) FBS (Invitrogen), stained with cytochrome *c* antibody (sc-13561, Santa Cruz Biotechnology) overnight at 4 °C. Postincubation, the cells were washed with PBS and then incubated with secondary antibody (goat anti-rabbit AlexaFluor-488; Millipore). Cells were then counterstained with phalloidin (millipore) to stain the cell boundaries and mounted on glass slides (Micro-Aid, India). Cell images were taken in were taken using Leica sp8 confocal microscope using 63x oil-immersion objective.

Immunoblot analysis: MCF-7 cells were seeded at a density of 1×10^{6} cells per well in 6-well tissue culture treated plates (Corning) and maintained at 37 °C for 24 h. Cells were then treated with **2** (1 μM) by direct addition of drug to the culture medium for 24 h. Control cells were treated with equivalent volume of DMSO. After 24 h treatment, medium containing **2** was aspirated and cells were washed once with 1X phosphate buffered saline (PBS; PAN-Biotech GmbH). Cells were lysed in sample buffer containing 60 mM Tris (pH 6.8), 6% glycerol, 2% sodium dodecyl sulfate (SDS), 0.1 M dithiothreitol (DTT) and 0.006% bromophenol blue and lysates were stored at –20 °C.

Cell lysates were resolved using sodium dodecyl sulfate polyacrylamide gel electrophoresis (SDS-PAGE) and transferred to Immobilon–P polyvinylidene difluoride (PVDF) membrane (Millipore). Blocking was performed in 5% (w/v) skimmed milk (SACO Foods, USA) prepared in 1X Tris buffered saline containing 0.1% Tween 20 (1X TBS-T) for 1 h at room temperature. Blots were incubated for 16 h at 4°C temperature in primary antibody for GAPDH, PARP (Calbiochem, anti-mouse), caspase 9 (Abcam, anti-rabbit) as per the recommended dilutions. Following washes with PBS, blots were incubated with peroxidase-conjugated secondary antibody (anti rabbit, Jackson) prepared in 5% (w/v) skimmed milk in 1X TBS-T for 1 h at room temperature following which blots were developed using Immobilon Western Detection Reagent kit (Millipore) and visualized using ImageQuant LAS 4000 (GE Healthcare).

Propidium iodide staining:[43] MCF-7 cells were seeded in glass bottom 35 mm dishes at the concentration of 1×10^6 cells per plate. Cells were incubated with 1 µM of **2** for 24 h. The cell plate was washed thoroughly with PBS 2 to 3 times. Then, propidium iodide dye (10 µg/mL) was added to the plate in dark and the plate was incubated for 15 minutes at 37°C in CO_2 incubator. After 15 minutes, plates were removed from incubator, dye was removed and the scaffolds were washed thoroughly with PBS to remove the excess stain. 1 mL of fresh PBS was added to the scaffolds, and then analyzed for cell under confocal fluorescence microscope (Leica Sp8).

Treatment protocol for the evaluation of anticancer activity of compound 2: Three doses of compound **2** (2 µM) were administered to the cells on day 4, 5 and 6. This was further incubated for additional 24 hours following which the cultures were fixed as described below. Cell treated with DMSO were used as controls and doxorubicin (0.8 µM) was used as a positive control.

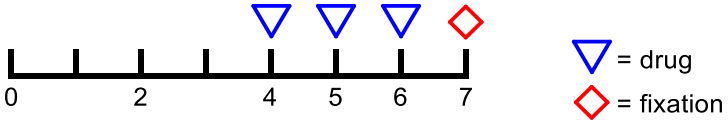

Figure 4.15. Protocol used for the induction of 3D cultures of MCF-7 cells. Compound **2** (2 µM) was administered to the growing cultures on days 4, 5 and 6.

Immunoflourescence for 3D cultures: Post treatment with the different compounds, on day 7, the 3D cultures were fixed using 4% paraformaldehyde in PBS for 20 minutes at room temperature. Cells were washed with 1X PBS twice for 10 minutes after fixation. Permeablization of the cells was performed using ice-cold 1X PBS containing 0.5% Triton-X 100 for 10 minutes at 4 °C. After permeablization, cells were washed with PBS-glycine twice, followed by a PBS wash. Blocking was done with 10% goat serum (Abcam) for 1 hour at room temperature followed by secondary blocking with 1% F(ab')2 fragment goat anti-mouse IgG (Jackson ImmunoResearch) in goat serum for another 1 hour. Alexa Flour® Phalloidin 488 prepared 1:100 in goat serum (diluted in IF buffer) was incubated for 1 hour at room temperature. After incubation, cells were washed with 1X IF buffer for 20 minutes followed by two washes with 1X PBS for 10 minutes each. The nuclei were stained with Hoechst 33258 in

PBS (0.5µg/ml) for 5 minutes. Cells were finally washed thrice with 1X PBS, mounted using Slow Fade® Gold antifade reagent, and imaged using a Leica Sp8 confocal microscope using 63x oil immersion objective.

Morphometry of 3D spheroids: Morphometric parameters like IsoVolume and Surface Area of spheroids were obtained using the Phalloidin channel in the Huygens Essential software (Scientific Volume Imaging). The number of cells per spheroid was quantified by counting the number of nuclei per spheroid using ImageJ software. Data was plotted and analyzed using GraphPad Prism software.

Statistical Analysis

All cellular experiments were performed in triplicate and the results have been presented as Mean $\pm$ SEM unless stated otherwise, where SEM refers to the standard error of mean and is expressed as sample standard deviation divided by the square root of the sample size. Statistical analysis was performed by one-way ANOVA; Tukey HSD post-hoc test; p-value < 0.05 was considered significant when comparing groups.

4.5. NMR SPECTRA:

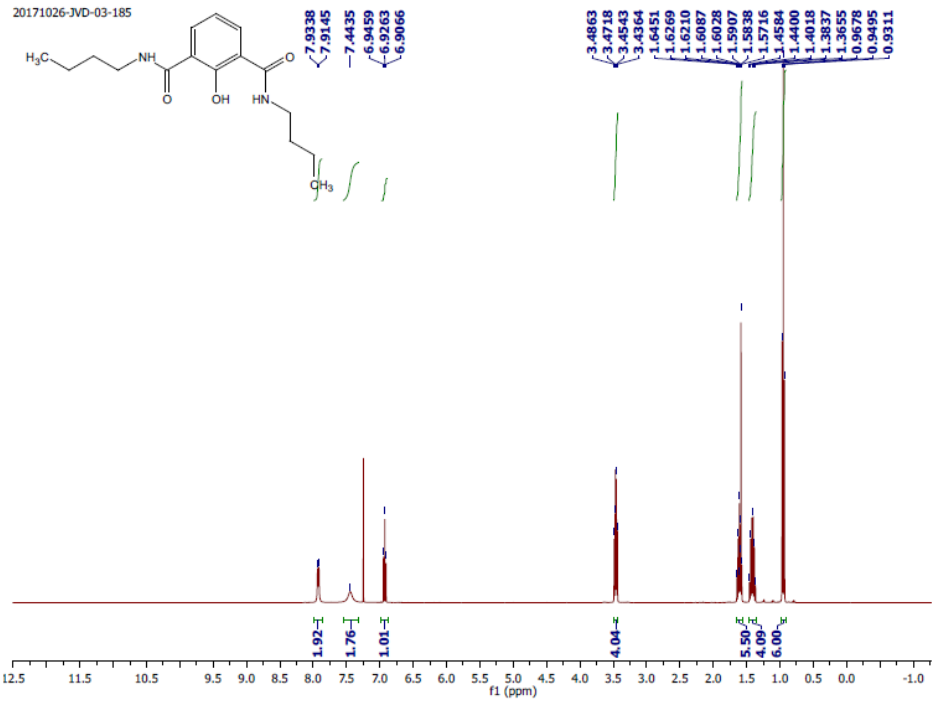

Figure 4.16. ^{1}H NMR spectrum of **1a** in $CDCl_3$.

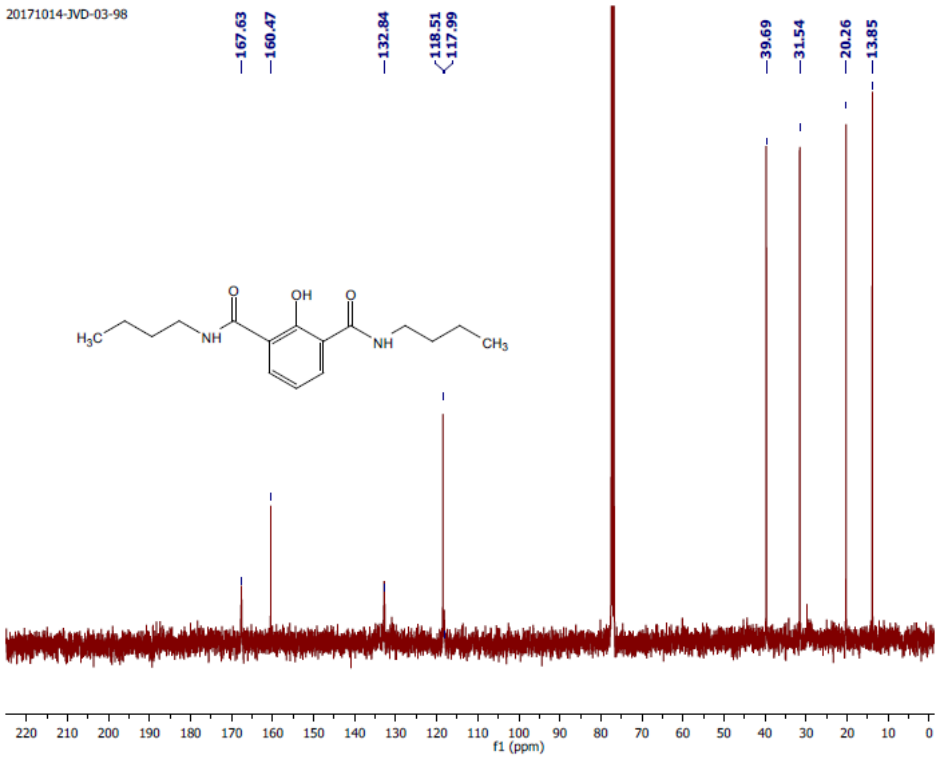

Figure 4.17. ^{13}C NMR spectrum of **1a** in $CDCl_3$.

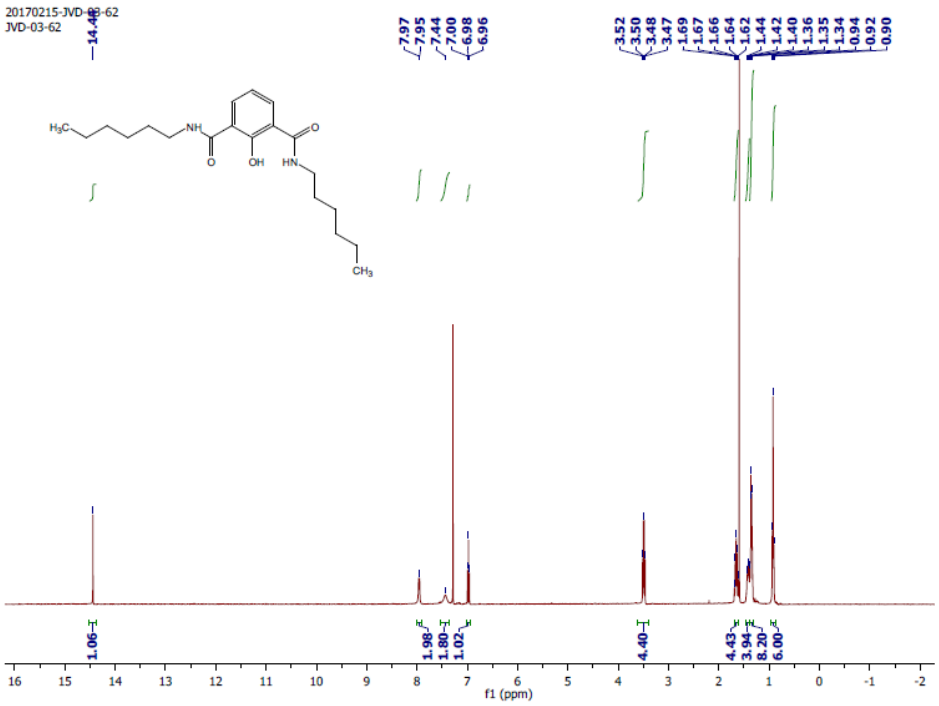

Figure 4.18. ^{1}H NMR spectrum of **1b** in $CDCl_3$.

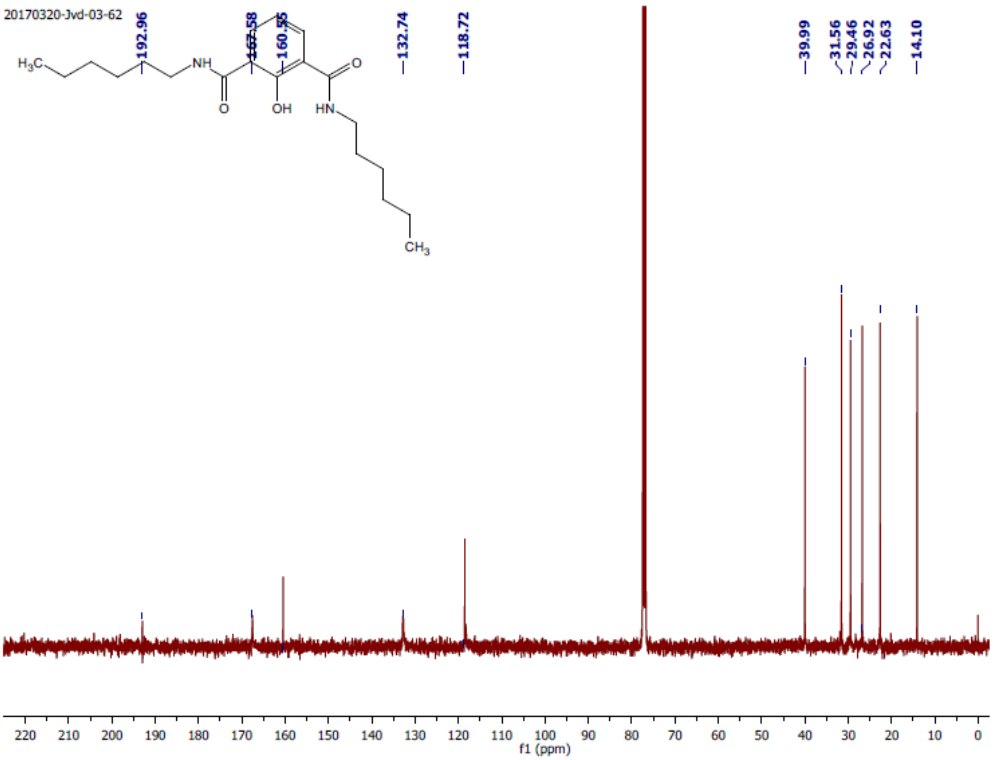

Figure 4.19. ^{13}C NMR spectrum of **1b** in $CDCl_3$.

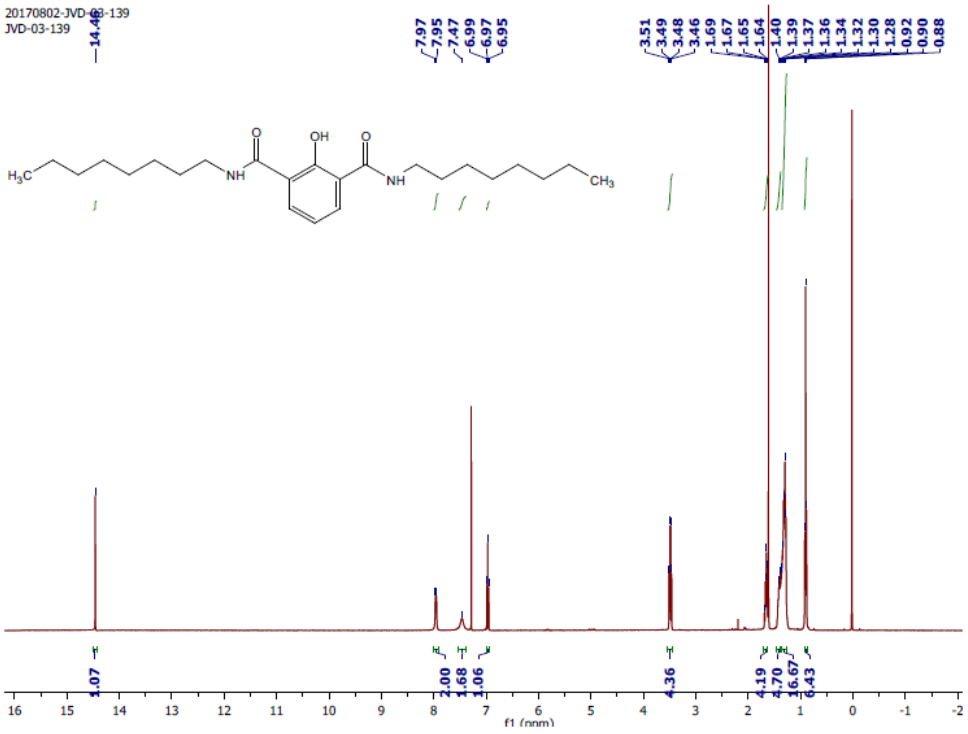

Figure 4.20. ^{1}H NMR spectrum of **1c** in $CDCl_3$.

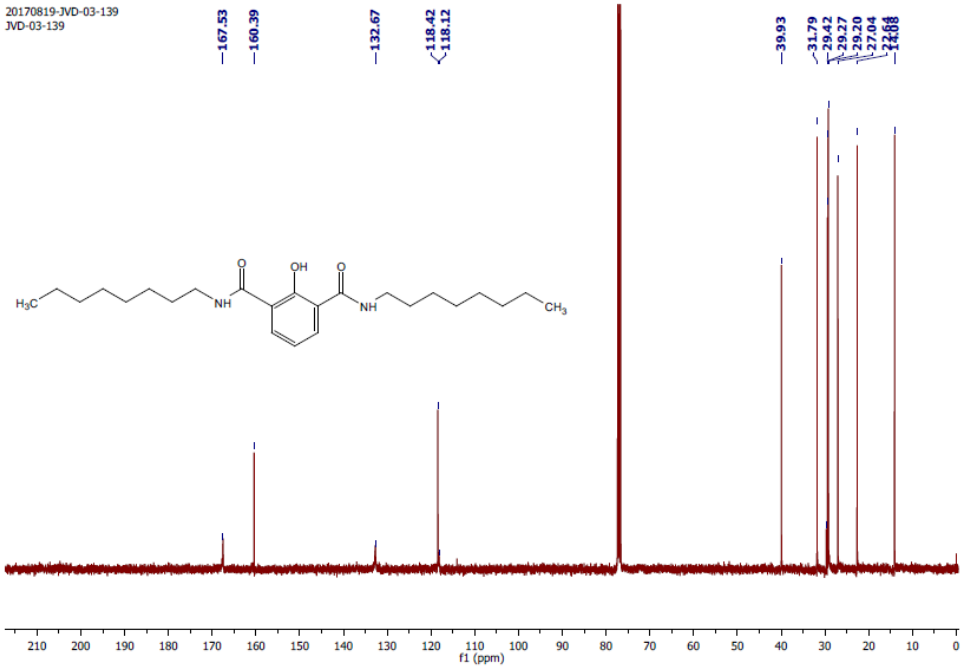

Figure 4.21. ^{13}C NMR spectrum of **1c** in $CDCl_3$.

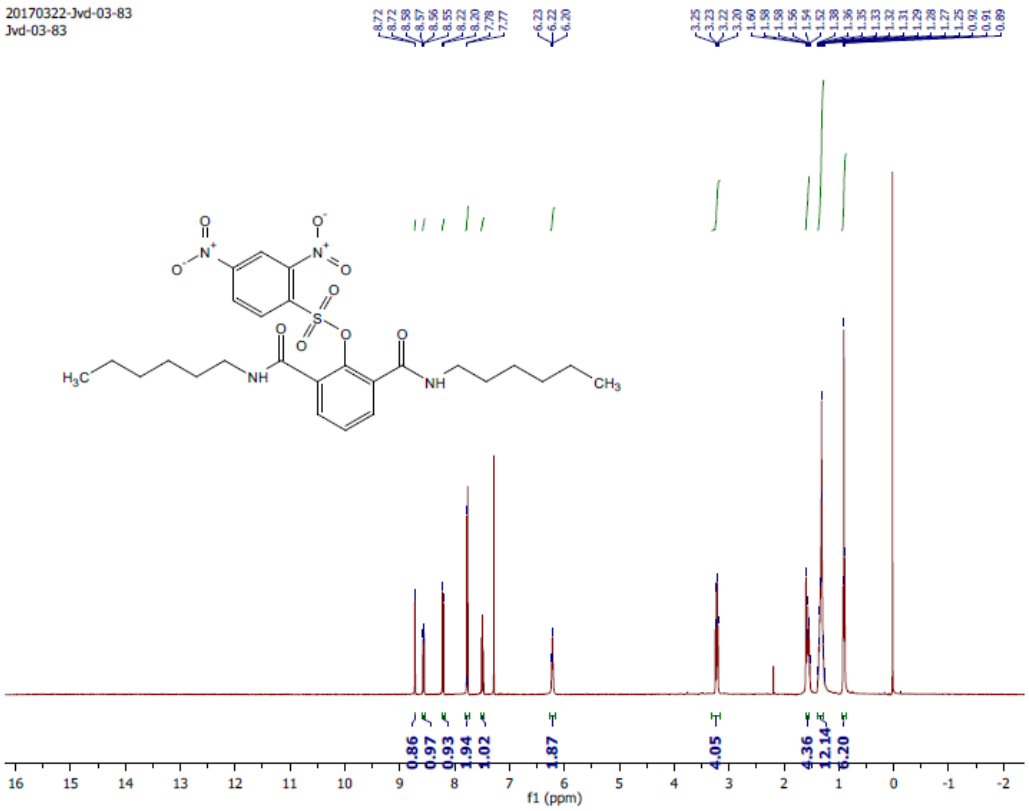

Figure 4.22. ^{1}H NMR spectrum of **2** in $CDCl_3$.

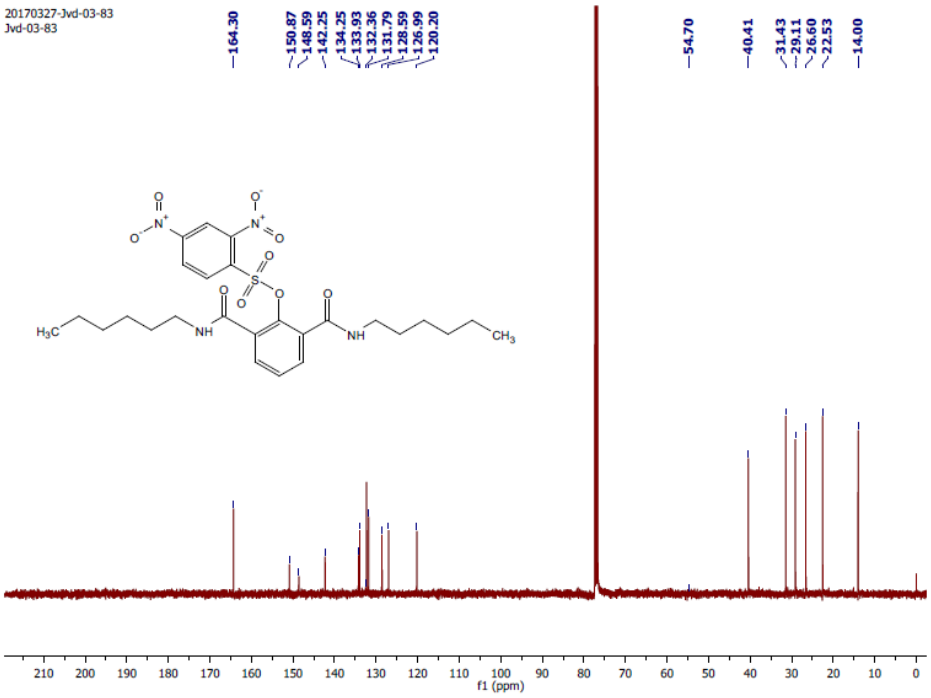

Figure 4.23. ^{13}C NMR spectrum of **2** in $CDCl_3$.

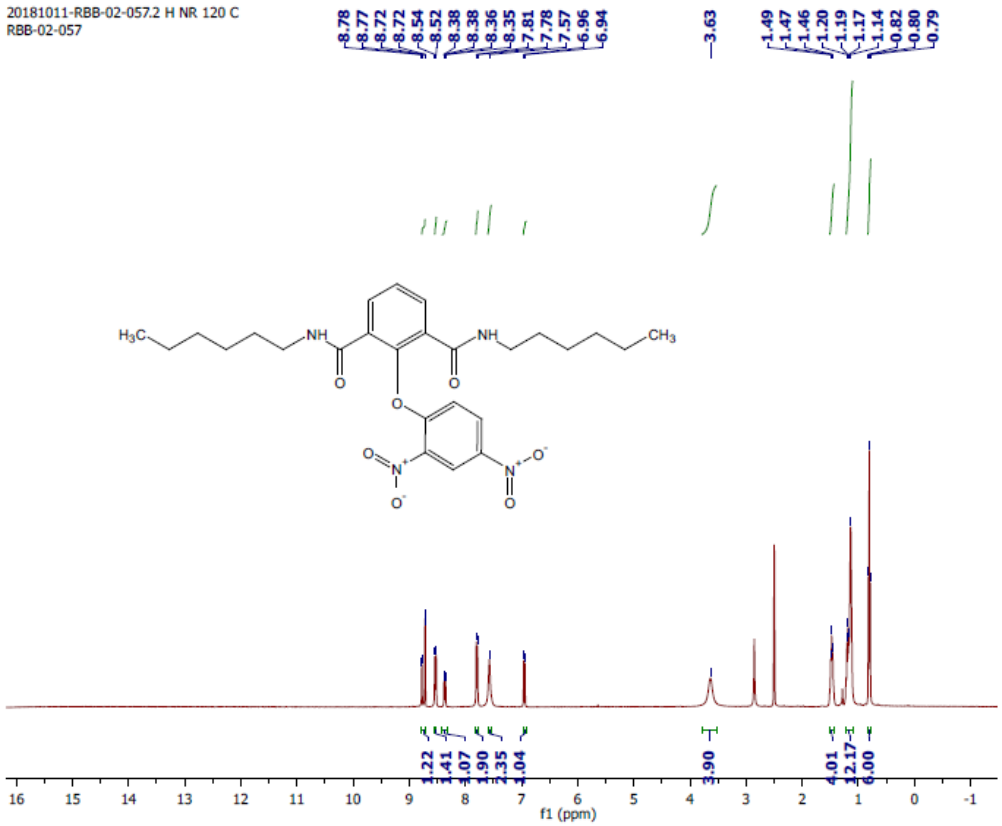

Figure 4.24. ^{1}H NMR spectrum of **3** in DMSO-*d*6.

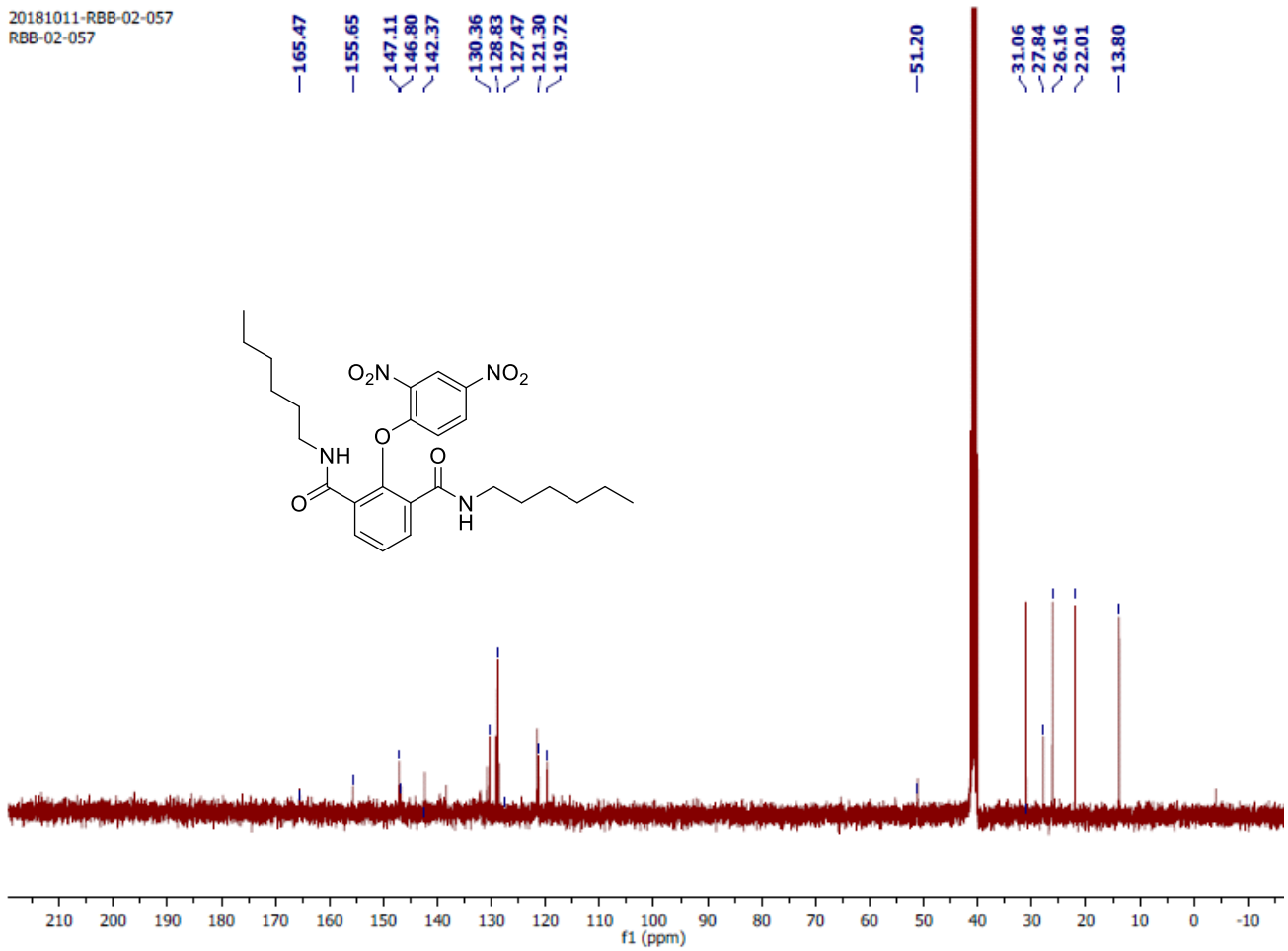

Figure 4.25. ^{13}C NMR spectrum of **3** in DMSO-*d*6

4.5. REFERENCES:

(1) Tannock, I. F.; Rotin, D. *Cancer RES.* **1989**, *49*, 4373.

(2) Van Rossom, W.; Asby, D. J.; Tavassoli, A.; Gale, P. A. *Org. Biomol. Chem.* **2016**, *14*, 2645.

(3) Ohkuma, S.; Sato, T.; Okamoto, M.; Matsukya, H.; Arai, K.; Kataoka, T.; Nagai, K.; Wasserman, H. H. *Biochem. J.* **1998**, *334*, 731.

(4) Davis, J. T. In *Anion Recognition in Supramolecular Chemistry*; Gale, P. A., Dehaen, W., Eds.; Springer Berlin Heidelberg: Berlin, Heidelberg, **2010**, p 145.

(5) Wojtkowiak, J. W.; Verduzco, D.; Schramm, K. J.; Gillies, R. J. *Mol. Pharm.* **2011**, *8*, 2032.

(6) Salunke, S. B.; Malla, J. A.; Talukdar, P. *Angew. Chem. Int. Ed.* **2019**, *58*, 5354.

(7) Fernald, K.; Kurokawa, M. *Trends Cell Biol.* **2013**, *23*, 620.

(8) Olinski, R.; Zastawny, T.; Budzbon, J.; Skokowski, J.; Zegarski, W.; Dizdaroglu, M. *FEBS Lett.* **1992**, *309*, 193.

(9) Ames, B. N.; Shigenaga, M. K.; Hagen, T. M. *Proc Natl Acad Sci U S A* **1993**, *90*, 7915.

(10) Sies, H. *Eur. J. Biochem.* **1993**, *215*, 213.

(11) Ighodaro, O. M.; Akinloye, O. A. *Alexandria Med. J.* **2018**, *54*, 287.

(12) Toyokuni, S.; Okamoto, K.; Yodoi, J.; Hiai, H. *FEBS Lett.* **1995**, *358*, 1.

(13) Quintana-Cabrera, R.; Fernandez-Fernandez, S.; Bobo-Jimenez, V.; Escobar, J.; Sastre, J.; Almeida, A.; Bolaños, J. P. *Nat. Commun.* **2012**, *3*, 718.

(14) Wu, G.; Fang, Y. Z.; Yang, S.; Lupton, J. R.; Turner, N. D. *Nutr. J.* **2004**, *134*, 489.

(15) Traverso, N.; Ricciarelli, R.; Nitti, M.; Marengo, B.; Furfaro, A. L.; Pronzato, M. A.; Marinari, U. M.; Domenicotti, C. *Oxidative Med. Cell. Longev.* **2013**, *2013*, 10.

(16) Lang, C.; Zhang, X.; Dong, Z.; Luo, Q.; Qiao, S.; Huang, Z.; Fan, X.; Xu, J.; Liu, J. *Nanoscale* **2016**, *8*, 2960.

(17) Akhtar, N.; Pradhan, N.; Saha, A.; Kumar, V.; Biswas, O.; Dey, S.; Shah, M.; Kumar, S.; Manna, D. *Chem. Commun.* **2019**, *55*, 8482.

(18) Li, X.; Shen, B.; Yao, X.-Q.; Yang, D. *J. Am. Chem. Soc.* **2007**, *129*, 7264.

(19) Kand, D.; Saha, T.; Lahiri, M.; Talukdar, P. *Org. Biomol. Chem.* **2015**, *13*, 8163.

(20) Bai, J.; Meng, Z. *Environ. Mol. Mutagen.* **2010**, *51*, 112.

(21) Liu, J.; Huang, Y.; Chen, S.; Tang, C.; Jin, H.; Du, J. *Oxidative Med. Cell. Longev.* **2016**, *2016*, 8.

(22) Xie, J.; Li, R.; Fan, R.; Meng, Z. *Inhal. Toxicol.* **2009**, *21*, 952.

(23) Peng, S.; Zhong, T.; Guo, T.; Shu, D.; Meng, D.; Liu, H.; Guo, D. *New J. Chem.* **2018**, *42*, 5185.

(24) Trifonov, A. L.; Levin, V. V.; Struchkova, M. I.; Dilman, A. D. *Org. Lett.* **2017**, *19*, 5304.

(25) Kim, S. K.; Lim, J. M.; Pradhan, T.; Jung, H. S.; Lynch, V. M.; Kim, J. S.; Kim, D.; Sessler, J. L. *J. Am. Chem. Soc.* **2014**, *136*, 495.

(26) Routasalo, T.; Helaja, J.; Kavakka, J.; Koskinen, A. M. P. *Eur. J. Org. Chem.* **2008**, *2008*, 3190.

(27) Roy, A.; Saha, D.; Mukherjee, A.; Talukdar, P. *Org. Lett.* **2016**, *18*, 5864.

(28) Roy, A.; Gautam, A.; Malla, J. A.; Sarkar, S.; Mukherjee, A.; Talukdar, P. *Chem. Commun.* **2018**, *54*, 2024.

(29) Saha, T.; Dasari, S.; Tewari, D.; Prathap, A.; Sureshan, K. M.; Bera, A. K.; Mukherjee, A.; Talukdar, P. *J. Am. Chem. Soc.* **2014**, *136*, 14128.

(30) Malwal, S. R.; Sriram, D.; Yogeeswari, P.; Konkimalla, V. B.; Chakrapani, H. *J. Med. Chem.* **2012**, *55*, 553.

(31) Gilles, A.; Barboiu, M. *J. Am. Chem. Soc.* **2016**, *138*, 426.

(32) Malla, J. A.; Roy, A.; Talukdar, P. *Org. Lett.* **2018**, *20*, 5991.

(33) Dias, C. M.; Li, H.; Valkenier, H.; Karagiannidis, L. E.; Gale, P. A.; Sheppard, D. N.; Davis, A. P. *Org. Biomol. Chem.* **2018**, *16*, 1083.

(34) Park, S.-H.; Park, S.-H.; Howe, E. N. W.; Hyun, J. Y.; Chen, L.-J.; Hwang, I.; Vargas-Zuñiga, G.; Busschaert, N.; Gale, P. A.; Sessler, J. L.; Shin, I. *Chem* **2019**, *5*, 2079.

(35) Mondal, D.; Sathyan, A.; Shinde, S. V.; Mishra, K. K.; Talukdar, P. *Org. Biomol. Chem.* **2018**, *16*, 8690.

(36) Jentzsch, A. V.; Emery, D.; Mareda, J.; Nayak, S. K.; Metrangolo, P.; Resnati, G.; Sakai, N.; Matile, S. *Nat. Commun.* **2012**, *3*, 905.

(37) Ghosh, P.; Federwisch, G.; Kogej, M.; Schalley, C. A.; Haase, D.; Saak, W.; Lützen, A.; Gschwind, R. M. *Org. Biomol. Chem.* **2005**, *3*, 2691.

(38) Eckshtain-Levi, M.; Lavi, R.; Yufit, D. S.; Daniel, B.; Green, O.; Fleker, O.; Richman, M.; Rahimipour, S.; Gruzman, A.; Benisvy, L. *Chem. Commun.* **2016**, *52*, 2350.

(39) Stewart, J. J. P. MOPAC2012; Stewart Computational Chemistry: Colorado Springs, CO, USA, **2012**.

(40) Korth, M. *J. Chem. Theory Comput.* **2010**, *6*, 3808.

(41) Zhang, H.; Zhang, C.; Liu, R.; Yi, L.; Sun, H. *Chem. Commun.* **2015**, *51*, 2029.

(42) Yuan, L.; Zuo, Q.-P. *Sens. Actuators B.* **2014**, *196*, 151.

(43) Suzuki, T.; Fujikura, K.; Higashiyama, T.; Takata, K. *J. Histochem. Cytochem.***1997**, *45*, 49.

(44) Benderra, Z.; Trussardi, A.; Morjani, H.; Villa, A. M.; Doglia, S. M.; Manfait, M. *Eur. J. Cancer* **2000**, *36*, 428.

(45) Gamcsik, M. P.; Millis, K. K.; Colvin, O. M. *Cancer Res.* **1995**, *55*, 2012.

(46) Pardeshi, K. A.; Malwal, S. R.; Banerjee, A.; Lahiri, S.; Rangarajan, R.; Chakrapani, H. *Bioorg. Med. Chem. Lett.* **2015**, *25*, 2694.

(47) Pardeshi, K. A.; Ravikumar, G.; Chakrapani, H. *Org. Lett.* **2018**, *20*, 4.

(48) Yousf, S.; Sardesai, D. M.; Mathew, A. B.; Khandelwal, R.; Acharya, J. D.; Sharma, S.; Chugh, J. *Metabolomics* **2019**, *15*, 55.

(49) Saha, T.; Gautam, A.; Mukherjee, A.; Lahiri, M.; Talukdar, P. *J. Am. Chem. Soc.* **2016**, *138*, 16443.

(50) Saha, T.; Hossain, M. S.; Saha, D.; Lahiri, M.; Talukdar, P. *J. Am. Chem. Soc.* **2016**, *138*, 7558.

(51) Gale, P. A.; Davis, J. T.; Quesada, R. *Chem. Soc. Rev.* **2017**, *46*, 2497.

(52) Busschaert, N.; Park, S.-H.; Baek, K.-H.; Choi, Y. P.; Park, J.; Howe, E. N. W.; Hiscock, J. R.; Karagiannidis, L. E.; Marques, I.; Félix, V.; Namkung, W.; Sessler, J. L.; Gale, P. A.; Shin, I. *Nat. Chem.* **2017**, *9*, 667.

(53) Ko, S.-K.; Kim, S. K.; Share, A.; Lynch, V. M.; Park, J.; Namkung, W.; Van Rossom, W.; Busschaert, N.; Gale, P. A.; Sessler, J. L.; Shin, I. *Nat. Chem.* **2014**, *6*, 885.

(54) Sakamuru, S.; Attene-Ramos, M. S.; Xia, M. *Methods Mol. Biol.* **2016**, *1473*, 17.

(55) Patil, S.; Kuman, M. M.; Palvai, S.; Sengupta, P.; Basu, S. *ACS Omega* **2018**, *3*, 1470.

(56) Ashkenazi, A. *Nat. Rev. Drug Discov.* **2008**, *7*, 1001.

(57) Bortner, C. D.; Cidlowski, J. A. *Cell Death Differ.* **2002**, *9*, 1307.

(58) Smiley, S. T.; Reers, M.; Mottola-Hartshorn, C.; Lin, M.; Chen, A.; Smith, T. W.; Steele, G. D.; Chen, L. B. *Proc. Natl. Acad. Sci. U S A.* **1991**, *88*, 3671.

(59) Cossarizza, A.; Baccarani-Contri, M.; Kalashnikova, G.; Franceschi, C. *Biochem. Biophys. Res. Commun.* **1993**, *197*, 40.

(60) Wu, D.; Yotnda, P. *J. Vis. Exp.***2011**, 3357.

(61) Armstrong, J. S.; Steinauer, K. K.; Hornung, B.; Irish, J. M.; Lecane, P.; Birrell, G. W.; Peehl, D. M.; Knox, S. J. *Cell Death Differ.***2002**, *9*, 252.

(62) Halestrap, A. P. *J. Mol. Cell Cardiol.* **2009**, *46*, 821.

(63) Crompton, M. *Biochem. J.* **1999**, *341 (Pt 2)*, 233.

(64) Madesh, M.; Hajnóczky, G. *Eur. J. Cell Biol.* **2001**, *155*, 1003.

(65) Park, S.-H.; Choi, Y. P.; Park, J.; Share, A.; Francesconi, O.; Nativi, C.; Namkung, W.; Sessler, J. L.; Roelens, S.; Shin, I. *Chem. Sci.* **2015**, *6*, 7284.

(66) Chaitanya, G. V.; Alexander, J. S.; Babu, P. P. *Cell Commun. Signal.***2010**, *8*, 31.

(67) Boulares, A. H.; Yakovlev, A. G.; Ivanova, V.; Stoica, B. A.; Wang, G.; Iyer, S.; Smulson, M. *J. Biol. Chem.* **1999**, *274*, 22932.

(68) Lovitt, C. J.; Shelper, T. B.; Avery, V. M. *BMC Cancer* **2018**, *18*, 41.

(69) Kuebel-Pollak, A.; Rüttimann, S.; Dunn, N.; Melich, X.; Williams, A. F.; Bernardinelli, G. *Helv. Chim. Acta* **2006**, *89*, 841.

(70) Li, F.; Basile, V. M.; Pekarek, R. T.; Rose, M. J. *ACS Appl. Mater. Interfaces* **2014**, *6*, 20557.

(71) Galadari, S.; Rahman, A.; Pallichankandy, S.; Thayyullathil, F. *Free Radic. Biol. Med.* **2017**, *104*, 144.

(72) Ulrich, E. L.; Akutsu, H.; Doreleijers, J. F.; Harano, Y.; Ioannidis, Y. E.; Lin, J.; Livny, M.; Mading, S.; Maziuk, D.; Miller, Z.; Nakatani, E.; Schulte, C. F.; Tolmie, D. E.; Kent Wenger, R.; Yao, H.; Markley, J. L. *Nucleic Acids Res.* **2008**, *36*, D402.

(73) Wishart, D. S.; Tzur, D.; Knox, C.; Eisner, R.; Guo, A. C.; Young, N.; Cheng, D.; Jewell, K.; Arndt, D.; Sawhney, S.; Fung, C.; Nikolai, L.; Lewis, M.; Coutouly, M. A.; Forsythe, I.; Tang, P.; Shrivastava, S.; Jeroncic, K.; Stothard, P.; Amegbey, G.; Block, D.; Hau, D. D.; Wagner, J.; Miniaci, J.; Clements, M.; Gebremedhin, M.; Guo, N.; Zhang, Y.; Duggan, G. E.; Macinnis, G. D.; Weljie, A. M.; Dowlatabadi, R.; Bamforth, F.; Clive, D.; Greiner, R.; Li, L.; Marrie, T.; Sykes, B. D.; Vogel, H. J.; Querengesser, L. *Nucleic Acids Res.* **2007**, *35*, D521.

Chapter 5

Esterase Activatable Synthetic M^+/Cl^- Channel Induces Apoptosis and Disrupts Autophagy in Cancer Cells

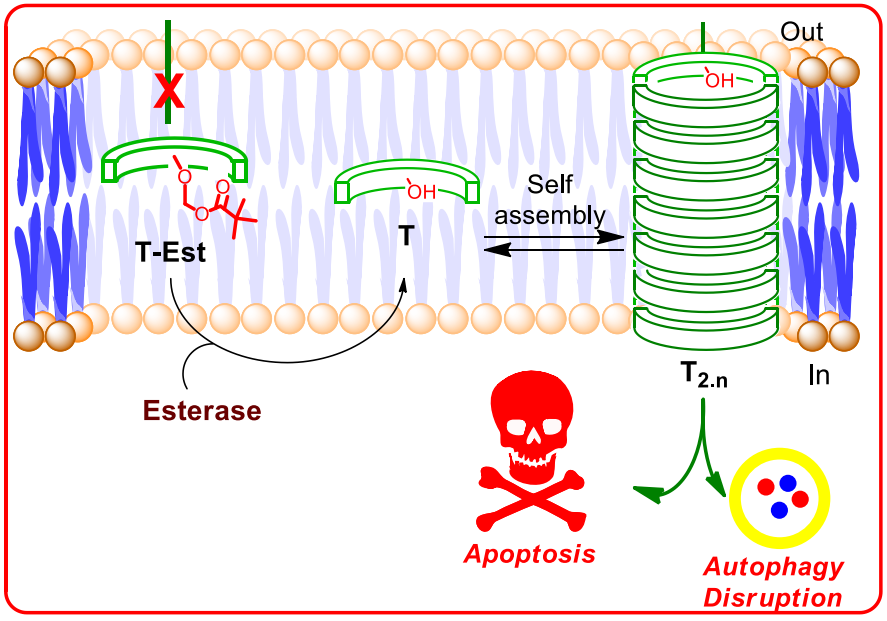

5.1. INTRODUCTION:

As discussed in previous chapter, we have successfully designed a glutathione activatable M^+/Cl^- ion channel which is capable to induce the apoptosis the cells by decreasing the GSH levels. The strategy is of great potential for taking these synthetic ion transport systems to next levels with respect to their therapeutic applications. However, the next question that pops up is "*what is the scope of such systems with respect to the applications of different stimuli"*. In other words can we use this system by using some other kind of stimulus to activate the ion transport through channel? Among the different stimuli, enzymes caught our interest. The enzymes serve as gates for activation and deactivation of Na-K-2Cl (NKCC) and K-Cl (KCCs) cotransporters. The gating occurs via phosphorylation and dephosphorylation of serine, threonine and tyrosine units, for both NKCCs and KCCs in a reciprocal manner. The phosphorylation process is known to activate the NKCCs but inhibit KCCs whereas the dephosphorylation activates the KCCs and inhibits the NKCCs.[1,2] As we have already shown that compound **1b** (Figure 5.1 B) acts as the M^+/Cl^- cotransport channel, so to make it enzyme responsive can be really an interesting study, as it can be the closest synthetic mimic of NKCCs and KCCs. Further, it will ensure that the different stimuli can be used to activate the transport through the channel, which will help to make it more selective for cancer cells compared to healthy cells.

In 2016, Kyu-Sung Jeong and coworkers reported the enzyme responsive procarriers in which the active anion carrier was attached to a hydrophilic appendage which stops the permeation of anion carrier through the cell membrane. However, upon treating with respective enzymes, the hydrophilic appendages cleave off and release the free anion carrier which then transports the anions across liposomes and cell membrane.[3] However, the main drawback for this strategy is that enzymes are to be provided in extracellular media to activate the ion transport across the cell membrane.

Among the different enzymes, esterases are abundantly expressed in cancer cells, therefore, lot of esterase activatable systems have been reported to target the cancer cells.[4-6] We hypothesized that introduction of an esterase cleavable bulky group at the C-2 position of the isophthalamide would not allow efficient self-assembly of the monomers (as in previous chapter) thereby restricting the ion channel formation. However, in presence of intracellular esterases the bulky group will be cleaved off to release the free compound **1b**, which will initiate the channel formation in cell membrane (Figure 5.1 A). Furthermore, as these esterases are present in abundance in the lysosomes,[4] so the cleavage by esterase can initiate the channel formation in lysosomal membranes, which may lead to efflux the Cl^- efflux to cytosol, which will lead to disruption of lysosomal functions.[7]

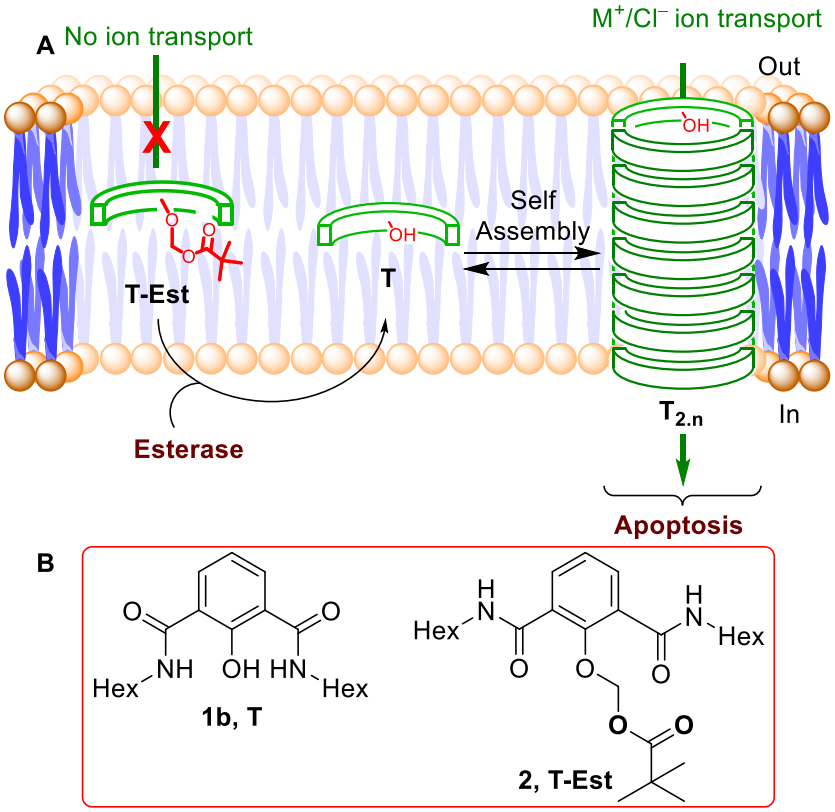

Figure 5.1. Schematic representation of esterase activitable M^+/Cl^- ion channel (A). Structure of active channel forming compound **1b** (**T**) and esterase activitable proactive channel **2** (**T-Est**) (B).

5.2. Results and discussion:

5.2.1. Synthesis.

The synthesis of **1b** was carried out as described in previous chapter. The compound **2** was synthesized by treatment of compound **1b** with iodomethyl pivalate in presence of triethyl amine to get the desired compound **2 (scheme 1)**.[8] The compound was characterized by ^{1}H NMR, ^{13}C NMR, and high resolution mass spectrometry.

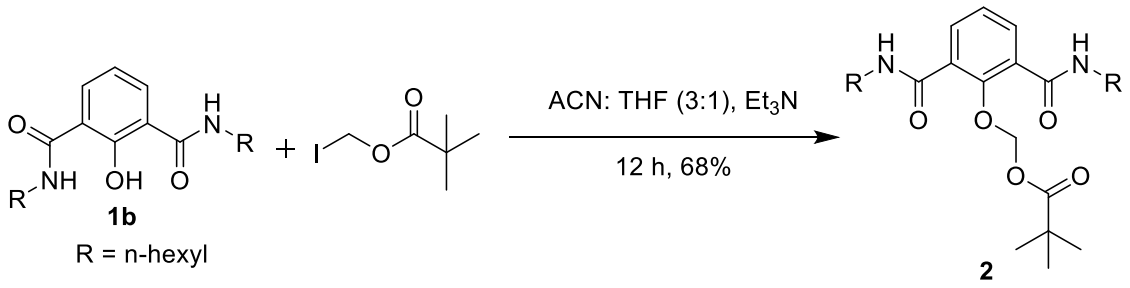

Scheme 1. Syntheis of compound **2** from **1b.**

5.2.2. Enzyme mediated cleavage assay.

After the successful synthesis of compound **2**, the release of compound **1b** from **2** upon enzymatic cleavage was evaluated by ^{1}H NMR studies.[9] The compound **2** (1 mM) in phosphate buffer saline (PBS) was treated with 4 U/mL of porcine liver esterase enzyme (Sigma Aldrich) prepared in PBS at pH 7.2 for different time intervals.[8] The disappearance of peak for $H_{b'}$ at δ = 5.6 ppm, shift of peak for H_a at δ = 8.0 ppm to 7.98 ppm as well as reappearance of peak for H_c around 14.4 ppm was monitored and it was found that almost 95% of the cleavage takes place within three hours of reaction time (Figure 5.2). These results suggest release of **1b** from compound **2** should be a very feasible process when incubated in cells due to higher concentrations of esterases.

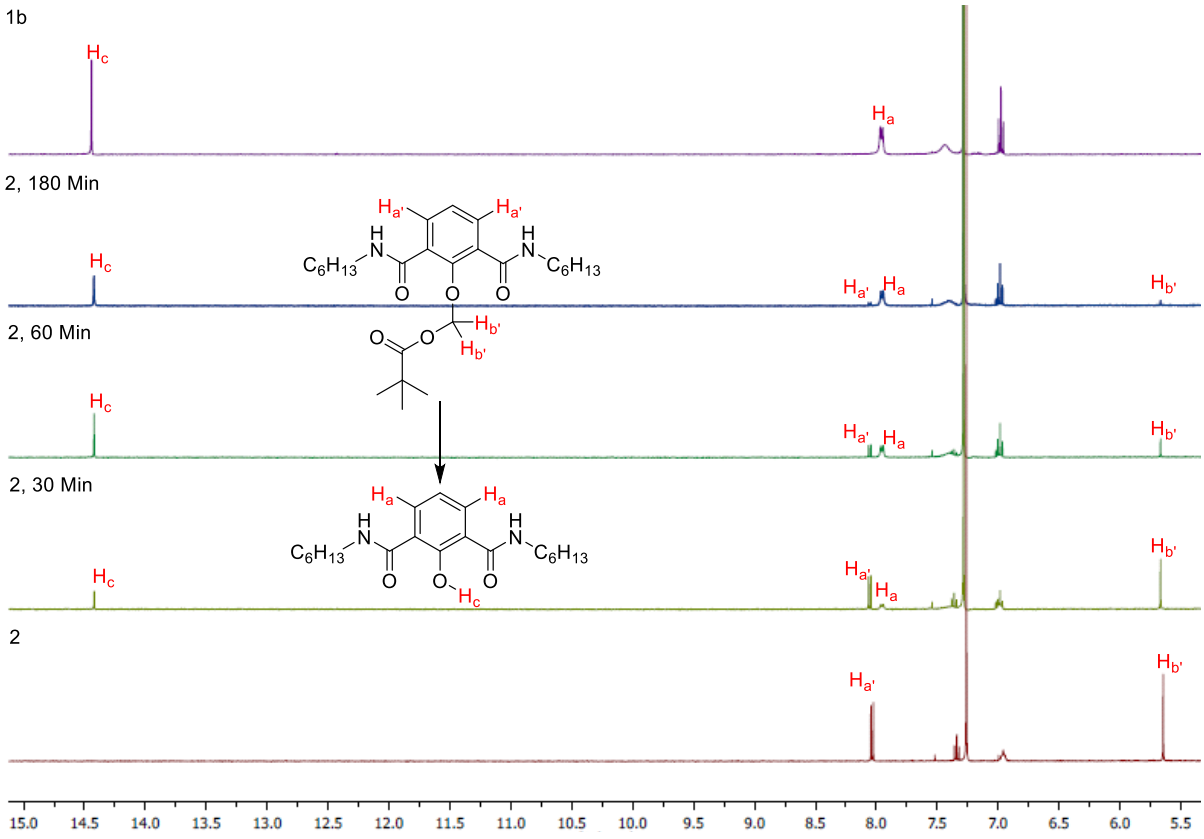

Figure 5.2. Esterase mediated release of **1b** form **2** monitored by ^{1}H NMR experiments.

5.2.3. Recovery of Ion Transport Activity.

The above ^{1}H NMR data encouraged us to evaluate the recovery of ion transport activity of each sample, after successful treatment with esterases. The ion transport activity of each sample was checked by lucigenin based fluorescence assay using large unilamellar vesicles (LUVs) composed of egg-yolk phosphatidylcholine (EYPC).[10] The EYPC-LUVs were entraped with $NaNO_3$ (200 mM) and lucigenin (1 mM) in 10 mM phosphate buffer pH = 7.2 and were

suspended in a solution of $NaNO_3$ (200 mM) in 10 mM phosphate buffer pH = 7.2. Then, the NaCl (2 M) was used to give a chloride gradient, followed by addition of each treated sample and the rate of quenching of fluorescence was monitored with time. The enhanced rate of fluorescence quenching with increased time of enzymatic reaction (Figure 5.3B) corroborated with the NMR data mentioned in Figure 5.2.

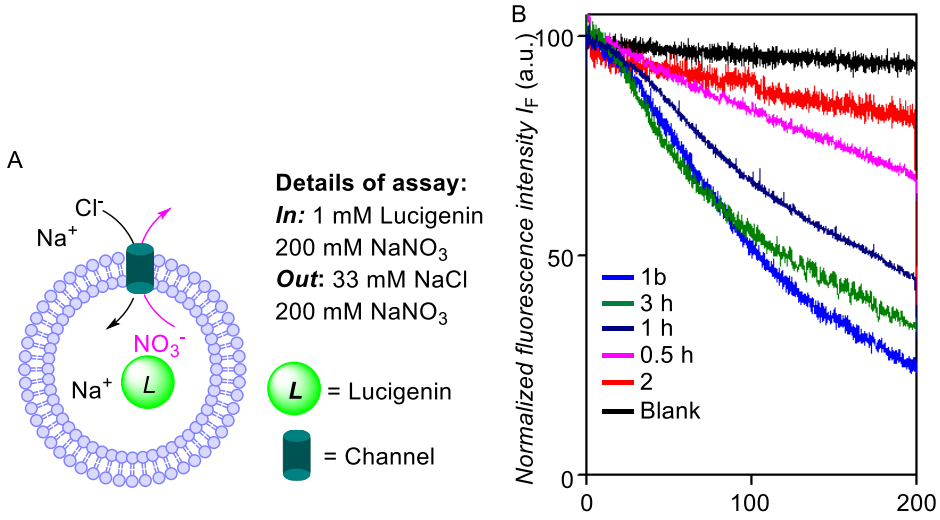

Figure 5.3. Schematic representation of lucigenin assay (A). Influx of Cl^- ions into EYPC-LUVs ⊃ lucigenin by compound **2** treated with esterase enzyme for different time intervals.

5.2.4. Biological Studies.

The successful release of compound **1b** from **2** by enzymatic cleavage inspired us to evaluate the release of **1b** by intracellular esterases. To do so, the live cell imaging of **2** was carried out in the human epithelial breast cancer cell line, MCF-7. The MCF-7 cells were incubated with compound **2** for 30 minutes and then the cells were analyzed under confocal microscope (Leica sp8). The results suggested that there is enhancement of blue fluorescence monitored by DAPI laser, compared to control cells, suggesting that the compound **1b** gets released from **2** by intracellular esterases (Figure 5.4 A, B).

The results of the cell imaging assay encouraged us to evaluate the cell viability of cancer cells in presence of compound **2**. The MCF-7 cells and HeLa cells were incubated with compound **2** in a dose dependent manner for 24 hours and then the cell viability was evaluated by MTT assay.[7,11,12] The results suggested that the compound **2** displayed enhanced cytotoxicity with enhancement in the concentration of compound giving IC_{50} values of 15 µM and 20 µM for MCF-7 cells and HeLa cells respectively (Figure 5.4 C).

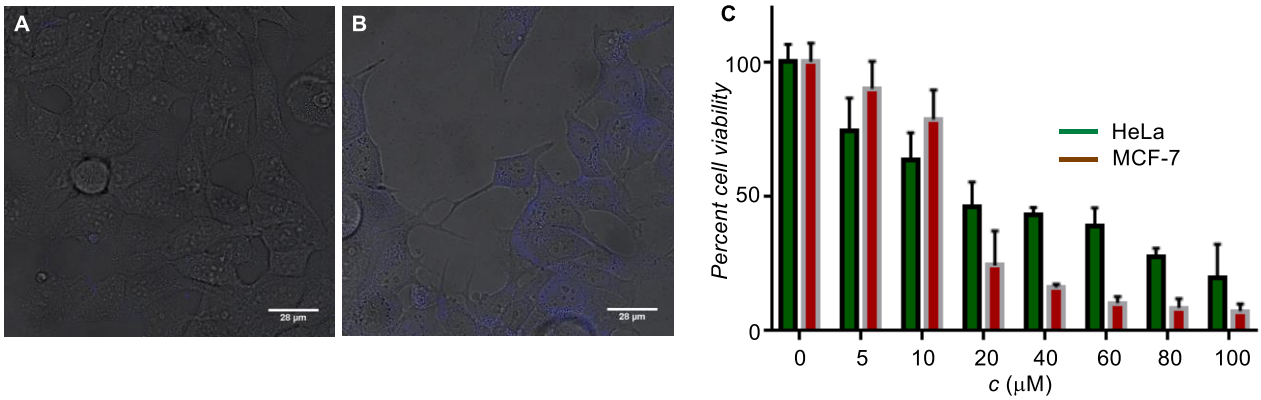

Figure 5.4. Live cell imaging MCF-7 cells incubated with compound **2** at 0 μM (A), and 15 μM (B). Dose-dependent cell viability assay of MCF-7 cells and HeLa cells incubated with compound **2** evaluated by MTT assay (C).

The above results indicated that the compound **2** is inducing the cell death in MCF-7 and HeLa cells. The next question to be addressed was to evaluate the path of cell death, *i.e.*, evaluate whether cell death is being mediated by necrosis or apoptosis. As discussed in previous chapters, apoptosis is evidenced by the disruption of mitochondrial membrane potential (MMP),[13,14] which subsequently results in cytochrome c release. The release of cytochrome c in the cytoplasm switches on the apoptotic signalling cascade.[15-17] Firstly, we evaluated the mitochondrial membrane potential (MMP) change by using the MMP sensitive JC-1 dye.[16,18] This dye exhibits red fluorescence emission due to the formation of J-aggregates in the healthy mitochondrial membrane. However, in the damaged mitochondria the depolarization of the mitochondrial membrane leads to scattering of the dye in the cytoplasm, resulting in green fluorescence emission. The MCF-7 cells were incubated with compound **2** (15 μM), followed by the treatment with JC-1 dye by the reported protocol. The cells were analysed under the confocal microscope (leica sp8) to monitor the changes in the red and green fluorescence in the treated cells compared to control. The study showed a significant decrease in the red fluorescence and a concomitant increase in the green emission (Figure 5.5 A, B).[16,18] The quantification of red/green fluorescence showed there is dose-dependent decrease, suggesting more damage with increasing concentrations (Figure 5.5 C). This MMP leads to generation of ROS in mitochondria which was quantified by mitosox, a mitochondria selective ROS probe. The results suggested a dose-dependent enhancement in ROS generation (Figure 5.5 D).

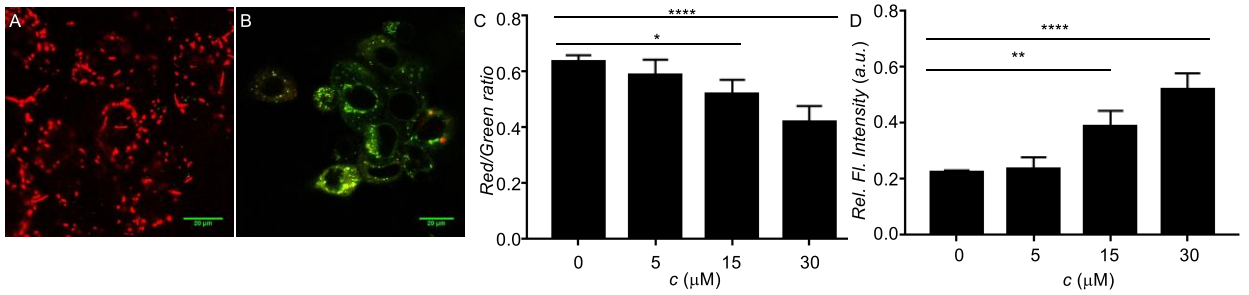

Figure 5.5. Live cell imaging of MCF-7 cells upon treatment with 0 μM (A) and 15 μM (B) of **2** for 24 h followed by staining with JC-1 dye. Red and green channel images were merged to generate the displayed image. Quantification of Red/Green ratio of treated cells treated with **2** in a dose dependent manner (C). Quantification of ROS generated in mitochondria of cells treated with compound **2** in a dose dependent manner for 24 h evaluated by mitosox dye (D). * represents $p < 0.05$, **, $p < 0.01$ and ***,$p < 0.001$.

Since this change in MMP of cells is known to cause the disturbance in the electron transport chain in the mitochondrial respiratory cycles, which ultimately results in generation of reactive oxygen species (ROS).[19,20] Thus, 2′,7′-dichlorodihydrofluorescein diacetate (H_2DCFDA),[14,21] was used as an ROS probe to monitor ROS generation in cells. This probe is non-fluorescent in nature when the acid groups are protected as diester. However, the cellular internalization of the probe leads to hydrolysis of the ester groups by the cellular esterases, which generates the diacid form of the dye. This diacid undergoes ROS-mediated oxidation which generates a green fluorescent 2',7'-dichlorofluorescein (DCF). Thus, this fluorescence can be used to monitor the ROS generation in cells. The MCF-7 cells were treated with **2 (**15 μM) and then stained with

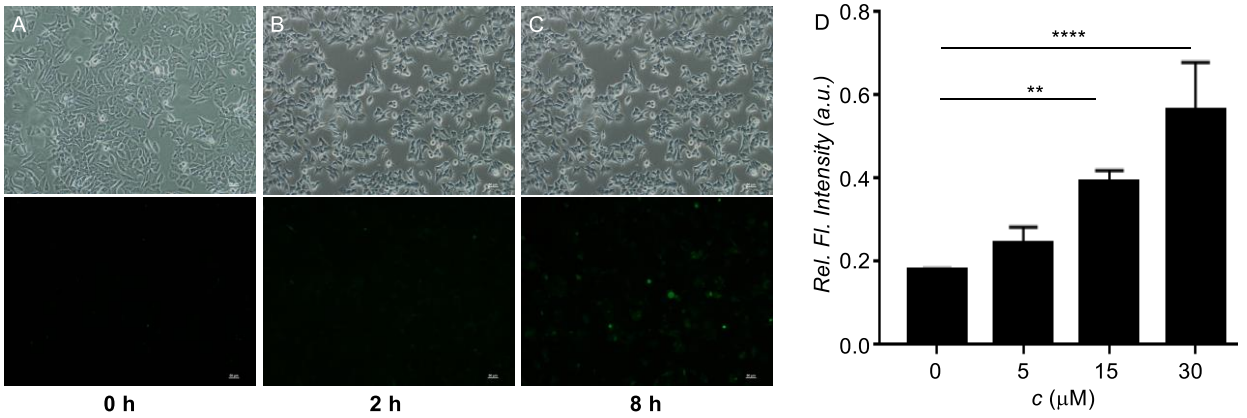

Figure 5.6. Live cell imaging of MCF-7 cells upon treatment with **2** (15 μM) at different time intervals (A–C). Quantification of ROS generation in MCF-7 cells upon incubation with **2** at different concentrations (D). * represents $p < 0.05$, **, $p < 0.01$ and ***,$p < 0.001$.

H_2DCFDA, in a time dependent manner followed by the analysis of cells under a fluorescence microscope. A significant enhancement in the green fluorescence was observed, which clearly

demonstrates the generation of ROS as a result of ion transport by **1b** released from **2** (Figure 5.6 A, B,C).

The quantification of the ROS generation was carried out by incubating the MCF-7 cells with compound **2** in a dose-dependent manner using H_2DCFDA dye. The MCF-7 cells were cultured in 96 well plates and incubated with compound **2** at different concentrations for 24 h. Then, the cells were stained using H_2DCFDA dye for 30 min followed by PBS washing. The cell plates were read using microplate reader in green channel to quantify the ROS. The results suggested that there is concentration dependent enhancement in the ROS generation in treated cells compared to control (Figure 6 D).

As discussed already in previous chapters that the intrinsic apoptotic pathway initiates from the mitochondria and releases cytochrome c which binds to the Apaf-1 to form an apoptosome. The apoptosome activates caspase 9 pathway, which switches the cells to apoptosis.[15,22-24] After getting the results about MMP from above experiments we probed the activation of caspase 9 pathway using the immunoblot analysis of MCF-7 cells upon treatment with compound **2** (15μM**)**. The incubation of the cells with **2** led to a significant increase in the expression of cleaved caspase 9 (Figure 5.7 A). The increase in the levels of caspase 9 was quantified with respect to the GAPDH as the loading control. The results showed the increased expression of cleaved caspase 9, which confirms the activation of the intrinsic pathway of apoptosis. To get further support for the activation of apoptotic pathway, the expression of cleaved poly(ADP-ribose) polymerase (PARP) was checked.[25,26] The significant amount of degradation of full-length PARP-1 (116 kDa) with a concomitant increase of cleaved PARP-1 (86 kDa) was observed upon immunoblot analysis of MCF-7 cells incubated with 15 μM concentrations of **2** (Figure 5.7 B), supporting the caspase 9 pathway of apoptosis.

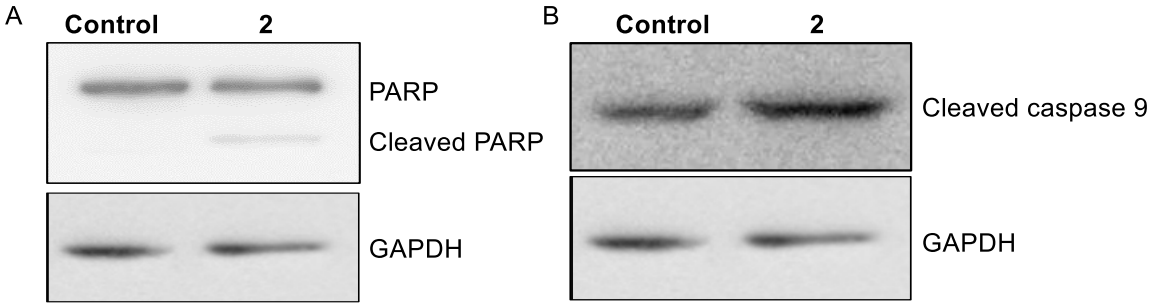

Figure 5.7. . Immunoblot assay for PARP cleavage (A) in MCF7 cells, and active caspase 9 (B) after 24 h incubation with 0 μM and 15 μM of **2**.

As mentioned already, the esterases are present in bulk inside lysosomes, so it may be possible that some compound inserts into lysosomes and after being acted upon by the esterases will release **1b**, which will form ion channels in the lysosomal membrane.[7,27] As the lysosomes have acidic pH (≈ 4.5 – 5.0) and are associated with high concentration of chloride ions,[28] it is possible that the channel formed in lysosomal membrane may facilitate the H^+/Cl^- cotransport

from lysosomes to cytosol, thereby, deacidifying the lysosomes. This deacidification and decrease in the chloride concentration leads to dysfunctioning of lysosomes. We analyzed the changes in pH of lysosomes by acridine orange (AO) assay.[27] AO is a cell-permeable dye which accumulates in acidic compartments, such as lysosomes, and shows a characteristic orange fluorescence emission. However, it emits green fluorescence at higher pH, such as in the cytosol. When MCF-7 cells were stained with AO, and typical granular orange fluorescence was observed, corresponding to cellular acidic compartments (Figure 5.8 A). Treatment with **2** induced complete loss of orange fluorescence. These results evidenced an increase in the pH of acidic organelles upon treatment with compound **2**.

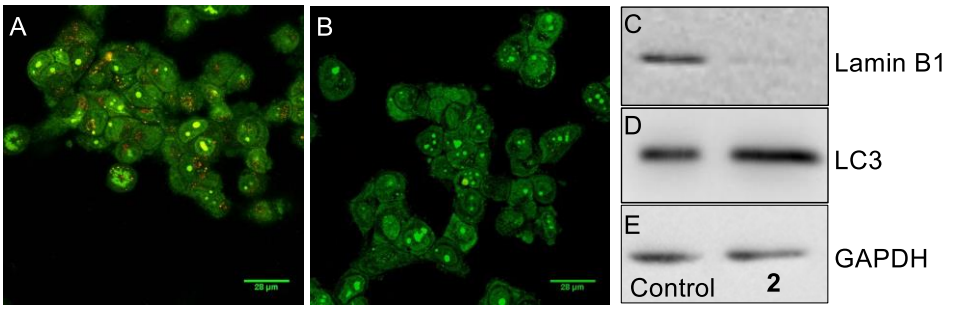

Figure 5.8. Live cell imaging of MCF-7 cells incubated with **2** at 0 μM (A), and 15 μM (B) concentrations followed by staining with acridine orange. Immunoblot assay for incresein in LC3 expression (C) and decrease in Lamin B1 expression (D) in MCF7 cells, with respect to GAPDH (E) as loading control.

One of the most important functions of the lysosomes is to mediate autophagy, and loss of lysosomal functions will directly affect the autophagy process. To evaluate the effect of compound **2** on autophagy, we carried out the immunoblot analysis for probing the expression of Lamin B1.[29] The Lamin B1 is constituent of nuclear lamina which decreases during the autophagy by interactions with LC3, which tethers the LC3 to the inner nuclear membrane. So, the decrease in Lamin B1 expression is considered as the marker of autophagy induction by lysosomal pathway. To analyze the expression of Lamin B1, the MCF-7 cells were incubated with compound **2** (15 μM) for 24 h, and then immunoblot analysis was carried out for treated and control cells, with GAPDH used as loading control. The results showed that the expression of Lamin B1 has decreased in treated cells compared to control cells (Figure 5.8 C), suggesting that the autophagy has been induced by compound **2**.

To get more support for the autophagy induction in MCF-7 cells treated with compound **2**, the microtubule-associated protein 1 light chain 3 (LC3) is used to monitor autophagy.[30] Typically increased expression of LC3 indicated that the autophagy is being induced in cells. Therefore, MCF-7 cells were incubated with compound **2** and then western blot analysis was carried out to study the changes in the expression of LC3. The results suggested that there is significant increase in the expression of LC3 in the treated cells compared to control cells (Figure 5.8D). These results corroborate with the lamin B1 results, thus, supports the fact that treatment of MCF-7 cells with compound **2** induces autophagy through lysososmal dysfunctions.

5.3. CONCLUSION:

In summary, we have introduced the novel concept of esterase activitable synthetic ion channels which can be activated by intracellular enzymes. The successful activation of ion channel inside cells leads to ion transport across the plasma membrane, which switches the cells to apoptosis through mitochondrial pathway. Further, the channel can dissipate the pH gradient of the lysosomes, which leads to lysosomal dysfunctions, and ultimately leads to autophagy induction in MCF-7 cells.

5.4. Experimental Section:

5.4.1. General Methods.

All reactions were carried out under the nitrogen atmosphere. All the chemicals were purchased from commercial sources and were used as received unless stated otherwise. Solvents were dried by standard methods prior to use or purchased as dry. Thin layer chromatography (TLC) was carried out with E. Merck silica gel 60-F_{254} plates and column chromatography was performed over silica gel (100-200 mesh) obtained from commercial suppliers. Egg yolk phosphatidylcholine (EYPC) lipid was purchased from Avanti Polar Lipids as a solution dissolved in chloroform (25 mg/mL). HEPES buffer, HPTS dye, Triton X-100, NaOH and all inorganic salts of molecular biology grade were purchased from Sigma. Size exclusion chromatography was performed on a column of Sephadex G-50. Large unilamellar vesicles (LUV) were prepared from EYPC lipid by using mini extruder, equipped with a polycarbonate membrane either of 100 nm or 200 nm pore size, obtained from Avanti Polar Lipids. The JC1 dye was the generous gift from Dr. Shilpy Sharma at Savitribai Phule Pune University. The H_2DCFDA was purchased from Sigma Aldrich.

5.4.2. Physical measurements.

The ^{1}H and ^{13}C NMR spectra were recorded on 400 MHz Jeol ECS-400 (or 100 MHz for ^{13}C) spectrometers using either residual solvent signals as an internal reference or from internal tetramethylsilane on the δ scale relative to chloroform (δ 7.26), dimethylsulphoxide (δ 2.50 ppm), acetone (δ 2.05) for ^{1}H NMR and chloroform (δ 77.20 ppm), dimethylsulphoxide (δ 39.50 ppm), acetone (δ 29.84 and 206.26) for ^{13}C NMR. The chemical shifts (δ) are reported in ppm and coupling constants (J) in Hz. The following abbreviations are used: s (singlet), d (doublet) m (multiplet), and td (triplet of doublet) while describing ^{1}H NMR signals. High-resolution mass spectra (HRMS) were obtained from MicroMass ESI-TOF MS spectrometer. Fluorescence spectra were recorded by using Fluoromax-4 from Jobin Yvon Edison equipped with an injector port and a magnetic stirrer. 10 mM HEPES (with 100 mM NaCl or other salts as per necessity) buffer solutions were used for fluorescence experiment and the pH of the buffers were adjusted to 7.0 or 8.0 by NaOH and pH of the buffer solutions was measured using Helmer pH meter. All melting points were measured in open glass capillary and values are uncorrected. All

fluorescence data were processed either by Origin 8.5 or KaleidaGraph and finally, all data were processed through ChemDraw Professional 15. MTT assay was recorded in a microplate reader (Varioskan Flash). Western blot was visualized in ImageQuant LAS 4000 (GE Healthcare). Cell images were taken using Leica sp8 confocal microscope and Nikon Eclipse TS 100 fluorescence microscope. The cell images were processed by image j software. The Grapgpad Prism 7 was used for plotting the data from biological assays.

5.4.3. Synthesis.

Synthesis of compound 2: In a clean dry round bottom flask was added compound **1b** (50 mg, 0.14 mmol) in dry acetonitrile (CAN, 3 mL) and tetrahedrofuran (THF, 1mL)) mixture (3:1) at room temperature. To this solution, was added iodomethyl pivalate (70 mg, 0.28 mmol), which was synthesized by reported protocol[8], and K_2CO_3 (60 mg, 0.42 mmol) at room temperature and the reaction mixture was stirred at room temperature overnight. After the TLC showed complete consumption of starting material, the compound was washed with brine and extracted with dichloromethane (DCM). The compound was purified by silica gel column chromatography to yield compound **2** as yellowish viscous semi-solid (45 mg, 68 %). **^{1}H NMR (400 MHz, $CDCl_3$)** δ 7.99 (d, *J* = 7.7 Hz, 2H), 7.30 (t, *J* = 7.7 Hz, 1H), 7.00 (t, *J* = 5.4 Hz, 2H), 5.63 (s, 2H), 3.41 (td, *J* = 7.3, 5.8 Hz, 4H), 1.59 (dd, *J* = 14.9, 7.6 Hz, 4H), 1.43 – 1.25 (m, 12H), 1.11 (s, 9H), 0.88 (t, *J* = 7.0 Hz, 6H). **^{13}C NMR (400 MHz, $CDCl_3$)** δ 177.79, 164.95, 151.26, 133.93, 128.90, 125.76, 89.71, 40.28, 38.94, 31.55, 29.48, 26.90, 26.80, 22.62, 14.09. **HRMS (ESI):** Calc. for $C_{26}H_{42}N_2O_5$ $[M+H]^+$: 463.3178; Found: 463.3173.

5.4.4. Esterase mediated cleavage of 2 to release using ^{1}H NMR spectroscopy.

The compound **2** in DMSO (1 mM) was dissolved in phosphate buffer solution (10 mM, pH = 7.2). To this solution was added esterase enzyme (4U/mL) at 37˚C and this enzymatic reaction was continued for different time intervals. After each interval, the compound was extracted using ethyl acetate, concentrated *in vacuo* and submitted for ^{1}H NMR spectroscopy.

5.4.5. Ion Transport Studies.

The ion transport experiments were carried out as mentioned in previous chapters with a small modification. To a cuvette containing EYPC-LUVs ⊃ lucigenin vesicle stock solution (2 mL), each of the sample solutions extracted from the above mentioned enzymatic reaction was added and compared to the parent compound **1b**. The rate of transport studies suggested that the almost complete recovery of ion transport of **2** treated with esterase takes place within 3 h.

5.4.6. Biological Studies.

I. Apoptosis Pathway.

All the protocols for evaluation of apoptosis were followed as discussed in previous chapters.

II. Autophagy Induction.

(A). Acridine Orange Staining.

MCF-7 cells (10^6 cells/mL) were seeded in 35 mm glass plates for 24 h and then after compound **2** (15 µM) was added. DMSO was added to control cells. After 1 hour of incubation, cells were washed twice with PBS and incubated in 5 µg/mL acridine orange solution (Sigma-Aldrich) during 30 min at room temperature. Finally, cells were washed with PBS-10% FBS three times and fluorescence was examined with a confocal microscope (Leica sp8) under green and red channels.

(B). Expression of Lamin B1 and LC3 by Immunoblot Analysis.

MCF-7 cells were seeded at a density of 6 x 10^5 cells per well in 6-well tissue culture treated plates (Corning) and maintained at 37 °C for 24 h. Cells were then treated with 15 µM of **2** by direct addition of drug to the culture medium for 24 h. Control cells were treated with equivalent volume of DMSO. After 24 h treatment, medium containing **2** was aspirated and cells were washed once with 1X phosphate buffered saline (PBS; PAN-Biotech GmbH). Cells were lysed in sample buffer containing 60 mM Tris (pH 6.8), 6% glycerol, 2% sodium dodecyl sulfate (SDS), 0.1 M dithiothreitol (DTT) and 0.006% bromophenol blue and lysates were stored at - 40 °C.

Cell lysates were resolved using sodium dodecyl sulfate polyacrylamide gel electrophoresis (SDS-PAGE) and transferred to Immobilon–P polyvinylidene difluoride (PVDF) membrane (Millipore). Blocking was performed in 5% (w/v) skimmed milk (SACO Foods, USA) prepared in 1X Tris buffered saline containing 0.1% Tween 20 (1X TBS-T) for 1 hour at room temperature. Blots were incubated for 16 h at 4 ^oC temperature in primary antibody solution. Following washes, blots were incubated with peroxidase-conjugated secondary antibody solution prepared in 5% (w/v) skimmed milk in 1X TBS-T for 1 h at room temperature following which blots were developed using Immobilon Western Detection Reagent kit (Millipore) and visualized using ImageQuant LAS 4000 (GE Healthcare).

5.5. NMR SPECTRA:

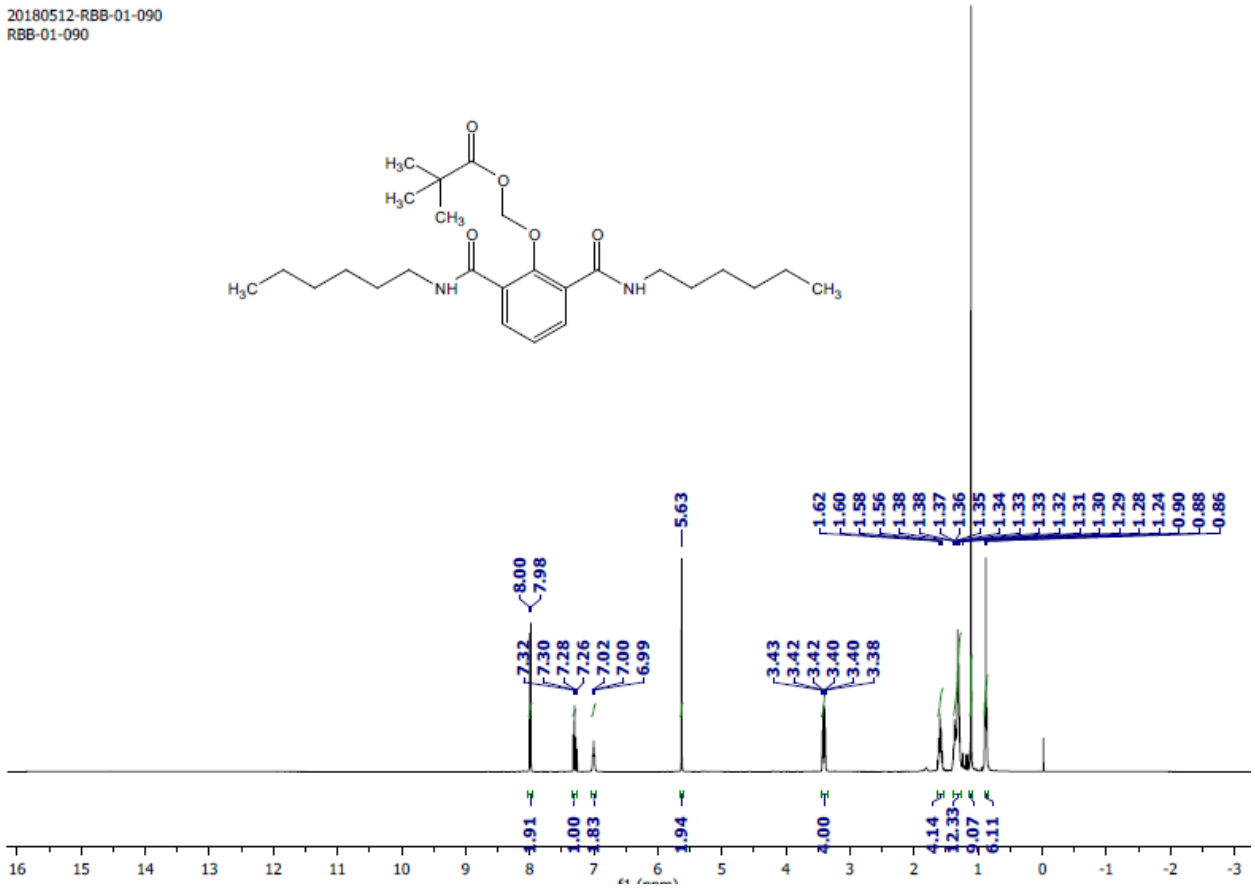

Figure 5.9. ^{1}H NMR spectrum of **2**.

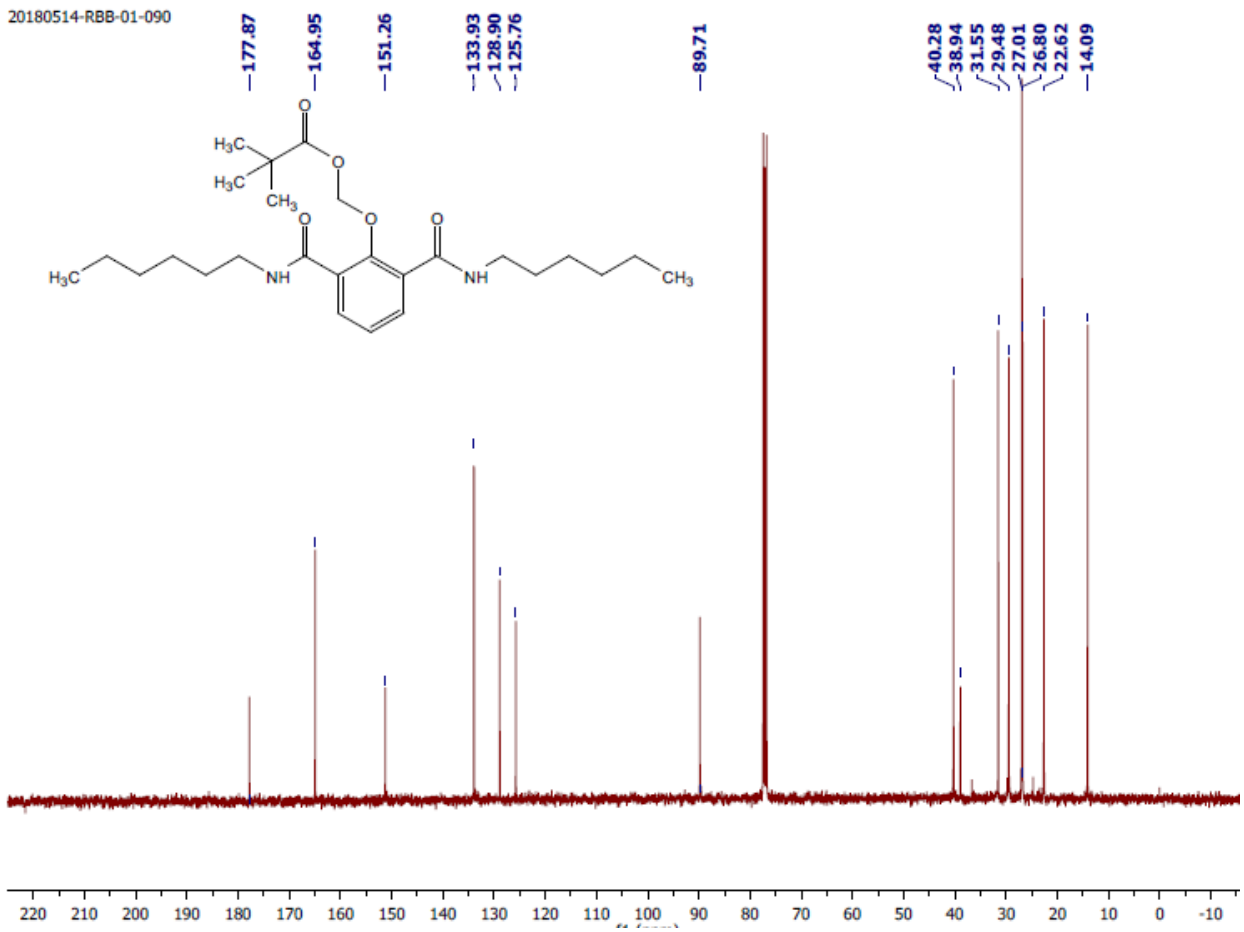

Figure 5.10. ^{13}C NMR spectrum of **2**.

5.6. REFERENCES:

(1) Rinehart, J.; Maksimova, Y. D.; Tanis, J. E.; Stone, K. L.; Hodson, C. A.; Zhang, J.; Risinger, M.; Pan, W.; Wu, D.; Colangelo, C. M.; Forbush, B.; Joiner, C. H.; Gulcicek, E. E.; Gallagher, P. G.; Lifton, R. P. *Cell* **2009**, *138*, 525.

(2) Kahle, K. T.; Deeb, T. Z.; Puskarjov, M.; Silayeva, L.; Liang, B.; Kaila, K.; Moss, S. J. *Trends Neurosci.* **2013**, *36*, 726.

(3) Choi, Y. R.; Lee, B.; Park, J.; Namkung, W.; Jeong, K.-S. *J. Am. Chem. Soc.* **2016**, *138*, 15319.

(4) Dong, H.; Pang, L.; Cong, H.; Shen, Y.; Yu, B. *Drug Deliv.* **2019**, *26*, 416.

(5) Li, X.; Gao, X.; Shi, W.; Ma, H. *Chem. Rev.* **2014**, *114*, 590.

(6) McGoldrick, C. A.; Jiang, Y. L.; Paromov, V.; Brannon, M.; Krishnan, K.; Stone, W. L. *BMC cancer* **2014**, *14*, 77.

(7) Busschaert, N.; Park, S.-H.; Baek, K.-H.; Choi, Y. P.; Park, J.; Howe, E. N. W.; Hiscock, J. R.; Karagiannidis, L. E.; Marques, I.; Félix, V.; Namkung, W.; Sessler, J. L.; Gale, P. A.; Shin, I. *Nat. Chem.* **2017**, *9*, 667.

(8) Chauhan, P.; Bora, P.; Ravikumar, G.; Jos, S.; Chakrapani, H. *Org. Lett.* **2017**, *19*, 62.

(9) Salunke, S. B.; Malla, J. A.; Talukdar, P. *Angew. Chem. Int. Ed.* **2019**, *58*, 5354.

(10) Malla, J. A.; Roy, A.; Talukdar, P. *Org. Lett.* **2018**, *20*, 5991.

(11) Saha, T.; Gautam, A.; Mukherjee, A.; Lahiri, M.; Talukdar, P. *J. Am. Chem. Soc.* **2016**, *138*, 16443.

(12) Saha, T.; Hossain, M. S.; Saha, D.; Lahiri, M.; Talukdar, P. *J. Am. Chem. Soc* **2016**, *138*, 7558.

(13) Sakamuru, S.; Attene-Ramos, M. S.; Xia, M. *Methods Mol. Biol.* **2016**, *1473*, 17.

(14) Patil, S.; Kuman, M. M.; Palvai, S.; Sengupta, P.; Basu, S. *ACS Omega* **2018**, *3*, 1470.

(15) Ashkenazi, A. *Nat. Rev. Drug. Discov.* **2008**, *7*, 1001.

(16) Smiley, S. T.; Reers, M.; Mottola-Hartshorn, C.; Lin, M.; Chen, A.; Smith, T. W.; Steele, G. D.; Chen, L. B. *Proc. Nat. Acad. Sci. U. S. A.* **1991**, *88*, 3671.

(17) Poncet, D.; Boya, P.; Métivier, D.; Zamzami, N.; Kroemer, G. *Apoptosis* **2003**, *8*, 521.

(18) Cossarizza, A.; Baccarani-Contri, M.; Kalashnikova, G.; Franceschi, C. *Biochem. Biophys. Res. Commun.* **1993**, *197*, 40.

(19) Sabharwal, S. S.; Schumacker, P. T. *Nat. Rev. Cancer* **2014**, *14*, 709.

(20) Liou, G. Y.; Storz, P. *Free Radic Res* .**2010**, *44*, 479.

(21) Wu, D.; Yotnda, P. *J J. Vis. Exp.* **2011**.

(22) Cullen, S. P.; Martin, S. J. *Cell Death Differ.* **2009**, *16*, 935.

(23) Wu, J.; Liu, T.; Xie, J.; Xin, F.; Guo, L. *Cell. Mol. Life Sci.* **2006**, *63*, 949.

(24) Shi, Y. *Mol. Cell* **2002**, *9*, 459.

(25) Chaitanya, G. V.; Alexander, J. S.; Babu, P. P. *Cell Commun. Signal.* **2010**, *8*, 31.

(26) Park, S. H.; Choi, Y. P.; Park, J.; Share, A.; Francesconi, O.; Nativi, C.; Namkung, W.; Sessler, J. L.; Roelens, S.; Shin, I. *Chem. Sci.* **2015**, *6*, 7284.

(27) Soto-Cerrato, V.; Manuel-Manresa, P.; Hernando, E.; Calabuig-Fariñas, S.; Martínez-Romero, A.; Fernández-Dueñas, V.; Sahlholm, K.; Knöpfel, T.; García-Valverde, M.; Rodilla, A. M.; Jantus-Lewintre, E.; Farràs, R.; Ciruela, F.; Pérez-Tomás, R.; Quesada, R. *J. Am. Chem. Soc.* **2015**, *137*, 15892.

(28) Leung, K.; Chakraborty, K.; Saminathan, A.; Krishnan, Y. N*at. Nanotechnol.* **2019**, *14*, 176.

(29) Dou, Z.; Xu, C.; Donahue, G.; Shimi, T.; Pan, J.-A.; Zhu, J.; Ivanov, A.; Capell, B. C.; Drake, A. M.; Shah, P. P.; Catanzaro, J. M.; Daniel Ricketts, M.; Lamark, T.; Adam, S. A.; Marmorstein, R.; Zong, W.-X.; Johansen, T.; Goldman, R. D.; Adams, P. D.; Berger, S. L. *Nature* **2015**, *527*, 105.

(30) Baek, K.-H.; Park, J.; Shin, I. *Chem. Soc. Rev.* **2012**, *41*, 3245.

❖*Overall Conclusion*

In the overall conclusion, I can say that the overall aim of doctoral research was to introduce the basic concepts of ion channel formation by using non-covalent interactions and to explore their therapeutic applications. The thesis deals with the basic concepts of self-assembly behavior of small molecules which can form transmembrane ion channels. The involvement of multiple ion binding sites by variation of the self-assembly of the individual monomeric units can be established to enhance the rate of ion transport across the bilayer membrane. Furthermore, the ion selectivity can also be modulated. The active self-assembly, and thus the active channel formation, can be hampered by the use of a stimulus-responsive linker, which can be cleaved by specific stimulus to regenerate the ion transport. Thus, the signal responsive ion transport systems can be generated. Moreover, these ion channels can mediate the apoptosis in cancer cells by perturbation of ionic homeostasis in cells, as well as disrupt autophagy. These studies will open new gates for the involvement of artificial ion transport systems in therapeutic applications.

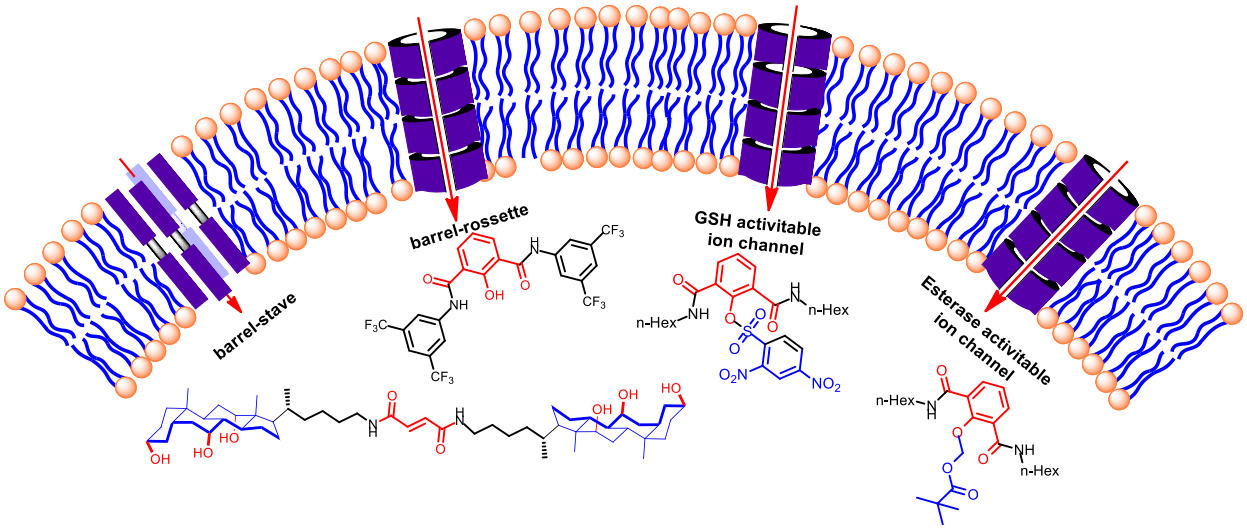

Figure:. Schematic representation of Ion transport systems discussed in thesis.

END OF THESIS